QUANTUM OPTICAL PROPERTIES OF NANOWIRE QUANTUM DOTS

Patrick Laferrière

Thesis submitted to the University of Ottawa in partial fulfillment of the requirements for the degree of

Doctor of Philosophy in Physics

Department of Physics
University of Ottawa

Abstract

Ideal sources of single-photons are required for proposed applications in quantum information technologies, such as quantum cryptography, and linear optical quantum computing. Quantum dots have become one of the most promising candidates for the generation of ideal single-photons due to its low multi-photon emission probability, entangled pair generation with high fidelity, and can be generated on-demand. The most common quantum dots studied are self-assembled quantum dots which nucleate on a surface in a random nature providing a series of dots randomly positioned and of random sizes. Much work has been done to achieve high extraction efficiencies by creating different photonic structures around these quantum dots. This work investigates the quantum optical properties of Indium Arsenide Phosphide (InAsP) quantum dots embedded within Indium Phosphide (InP) nanowire photonic waveguides grown bottom-up using selective-area vapour-liquid-solid epitaxy. These structures provide full control over the quantum dot size, composition, and its position along the nanowire waveguide axis. We characterize the sources in terms of their efficiencies, single-photon purity, and spectral purity. We show that our devices operate at efficiencies up to 30% with a single-photon purity as high as 99.4% and can reach linewidths that are twice the lifetime limited value, unprecedented for the above-band excitation scheme employed.

Studies of the second-order auto- and cross-correlations of the nanowire quantum dots is provided, which shows rich temporal features. We show that different excitonic complexes exhibit different correlation spectra and are unique to each complex. The study of cross-correlation measurements provided an unbiased, accurate method to distinguish and identify different complexes emitted by the quantum dots. A stochastic model is provided to model auto-correlation measurements which highlight the complex nature of the carrier dynamics within nanowire quantum dots. Such studies are a step closer to the full understanding of the dot dynamics within nanowire waveguides.

An interesting consequence of growing nanowires using the bottom-up epitaxial growth method is that quantum dots can be selectively positioned within the core of the nanowire waveguide. Such selectivity, along with wavelength tuning of the quantum dots, allows for the incorporation of multiple quantum dots within the same nanowire waveguide emitting at specific wavelengths. We show that the total single-photon emission rate scales linearly with the number of incorporated emitters whilst maintaining a high single-photon purity. The

total emission rate of such wavelength multiplexed sources would then be limited only by the number of emitters, providing a route towards GHz emission rates.

Finally, a new growth approach to generate single-photons at telecom wavelengths is investigated: the dot-in-a-rod embedded in a photonic nanowire waveguide. We demonstrate that this new growth approach provides efficient and highly pure single-photons at telecom wavelengths operating at 4 K. We then investigate the single-photon purity as a function of temperature up to room temperature. The results at elevated temperatures are shown to outperform all other existing quantum dot based approaches at telecom wavelengths.

Acknowledgements

I would like to thank many people for their support during my PhD studies. First, I would like to thank my supervisor, Dr. Dan Dalacu, for welcoming me as his first graduate student. Thank you Dan for providing me continuous support, valuable advice, and always taking the time to help in any way that you could.

I would also like to thank my colleague and lab partner, Edith Yeung, who I had the pleasure to mentor for a few months before quickly being able to do many experiments on her own. Many of the work done in this thesis would not have been as enjoyable without having her work by my side.

I would like to thank the many co-op students. Thank you Henri Morin, Isabelle Miron, and Aria Xinyao Yin, who helped write many of the automation programs used in this thesis. I also thank Leila Kusmic, Isabelle Miron, and Aria Yin for helping me take linewidth measurements presented in this thesis.

I would like to thank Dr. Marek Korkusinski who always finds time to explain concepts in detail. I would like to also thank Marek for providing theory to go with the findings in this thesis and for writing MATLAB codes for simulating correlation functions.

I wish to thank Dr. Philip J. Poole for growing the nanowires analyzed in this thesis, as well as Dr. Sofiane Haffouz for his contribution to the telecom nanowire growth and sample preparations. I also thank, Dr. Robin L. Williams, Dr. David. B. Northeast, and Dr. Khaled Mnaymned for valuable discussions. I thank everyone at the National Research Council for providing an enjoyable work environment. Lastly, I would like to thank my family and friends for their continuous support.

Publications included in the thesis

Article 1: **P. Laferrière**, E. Yeung, M. Korkusinski, P. J. Poole, R. L. Williams, D. Dalacu, J. Manalo, M. Cygorek, A. Altintas, & P. Hawrylak, "Systematic study of the emission spectra of nanowire quantum dots", Applied Physics Letters **118**, 161107 (2021).

Article 2: **P. Laferrière**, E. Yeung, I. Miron, D. B. Northeast, S. Haffouz, J. Lapointe, M. Korkusinski, P. J. Poole, R. L. Williams, & D. Dalacu, "Unity Yield of deterministically positioned quantum dot single photon sources", Scientific Reports **12**, 6376 (2022).

Article 3: **P. Laferrière**, E. Yeung, M. Korkusinski, P. J. Poole, R. L. Williams, & D. Dalacu, "Correlation spectroscopy of nanowire quantum dots", in preperation (2022).

Article 4: **P. Laferrière**, A. Yin, E. Yeung, L. Kusmic, M. Korkusinski, P. Rasekh, D. B. Northeast, S. Haffouz, J. Lapointe, P. J. Poole, R. L. Williams, & D. Dalacu, "Approaching transform-limited photons using nanowire quantum dots", arXiv:2208.00066 (2022).

Article 5: **P. Laferrière**, E. Yeung, L. Giner, S. Haffouz, J. Lapointe, G. C. Aers, P. J. Poole, R. L. Williams, & D. Dalacu, "Multiplexed Single-Photon Source Based on Multiple Quantum Dots Embedded within a Single Nanowire", Nano Letters **20**, 3688-3693 (2020).

Article 6: **P. Laferrière**, S. Haffouz, D. B. Northeast, P. J. Poole, R. L. Williams, & D. Dalacu, "Position-controlled Telecom Single Photon Emitters Operating at Elevated Temperatures", Nano Letters **23**, 3, 962-968 (2023).

Statement of contribution

Chapter 3 contains data taken by P. Laferrière with the exception of the linewidth polarization data presented in Chapter 3.5 which was taken by A. Yin. The coherence and HOM measurements presented in Chapter 3.9 and 3.10 were performed alongside E. Yeung. Chapter 4 contains a simulation provided by R. L. Williams (see Figure 4.3 (a)) and the As concentration data and TEM image were provided by Xiaohua Wu (see Figure 4.4).

In the following, Articles 1-6, J. Lapointe did the e-beam patterning and S. Haffouz did the sample preparation. P. J. Poole grew the nanowires for Articles 1-5. The experiments were conducted in at the National Research Council Canada (R. L. Williams lab).

Article 1 presented in Chapter 5 was done in collaboration with the quantum theory group at UOttawa where P. Laferrière, D. Dalacu and P. Hawrylak conceived the idea for the work. P. Laferrière and E. Yeung performed the experiment and data analysis. J. Manalo and A. Altintas performed the calculation. P. Laferrière, D. Dalacu, J. Manalo, and P. Hawrylak wrote the manuscript. All authors discussed the results and contributed to the text of the manuscript.

P. Laferrière, D. Dalacu, and P. J. Poole conceived the idea for the work presented in Chapter 6 (Article 2). I. Miron wrote the python script for taking linewidth measurements. P. Laferrière and I. Miron performed the linewidth and lifetime measurements and its analysis. P. Laferrière and E. Yeung performed the photoluminesence and auto-correlation measurements and its analysis. P. Laferrière and D. Dalacu wrote the manuscript and all authors discussed the results and contributed to the text of the manuscript.

P. Laferrière and D. Dalacu conceived the idea for the work presented in Chapter 7 (Article 3). M. Korkusinski provided the model to simulate the second-order correlation functions. P. Laferrière conducted the experiment along with the data analysis and provided the simulation results. P. Laferrière wrote the manuscript with the guidance of D. Dalacu.

P. Laferrière, D. B. Northeast, and D. Dalacu conceived the idea for the work presented in Chapter 8 (Article 4). A. Yin wrote the python script for taking the linewidth measurements. P. Laferrière and A. Yin investigated the linewidth dependence on excitation power and temperature. P. Laferrière and L. Kusmic investigated the optimal achievable linewidths from

nanowires grown under different growth temperatures. P. Laferrière and E. Yeung analyzed other nanowires as a function of power and temperature, not included in the article. P. Laferrière analyzed the data and M. Korkusinski provided the theory. The manuscript was written by P. Laferrière, D. Dalacu, and M. Korkusinski. All authors discussed the results and contributed to the text of the manuscript.

D. Dalacu, and P. J. Poole conceived the idea for the work presented in Chapter 9 (Article 5). P. Laferrière conducted the experiment and analysis with the help of E. Yeung. G. C. Aers provided the second-order correlation model. P. Laferrière and D. Dalacu wrote the manuscript. All authors discussed the results and contributed to the text of the manuscript.

P. Laferrière, S. Haffouz, P. J. Poole, and D. Dalacu conceived the idea for the work presented in Chapter 10 (Article 6). P. Laferrière conducted the experiment and the data analysis was done alongside P. J. Poole. S. Haffouz and P. J. Poole grew the nanowires. All authors discussed the results and contributed to the text of the manuscript.

List of Figures

Contents

Chapter 1

Introduction

Sources of single-photons are a key component in many proposed schemes in quantum information processing applications. In such applications, photons act as quantum bits of information, qubits, the simplest unit of such quantum information. The fundamental difference between a classical bit of information and a qubit is that qubits can be prepared in a superposition of states. Applications that can utilize qubits include quantum cryptography[4][5][6], linear optical quantum computing[7, 8], and quantum sensing[9, 10, 11, 12]. Secure communication schemes such as quantum key distribution (QKD) have already been implemented with single[4] and entangled photon pairs[13, 14] outside of the laboratory. Quantum computing[7], which is expected to solve complex algorithms at a much faster rate compared to classical computers, utilizes the superposition of states and would allow for trying all solutions at once. Quantum sensing and metrology can also benefit from qubits, resulting in more precise measurements. These example-applications have led to the rapid development of single-photon sources. Available sources of single-photons include probabilistic sources based on spontaneous parametric down-conversion (SPDC) and four-wave mixing (FWM), as well as deterministic sources such as atoms, ions, molecules, defect centers, and semiconductor quantum dots.

Single-photons are particularly interesting candidates for qubits due to the various available degrees of freedom (DOF) (e.g., frequency, polarization, position, and momentum). The most commonly employed DOF is the photon polarization[15], which can be easily manipulated using standard optical elements. Another often used DOF is arrival time used in time-bin encoded qubits. There the information is stored in the arrival time, within some time window, of the photons that can be tuned using a Mach-Zhender interferometer[16]. Other

DOF include orbital angular momentum[17] and frequency; the latter providing a route to wavelength division multiplexing[18] for increased scalability.

1.1 Ideal single-photons

In order for a source of single-photons to be useful for applications, they must satisfy various application-specific requirements. An ideal source of single-photons will have the following four basic properties:

- High efficiency (and high brightness): The source should be able to emit single-photons on-demand after an excitation event such as a short laser pulse and be able to operate at high repetition rates with high efficiency (i.e. low loss).
- High single-photon purity: The source should emit single-photons with zero probability of multi-photon emission events.
- High degree of coherence: The linewidth of the emitted photons should be equal to its Fourier-limited linewidth.
- High indistinguishability: The emitted photons from the source should be identical in every aspect (spectral bandwidth, pulse width, polarization, and mode profile).

These four properties are visually shown in Figure 1.1[1]. In (a) we show a stream identical single-photons generated from an ideal single-photon source. In this case, individual identical photons are triggered with 100% efficiency. In Figures 1.1 (b)-(e) we show a stream of photons from a source that does not meet one of the basic requirement discussed above. An efficiency lower than 100%, shown in (b), will generate a stream of single-photons with some missing photons, e.g. due to losses in the optical system in question or the internal quantum efficiency of the emitter. It is also important that a stream of photons carrying information is composed of only single-photons. A low single-photon purity, as shown in (c) will generate multi-photon emission events and can disrupt the information a photon is carrying. A single-photon source should also retain its phase coherence for long periods of time. Electron-hole pairs used to generate single-photons are subject to interactions with their environment which can lead to a loss of coherence shown in (d) and will broaden the linewidth of the photons. Having a coherence time, limited only by the lifetime of the emitter, is a fundamental requirement to generate indistinguishable photons. Photons are indistinguishable if they are identical

in terms of their spectral bandwidth, pulse width, polarization, and mode profile and are required to perform low error quantum computation. These properties will be discussed further in Chapter 2 and throughout the thesis. A comparison of the source requirements for various applications can be found in Ref. [19].

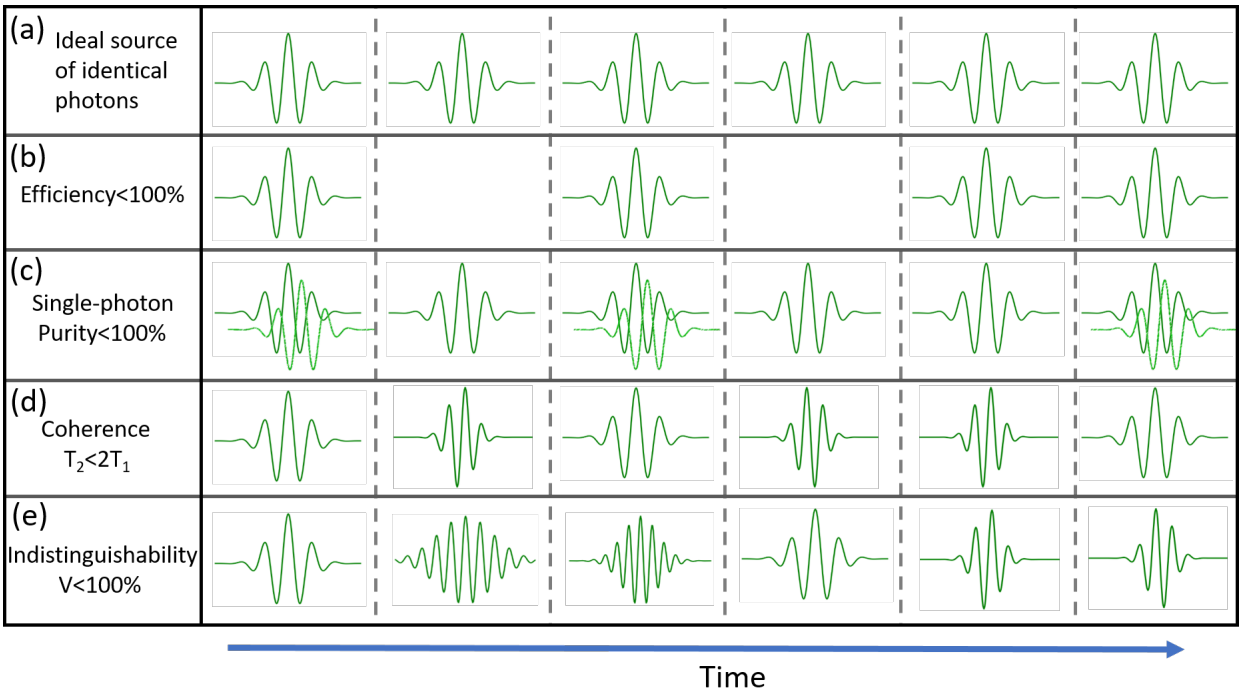

Figure 1.1: Electric fields of photon wavepackets having different characteristics: (a) Ideal source: a stream of single, identical photons, are generated per excitation event. (b) Example of a source with an efficiency less than 100% where some excitation events do not trigger a single-photon. (c) After each excitation event there's a probability of generating multiple photons. (d) Loss of photon phase coherence. (e) Non-ideal indistinguishability: the photon wave packet changes due to phase variations or spectral wandering (adapted from Ref. [1]).

As well as the four basic properties discussed above, several other properties are typically required:

- Gaussian emission mode: Photons emitted in a Gaussian mode are required for efficient fiber coupling.
- Frequency tuning: Photons should be able to emit at desired wavelengths, which is especially important in order to implement multiple sources capable of generating indistinguishable photons required for quantum communication or linear optics quantum computation based on two photon interference. The source should also be able to

be tuned to telecom wavelengths (1310 nm and 1550 nm) for low loss long distance communication in optical fibers.

- Entanglement: For long distance quantum communication, entangled photon pair generation is required for the implementation of quantum repeaters. These sources are also particularly important for quantum computing.

- Electrically driven: In order to simplify the integration of single-photon sources with small scale devices, a source should be able to generate single-photons using electrical triggers, thereby removing the need for laser excitation.

- Room temperature operation: A single-photon emitter should, preferably, be able to operate at room temperature. The optimal performance of solid-state emitters such as quantum dots are limited to cryogenic temperatures due to interactions with phonons that broaden linewidths at higher temperatures.

Among available sources of single-photons, quantum dots have become interesting candidates as ideal sources. They have demonstrated most of the properties listed above with some exceptions. Challenges remain in the generation of single-photons and entangled-photon pairs with 100% efficiencies. Quantum dot single-photon sources are also optimized at low operating temperature, in most cases $\sim 4\,\mathrm{K}$ due to linewidth broadening from phonons at higher operating temperatures. In this thesis, the quantum optical properties of InP/InAsP nanowire quantum dots grown epitaxially are investigated.

1.2 Quantum optical properties of nanowire quantum dots: outline of the thesis

In this chapter ,I have briefly introduced different applications requiring the need for good single-photon sources. I also describe different properties required from such sources. The next chapters of the thesis, Chapters 2-4, provide background information on single-photons, quantum dots, measurement techniques and growth methods, whilst in Chapters 5-10, I present a series of articles.

Chapter 2: In Chapter 2, I introduce methods to characterize various properties of non-classical light sources, including source efficiency, single-photon purity, coherence, and indistinguishability. These fundamental characteristics of single-photons are utilized throughout the thesis.

Chapter 3: In Chapter 3, I provide the basic physics behind quantum dots. This includes quantum confinement, selection rules, and optical spectroscopy. In this chapter, I also provide example measurements on InP/InAsP nanowire quantum dots and describe the experimental setups for the different measurements.

Chapter 4: In Chapter 4, I describe the experimental methods used to grow the nanowire quantum dot devices. We then suggest a new growth method in order to achieve bright quantum dot emission at telecom wavelengths. This chapter also contains the general setup used in the laboratory for the measurements presented in Chapter 3 and in Chapters 5-10 (Articles 1-6).

Chapter 5 (Article 1): In Article 1, we performed a systematic study of nominally identical nanowire quantum dots having similar emission spectra. The different excitonic complexes were identified using power-dependent photoluminescence measurements along with correlation measurements. We show that different excitonic complexes have unique correlation spectra and provide a more accurate method of distinguishing between complexes. This method is utilized in the subsequent articles. We characterize individual excitonic complexes in terms of their emission energies and energy separation. The experimental spectra are understood using atomistic multi-million atom theory and provide a step towards the full understanding of the dot dynamics within a nanowire waveguide.

Chapter 6 (Article 2): In Article 2, we characterize an array of 10×10 nanowire quantum dots in terms of their efficiencies, single-photon purity, emission lifetime, and spectral purity. We demonstrate that the bottom-up epitaxial nanowire growth method provides unity device yield.

Chapter 7 (Article 3): Article 3 provides a more detailed analysis of the correlation measurement of the different excitonic complexes observed in our nanowire quantum dots. The rich, temporal features observed are modeled stochastically, providing another step towards the full understanding of the dot dynamics within nanowire waveguides.

Chapter 8 (Article 4): In Article 4, we study the linewidth dependence on excitation power and temperature in order to understand the possible mechanisms leading to the observed broadening. In the article, we describe the linewidth broadening in terms of an independent Boson model that includes both deformation and piezoelectric exciton-phonon coupling.

Chapter 9 (Article 5): In Article 5, we show that the bottom-up epitaxial growth method of the nanowires allows for the incorporation of multiple quantum dots within the same

nanowire waveguide. We characterize a source containing five quantum dots, each individually tuned to emit at specific wavelengths, in terms of their single-photon purity and overall detected count rate.

Chapter 10 (Article 6): In Article 6, we present a dot-in-a-rod growth method in order to generate quantum dot emission at telecom wavelengths. The quantum dot is characterized by its single-photon purity and efficiency at 4 K. We then study the single-photon purity as a function of temperature up to room-temperature.

Chapter 11: A brief conclusion of the results is presented along with future directions of the research.

Chapter 2

Characterization of non-classical light sources

This chapter provides general background information on the characterization of non-classical light which will then be expanded upon in later chapters. Mainly, the four main characteristics a single-photon source should have in order to be an ideal source: the efficiency, single-photon purity, coherence, and indistinguishability; all of which should be optimized. For single-photon purity, I also discuss different properties of light in terms of photon statistics that can exist such as coherent light, thermal light and anti-bunched light (single-photons). Finally, I provide examples of different types of sources that generate single-photons.

Single-photons have become interesting candidates for qubits to encode quantum information. They provide the opportunity to utilize different degrees of freedom such as polarization, spacial modes, and frequency in order to encode information.

We have seen in Chapter 1 that an ideal source of single-photons is a source where, once triggered, provides one and only one photon. This emitted photon would then be in a pure single-photon Fock state in a well defined mode:

$$|\psi>=|1>. \tag{2.1}$$

Typically this state is interesting, but to be useful for many applications we would require a stream of single-photons each having a well defined time dependency. To describe a single-photon wave packet, one needs to write the single-photon state as a superposition of different

frequencies. Decomposing it in terms of plane waves, having wave vector k, angular frequency $\omega = c|k|$ and polarization ϵ, we can write it as [20]

$$|\psi >= \sum_{k,\epsilon} c_{k,\epsilon}|1 >_{k,\epsilon}, \tag{2.2}$$

where $\sum_{k,\epsilon} |c_{k,\epsilon}|^2 = 1$ and $|\psi >$ is an eigenstate of the total photon number. In this chapter the performance of sources in the form of Eq. 2.2 will be described in terms of efficiency, single-photon purity, coherence and indistinguishability.

2.1 Efficiency

A quantum light source should produce a large flux of photons which can couple into an optical system. If the efficiency of the source is limited, it will generate a state composed of vacuum and single-photons in the form[21]

$$|\psi >= a|0 > +b|1 >, \tag{2.3}$$

where $|a|^2 + |b|^2 = 1$ and $|a|^2$ and $|b|^2$ is the probability of generating a vacuum state and a single-photon Fock state respectively. The maximum photon count will be limited by the internal quantum efficiency of the source η_{IQE}, the spontaneous emission rate Γ, and the efficiency to couple the emission to external optics α. We define the source efficiency as

$$\eta = \alpha\beta_M\eta_{IQE} = \alpha \times \frac{\Gamma_M}{\Gamma_M + \Gamma_{\text{Rad}}} \times \eta_{IQE}, \tag{2.4}$$

with Γ_M the emission rate of the emission mode M in question, Γ_{Rad} any other radiative modes.

2.2 Single-photon purity

The single-photon purity measures the likeliness that one and only one photon is emitted (i.e. how well suppressed are multiphoton emissions) from the source. In general Eq. 2.2 can be generalized to

$$|\psi>=\sum_{k,\epsilon} P_{k,\epsilon}|n>_{k,\epsilon}, \tag{2.5}$$

where n is not restricted to be 1. The presence of multiple photons will limit the performance of a device as a single-photon source and is measured through the second-order correlation function.

2.2.1 Second-order correlation function

Introduced by Glauber[22], the second-order correlation function has become the standard metric to gain information about photon statistics. In terms of intensity (or electric field), the normalized second-order correlation function can be written as

$$g^{(2)}(\tau) = \frac{< I(t)I(t+\tau)) >}{< I(t) >^2} = \frac{< E^*(t)E^*(t+\tau)E(t)E(t+\tau) >}{< E^*(t)E(t) >^2}, \tag{2.6}$$

where $I(t) = E(t)E^*(t)$ is the intensity at some time t and $I(t) = E(t+\tau)E^*(t+\tau)$ is the intensity at some time t after some time delay τ. For a single-mode plane wave traveling with wave vector $\mathbf{k}$, $E(t)$ is given by $E(t) = iE_0 a e^{i(\boldsymbol{k}\cdot\boldsymbol{r}-\omega t)}$, so that Eq. 2.6 can be rewritten and reduced to

$$g^{(2)}(0) = \frac{< a^\dagger a^\dagger a a >}{< a^\dagger a >^2} = \frac{< n(n-1) >}{< n >^2} = 1 + \frac{< (\Delta n)^2 > - < n >}{< n >^2} \tag{2.7}$$

for $\tau = 0$ where $a^\dagger(a)$ is the creation (annihilation) operator. Whereas, n is the photon number and $(\Delta n)^2$ is the variance. This can be measured directly using a Hanbury-Brown and Twiss (HBT) experiment[23]. A single-photon is sent to a 50:50 beamsplitter and each output paths are sent to two single-photon detectors. A counting card is used to measure the delay between detection events. The experimental realization will be discussed in further chapters. This measurement can be used to measure statistics to discern between different types of light, such as distinguishing between coherent light, thermal light, and anti-bunched light (single-photons), which are described below.

Coherent light

In an HBT measurement, using a coherent light source, such as a laser source, one measures a $g^{(2)}(\tau = 0)$ value of one, meaning the probability of detecting a photon at any time is always the same (i.e. each emission event is completely uncorrelated). A coherent state $|\alpha>$ is the eigenstate of the photon annihilation operator. In the Fock state basis it is given by[24]:

$$|\alpha >= e^{-\alpha^2/2} \sum_{0}^{\infty} \alpha^n |n> /\sqrt{n!}. \tag{2.8}$$

These states follow a Poisson distribution of photon number states. The probability of detecting n photons is given by

$$P_n = e^{|\alpha|^2} \frac{|\alpha|^{2n}}{n!}, \tag{2.9}$$

where the variance $(\Delta n)^2 =< n^2 > - < n >^2$ is equal to the mean photon number $< n >$. Eq. 2.9 gives a probability distribution that peaks around this mean value as shown in Figure 2.1 (a).

Thermal light

Thermal light, such as a light bulb, provides a source of radiation in thermal equilibrium with the environment (blackbody radiation). In such a case the probability of detecting n photons follows the Bose-Einstein statistics and is given by:

$$P(n) = \frac{< n >^n}{(1+ < n >)^{1+n}}. \tag{2.10}$$

The resulting statistics are defined as super-Poissonian where the variance of the photon number is $(\Delta n)^2 =< n^2 > + < n >$[25]. Here, the maximum probability of detecting a photon is achieved for $n = 0$, independent of the mean photon number $< n >$ as shown in Figure 2.1 (b). In the case of thermal light, we obtain $g^{(2)}(\tau = 0) = 2$. There are also other states that are considered super thermal (or super-bunching) with $g^{(2)}(\tau) > 2$ which I do not discuss.

Antibunched light

The Fock state, or number state is an eigenstate of the photon number operator n_i:

$$\hat{n}_i|n_i>=n_i|n_i>, \tag{2.11}$$

where n_i describes the number of photons in a specific mode i. The probability to find n_i photons in one mode is:

$$P(Fock_n) = \begin{cases} 1 & n = n_i \\ 0 & n \neq n_i \end{cases}. \tag{2.12}$$

For a number state $(\Delta n)^2 = 0$ as shown in Figure 2.1 (c), and thus, from Eq. 2.7

$$g^{(2)}(\tau = 0) = 1 - \frac{1}{n} < 1, \tag{2.13}$$

and for a single-photon state $n = 1$ implies a $g^{(2)}(\tau = 0)$ value of zero. For a state in which $n = 2$ (i.e. comprises of two photons) then $g^{(2)}(\tau = 0) = 0.5$. It is therefore generally accepted that a source is a single-photon source if $g^{(2)}(\tau = 0) < 0.5$. Such sub-Poisson statistics violates the classical limit for the second-order correlation function, determined by the Cauchy–Schwarz inequality:

$$< n(0) >^2 \leq < n(0)^2 > . \tag{2.14}$$

For this reason photon Fock states are defined as non-classical states of light.

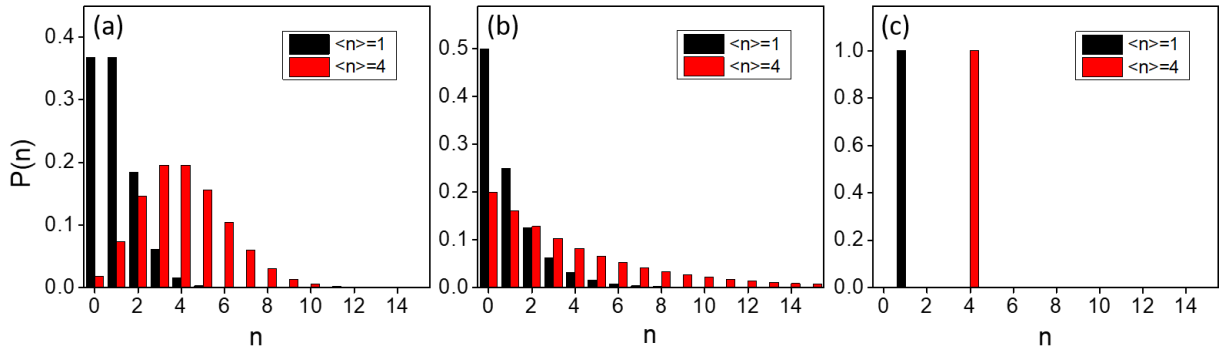

Figure 2.1: Probability distribution to find n photons for (a) coherent light, (b) thermal light and (c) antibunched light for average photon number $< n >= 1$ (black) and $< n >= 4$ (red).

2.3 Coherence

The next important fundamental characteristic of single-photons is the photon coherence, which represents the phase stability of a quantum state over time. The coherence time T_2 of a photon is the amount of time the phase correlation of the photon is maintained. The coherence length $L_c = cT_2$, where c is the speed of light, is the length over which this phase is maintained. This is described by the normalized first order correlation function and can be written as:

$$g^{(1)}(\tau) = \frac{< E^*(t)E(t+\tau)}{< |E(t)| >^2}. \tag{2.15}$$

This can be directly measured experimentally using a Michelson interferometer shown in Figure 2.2 (a). For a monochromatic source of light input on the beamsplitter of the Michelson interferometer, the electric field at the detector, D, is given by

$$E_{out} = \frac{1}{2}E_0 e^{i\frac{4\pi}{\lambda}L_1} + \frac{1}{2}E_0 e^{i\frac{4\pi}{\lambda}L_2}, \tag{2.16}$$

where L_1 and L_2 is the distance between the two mirrors and the beamsplitter and a relative phase shift is acquired at the output (detector D), which is given by $\phi = 4\pi(L_2 - L_1)/\lambda = 4\pi c\tau/\lambda$ where $\tau = (L_2 - L_1)/c$. As a consequence of interference at the beamsplitter, the measured intensity at the output of the Michelson interferometer will show oscillations (fringes)

with maxima observed for $\phi = 2\pi m$, where m is an integer. I have assumed a monochromatic light source however the same effect can be seen from single-photons[26]. Monochromatic light has a long coherence length and thus fringes would be observed for a long delay time τ. Since fringes would only be visible when τ is on the order of the coherence time, fringes from a white light source, for example, would be difficult to resolve.

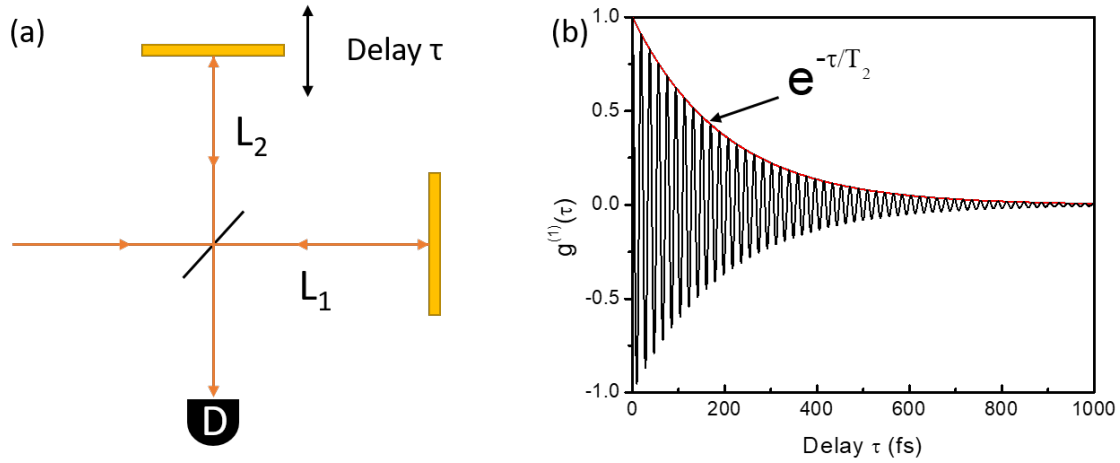

Figure 2.2: (a) Schematics of a Michelson interferometer. (b) Example of the decay of the interference fringes for a source having a coherence time of $T_2 = 200\,\text{fs}$ and a Lorentzian lineshape, $\tau = (L_2 - L_1)/c$, where c is the speed of light.

In Figure 2.2 (b), I plot a simulated $g^{(1)}(\tau)$ measurement for a source having a coherence time of $T_2 = 200\,\text{fs}$, for which the envelope of the interference fringes shows an exponential decay, $\text{e}^{-\tau/T_2}$, corresponding to a coherence length of $L_c = 60\,\text{nm}$. There is a fundamental limit in which there's an uncertainty as per when a photon will be emitted leading to a photon emission lifetime T_1. The emission energy distribution of an ideal source would then have a full-width half maximum (FWHM) equal to $\Delta f = 1/2\pi T_1$[27]. Several mechanisms may result in this bandwidth to be broadened and the coherence time should then be expressed as:

$$\frac{1}{T_2} = \frac{1}{2T_1} + \frac{1}{2T_2^*}. \tag{2.17}$$

For an non-ideal source where T_2^* is known as a pure dephasing term, which can be do to various fluctuations, and will be described further in Chapter 3. We can directly link the bandwidth of the source with the coherence time by $\Delta f = 1/\pi T_2$ and if $T_2^* = 0$ we obtain a Fourier lifetime limited ratio from Eq. 2.17:

$$\frac{2T_1}{T_2} = 1. \tag{2.18}$$

The main goal is to create a single-photon source such that the equality in Eq. 2.18 holds, which is a condition required to generate highly indistinguishable photons, as described below. An experimental attempt to achieve this is shown in Article 4 and an example of the direct measurement of the coherence time of our source is shown in Chapter 3.

2.4 Indistinguishability

Having a stream of photons that are indistinguishable from one another is a resource required for linear optical quantum computing[7] as well as quantum teleportation[28]. They are required for quantum key distribution to be realized at long distances[4, 5], quantum sensing[11, 29, 30] and large scale quantum networks such as the quantum internet[31]. These example applications utilize the interference of indistinguishable photons on beamsplitters.

2.4.1 Interference of single-photons

I start by describing the interference of single-photons on a beamsplitter. Identical incident photons can be described as:

$$a_1^\dagger a_2^\dagger |0,0>_{a_1 a_2} = |1,1>_{a_1 a_2}, \tag{2.19}$$

where $|0>$ and $|1>$ are the vacuum state and a single-photon ground state, respectively, whilst $a_1^\dagger$ and $a_2^\dagger$ are the two input states. When two identical photons interact at a beamsplitter, they undergo a unitary transformation (if there is no phase delay between each input path) where the output states $a_3^\dagger$, and $a_4^\dagger$ can be described as:

$$a_3^\dagger = \frac{a_1^\dagger + a_2^\dagger}{\sqrt{2}} \tag{2.20}$$

$$a_4^\dagger = \frac{a_1^\dagger - a_2^\dagger}{\sqrt{2}}. \tag{2.21}$$

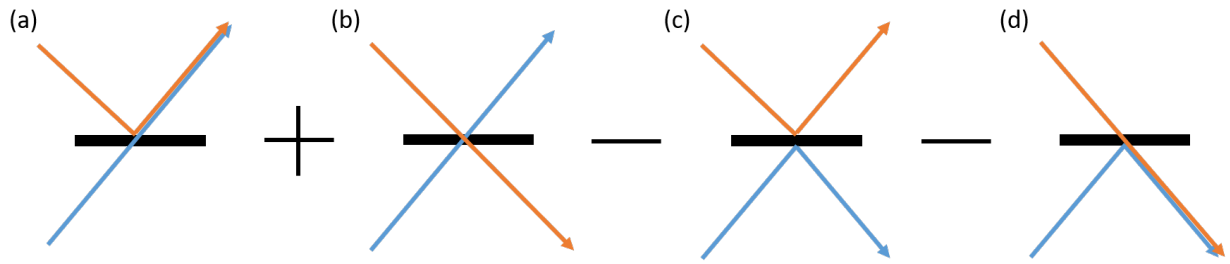

Figure 2.3: Hong-Ou-Mandel interference between two single-photons. The four figures represent the four possible outcomes of two photons on a beamsplitter: (a) the first photon is reflected and the second transmitted, (b) both transmitted, (c) both reflected, (d) the first transmitted and the second reflected. When the two photons are indistinguishable the cases (b) and (c) destructively interfere.

Therefore, the state of the output photons can be written as:

$$\begin{aligned} |1,1\ >_{a_1a_2} &= a_1^\dagger a_2^\dagger |0,0>_{a_1a_2} = (\frac{a_3^\dagger + a_4^\dagger}{\sqrt{2}})(\frac{a_3^\dagger - a_4^\dagger}{\sqrt{2}})|0,0>_{a_3^\dagger a_4^\dagger} \\ &= \frac{1}{2}(a_3^\dagger a_3^\dagger - a_4^\dagger a_4^\dagger)|0,0>_{a_3^\dagger a_4^\dagger} = \frac{|2,0>_{a_3^\dagger a_4^\dagger} - |0,2>_{a_3^\dagger a_4^\dagger}}{2}. \end{aligned} \tag{2.22}$$

Which means that the state $|1,1>$ vanishes and the photons are always exiting the beamsplitter together, which is known as the Hong-Ou-Mandel (HOM) effect[32]. The two processes in which the two photons are either both reflected or both transmitted interfere destructively with each other. However, if the photons are distinguishable (labeled a and b) we can write the input and output state as

$$|1_a,1_b>_{a_1a_2} = \frac{|2_{ab},0>_{a_3^\dagger a_4^\dagger} - |0,2_{ab}>_{a_3^\dagger a_4^\dagger} + |1_a,1_b>_{a_3^\dagger a_4^\dagger} - |1_b,1_a>_{a_3^\dagger a_4^\dagger}}{2}, \tag{2.23}$$

where, in this case, the four outcomes presented in Figure 2.3 are possible with equal probability because they are in fact distinguishable photons. The experimental realization of this effect will be revisited in Chapter 3.

2.5 Available single-photon sources

Many different sources have been suggested for the generation of single-photons, which I describe in this section together with some pioneering work.

Probabilistic sources

An approach widely used to achieve single-photons is based on spontaneous parametric down-conversion (SPDC) or four-wave mixing (FWM) in a non-linear medium. A process where a laser beam undergoes χ^2 or χ^3 processes within the medium in order to generate heralded single-photons (a single-photon pair production where the detection of a one photon guarantees the presence of a second). It provides a source which operates at room temperature and with high photon indistinguishability[33], purity[34], flexibility[35], and multiplexed capabilities for increased scalability[36]. The main limits of these sources is that they are probabilistic and cannot operate at high efficiencies whilst maintaining low multi-photon emissions[34].

Deterministic sources

Atoms, ions, and molecules: Single quantum emitters can be used as on-demand sources of single-photon Fock states. They are based on spontaneous emission processes, triggered by vacuum fluctuations of an electronic transition between two discrete energy levels, which can only generate a single-photon at a time. It is no surprise that the first measured single-photon source showing antibunching was from single atoms and ions[37, 38]. More recent work has been done on such sources [39, 40, 41]. The main problem with these sources is the complexity involved to integrate them with photonic devices for practical applications. Molecules, like atoms and ions, have discrete energy levels and can be optically excited to emit single-photons [42, 43, 44, 45, 46, 47].

Color centers in diamonds: Color centers in diamonds have been subject to extensive research as single-photon sources. Color centers in diamonds are due to defects in the crystal and the most studied is the Nitrogen-Vacancy[48, 49, 50]. The crystal defect consists of a carbon atom which is replaced with a nitrogen atom and an adjacent atom is left empty. Other color centers such as silicon[51] and nickel-nitrogen[52] have also been studied among many.

Quantum dots: Quantum dots are semiconductor nanostructures composed of tiny regions of smaller bandgap material surrounded by a larger bandgap semiconductor material. Examples of such materials used for quantum dots are CdSe in ZnS, InP in GaInP, InAs in GaAs, and InAsP in InP, which are the materials used throughout this work. The first demonstration of single-photon emission from a quantum dot was in 2000 by Michler et al.[53], which quickly gained attention from the scientific community[54, 55, 56, 57, 58, 59]. Subsequent work demonstrated electrical triggered single-photon emission[60] and the generation of entangled photon pairs with quantum dots[61, 62, 63]. Quantum dots show promising results as an ideal source of single-photons, capable of generating highly indistinguishable photons[64, 65] with high single-photon purity[66] and entangled pair generation with high fidelity[67], and can be potential ideal candidates for integration with photonic circuits[68]. Notably, there are different types of quantum dots, such as colloidal[69], gate-defined[70], and epitaxial[71, 72].[1]

[1]Note that a source which is not 100% efficient is inherently not perfectly deterministic due to losses (i.e. it is impossible to tell which photons were lost).

Chapter 3

Background on quantum dots

This chapter describes the basic physics of quantum dots including quantum confinement, selection rules, and optical spectroscopy. Most of the chapter applies to quantum dots in general, but we focus on Indium Arsenide Phosphide (InAsP) quantum dots within Indium Phosphide (InP), more specifically, InAsP quantum dots within InP nanowire photonic waveguides, which will be described in Chapter 4. The chapter contains data measured on such nanowire quantum dot samples and is complementary to the articles presented in Chapters 5 through 10. All data in this chapter is taken at a temperature of 4 K within a closed cycle helium cryostat (see Chapter 4 for details).

3.1 Quantum confinement

Precise calculations of the electronic states of quantum dots depend on the geometry and composition of the quantum dot in question and have been extensively developed[73]. In order to qualitatively understand the basics of the electronic states of quantum dots, one can consider a simple particle in a box where confinement effects become important when the physical size of the potential well is comparable to the de Broglie wavelength of the carriers[74], $\lambda_{deBroglie} = h/\sqrt{m^* k_b T}$, where h is the Planck's constant, m^* is the effective mass of the carriers, k_b is Boltzmann constant and T is the temperature. In the case of quantum dots, a small bandgap semiconductor material is placed within a semiconductor material with a larger bandgap, for example, InAsP within InP, where the larger bandgap material is typically a bulk structure. The energy of the discrete levels are given roughly by,

$$E = \frac{\pi^2\hbar^2}{2}\left(\frac{n_x^2}{L_x^2} + \frac{n_y^2}{L_y^2} + \frac{n_z^2}{L_z^2}\right)\left(\frac{m_e^* + m_h^*}{m_e^* m_h^*}\right), \tag{3.1}$$

where n_x, n_y, n_z are the principal quantum numbers, m_e^* and m_h^* are the effective mass of the electrons and holes, respectively, whilst L_x, L_y and L_z are the confinement dimensions and $\hbar = h/2\pi$ is the reduced Plank's constant. One can easily see that the energy levels are discrete. Furthermore, the energy levels can be tuned by changing the quantum dot size, or the quantum dot material, for example, by changing the concentration of As within an InAsP quantum dot. This bandgap tuning can be utilized to achieve quantum dot emission at very specific energies.

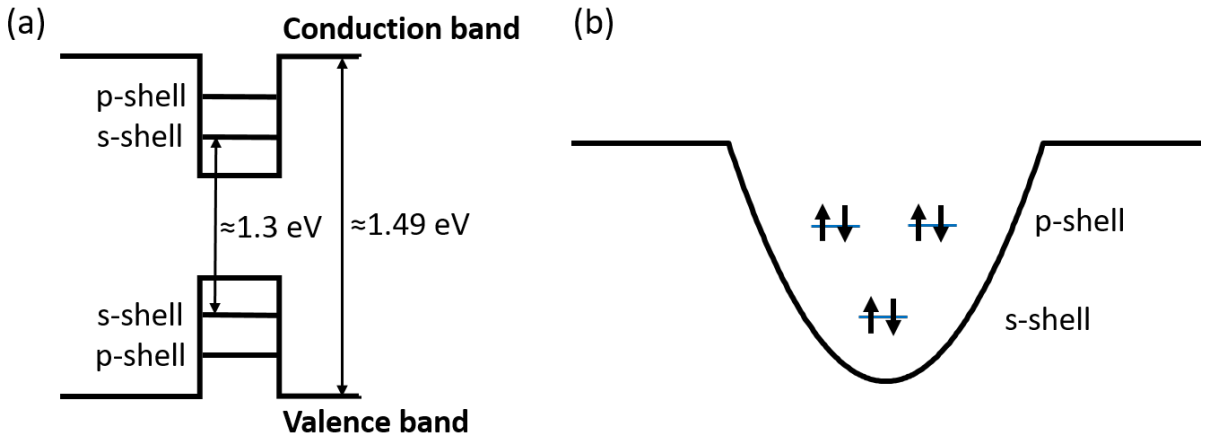

Figure 3.1: (a) Energy band diagram of a typical InAsP quantum dot within an InP host. The confinement allows for two bound energy levels, the s-shell and the p-shell. (b) Schematic of the conduction band for a parabolic potential populated with spin carriers. The valence band can be represented similarly.

The general schematic typically used to represent quantum dot energy levels is shown in Figure 3.1 (a), highlighting the confined s- and p- orbitals. In the InAsP/InP quantum dots studied in this thesis, the s-shell appears around 1.3 eV, the p-shell around 1.35 eV, and the energy of the bulk InP structure appears around 1.49 eV. Figure 3.1 (b) shows a schematic of the conduction band based on a lateral harmonic oscillator confinement potential with a doubly degenerate p-shell. The up (down) arrows indicate spin-up (down) electrons.

3.2 Optical transitions and selection rules

In all III-V semiconductors, electrons in the conduction band have s-like orbital symmetry implying an angular momentum $\boldsymbol{L} = 0$ and holes at the top of the valence band have p-like orbital symmetry implying an angular momentum of $\boldsymbol{L} = 1$. Both electrons and holes have spin $\boldsymbol{S} = 1/2$. Therefore, electrons have total angular momentum $\boldsymbol{J} = \boldsymbol{S} = 1/2$ whilst for the holes $\boldsymbol{J} = \boldsymbol{L} + \boldsymbol{S} = 1/2$ or $3/2$. Therefore, the projection of the angular momentum j_z for electrons will have values of $j_z = \pm 1/2$ (represented in the following by the arrows $\uparrow$ or $\downarrow$), whilst holes $j_z = \pm 1/2, \pm 3/2$ (represented by $\Uparrow$ or $\Downarrow$ arrows). The case for holes in the valence band for which $\boldsymbol{J} = 1/2$ is known as the split-off band, located a few hundreds of meV's away from the $\boldsymbol{J} = 3/2$ band and is ignored[75]. The $\boldsymbol{J} = 3/2$ state is further divided into two categories, heavy holes with $j_z = \pm 3/2$ and light holes with $j_z = \pm 1/2$. I should note that we are only interested in heavy holes because light holes are found to be a few tens of meV below heavy holes[76][77], but under certain conditions, such as applying elastic stress[78], they can be important to consider.

If the conduction band is unoccupied, the system has a total momentum of $\boldsymbol{J} = 0$. A photon carries an angular momentum of $\boldsymbol{J} = 1$. Depending on the helicity of the photon ($m_J = \pm 1$ for $\sigma+$, $\sigma-$ polarization), only transitions with $\Delta m_J = \pm 1$ are optically allowed. Excitons with a total momentum of $m_J = \pm 1$ ($|\uparrow\Downarrow>$, $|\downarrow\Uparrow>$) are termed bright, while excitons with $m_J = \pm 2$ ($|\downarrow\Downarrow>$, $|\uparrow\Uparrow>$) are dipole forbidden and, hence, referred to as dark excitons[79]. The dark exciton is termed dark because of its very low probability of emitting a photon as it does not obey the selection rules. However, it can be experimentally observed through an applied external magnetic field[80] or a more general spin-flip process[81], such as a phonon-mediated process[82, 83], which can be long lasting and affect device performances[84, 85].

3.3 Spectroscopy of quantum dots

In the simplest case, considering only the s-shell, which can host up to two electrons and two holes, several excitonic complexes may be observed: the neutral bright exciton X, the negatively charged exciton X^-, the positively charged exciton X^+, and the biexciton XX. Each specific charge configuration will lead to modified Coulomb interactions, which will shift the energy of the photon emitted. The energy of these four possible states may be written as

$$E_X = E_e + E_h - V_{eh}, \tag{3.2}$$

$$E_{X^-} = 2E_e + E_h - 2V_{eh} + V_{ee}, \tag{3.3}$$

$$E_{X^+} = E_e + 2E_h - 2V_{eh} + V_{hh}, \tag{3.4}$$

$$E_{XX} = 2E_e + 2E_h - 4V_{eh} + V_{ee} + V_{hh}, \tag{3.5}$$

where E_e and E_h is the confinement energy of the electrons and holes, respectively, and $V_{ij} = e^2/4\pi\epsilon r$ is the coulomb interaction energies, where ϵ is the dielectric constant of the semiconductor material and r is the distance between the particles. These four possibilities are presented in Figure 3.2 (a). It's interesting to note that the bright neutral exciton can be generated through different processes. It can be built directly through the capture of electrons and holes within the quantum dot or indirectly through a biexciton-exciton cascade event or even through a spin-flip process from which the dark exciton becomes bright.

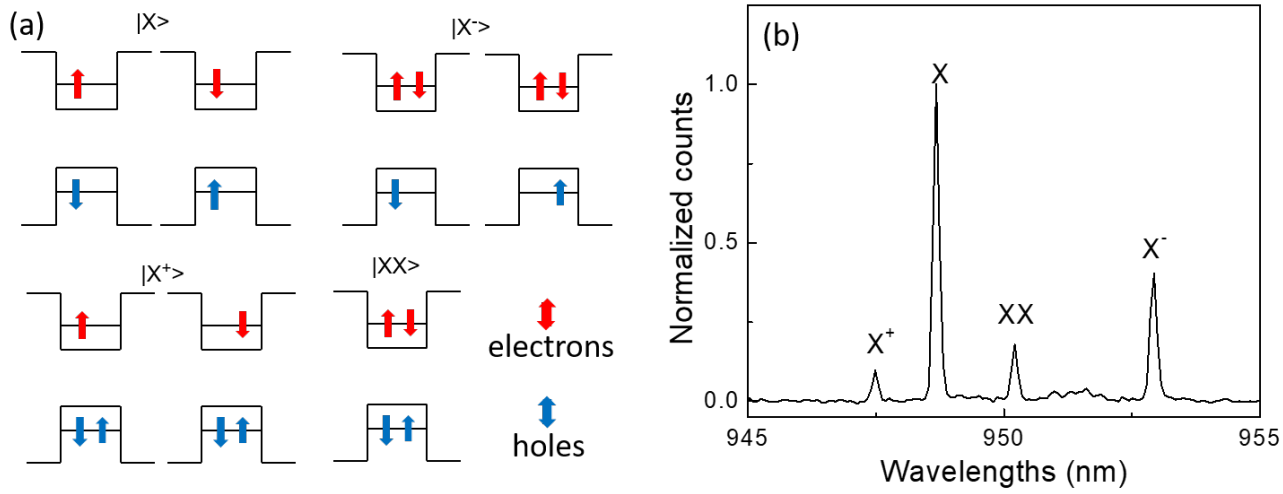

Figure 3.2: (a) The four possible bright excitonic states in the s-shell of a quantum dot. (b) Spectrum of an InAsP quantum dot embedded within an InP nanowire under above-band excitation.

Figure 3.2 (b) shows a quantum dot photoluminescence spectrum taken from a InAsP quantum dot embedded within an InP nanowire which shows the four emission peaks corresponding to the radiative recombination of the excitonic complexes in Figure 3.2 (a). The spectrum

is taken using above-band excitation, which is discussed in the next section. It is important to note that Eqs. 3.2 - 3.5 do not represent the emission energies of the photons in question. Note that excitons are electron-hole pairs, and photons are produced when these pairs recombine radiatively. In fact, a biexciton XX will emit an electron-hole pair, leaving behind another electron-hole pair which can then recombine as an exciton, X, both of which can emit at different energies. The emission energies of these four transitions should be written as:

$$\Delta E_X = E_X, \tag{3.6}$$

$$\Delta E_{X^-} = E_X + V_{ee} - V_{eh}, \tag{3.7}$$

$$\Delta E_{X^+} = E_X + V_{hh} - V_{eh}, \tag{3.8}$$

$$\Delta E_{XX} = E_X + V_{hh} + V_{ee} - 2V_{eh}. \tag{3.9}$$

Given that holes have a heavier mass compared to electrons, we should expect $V_{hh} > V_{eh} > V_{ee}$ and, as the spectrum shown in Figure 3.2 (b) suggests, the X^- emission will be present at a lower energy (longer wavelength) compared to the X^+ emission. These emission energies are calculated very simplistically, where an atomistic theory of the electronic and optical properties of InAsP quantum dots within InP nanowires is provided in Ref. [86].

3.4 Excitation methods

The excitation of quantum dots with an optical field can be done using different schemes, represented in Figure 3.3. Electron-hole pairs can be generated either within the bulk material outside the quantum dot or directly within the quantum dot.

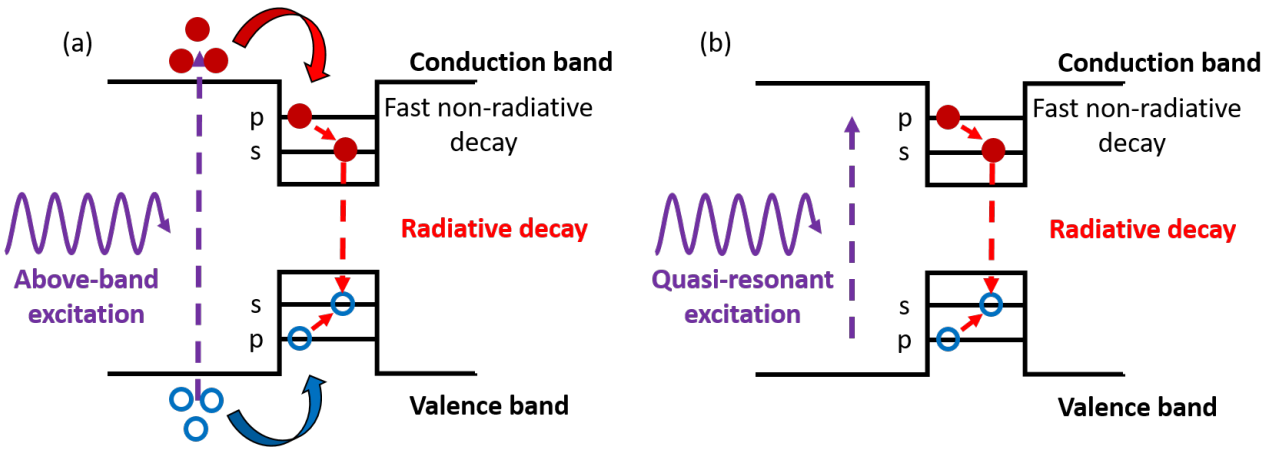

Figure 3.3: (a) above-band excitation. Carriers are generated in the conduction and valence band and thermally decay within the quantum dot to the lowest s-shell before radiatively decaying and emitting a single-photon. (b) Quasi-resonant excitation. Carriers are generated within the quantum dot directly within a p, or d-shell and thermally decay to the lowest energy state (i.e. the s-shell) before radiatively decaying and emitting a single-photon.

3.4.1 Above-band excitation

In the case of above-band excitation, the energy of the excitation laser is tuned to be larger than the bandgap of the bulk material. The charge carriers from the bulk valence band are excited to the conduction band. These carriers will eventually radiatively decay, producing photons at the bandgap energy of the bulk. For InP nanowires, the bulk can exist in either wurtzite (WZ) or zincblend (ZB) crystal phases, each having distinct bandgap energies. The carriers can also thermally decay within defects that include point crystal defects and impurities known as donor-acceptor (D-A) levels, as well as stacking faults (SF) (different crystal phases), or within the quantum dot. In Figure 3.4 (a), the different radiative recombination paths are shown schematically. In this case, the total emission spectrum will comprise: bulk emission, donor-acceptor levels, stacking faults, and quantum dot emission. In Figure 3.4 (b) we show the full spectrum of an InAsP quantum dot embedded within a wurtzite InP nanowire, which I present also in Article 2.

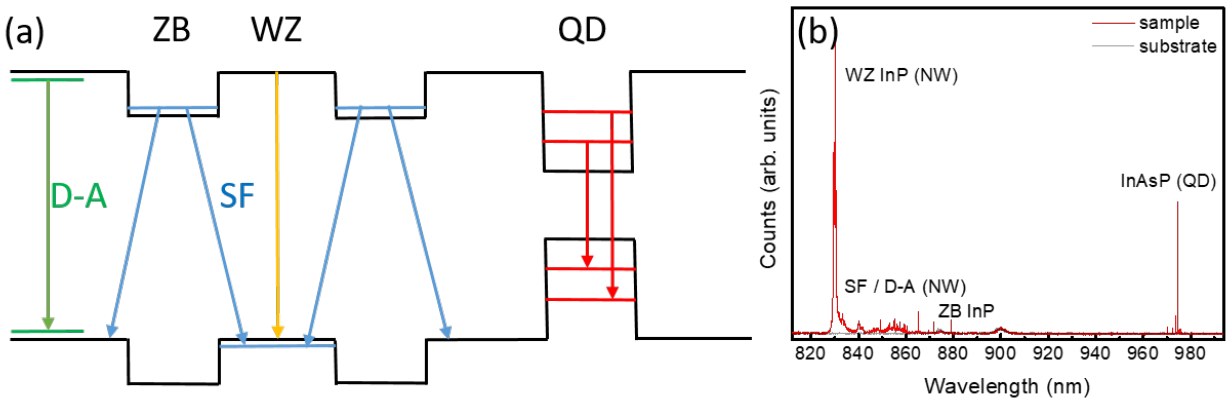

Figure 3.4: (a) Energy diagram showing the expected radiative decay paths within an InAsP/InP nanowire quantum dot. (b) A typical photoluminescence spectrum at 4 K showing wurtzite InP emission at 830 nm, stacking faults and defects between 840 nm and 860 nm, and the quantum dot emission around 980 nm[2].

The peak at 830 nm is the wurtzite InP nanowire bandgap transition[87], whilst peaks around 840 nm and 860 nm are expected from stacking faults and defects in the nanowire, respectively. Emission from the zincblend crystal structure is also expected around 875 nm if the nanowire is composed of mixed bulk crystal phases. In the case of Figure 3.4 (b), emission from the substrate is also visible where two broad features around 875 nm and 900 nm are associated with band-to-band and D-A recombination of zincblend.

The above-band excitation scheme is the easiest to implement as the laser does not need to be tuned to a specific wavelength and it is spectrally far enough away from the quantum dot emission for facile filtering. The scheme, however, has some drawbacks. One, which will be evident throughout this work, is the process of re-excitation. Additional electron-hole pairs can be recaptured in the quantum dot shortly after a first one has radiatively recombined[88, 89]. As the excitation power is increased, more carriers are generated and re-excitation becomes much more dominant (see Article 5), which is not ideal for a source that needs to operate at its highest efficiency. Above-band excitation is utilized throughout the articles presented in this thesis.

3.4.2 Quasi-resonant excitation

In the case of quasi-resonant excitation, the energy of the excitation laser is tuned below the bandgap of the host and on resonance with an excited state of the dot, such as the p-shell.

In Figure 3.5, we compare above-band excitation to quasi-resonant excitation. In the case of above-band excitation, Figure 3.5 (a) shows a spectrum of a nanowire quantum dot excited above-band as a function of excitation power. In this case, the X^- emission dominates the X transition line. In Figure 3.5 (b), we pump quasi-resonantly within the p-shell of the same nanowire quantum dot. In the later case, the X emission line dominates the X^- line. Here, the energy required to saturate a transition is much higher than the above-band excitation because of the low absorption cross-section of the energy levels in question (i.e. most of the laser sees the quantum dot as a transparent material). The reason the X emission line dominates the X^- emission line under this excitation scheme is that there's a reduced number of free charges produced that can decay into the s-shell and create the X^- emission. In this excitation scheme, the laser is still easily extinguished with proper filtering and has some advantages which include having better control over the charge carriers and reduced probability of populating defect states.

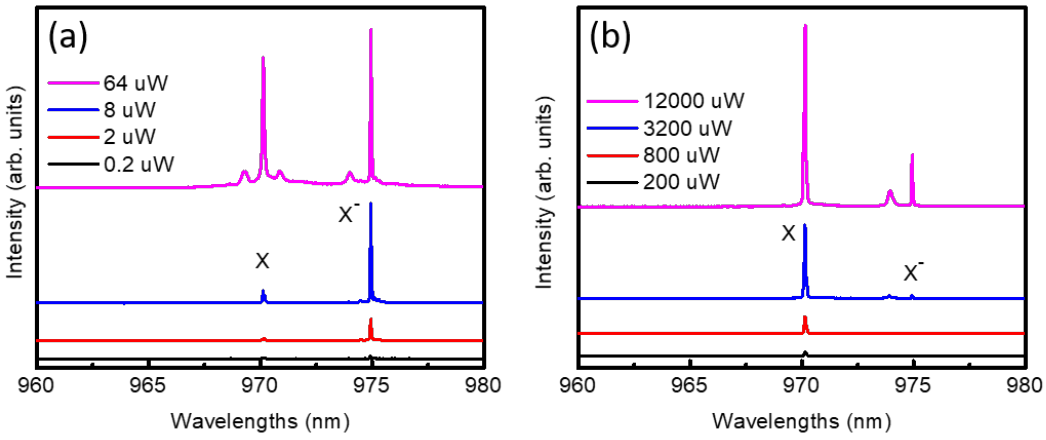

Figure 3.5: Example of a power dependence of the photoluminescence of a quantum dot using (a) above-band excitation and (b) the power dependence of the photoluminescence of the same quantum dot using p-shell excitation.

3.4.3 Resonant excitation

For resonant excitation, the laser energy is fixed at the energy of the fundamental exciton state (the s-shell). In this case, since the excitation source has the same energy as the quantum dot emission, it is not possible to spectrally filter the laser. This excitation scheme, however, would be ideal in order to have full control over the generated carriers within the quantum dot. There would be no relaxation process from the bulk to higher order shells

before reaching the s-shell, thereby reducing unwanted effects including: charge fluctuations, excitation time jitter, and phonon-related dephasing. One straightforward way to achieve the rejection of the pump laser is to excite the sample off the emission axis[90, 91] of the source. This may make the collection from the source more difficult depending on the optical setup. Two other ways include polarization rejection[92, 33, 93], which results in a 50% drop in efficiency, or two photon excitation[94, 95, 96].

3.5 Time-resolved Photoluminescence

We have already seen that source efficiencies and optimal coherence times, T_2, rely on the lifetime of the excitonic complexes, T_1. The lifetime is defined as the time an excitonic complex takes to emit a photon. The lifetime can be measured directly through time-resolved photoluminescence spectroscopy[97, 98, 99, 100, 101, 102] shown schematically in Figure 3.6 (a). To measure the lifetime of a specific excitonic complex, the source is excited using pulsed excitation operating at 670 nm and provides a train of 100 ps pulses with a variable repetition rate. The emission line of the excitonic complex to be analyzed is filtered and the photons are sent directly to a single-photon detector (SPD) connected to a counting card. A trigger signal is used, either a voltage output or a laser pulse, which is connected to the counting card. The trigger informs the counting card when a pulse has been applied and waits to detect a photon at the detector. A histogram can then be built-up through many repetitions of the process.

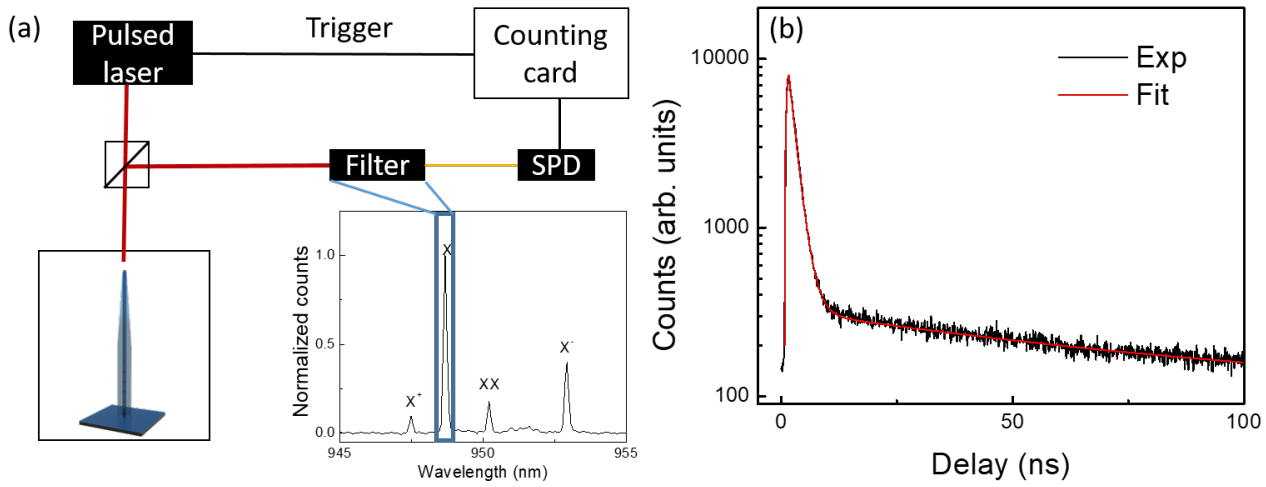

Figure 3.6: (a) Schematic of time-resolved photoluminescence measurement using a pulsed laser for excitation and as trigger. (b) Semi-log histogram of a time-resolved photoluminescence measurement of an exciton, X, from an InAsP/InP nanowire quantum dot.

Figure (b) shows a typical time-resolved PL measurement of a neutral exciton line of a nominal InAsP/InP nanowire quantum dot using an excitation repetition rate of 10 MHz to allow the full decay of the emission process. The lifetime trace shows three distinct features characterized by exponentials which takes the form

$$I(t) = A(1 - e^{(-t/\tau_r)}) + Be^{(-t/T_1)} + Ce^{(-t/\tau_d)}. \tag{3.10}$$

The rise time, $\tau_r = 0.38\,\text{ns}$, is linked to the capture of carriers within the quantum dot (emission time jitter) whilst the two exponential decay rates, $T_1 = 1.6\,\text{ns}$ and $\tau_d = 73\,\text{ns}$, correspond to the emission lifetimes of the bright neutral exciton and dark exciton respectively. The second decay time τ_d is specific to the neutral exciton, and the biexciton, which is always bright, should only exhibit one decay time. Charged complexes, on the other hand, can also exhibit a second decay time linked to a dark state, which can be explained by a charged state generated by populating electrons or holes in the p-shell and is discussed in Article 2.

3.6 Fine-structure splitting

In a typical quantum dot system, the quantum dot confining potential is not perfectly symmetric. Asymmetries such as an elliptical nanowire cross-section (in the case of nanowire

quantum dots), a non-uniform distribution of atoms, or strain will lead to an asymmetry in the electron and hole confining potential[103, 104]. Let us now discuss the emission of the biexciton and exciton photons. From the selection rules, the biexciton cannot directly decay to the ground state as it is not a dipole allowed transition. Instead the biexciton decays to the exciton state and subsequently to the ground state via a biexciton-exciton cascade event. There are two possible exciton states $|\downarrow\Uparrow>$ and $|\uparrow\Downarrow>$ and therefore two possible decay paths for the cascade emission as shown in Figure 3.7. Due to a possible asymmetry of a quantum dot, a fine structure splitting (FSS) between the two intermediate exciton levels will likely be present.

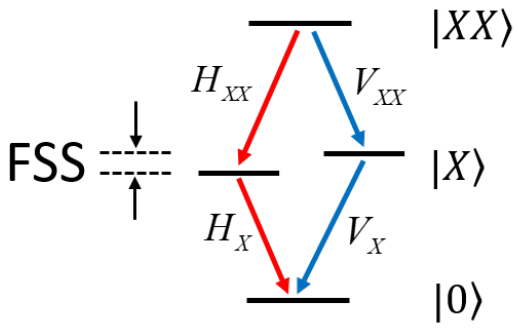

Figure 3.7: Schematic representation of a biexciton-exciton cascade. There are two decay paths, each with its own polarization. The intermediate exciton states are separated by a fine structure splitting (FSS).

It can easily be seen that both the neutral exciton (X) and the neutral biexciton (XX) can have a FSS in their spectrum whilst the charged excitons (X^- and X^+) will not because they both have only one possible decay path (either to a single hole state, or a single electron state, both of which cannot emit). In Figure 3.8 I show a typical spectrum of an (a) X emission and (b) XX emission where the FSS is $\sim 23\,\mu$eV. As expected from the X^- emission shown in (c), a FSS is not seen. The FSS of the neutrals are typically on the order of a few μeV up to a few hundred μeV[105, 106, 107].

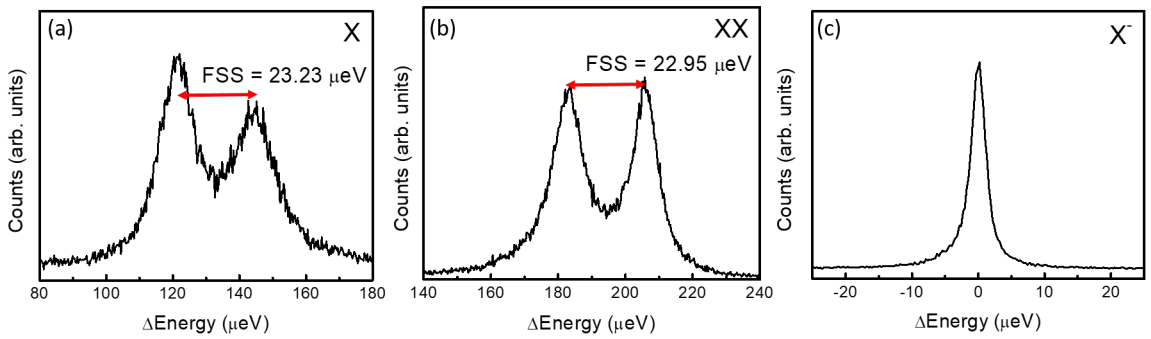

Figure 3.8: High resolution photoluminescence spectra of a typical nanowire quantum dot: (a) X emission, (b) XX emission, and (c) X^- emission as a function of relative energy ΔEnergy.

The photons emitted by the decay carry angular momentum values of ± 1, which represents left- or right-hand circular polarized emission. Since the total spin angular momentum needs to be zero, both emitted photons need to have a polarization with opposite handedness. Therefore, the state can be written as

$$|\Psi>=\frac{1}{\sqrt{2}}(|R_{XX}L_X>+|L_{XX}R_X>), \tag{3.11}$$

in the circular basis where R (L) labels a right (left) circular polarized light. Via transformation, the linear polarization state can be written as

$$|\Psi>=\frac{1}{\sqrt{2}}(|H_{XX}H_X>+|V_{XX}V_X>), \tag{3.12}$$

which is a Bell state. In Figure 3.7 a FSS exists between the two emission paths making the photons distinguishable (i.e. the photons emit at different energies). This creates a state which is no longer time-independent[108], and the general entangled state is modified to[109]

$$|\Psi>=\frac{1}{\sqrt{2}}(|H_{XX}H_X>+e^{i\phi(t)}|V_{XX}V_X>), \tag{3.13}$$

where $\phi(t)=t\Delta/\hbar$, t is the time interval between the biexciton and the exciton emission, Δ is the fine FSS, and $\hbar$ is the reduced Plank's constant. This means that there is an oscillation between the two Bell states $\frac{1}{\sqrt{2}}(|H_{XX}H_X>+|V_{XX}V_X>)$ and $\frac{1}{\sqrt{2}}(|H_{XX}H_X>-|V_{XX}V_X>)$.

It has been shown that the state in the form of Eq. 3.13 is still a maximally entangled Bell state[110, 111]. Figures 3.9 (a) and (b) show the polarization-resolved emission of Figure 3.8 (a) and (b) respectively. In each case, the polarizer is set for either horizontal or vertical polarization, clearly highlighting the different polarization of the emitted photons.

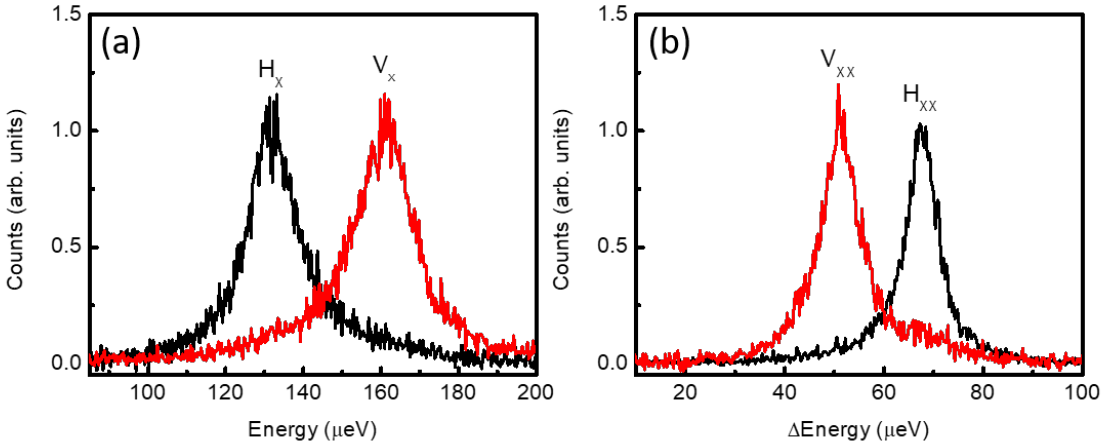

Figure 3.9: (a) High-resolution photoluminescence spectrum of the X emission for horizontal polarization (black line) and vertical polarization (red line). (b) High-resolution spectrum of the XX emission for horizontal polarization (black line) and vertical polarization (red line).

3.7 Auto-correlation measurements

In order to measure the second-order correlation function (also known as an auto-correlation measurement) described in Chapter 2, one needs to perform a standard Hanbury-Brown and Twiss experiment (HBT)[23]. A single-photon source is directed to a 50:50 beamsplitter and each output arm is sent to a single-photon detector (SPD) with a counting module (counting card) that provides a time delay between the arrival of individual photons which provides a start click on one detector and a stop click on the other, as shown in Figure 3.10 (a). If a source only emits one photon at a time it is not possible to register a start click followed immediately by a stop click and so zero coincidence counts are registered at zero time delay.

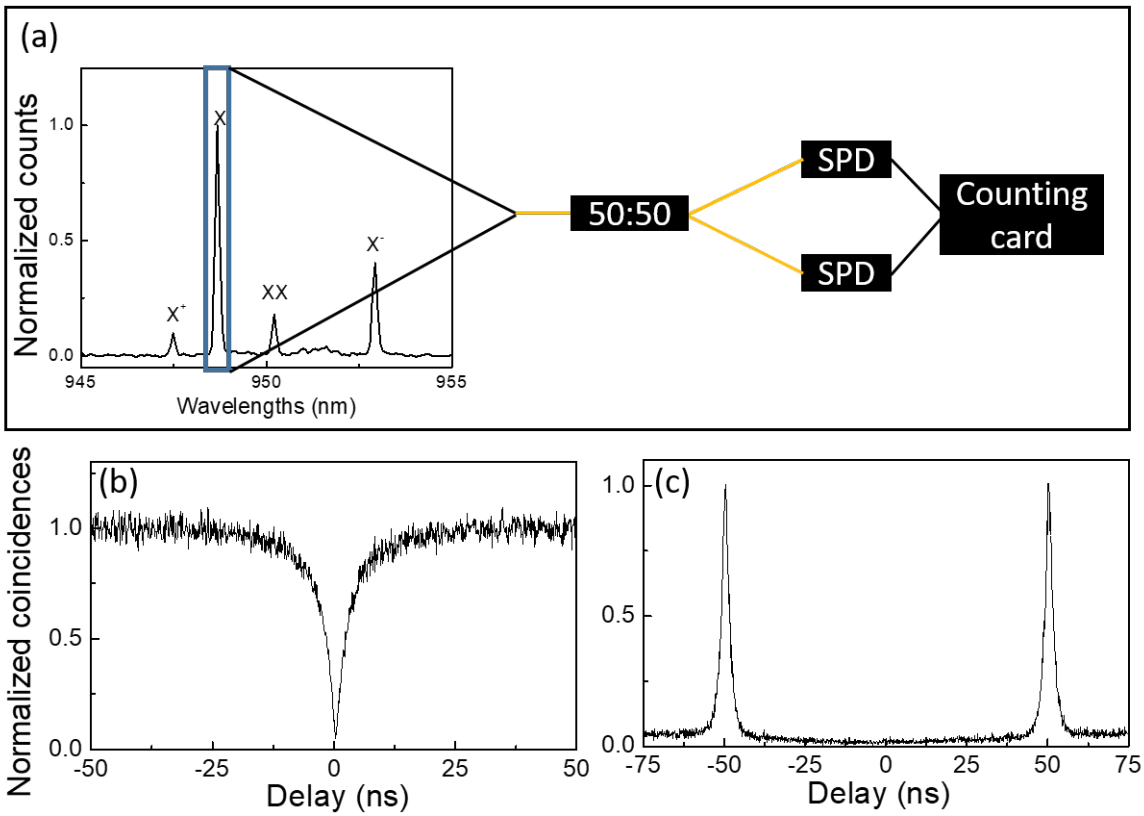

Figure 3.10: (a) a Schematic of a Hanbury-Brown and Twiss experimental configuration. (b) a typical continuous-wave (CW) $g^{(2)}(\tau)$ measurement and (c) pulsed.

In Figure 3.10, I show a near ideal outcome from an InAsP/InP nanowire quantum dot excited above-band using (a) continuous-wave (CW) excitation and (b) pulsed excitation at 20 MHz. I will show in Articles 1 and 3 that different excitonic complexes exhibit different auto-correlation spectrum, especially under CW excitation. The neutral exciton, X, follows a behaviour expected from a two-level system that consists of the vacuum and the X state, where $g^{(2)}(\tau) = 1 - e^{-(R+\Gamma)|\tau|}$[112], where R is the pump rate, $\Gamma = 1/T_1$ is the radiative rate and τ is the delay time. However, the biexciton (XX) shows a very different behaviour at lower excitation power, where bunching is observed at short delays, which decays with a rate corresponding to the exciton lifetime[112, 113] (see Articles 1 and 3).

More often than not, the experimental second-order correlation function will be "polluted". This can be due to the excitation scheme employed, such as above-band excitation where re-excitation, which appears as side lobes around a dip at zero time delay, can be seen[114] or uncorrelated emissions. By uncorrelated emission, I mean anything that is not specific to the emission line in question, such as a second emission line from a different excitonic complex or light pollution from room light. If this experiment is done properly with fine filtering on a

clean emission line and using resonant excitation, $g^{(2)}(0) \sim 0$ can be achieved. $g^{(2)}(0)$ values as low as 0.000075 have been reported in quantum dots[66].

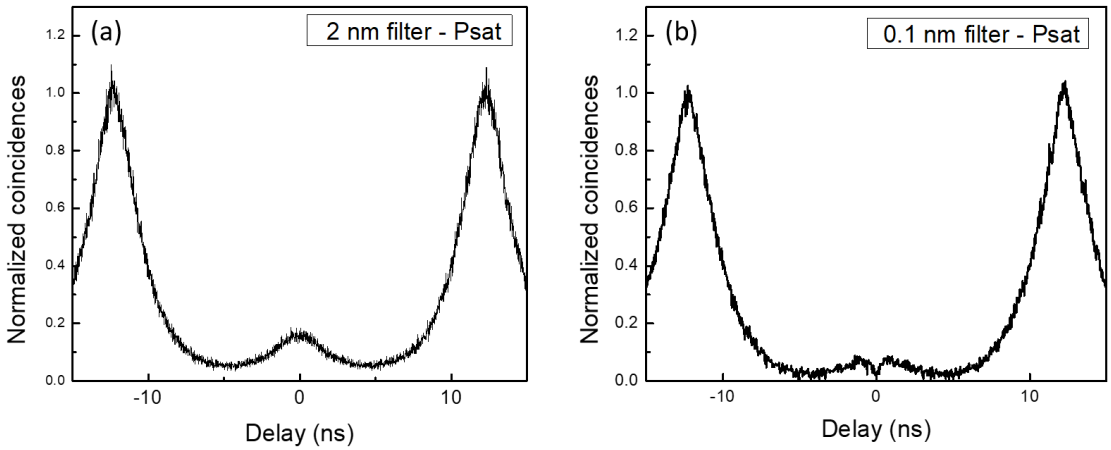

Figure 3.11: Example $g^{(2)}(\tau)$ of a nanowire quantum dot excited above-band using (a) poor filtering and (b) better filtering. Both measurements are done using an excitation power of $\sim P_{sat}$, where the count rates are maximized at the detectors.

In Figure 3.11 (a) I show a $g^{(2)}(\tau)$ from a nanowire quantum dot excited above-band using a pulsed laser operating at $\sim 670\,\text{nm}$, with a repetition rate of 80 MHz, where poor filtering was used (a free-space 2 nm bandpass filter). The measurement is likely polluted by a combination of room light and/or other emissions the filter cannot properly suppress. In (b) I show an example where the emission line is filtered using a 0.1 nm fiber-coupled bandpass filter. In this case the measurement is polluted mainly by the re-excitation process from the pulsed laser employed at relatively high excitation power (near P_{sat}, defined as the power that saturates the transition and where the detected count rates are maximum). It is interesting to note that the re-excitation process will not be visible in a $g^{(2)}(\tau)$ measurement performed under CW excitation.

3.8 Cross-correlation measurements

In the previous section, we examined photon correlations between a single emission line. Correlations can also be done between two different emission lines, i.e. cross-correlations. The measurement method is mostly the same except, in this case, the distinct emission lines are filtered individually after passing through a 50:50 beamsplitter and one emission line is

sent to a "start" detector whilst the other is sent to a "stop" detector. A schematic of the experimental setup is shown in Figure 3.12 (a). This measurement technique is now widely used to differentiate between different excitonic complexes, which is a technique that will be utilized in this thesis.

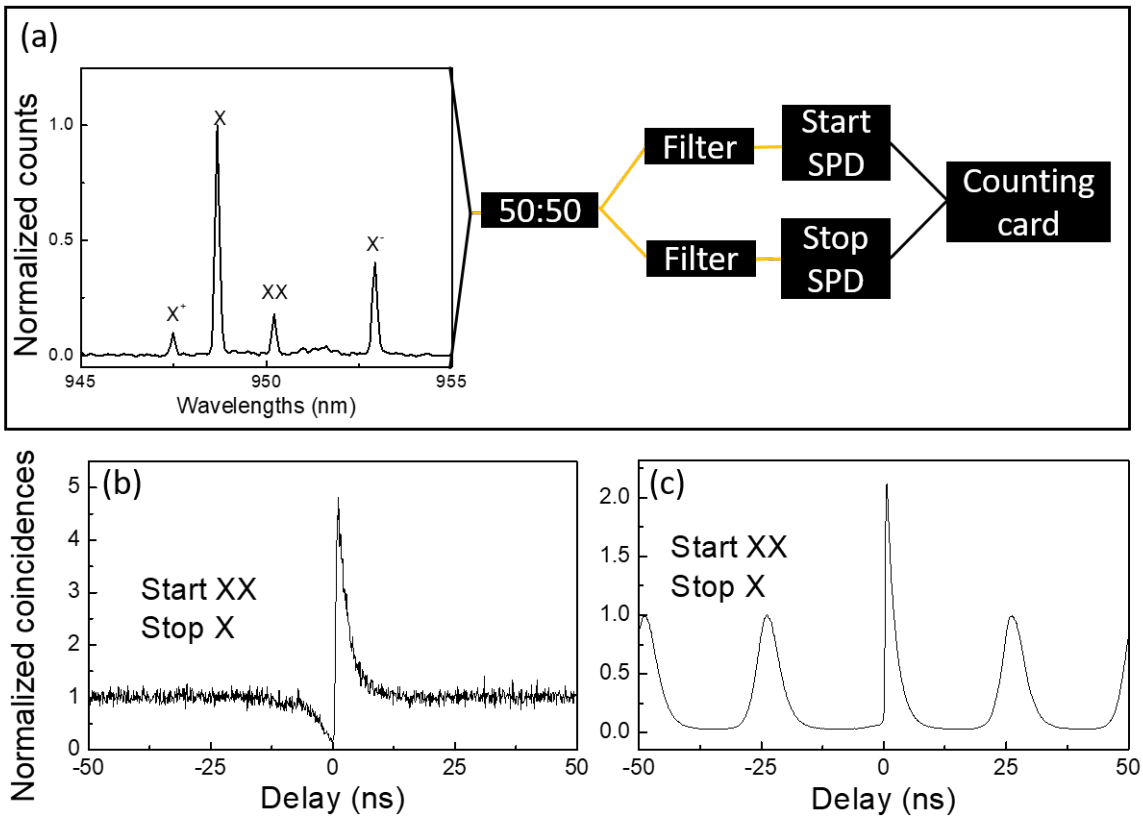

Figure 3.12: (a) A cross-correlation measurement setup where a full spectrum is sent to a 50:50 beamsplitter and individual emission lines are filtered and sent to either a start single-photon detector (SPD) or a stop SPD connected to a counting card. A typical cross-correlation measurement where an XX photon is sent to the start SPD and an X photon to the stop SPD under (b) CW excitation and (c) pulsed excitation.

Figure 3.12 shows a typical cross-correlation measurement under (b) CW excitation and (c) pulsed excitation. The XX photon is sent to a start detector and the X photon is sent to a stop detector. At zero time delay, right after a XX photon is detected, due to the $XX - X$ cascade process discussed in Section 3.5, an X photon is extremely likely to be emitted. This is seen by the sharp rise at short positive time $\tau > 0$ because this process is instantaneous. Such measurements are used to show that the $XX - X$ emission is a cascaded process and has been widely reported[115, 116, 117, 113, 118, 119, 96]

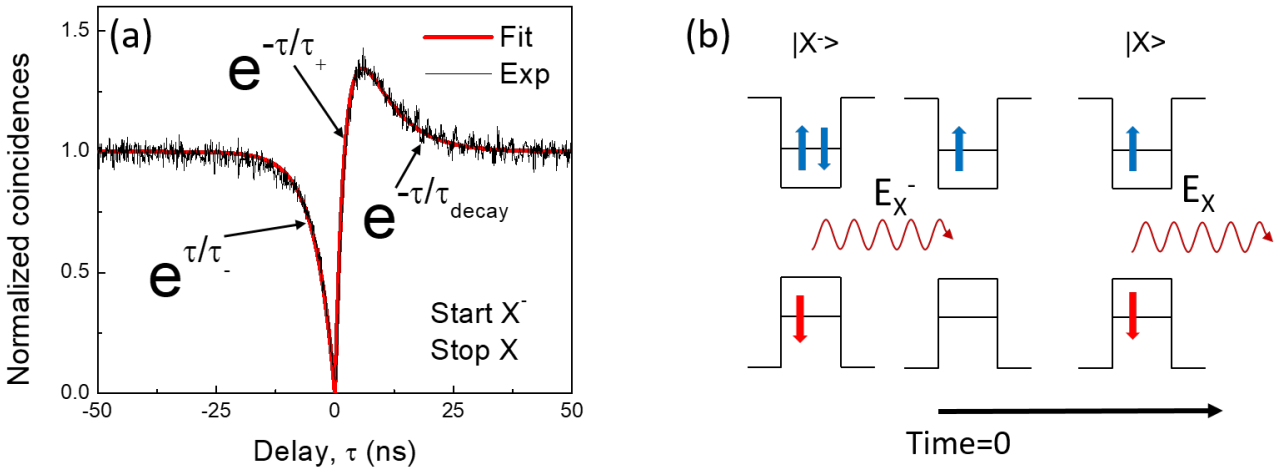

Figure 3.13: (a) Cross-correlation between an X^- (start) and an X (stop) photon under CW excitation. Data is taken from Article 1. (b) Schematic representation of the emission process in (a) for time, $\tau > 0$. At zero time delay, the quantum dot emits a single X^- photon and the dot is left in a one electron state. In order to detect an X photon on the stop detector, the system has to wait to capture a hole, represented by the rise time, τ_+, for short positive delays.

As another example, Figure 3.13 (a) shows a cross correlation where an X^- photon is sent to a start detector whilst an X photon is sent to a stop detector. The emission of an X^- photon triggers the start detector, leaving the system in a one electron state at $\tau = 0$. Since we have set our stop detector to measure an X photon, the system must wait in order to capture a single hole. This "wait time" is the time the system takes to capture a single hole and is represented by the rise time at short positive delays, τ_+. On the other hand, for short negative delays, after the emission of the X photon, the system is left in an empty state and the correlation measurement decays back to its normalized value after τ_- time. Where here τ_- is linked to the capture of three carriers (two electrons and one hole) needed to generate an X^- photon. The spectrum takes a functional form of

$$g^{(2)}(\tau) = A(1 - e^{(t/\tau_-)}) - Be^{(-t/\tau_+)} + Ce^{(-t/\tau_{decay})} \tag{3.14}$$

from which the capture rate of three carriers, $\tau_- = 4.45\,\text{ns}$, the capture rate of a single hole $\tau_+ = 1.6\,\text{ns}$ and a decay rate of $\tau_{decay} = 8.44\,\text{ns}$ are extracted. I note, in this case, that the bunching at short positive delays decays on a time scale longer than expected from the radiative recombination lifetime. This behaviour is seen also in auto-correlation

measurements and is attributed to blinking, which is a process linked to changes in the charge configuration of the dot and is seen in many quantum dot systems[89, 120, 121, 122]. The cross-correlation measurements presented here will be an important tool for the analysis of the nanowire quantum dot system presented in the upcoming chapters and blinking will be addressed in Article 3.

We have seen that both CW excitation and pulsed excitation can be utilized for the study of correlation measurements. Both provide the same information in terms of $g^{(2)}(\tau)$ at $\tau = 0$, an important parameter that establishes the single-photon purity of a source. However, in terms of its full $g^{(2)}(\tau)$ correlation spectrum, the two excitation methods provide different information. In a CW excitation mode, a quantum dot is constantly re-excited with carriers, and one cannot distinguish between re-excitation and uncorrelated emissions, both of which pollute the $g^{(2)}(\tau = 0)$ value. Under pulsed excitation, one can get a good estimate of the re-excitation process and will be investigated in Article 5. CW excitation, however, has its benefits in term of $g^{(2)}(\tau)$ measurements, especially when it comes to cross-correlation measurements. Processes which occur on fast time scales, such as the capture rates of electrons and holes within a quantum dot, can be observed under CW excitation, making these measurements ideal for distinguishing between different excitonic complexes or to understand the electron-hole capture dynamics, which is discussed in subsequent chapters.

3.9 Coherence

There are several factors that will limit the generation of perfectly coherent photons, which, in turn, will broaden its emission linewidth compared to the lifetime transform limited value. These processes include inelastic phonon scattering, charge noise fluctuation coming from trap states around a quantum dot, and carrier interactions with acoustic phonons leading to pure dephasing.

First, consider inelastic phonon scattering (Figure 3.14 (a)). In such a process, a two-level system interacts with the crystal lattice of its environment such that the emission process involves the emission or absorption of a phonon while conserving energy. For example, an excitonic state, after the absorption of a phonon, will emit a photon at a higher energy to compensate for the added energy of the phonon. This broadening mechanism is present when a source is introduced to a high number of phonons, e.g. sources operating at room-temperature. The zero phonon line (ZPL) (i.e. not affected by inelastic phonon scattering) is shown in blue of Figure 3.14 (a).

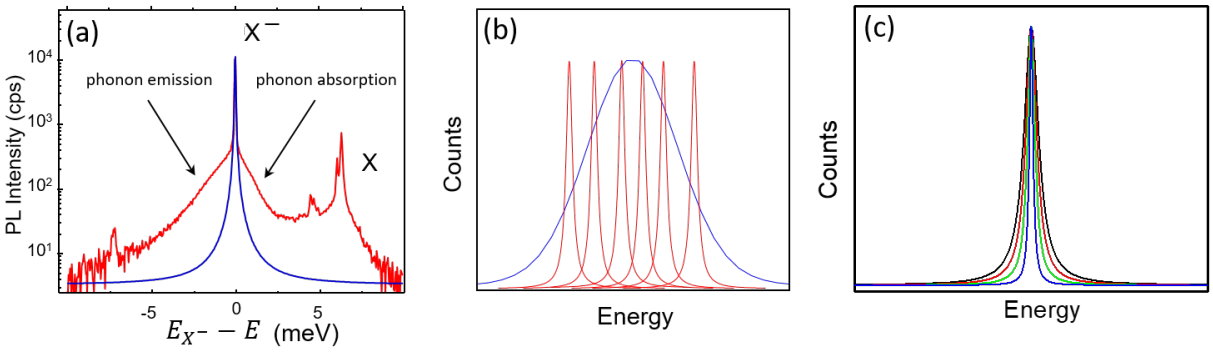

Figure 3.14: Broadening due to (a) inelastic phonon scattering (adapted from Ref. [3]), (b) inhomogeneous broadening due to a fluctuating charge environment and (c) Pure dephasing e.g. elastic phonon scattering.

Charge fluctuation around a quantum dot will also impact the linewidth of the emitted photons. In this process, photons emit a slightly different energy due to a time-dependent Stark shift of population of traps near the quantum dot. Such traps may be associated with donor-acceptor levels (defects), stacking faults, nearby quantum dots (as seen in self-assembled quantum dots), wetting layers, or surfaces. Figure 3.14 (b) shows the emission of several single-photons at different energies (in red) generating a voigt lineshape (in blue). This process is called an inhomogeneous broadening mechanism and the optimal Lorentzian lineshape is convoluted with a broader Gaussian component. The influence of this broadening mechanism can be reduced by employing resonant excitation in high-quality samples[64, 123].

I discussed that inelastic phonon scattering contributes to the emission line broadening by phonon absorption and emission. These phonon sidebands can be readily filtered out, leaving the ZPL. The two-level system can also couple to phonons through elastic phonon scattering. This contributes to a pure dephasing T_2^* term to the coherence time. The dephasing will broaden the ZPL compared to the lifetime-limited value but, in this case, the lineshape remains Lorantzian, as shown in Figure 3.14 (c).

These broadening mechanisms can be limited through the use of resonant excitation which significantly reduces charge noise[64, 124, 125, 126, 127, 128, 129, 123]. Optical cavities can also mitigate the influence of charge noise by decreasing the lifetime T_1 relative to the scale associated with the fluctuations[130, 131, 132]. Article 4 presents results on an optimized InAsP/InP nanowire quantum dot system aimed at reducing many of the sources of charge noise described above.

3.10 Coherence measurement

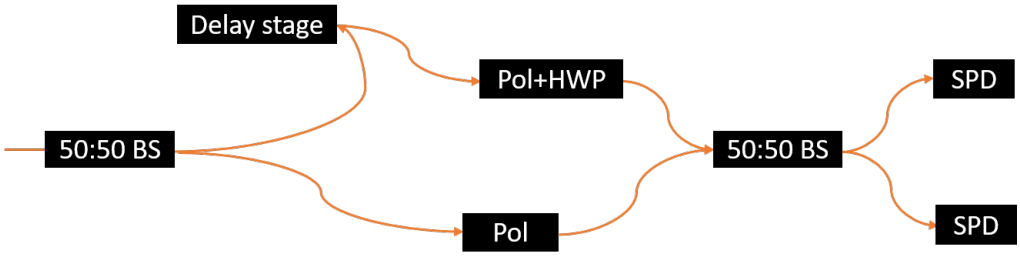

Figure 3.15: Experimental setup for coherence and HOM measurements: Filtered quantum dot emission is sent to a 50:50 beamsplitter (BS) where one exit path is sent to a variable delay stage, then to a linear polarizer (Pol) followed by a half-wave plate (HWP) whilst the other exit path is sent through a linear polarizer. The two paths are then recombined at a 50:50 beamsplitter and the two exit ports are sent to single-photon detectors (SPDs).

As seen in Chapter 2, the coherence time T_2 can be obtained from a fit to the fringe visibility measured with a Michelson interferometer. To measure the visibility we use a Mach-Zehnder interferometer[133, 134] shown in Figure 3.15. The fiber-coupled filtered emission is sent to a fiber 50:50 beamsplitter where one exit path is sent to a variable delay stage, then to a linear polarizer followed by a half-wave plate. The other exit path is sent to a linear polarizer. The two paths are then recombined at a 50:50 beamsplitter and the two exit ports are sent to single-photon detectors. The two paths are adjusted by adding additional fiber to one of the arms to provide zero delay between photons at the second beamsplitter.

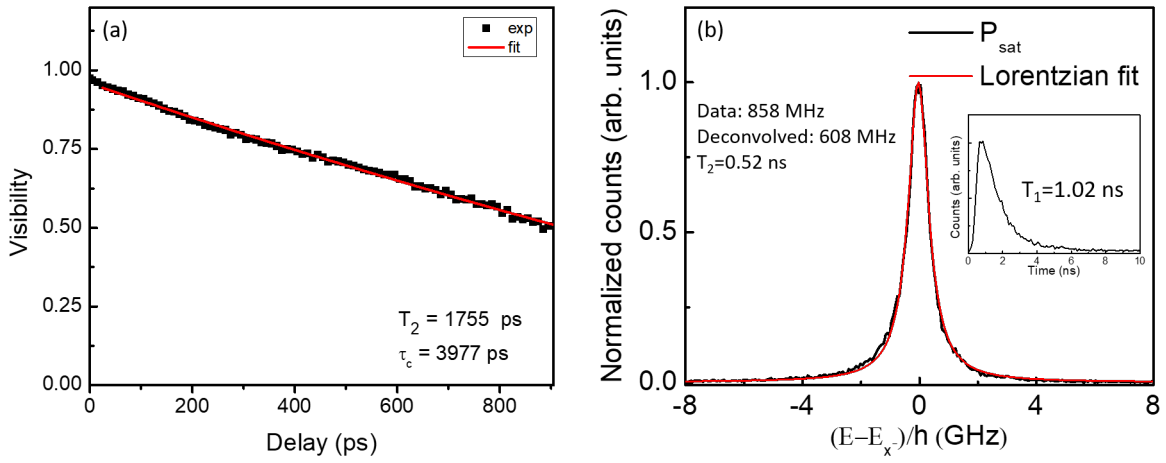

Figure 3.16: (a) Fringe visibility as a function of time delay between the arms of the Mach-Zehnder. The experimental data is fit with a Voigt lineshape. (b) Measurement of the linewidth of the emission using a Fabry-Perot etalon taken at $P = P_{sat}$ (black) and Lorantzian fit (red). The inset shows the time-resolved photoluminescence measurement showing a lifetime of $T_1 \sim 1\,\text{ns}$.

Using a motorized, fiber-based delay stage, we scan across 1.2 ns using steps of 10 ps and measure the visibility at each delay. The visibility is calculated using

$$V = \frac{I_{\text{max}} - I_{\text{min}}}{I_{\text{max}} + I_{\text{min}}}, \tag{3.15}$$

where I_{max} is the maximum detected intensity and I_{min} is the minimum detected intensity at each detector. Figure 3.16 (a) shows the visibility decay of the X^- emission from Article 4 measured at saturation using an 80 MHz pulsed source at 670 nm. Figure 3.16 (b) shows the high-resolution spectrum of the X^- photon with emission wavelength of $\sim$ 971.8 nm. The fringe visibility is fit using a Voigt profile, which is a product of a Gaussian and Lorantzian[125],

$$g^{(1)}(\tau) \sim \exp\left[\frac{-\pi}{2}(\frac{\tau}{\tau_{\text{c}}})^2 - \frac{|\tau|}{\text{T}_2}\right], \tag{3.16}$$

where the $1/\tau_c$ is the Gaussian component and the $1/T_2$ term is the Lorantzian component. The fit to the data provides $T_2 = 1.76\,\text{ns}$ and $\tau_c = 3.98\,\text{ns}$. The Lorentzian component represents the homogeneous linewidth $\Delta f_L = 1/\pi T_2 = 181.4\,\text{MHz}$. Using the measured radiative

lifetime $T_1 = 1.02\,\text{ns}$ (see inset Figure 3.16(b)), we obtain a value of excess broadening above the lifetime limit of $2T_1/T_2 = 1.16$. This excess broadening we attribute to pure dephasing and, using Eq. 2.17, we extract a pure dephasing time of $T_2^* = 6.28\,\text{ns}$. The Gaussian term represents the inhomogeneous broadening (from e.g. spectral fluctuations) with associated width $\Delta f_G = \sqrt{2ln(2)}/\sqrt{\pi}\tau_c = 167\,\text{MHz}$.

Figure 3.16 (b) shows a high resolution spectrum of X^- photon. The lineshape is Lorentzian with width $\Delta f = 608\,\text{MHz}$. From this measurement we calculate a coherence time of $T_2 = 1/\pi\Delta f = 0.52\,\text{ns}$, which is inconsistent with the $g^{(1)}(\tau)$ measurement. We speculate that the fitting routine of the lineshape in the frequency domain is not sensitive to a moderate contribution of a Gaussian component. Under this assumption, a more appropriate comparison between frequency and time domain results would be to compare 608 MHz with the Voigt linewidth in the $g^{(1)}(\tau)$ measurement which is given by[135]

$$\Delta f_V = 0.535\Delta f_L + \sqrt{0.217\Delta f_L^2 + \Delta f_G^2} = 283.4\,\text{MHz}. \tag{3.17}$$

This still results in a factor of 2 difference between the two measurements the reason for which is not as yet understood. We note here, that the data taken in Figure 3.16 (a) and (b) are taken during different cool-downs which can lead to a difference in the charge environment of the quantum dot in question which may make the comparison inaccurate. Such effect has been reported in quantum dot systems (see for example, Ref [136]).

3.11 Hong-Ou-Mandel Effect

As mentioned in Chapter 1, an ideal single-photon source should emit sequential photons that are indistinguishable from each other, e.g. identical in all degrees of freedom (wavelength, time, space, polarization). Such indistinguishability is required for most quantum photonic applications such as measurement-device-independent quantum key distribution[137], quantum repeater-based entanglement distribution[138], and linear optical quantum computing[7]. The level of indistinguishability of sequentially emitted photons is determined from the visibility in a HOM measurement using an unbalanced Mach-Zehnder interferometer. The setup is as shown in Figure 3.15 and is similar to the one used for the coherence measurements. In this setup, the length of one arm is adjusted such that a photon traveling in the arm is delayed by the repetition rate of the pulsed source (in this case, 12.5 ns). The indistinguishability is given by the HOM visibility

$$V_{HOM}(\tau) = \frac{g_{\perp}^{(2)}(\tau) - g_{\parallel}^{(2)}(\tau)}{g_{\perp}^{(2)}(\tau)}, \tag{3.18}$$

where $g_{\parallel}^{(2)}(\tau)$ is the measurement when the two photons input at the second beamsplitter have the same polarization and $g_{\perp}^{(2)}(\tau)$ is the measurement when the two photons have perpendicular polarization, i.e. perfectly distinguishable. A perfectly indistinguishable source of photons would give $g_{\parallel}^{(2)}(\tau) = 0$ and $g_{\perp}^{(2)}(\tau) = 0.5$ and would have a visibility of $V_{HOM}(\tau) = 1$.

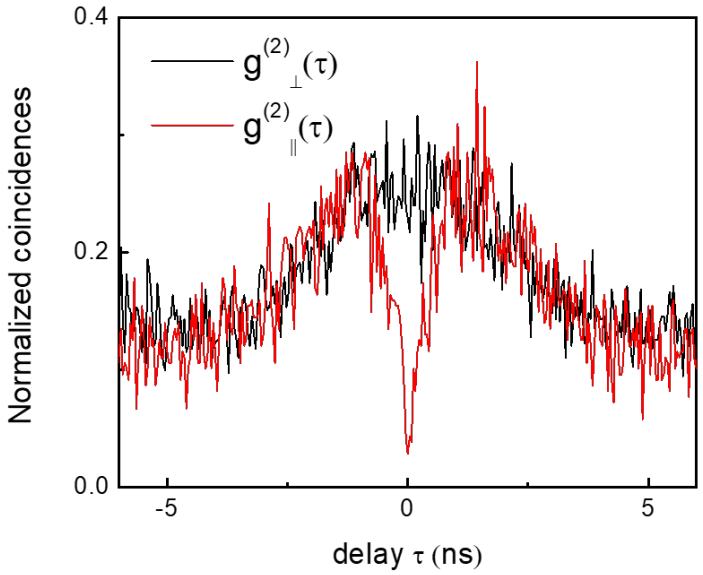

Figure 3.17: Hong-Ou-Mandel measurement from an InAsP/InP nanowire quantum dot excited at $P = P_{sat}$ for the X^- emission shown in Figure 3.16.

In Figure 3.17 we plot $g_{\parallel}^{(2)}(\tau)$ (red curve) and $g_{\perp}^{(2)}(\tau)$ (black curve) measured using the emission line presented in Article 4. We used a pulsed diode laser operating at 670 nm providing 100 ps pulses at 80 MHz and we excite the quantum dot at $P = P_{\text{sat}}$. From Eq. 3.18 we determine a HOM visibility of $V_{HOM} = 0.1$ using $g^{(2)}(\tau)$ values corresponding to the integrated counts from ± 6.5 ns. Such a low visibility is attributed to the above-band excitation scheme employed. On one hand, the linewidth under these pumping conditions (i.e. above-band at P_{sat}) were $\sim 4\times$ the lifetime limited value. The mechanisms[139] responsible for this excess broadening will reduce the two-photon interference visibility. On the other hand, excitation time-jitter[140] will create an uncertainty in the emission time of a photon, and therefore, an uncertainty in the arrival time of a photon at the beamsplitter. The

HOM visibility can thus be improved by lowering the excitation power or, ideally, employing resonant excitation. Quantum dots have been shown to be able to operate with $V_{HOM} > 0.9$[141, 142, 143, 144, 34] where resonant excitation was utilized.

Chapter 4

Experimental methods

In this chapter, I briefly describe the experimental techniques employed for the growth of nanowire quantum dot devices. We then suggest a new growth technique in order to achieve bright quantum dot emission at telecom wavelengths. The general setup used in the laboratory for the measurements presented in the previous chapter and in the following chapters is introduced.

4.1 Growth of quantum dots

Quantum dots as sources of single-photons date back to 2000 when Michler et al.[53] demonstrated negligible multi-photon emission from quantum dots in a micro-disk. Since this early demonstration, the field has rapidly expanded. The most studied sources are based on self-assembled quantum dots nucleated using the Stranki-Krastanov growth mode[145]. In this approach, a thin layer of indium arsenide (InAs), for example, is placed onto a layer of gallium arsenide (GaAs). The two layers are not lattice matched and at some critical thickness of the top layer, the strain accumulation induces a relaxation of stress by growing small islands. These small islands naturally provide quantum confinement.

These quantum dot systems provide near ideal single-photon purity, but there remain many long term challenges. The position and size of the quantum dots are random due to the random nature of the nucleation process. This provides challenges when looking for isolated dots emitting at desired wavelengths. Another issue in these structures arises from the fact that they are typically capped with another semiconductor material in order to preserve the

quality of their surfaces (i.e. keeping the surface defect density low) making collection a challenge due to total internal reflection. Several methods have been employed in order to overcome the collection issue, such as: employing microlenses[146], micropillars[58], circular Bragg gratings[147], and etching nanowires[148] around the quantum dots. In this work, we move away from these methods and grow nanowires epitaxially and can selectively embed quantum dots within the core.

4.1.1 Selective-area vapour-liquid-solid growth of InAsP QDs within InP nanowires

We use a combination of selective-area (SA) and vapour-liquid-solid (VLS) epitaxial growth modes to grow InAsP quantum dots within InP nanowires. In order to do this, chemical beam epitaxy (CBE) is employed, where trimethylindium (TMI) and pre-cracked PH_3 and AsH_3 are used as sources of In, P, and As, respectively. First, a growth substrate is prepared where circular openings 20 nm thick SiO_2 mask are created using electron-beam lithography and hydrofluoric acid wet-etching. A gold particle is deposited in these openings using a self-aligned lift-off process[149]. The diameter of the gold particle ($\sim$ 20 nm) defines the diameter of the quantum dot whereas the diameter of the mask opening ($\sim$ 250 nm) defines the base waveguide diameter. The latter is chosen to maximize the coupling efficiency, β, of the dot emission to the waveguide mode. Figure 4.1 shows the main steps of the nanowire and quantum dot growth process.

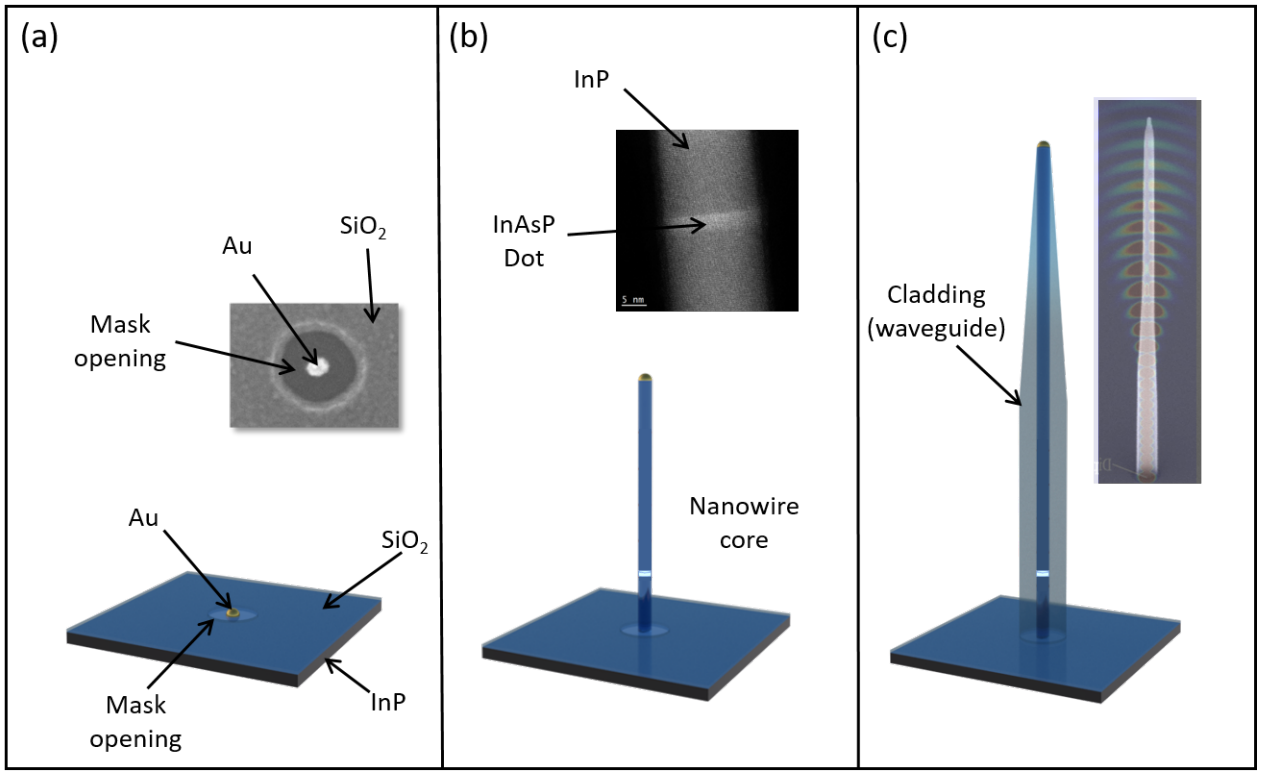

Figure 4.1: (a) Schematic of an opening in an SiO_2 mask defined using e-beam lithography and wet-etching. A gold particle is deposited in the middle of the opening using e-beam evaporation and lift-off. The SiO_2 mask inhibits any unwanted growth. Also shown: scanning electron microscopy (SEM) image of the gold particle centered in a circular opening of the SiO_2 mask. (b) VLS epitaxy defines the nanowire core diameter catalyzed by a gold particle where a quantum dot can be selectively positioned within the core axis. Also shown: transmission electron microscopy (TEM) of the core of a nanowire containing a single quantum dot. (c) SA epitaxy defines the shell diameter (i.e. the waveguide) where a tapered region is inherently grown which improves the collection efficiency. Also shown: SEM image of the photonic nanowire where a simulation of the mode expansion is provided.

After introducing the patterned substrate into the CBE reactor, growth proceeds by first growing the nanowire core. This is grown using VLS epitaxy with the Au particle acting as a catalyst. The process is controlled by the flux of TMI and pre-cracked PH_3 and using a temperature of ~420 - 435°C . The quantum dot is selectively incorporated anywhere along the core by switching the flow of PH_3 to AsH_3 and its thickness is controlled by the length of time the AsH_3 is incorporated in the growth chamber before it is switched back to PH_3[87]. In general, in this work, the $InAs_xP_{1-x}$ contains an As concentration of $x \sim 0.2$. During this step, since a single quantum dot can be selectively incorporated along the growth axis of the core, multiple quantum dots may be added which is investigated in Article 5.

The final step of the growth process employs a SA growth mode. Here a higher flux of PH_3 and a higher temperature is used in order to promote radial growth of the nanowire core. During the SA growth, the VLS growth is not completely suppressed creating cladded nanowires nearly twice the height of the original nanowire core whilst maintaining a wurtzite structure. This has the benefit of generating a tapered tip to the nanowire cladding and acts as a mode expander. The expanded mode reduces reflections from the tip of the nanowire and also reduces the divergence of the out-coupled mode. The latter relaxes the N.A. requirements of the output lense for a given collection efficiency. These nanowire devices generally have a base diameter of $D \sim 250\,\text{nm}$, a height of $h \sim 10 - 15\,\mu\text{m}$ tapered to 20 nm at the tip. The quantum dot within the core has a diameter of $D_{\text{dot}} \sim 20\,\text{nm}$ and a thickness of $\sim 5\,\text{nm}$. The growth is optimized to create a nearly perfect wurtzite structure[3].

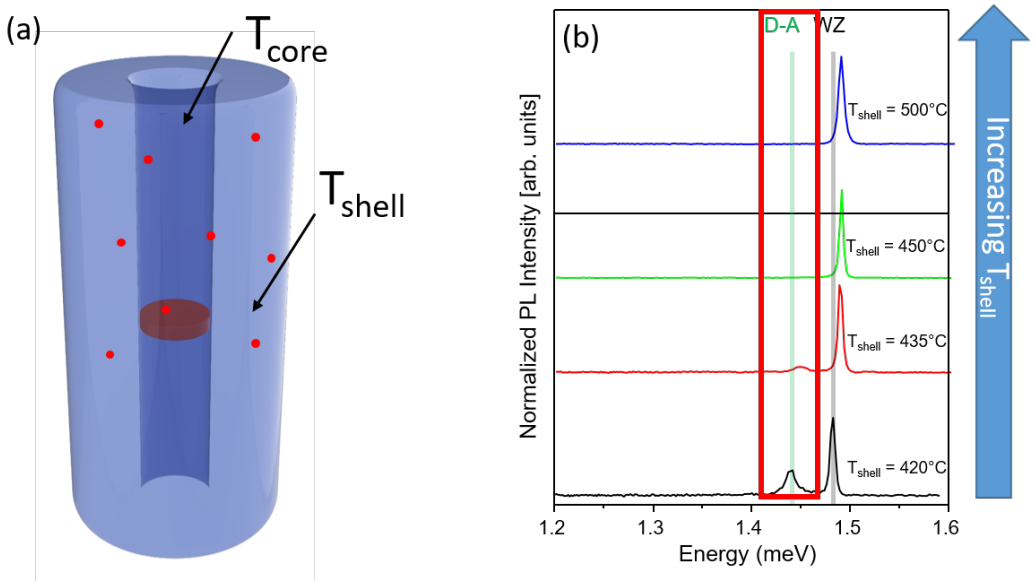

Figure 4.2: (a) Schematic representation of a section of a nanowire quantum dot where the growth temperature of the core and the shell are specified. Defects may reside in either the core or the shell (represented as red dots). (b) Spectra of InP nanowire waveguides as a function of shell growth temperature showing the reduced contribution of emission from donor-acceptor (D-A) levels with increased temperature (adapted from Ref. [3]).

Since the core of the nanowire and its shell are grown using different growth conditions/techniques, independent control of each part is possible. Figure 4.2 (a) shows a representation of a section of a nanowire quantum dot where the core is grown at a temperature, T_{core}, and the shell is grown at a temperature T_{shell}. Point defects may reside anywhere within the core of the nanowire or the shell and are represented by red dots. These defects lead to donor-acceptor levels (D-A) in the material. In (b), we show PL results, where the core of the

nanowire is consistently grown using the same temperature,$T_{core} = 420°C$, whilst the growth temperature of the shell is increased from $T_{shell} = 420°C$ to $T_{shell} = 500°C$. At a temperature $T_{shell} = 450°C$, emission from donor-acceptor levels are almost completely suppressed. We will investigate the resulting effect from the increased growth temperature of the shell in Article 4.

4.1.2 Source efficiency

I have defined in Chapter 2 the source efficiency and here I will briefly extend the discussion to nanowire quantum dots (See Eq. 2.4). The source efficiency, η, will be limited by the source internal quantum efficiency, η_{IQE}, the coupling efficiency, β_{mode}, of the emitted photons to the nanowire waveguide mode, and the fraction of the photons that couple to the external optics, α. Figure 4.3 (a) shows a calculation of the spontaneous emission rate into the fundamental mode, HE_{11}, of an InP nanowire waveguide, $\Gamma_{HE_{11}}$, of an electric dipole placed on the axis of the nanowire and orthogonal to the nanowire. The emission rates presented in the figure is normalized to the calculated spontaneous emission rate of the bulk, Γ_{bulk}, and includes $\Gamma_{HE_{11}}$ and all other "leaky" modes, γ, and is plotted as a function of normalized waveguide diameter, D/λ. The coupling efficiency,

$$\beta_{HE_{11}} = \frac{\Gamma_{HE_{11}}}{\Gamma_{HE_{11}} + \gamma}, \tag{4.1}$$

is also plotted as a function of D/λ. If D/λ is ~ 0.23, $\beta_{HE_{11}} = 95\%$ is predicted[3]. For a dot emitting at 950 nm, for example, a waveguide of diameter $D \sim 220$ nm would provide optimized values for $\Gamma_{HE_{11}}$ and $\beta_{HE_{11}}$ whilst for a dot emitting at 1310 nm (O-band of telecom), a waveguide of $D \sim 300$ nm would be required.

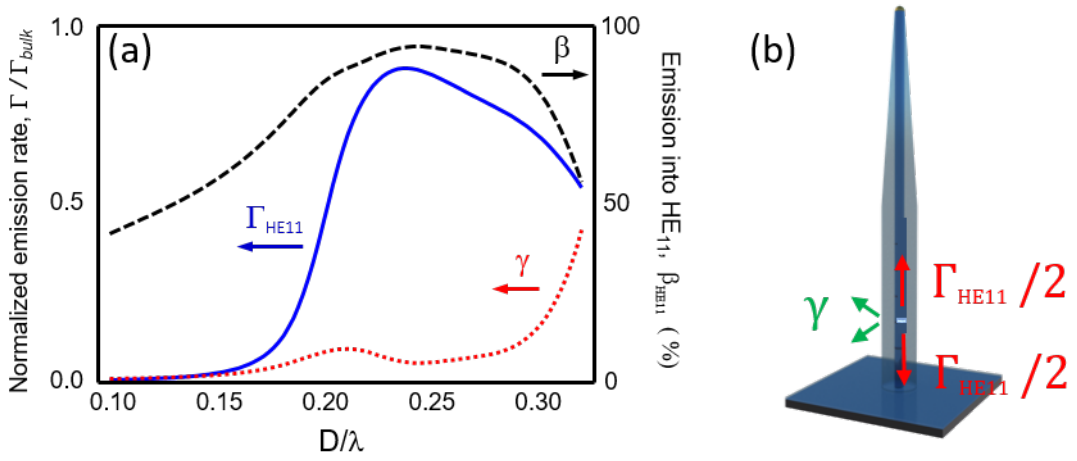

Figure 4.3: (a) Calculated spontaneous emission rate into the fundamental HE_{11} nanowire mode, $\Gamma_{HE_{11}}$ (blue solid line), and into all other modes γ (red dotted line) normalized to the spontaneous emission rate of the bulk InP, Γ_{bulk} as a function of normalized nanowire diameter, D/λ. The black dashed line is $\beta_{HE_{11}}$in percentage (adapted from Ref. [3]). (b) Tapered nanowire showing the emission direction of the confined $\Gamma_{HE_{11}}$ mode as well as the "leaky" modes γ.

Our sources are engineered to optimize $\Gamma_{HE_{11}}$, and $\beta_{HE_{11}}$ leading to measured lifetimes of around $1-2$ ns. Furthermore, approximately $\sim 50\,\%$ of the quantum dot emission is emitted towards the substrate (see Figure 4.3 (b)) and cannot be collected, which will give an upper limit of $\alpha = 50\,\%$. This can be mitigated with a metallic mirror at the nanowire base[150, 148, 151]. However, even with the upper limit on α, these nanowire structures have demonstrated efficiencies exceeding $40\,\%$[125, 150]. This is on par with the current state-of-the-art provided by quantum dot micropillar cavities, which achieved an efficiency close to $80\,\%$[152].

4.1.3 Benefits of SA-VLS grown nanowire quantum dots

Unlike other collection methods based on etching photonic structures around a self-assembled quantum dots, the SA-VLS grown nanowire quantum dots benefit from having control over the number of quantum dots incorporated within the core and the location of each nanowire on the substrate. The former provides a route to wavelength multiplexing which is investigated in Article 5. The latter is an essential aspect of scalable technologies.

4.2 Towards telecom emission

Of particular interest to quantum information technologies is the generations of single-photons at room-temperature and at telecom wavelengths (1310 nm or 1550 nm). Telecom sources of entangled photon pairs and single-photons based on spontaneous parametric down conversion (SPD) and four-wave mixing (FWM) have been demonstrated at room-temperature. For example, using a $LiNbO_3$ non-linear crystal, Brendal et al. have demonstrated entangled photon pair generation in the near-infrared at 1310 nm[153]. The experiments typically employ, non-linear crystals such as BBO[154] and PPKTP[155] for SPDC. The sources are promising for their room-temperature operation but, as mentioned in Chapter 2, suffer from low efficiencies.

Telecom emission using the InAs/InP material system is possible[156]. For the nanowire quantum dots discussed thus far, emission wavelengths were around 950 nm due to low As concentration of $x \sim 0.25$. To tune the emission towards telecom whilst maintaining the same dot geometry requires higher As concentration. Due to certain peculiarities of the VLS growth mode, it has proven extremely difficult to tune the dot emission to telecom without drastically affecting the device performance[157]. A particular constraint is the avoidance of growth interrupts during dot incorporation. The interrupts can be used to increase the As composition, however in nanowires, they can nucleate stalking faults, causing severe charge fluctuations[158, 87]. An alternative approach to tune the emission towards telecom without altering the dot properties has been proposed by Haffouz et al.[159].

In their approach, the dot growth is carried out under the same conditions for growing 950 nm emitters except that instead of growing the dot in the InP core, it is grown in an $InAs_yP_{1-y}$ section within an InP core. This "dot-in-a-rod" approach (shown schematically in Figure 4.4 (a)) uses rod compositions having lower As content than the dot, which is shown in (b), producing the band structure shown in (c), and provides longer emission wavelengths.

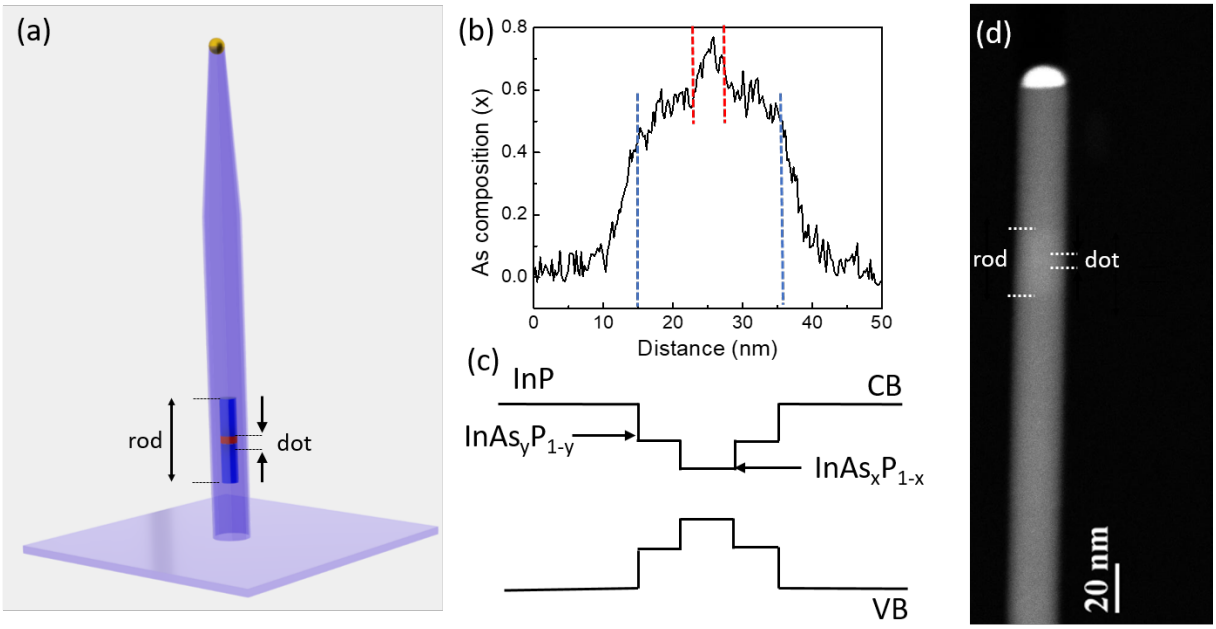

Figure 4.4: (a) Schematic drawing of a dot-in-a-rod nanowire. (b)As content of an unclad dot-in-a-rod structure. (c) Energy diagram of a $InAs_xP_{1-x}$ quantum dot within an $InAs_yP_{1-y}$ rod embedded within an InP nanowire. (d) Transmission electron microscope image of an InP nanowire core containing a dot-in-a-rod structure.

Figure 4.4 (d) shows a transmission electron microscope image of such structure. This device provided reasonable count rates (twice that reported for the source without the rod[156]). In Article 6, I present results of measurements of an optimized dot-in-a-rod structure, and show that these can operate with high count rates (similar to $950 - 980\,\text{nm}$ quantum dots) and can potentially operate as a single-photon source at room temperature.

4.3 Optical experimental methods

4.3.1 The setup

The experimental setup consists of a micro-photoluminescence configuration shown in Figure 4.5 and consists of an excitation laser incident on a 8:92 pellicule beamsplitter (BS) via a variable attenuator (VA) for controlling the power. In the setup, 8 % of the incident beam is reflected towards a closed-cycle Helium cryostat operating at a base temperature of 4 K, containing the nanowire samples. A microscope objective (MO) (100X, NA=0.81) focuses

the excitation beam onto the nanowire sample and the emission from the nanowire travels back through the microscope objective where 92 % of the available quantum dot emission is collected by external optics. Two steering mirrors (SM) and a lens (L) on an x-y-z stage are used to couple the quantum dot emission to a single mode fiber. A white light (WL) source is used to illuminate the sample and a flip mirror (FM), between the two steering mirrors, is used for imaging. The fiber coupled emission can then be sent to different set-ups depending on the measurement to be performed. The setups for the measurements are described in Chapter 3 and include:

1. Standard photoluminescence (PL) measurements.
2. High-resolution PL (HRPL) measurements.
3. Time-resolved PL (TRPL) measurements.
4. 2^{nd} order correlation (HBT) measurements.
5. 1^{st} order correlation (Coherence) measurements.
6. Hong-Ou Mandel measurements (HOM).

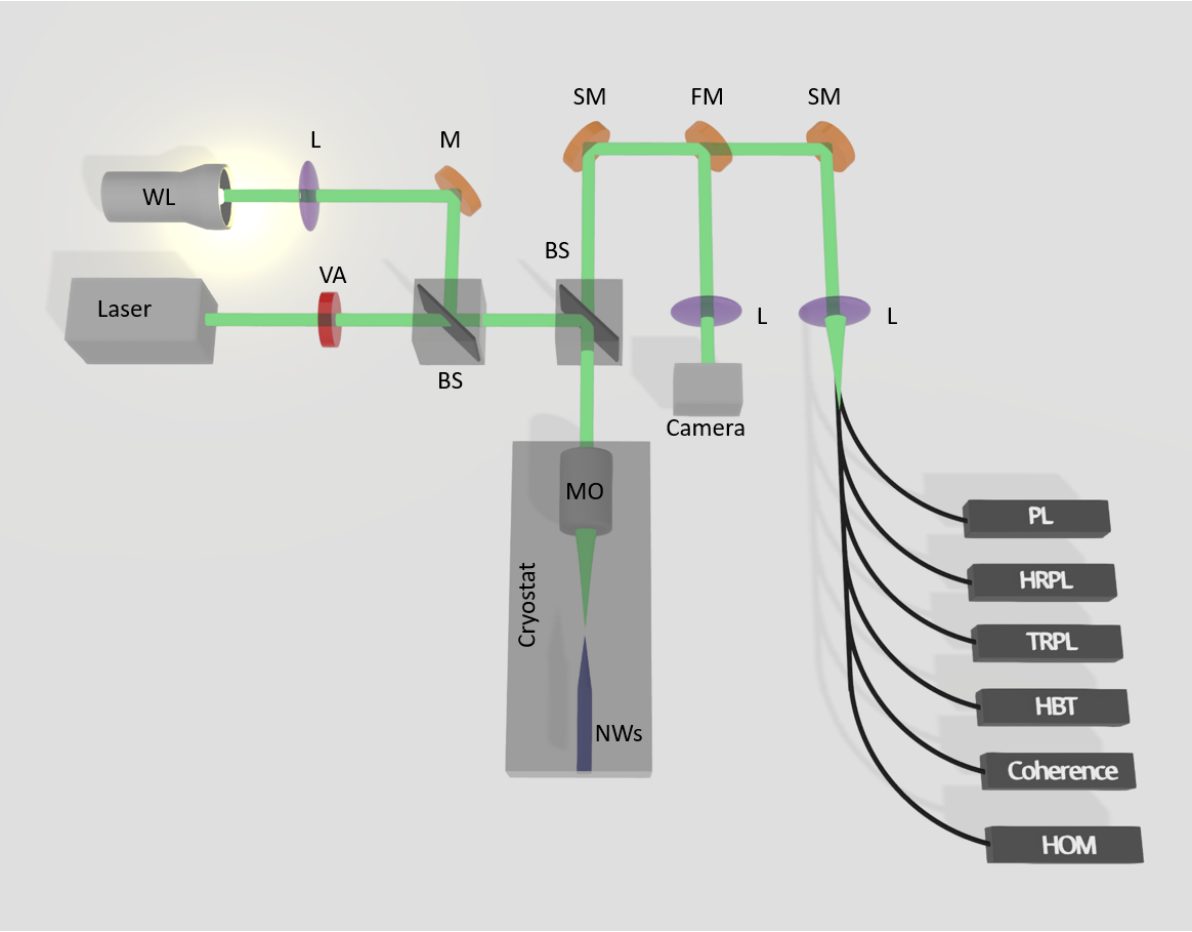

Figure 4.5: Micro-photoluminescence setup: A laser source (CW or pulsed) is sent to an 8:92 beamsplitter (BS), via a variable attenuator (VA), where 8 % of the laser is sent towards the cryostat containing the nanowire samples. The nanowire quantum dots are excited along the axis of the nanowire waveguide through a 100X microscope objective (MO) (NA=0.81), situated within the cryostat, and the emission is collected through the same microscope objective. A white light (WL) source is used to image the samples using the same optical path as the laser and focused via a lens (L) on a camera using a flip mirror (FM). The emission can either be fiber-coupled using two steering mirrors (SM) to different experimental setups.

The equipment required to perform these measurements are listed below:

- **Spectrometer:** 75 cm monochromator equipped with a liquid nitrogen cooled silicon charged coupled device (CCD). A grating on a rotation stage, with a groove density of 1200 mm^{-1} provided a spectral coverage of ~ 30 nm and the resolution was limited to $\sim 25\,\mu$eV. The spectrometer is also equipped with a liquid nitrogen cooled InGaAs detector, which provided a resolution of $\sim 45\,\mu$eV.

- **Tunable filters:** Unless using the spectrometer for standard PL measurements, filtering of emission lines was required, which generally comprised of piezo fiber-based tunable filters with a bandwidth of 0.075 nm. 930 nm ± 30 nm and 950 nm ± 30 nm filters were used to filter emission lines from the 950 − 980 nm quantum dots. Whilst a 1310 ± 30 nm filter was used for the measurements of the telecom nanowire quantum dots. Free space filters were also available and used during the study of nanowire quantum dots emitting at telecom wavelengths (see Article 6) which were out of range from the narrow bandpass fiber-based filters.

- **Single-photon detectors:** Unless using the spectrometer for standard PL measurements, a combination of silicon avalanche photodiodes (APDs) (jitter time $\sim$ 200 ps) and superconducting nanowire single-photon detectors (SNSPDs) (jitter time $\sim$ 60 ps) were used throughout the thesis.

- **Fabry-Perot etalon:** In order to measure the HRPL of the quantum dots, two etalons were utilized:

    1. A temperature controlled etalon having a bandwidth of 500 MHz with a free-spectral range (FSR) of 100 GHz which was used in Article 2.
    2. A Voltage controlled etalon having a bandwidth of 250 MHz with a FSR of 40 GHz which was utilized in Chapter 3 and Article 4.

- **Delay stage:** A delay stage was required for the coherence and HOM measurements presented in Chapter 3. We use a motor driven delay line, capable of providing 1.2 ns delay with a step resolution of 1 ps.

Chapter 5

Article 1: Systematic study of the emission spectra of nanowire quantum dots

This chapter contains the following article:

P. Laferrière, E. Yeung, M. Korkusinski, P. J. Poole, R. L. Williams, D. Dalacu, J. Manalo, M. Cygorek, A. Altintas, & P. Hawrylak, "Systematic study of the emission spectra of nanowire quantum dots", Applied Physics Letters **118**, 161107 (2021).

DOI: https://doi.org/10.1063/5.0045880

Applied Physics Letters

Systematic study of the emission spectra of nanowire quantum dots

Cite as: Appl. Phys. Lett. **118**, 161107 (2021); https://doi.org/10.1063/5.0045880
Submitted: 29 January 2021 • Accepted: 27 March 2021 • Published Online: 22 April 2021

Patrick Laferrière, Edith Yeung, Marek Korkusinski, et al.

Applied Physics Letters ARTICLE scitation.org/journal/apl

Systematic study of the emission spectra of nanowire quantum dots

Cite as: Appl. Phys. Lett. **118**, 161107 (2021); doi: 10.1063/5.0045880
Submitted: 29 January 2021 · Accepted: 27 March 2021 ·
Published Online: 22 April 2021

Patrick Laferrière,[1,2,a)] Edith Yeung,[1,2] Marek Korkusinski,[1] Philip J. Poole,[1] Robin L. Williams,[1] Dan Dalacu,[1,2] Jacob Manalo,[2] Moritz Cygorek,[2,3] Abdulmenaf Altintas,[2] and Pawel Hawrylak[2]

AFFILIATIONS

[1]National Research Council Canada, Ottawa, Ontario K1A 0R6, Canada
[2]University of Ottawa, Ottawa, Ontario K1N 6N5, Canada
[3]Heriot-Watt University, Edinburgh EH14 4AS, United Kingdom

Note: This paper is part of the APL Special Collection on Non-Classical Light Emitters and Single-Photon Detectors.
[a)]**Author to whom correspondence should be addressed:** plaferr3@uottawa.ca

ABSTRACT

A systematic study of the emission spectra of single InAsP nanowire quantum dots in position-controlled InP photonic nanowire waveguides is presented. Using excitation power-dependent photoluminescence and correlation measurements, we distinguish between the different excitonic complexes responsible for s-shell emission. From measurements of over 40 nominally identical devices, we obtain a standard deviation of ∼5 meV in the emission energy of excitons, biexcitons, and charged exciton photons. The mean biexciton binding energy was 1.9 meV with a standard deviation of ∼0.8 meV. The experimental spectra are understood using atomistic multi-million atom theory of neutral and charged multi-exciton complexes implemented in the design tool QNANO.

https://doi.org/10.1063/5.0045880

In semiconductor quantum dots, the photon emission spectrum depends on the number of photo-excited carriers.[1] Hence, a single photon can be spectrally identified as a recombination from a single exciton. Similarly, entangled photons can be generated by multi-exciton cascades.[2–5] The difficulty in generating entangled photons by the bi-exciton (XX)-exciton (X) cascade is due to the exciton fine structure.[6–10] This difficulty is overcome by using symmetric quantum dot systems in which fine structure splittings are negligible.[11–13] Alternatively, entangled photon generation can be facilitated using quantum dots where the XX photon emission energy is degenerate with that of the X photon. The biexciton-exciton cascade in such a system is predicted to be less susceptible to deterioration of the degree of entanglement of the emitted photon due to electron-phonon interactions.[14] A vanishing biexciton binding energy can be achieved, for example, by gating[15–17] but may also occur naturally for specific structural parameters.[18,19]

Nanowires have shown promise as efficient sources of non-classical light.[20–23] To investigate the possibility of creating a system having the desired excitonic energy configuration for high fidelity entanglement generation, we study InAsP quantum dots incorporated in bottom-up InP nanowire structures. This system is ideally suited for engineering single and entangled photon sources as their diameter, height, and composition are well controlled. In particular, we combine selective-area (SA) epitaxy and vapour–liquid–solid (VLS) epitaxy[24] to grow position-controlled devices consisting of a single quantum dot with a precisely defined geometry optimally located within a photonic nanowire waveguide.[25]

Producing high-optical quality quantum dots using VLS epitaxy necessitates avoiding some of the typical epitaxial techniques employed when growing heterostructures. For example, (i) the crystal structure of VLS nanowires depends on the growth rate[26] and (ii) the steady-state alloy composition of the metal catalyst is dependent on the group V element, resulting in growth rate transients when switching precursors.[27] These two effects necessitate avoiding growth interrupts (i.e., pumping out the Group III species for a short period of time) in order to grow pure single phase heterostructures (i.e., with no stacking faults that can lead to significant spectral fluctuations[24]). Without the use of growth interrupts, which are typically required to obtain abrupt interfaces separating sections having well-defined compositions,[28] ternary InAsP quantum dots are produced containing a significant fraction of phosphorus atoms carried over from the growth of the InP barrier.

The dilute nature of the quantum dot composition produces dots with different optical properties even if they have nominally the same size and have the same total composition, a consequence of strong local fluctuations in confining potentials and strain fields.[11] In order to

gain a better understanding of the role of the distribution of the As and P atoms within the quantum dot, we have performed a systematic experimental and theoretical study of the emission spectra observed in nominally identical dots. The different excitonic complexes are identified using excitation power-dependent measurements and comparison with results of atomistic many-body calculations.

The nanowire quantum dots studied were grown in the InAs/InP material system using chemical beam epitaxy and the SA-VLS growth technique described in Ref. 24. This technique allows for the growth of $InAs_xP_{1-x}$ quantum dots embedded in position-controlled InP photonic nanowires having a wurtzite crystal phase free of stacking faults.[22] The quantum dots are incorporated in an InP nanowire core, $\sim$1 μm above the base, and have a diameter of $D_{dot} \sim 20$ nm, a height of $H_{dot} \sim 4$ nm, and a composition of $x \sim 20\%$. A cross-sectional transmission electron microscopy image of a dot in a wurtzite InP nanowire core is shown in Fig. 1(a). The core is the clad with an InP shell to produce a photonic nanowire having a geometry optimized for collection of dot emission around $\lambda = 950$ nm with a base diameter of 250 nm tapered to 20 nm over a length of ~ 10 μm.

Optical measurements were carried out at 4 K in a closed-cycle helium cryostat. Individual nanowires were excited above-band using continuous-wave excitation at $\lambda = 780$ nm (for photoluminescence measurements) or $\lambda = 633$ nm (for correlation measurements) focused to a few micrometers by a 100× objective with a numerical aperture of 0.81. Photoluminescence from the dot was collected through the same objective and spectrally resolved using a grating spectrometer with an Si CCD array detector. For autocorrelation measurements, individual lines were selected using a fiber-based tunable filter with a 0.075 nm bandpass and the filtered emission was sent to two fiber-coupled avalanche photodiodes (APDs) via a 50:50 fiber beam splitter. For cross correlation measurements, two filters were used, one placed on each output arm of the splitter. The selected lines from each filter were sent to either the "start" or the "stop" APD.

Figure 1(b) shows a characteristic emission spectrum of a nanowire quantum dot at low excitation power. At the lowest excitation power, we observe an emission line at high energy identified as neutral exciton X and one at low energy identified as charged exciton X^-. The fine structure splitting of the neutral exciton is typically a few μeV[29] and is not resolved in the spectrum. With increasing pump power, biexciton XX appears in between these two lines. The assignment of emission lines is based on the excitation power dependent-photoluminescence and correlation experiments discussed below.

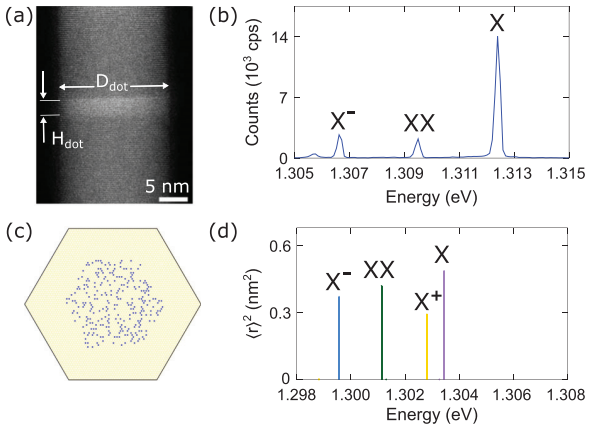

FIG. 1. (a) Transmission electron microscopy image of an InAsP nanowire quantum dot. (b) Characteristic s-shell emission spectrum of a dot. (c) Cross section of the InAsP dot used in the calculated emission spectrum shown in (d), with the blue dots indicating the position of As atoms.

In Fig. 1(d), we show the results of atomistic calculations of the emission from multi-exciton complexes in a quantum dot with specifications similar to the dot shown in Fig. 1(a): arsenic composition $x = 20\%$, diameter $D_{dot} = 18.2$ nm, and height $H_{dot} = 4.1$ nm. The calculations are performed for the specific distribution of As atoms in the hexagonal InP nanowire shown in Fig. 1(c). The computed transition energies reproduce the ordering of levels observed experimentally, shifted by 9 meV. They also predict similar values for the binding energies of the biexciton (difference in X and XX photon energies, $E_B = E_X - E_{XX}$) and charged exciton (difference in X and X^- photon energies, $E_C = E_X - E_{X^-}$). The calculations confirm that the lowest energy peak corresponds to the negatively charged exciton, while the emission from the positively charged exciton (not observed experimentally) appears between XX and X. We note the calculated energy splitting of the intermediate exciton state due to the fact that the fine structure is too small to be observed on this energy scale.

Although we obtained good agreement between theory and experiment for this particular dot, previous measurements on the same quantum dot system have demonstrated a wide range of biexciton binding energies, including both positive and negative values.[19] This variation was attributed, at least in part, to the random distribution of arsenic atoms in the dilute quantum dot.[11] To better quantify the statistical distribution of emission energies in the nanowire quantum dot system, we performed a systematic study of 42 nominally identical nanowire quantum dots having similar emission spectra. The different emission lines were identified using power-dependent photoluminescence and correlation measurements as described below.

In Fig. 2, we show power-dependent emission spectra from three representative dots in terms of the power at which the X emission peak saturates, P_{sat}. At the lowest excitation power shown, the spectrum from each dot consists of two dominant emission lines around 1.3 eV separated by $\sim$6 meV. A third weaker emission line is also evident, spectrally located in between the two dominant peaks, which becomes proportionately brighter as the excitation power is increased. At the highest power shown, we observe additional peaks appearing around 1.3 eV as well as a new set of peaks around 1.35 eV. We associate the peaks around 1.3 eV with radiative recombination of electron-hole pairs from the s-shell of the quantum dot, while those around 1.35 eV with p-shell recombination. As mentioned above, the typical s-shell emission in this quantum dot system for above-band excitation[30] consists of photons from radiative recombination of excitons (X), biexcitons (XX), and negatively charged excitons (X^-). One can readily distinguish between photons originating from excitonic complexes with only one possible decay pathway (e.g., X, X^-) and those with two possible pathways (e.g., XX) from the power dependence of the count rate. In Figs. 2(d)–2(f), we plot the count rate as a function of pump power for the three dominant peaks for each of the three representative quantum dots. In each case, XX can be distinguished from X and X^- by the stronger dependence of the count rate on pump power (exponent $n \sim 2$) as well as the later onset of emission with pump power.

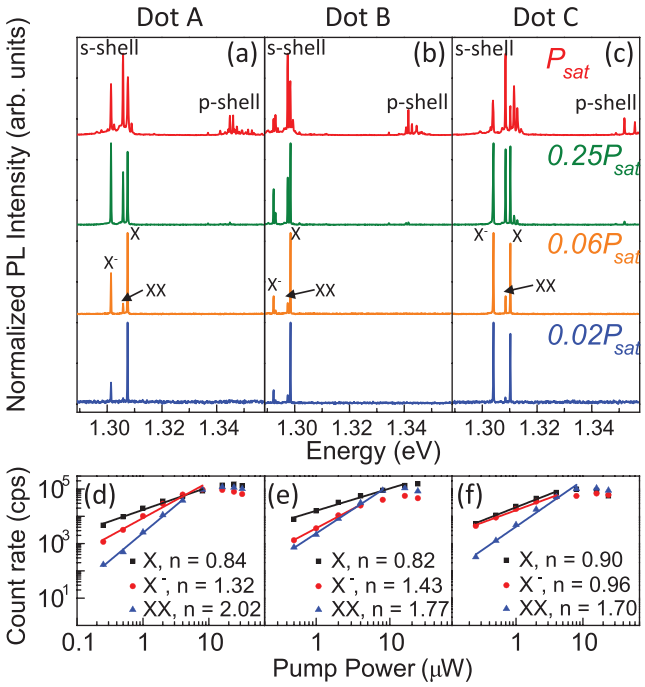

FIG. 2. (a)–(c) Representative excitation power-dependent photoluminescence (PL) measurements of three nanowire quantum dots. (d)–(f) PL intensity as a function of power for the main three excitonic complexes X, XX, and X^-.

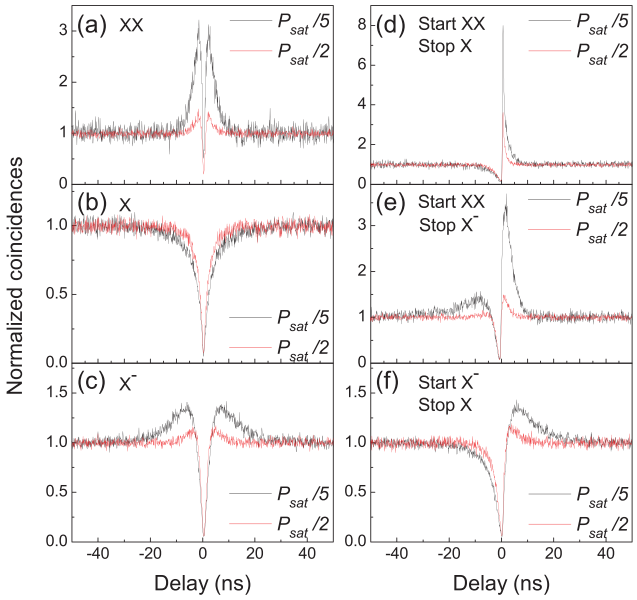

FIG. 3. Power-dependent second-order autocorrelation measurements of (a) exciton, (b) biexciton, and (c) charged exciton photons of a characteristic dot. Power-dependent cross correlation between (d) XX-X, (e) XX-X^-, and (f) X^--X of a characteristic dot.

Using the count rate power dependence to distinguish between X and X^- is not completely reliable and may lead to incorrect peak identification. For example, two of the peaks in Dot C in Fig. 2 show a very similar power dependence. One can instead use the presence of the anisotropic exchange interaction-induced fine structure splitting of the neutral exciton X that is absent in charged exciton X^-. However, the high symmetry of the wurtzite nanowire quantum dot system[11,12] results in extremely small splittings,[23] which are difficult to resolve with a typical grating spectrometer.

Alternatively, correlation measurements can provide additional information on the nature of the excitonic complex from which the photons are produced. In Fig. 3, we show the second-order autocorrelation measurements, $g^{(2)}(\tau)$, of the three peaks observed in a characteristic dot. Biexciton photons are readily identified from the bunching observed at short time delays when pumping weakly,[31] shown in Fig. 3(a). Right after the detection of a biexciton photon, the dot is populated with one electron-hole pair, which may then decay to the ground state or capture a second pair to form a new biexciton. As the excitation power is decreased, reducing the capture rate of electron-hole pairs, it becomes comparatively more likely to form a new biexciton at short delays when the dot already contains one electron-hole pair relative to long delays when the dot will typically be empty and requires the capture of two electron-hole pairs. Hence, the decay of the bunching corresponds to the X lifetime.

Distinguishing between X and X^- using autocorrelations measurements is less trivial. In Figs. 3(b) and 3(c), we show the autocorrelation for the high and low energy peaks, respectively, at excitation powers of $\sim P_{sat}/5$ and $\sim P_{sat}/2$. In (b), the curve shows the behavior expected from a two-level system consisting of the vacuum and the excitonic state, for which $g^{(2)}(\tau) = 1 - e^{-(R+\Gamma)|\tau|}$, where R is the pump rate and Γ is the excitonic radiative lifetime. In both cases, the spectra display a strong antibunching dip down to $g^{(2)}(\tau = 0) \sim 0.05$ with a width that reflects the exciton lifetime when $R \ll \Gamma$, while for $R \gg \Gamma$, the width is limited by the excitation rate. In the case shown in Fig. 3(c), we also observe bunching at short delays that decays to average coincidence counts over an excitation power-dependent timescale that is longer than that expected from radiative recombination. The degree of bunching and the associated timescales vary from dot to dot, and we associate this behavior with changes in the charge configuration of the dot (e.g., blinking) that has been previously observed in different quantum dot systems.[32–34]

To distinguish between X and X^-, we measured the cross-correlations[31,33–36] between the three dominant peaks. In Fig. 3(d), we show the cross correlation between the central peak (XX) and the high energy peak measured for excitation powers of $P_{sat}/2$ and $P_{sat}/5$. We send XX to the start APD and the high energy emission peak to the stop APD. The observed asymmetric bunching behavior indicates a cascaded emission process typical of an XX–X cascade (i.e., XX photons are emitted first followed by X photons). We, thus, identify the high energy peak for this dot as originating from X recombination.

Figure 3(e) shows the cross correlation between the low energy peak, identified as X^- and XX for a characteristic dot. The correlation spectra show strong antibunching at $\tau = 0$ and bunching at both positive and negative delays with a higher degree of bunching at positive delays and at lower excitation. In the limit of low excitation, the average number of carriers in the dot tends to zero. At short positive delays, having just detected an XX photon, the dot is necessarily occupied with two carriers (one electron and one hole). To put the dot in

the X^- state then requires the capture of just a single electron. The probability of capturing a single carrier is more likely than capturing three carriers (two electrons and a hole), which is required at longer delays when the dot is typically empty (for low excitation rates). This produces the observed bunching at short positive delays. Similarly, at short negative delays, having just detected an X^- photon, the dot is left occupied with a single electron. To put the dot in the XX state requires capturing three additional carriers (one electron and two holes), which is more likely than the four carrier required (two electrons and two holes) if the dot were empty. This produces the observed bunching at short negative delays.

Finally, we look at the cross correlation between X^- and X [Fig. 3(f)], which shows an antibunching dip at $\tau = 0$ and short delay bunching, but only for $\tau > 0$. As above, at short positive delays, having just detected an X^- photon, the dot is left occupied with a single electron. To create the neutral exciton, a single hole is required, which is more likely than the requirement of capturing of two carriers (one electron and one hole) into an empty dot, and thus, bunching is observed at positive delays. No bunching is observed at negative delays as the dot is empty, having just detected an X photon.

The results of applying the above optical characterization methodology to 42 quantum dots to extract emission energies E_X, E_{XX}, and E_{X^-} as well as energy spacings E_B and E_C are summarized in Fig. 4 and Table I. In the table, we have included the standard deviations from Gaussian fits to the histograms in Fig. 4.

In order to gain a microscopic understanding and evaluate the ability to engineer the emission spectra of nanowire quantum dots, we use the atomistic million-atom many-body theory of multi-exciton complexes implemented in the code QNANO.[11,37,38] The simulations are targeted to provide insight into the observed distribution of biexcitonic binding energies, with the specific aim of identifying the

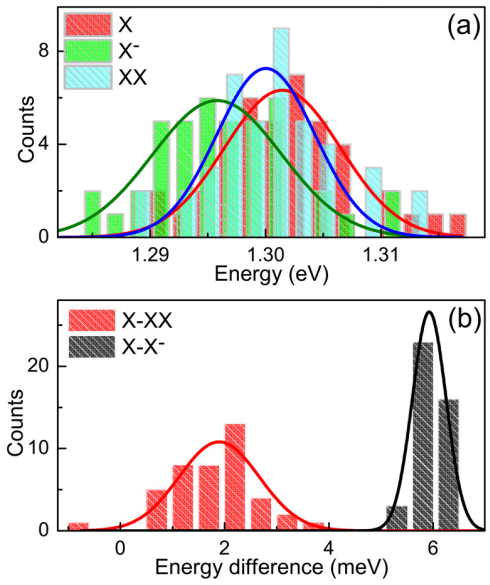

FIG. 4. (a) Energy distribution of the different complexes extracted from the measurements on 42 nanowire quantum dots. (b) Histograms of the energy difference between the X-XX emission lines, E_B (red), and the X-X^- emission lines, E_C (black).

TABLE I. Emission energies and spacings and their standard deviations from fits to the data in Fig. 4.

	Emission energy (meV)	σ (meV)	Energy spacing (meV)	σ (meV)
X	1301	5.0	…	…
X^-	1296	5.6	5.92	0.32
XX	1300	4.3	1.90	0.77

structural parameter required to achieve coincidences between X and XX emission lines.

The starting point of QNANO is the atomic positions of In and P in a hexagonal nanowire. Next, we replace 20% of the P atoms with As in the volume of a hexagonal quantum dot as shown in Fig. 1(c). Because InAs and InP lattice constants differ, such a replacement causes strain and displacement of the As atoms from the P positions. In the case of the InAsP quantum dot, this mismatch is about 3% and is accounted for in the model.[11] We, hence, find the actual atomic positions of all the atoms by minimizing the total elastic energy.

With the atomic positions of all the atoms defined, we obtain the single particle states from the strain parameterized tight-binding Hamiltonian,

$$H_{TB} = \sum_{i=1}^{N_a}\sum_{\alpha=1}^{N_{\rm orb}} \varepsilon_{i\alpha} c_{i\alpha}^{\dagger} c_{i\alpha} + \sum_{i=1}^{N_a}\sum_{\alpha,\beta=1}^{N_{\rm orb}} \lambda_{i\alpha\beta} c_{i\alpha}^{\dagger} c_{i\beta} + \sum_{i=1}^{N_a}\sum_{j=1}^{nn(i)}\sum_{\alpha,\beta=1}^{N_{\rm orb}} t_{i\alpha j\beta} c_{i\alpha}^{\dagger} c_{j\beta}\,, \tag{1}$$

where the Roman indices denote atomic positions and the Greek indices denote atomic orbitals. The parameters ε, t, and λ representing the on-site energy, tunneling matrix elements, and spin–orbit coupling, respectively, are obtained by fitting (1) to a density functional theory (DFT) band structure of the (strained) bulk materials, discussed in detail in Ref. 11. In this model, each atom is described by 20 *spds** orbitals. Using exact diagonalization, the conduction and valence band quantum dot states for structures with up to millions of atoms are obtained.

In the next step, we describe excited electrons and valence holes strongly interacting with each other. The multi-exciton complexes are described by the many-body Hamiltonian,

$$\begin{aligned} H_{MB} = &\sum_i E_i^{\rm CB} c_i^{\dagger} c_i + \frac{1}{2}\sum_{ijkl} \langle ij|V|kl\rangle c_i^{\dagger} c_j^{\dagger} c_k c_l \\ &+ \sum_p E_p^{\rm VB} h_p^{\dagger} h_p + \frac{1}{2}\sum_{pqrs} \langle pq|V|rs\rangle h_p^{\dagger} h_q^{\dagger} h_r h_s \\ &+ \sum_{iqrl} (\langle iq|V|rl\rangle - \langle iq|V|lr\rangle) c_i^{\dagger} h_q^{\dagger} h_r c_l, \end{aligned} \tag{2}$$

where $E_i^{\rm C(V)B}$ and $c_i(h_i)$ are the conduction (valence) band energies and electron (hole) annihilation operators, respectively. We then construct electron-hole configurations for a given excitonic complex, construct the Hamiltonian matrix in the space of electron-hole configurations, and diagonalize it to obtain the multi-excitonic energy levels and wavefunctions. Simultaneously, we compute dipole matrix elements and emission spectra.

One of the difficulties in calculating the many-body states lies in the Coulomb matrix elements. Since the nanostructure that we are dealing with contains hundreds of thousands of atoms, each with 20 orbitals, necessary approximations are made in order to maintain computational feasibility. These approximations include only computing two-centre integrals, i.e., integrals that only involve the scattering of electrons on one or two atoms, distinguishing between on-site and long-range terms, simplifying the latter by neglecting the overlap of wave functions on distant atoms.

Calculated emission spectra are shown in Figs. 1 and 5. Figure 1(c) shows a cross section of the simulated InAsP quantum dot having parameters similar to the grown structures: an arsenic composition of $x = 20\%$, a diameter of $D_{dot} = 18.2$ nm, and a height of $H_{dot} = 4.1$ nm. Since the distribution of As atoms is random, the calculated emission spectrum differs from experimental spectra [e.g., Fig. 1(b)], but emission lines do follow the same order as seen from Fig. 1(d), with X^- being the lowest energy line, followed by XX, X^+, and X lines.

We note that the distribution of XX binding energies shown in Fig. 4 includes samples where the XX and X emission lines coincide. If we repeat our simulations using randomly generated As atom distributions, we observe a distribution of XX binding energies with a mean value of 2.4 meV,[11] which overestimates the experimental value of 1.9 meV. We also obtain a standard deviation of only 0.72 meV, suggesting that an additional contribution is required in order to reproduce the experimentally observed negative XX binding energies.

The systematically higher theoretical value of the biexciton binding energy compared to the measurements can be explained by the assumption of a homogeneous distribution of the As atoms within the dot. We have previously demonstrated[15] that a lateral displacement between the centers of electron and hole wave functions results in a decreasing biexciton binding energy. While this was achieved in Ref. 15 using a lateral electric field, in the case of InAsP nanowire quantum dots, an inhomogeneous distribution of As atoms can play a similar role. Because of the larger deformation potential constant as well as the larger effective mass of holes compared to electrons, the hole wave function tends to be strongly localized in regions with a high As content, while electron wave functions have a more delocalized character, spanning the dot volume more smoothly.[11] As an example, Fig. 5 depicts the situation of inhomogeneous As distribution implemented as a linear lateral gradient. We find a significant reduction of the biexciton binding energy to a value of $\sim 200\ \mu$ eV, corroborating the trend toward a reduction in biexciton binding energies upon introducing inhomogeneities in the As distribution.

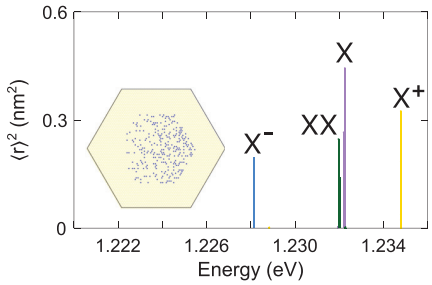

FIG. 5. Emission spectrum of the quantum dot with a gradient distribution of As atoms. The inset shows a cross section of the quantum dot used in the simulation, with the blue dots corresponding to the position of As atoms.

While both electron and hole wave functions depicted in Fig. 5 are shifted toward the right-hand side of the quantum dot, where the As density is large, the effect is stronger for the hole wave function. The net effect is a difference in the centers of the respective wave function. A similar effect can be expected from clustering of As atoms that can occur naturally during the growth, driven by a local lattice distortion of already incorporated As atoms, which may provide an energetic advantage for the incorporation of further As atoms nearby. Thus, while the overall theoretical description leads to good estimates of quantities like the biexciton binding energies, more detailed investigations of the As incorporation dynamics and the resulting As distributions would be beneficial for modeling the many-body properties in InAsP nanowire quantum dots.

Excitation power-dependent photoluminescence and autocorrelation measurements were used to identify the different excitonic complexes in nanowire quantum dots. The emission spectra were compared with predictions of the atomistic multi-million atom design tool QNANO. The observed variation of emission energies is associated with different distributions of arsenic atoms in the dilute quantum dot system, which has an otherwise well-defined geometry. Our findings summarize the characterization and atomistic theory of quantum dots in nanowires and are a step toward the full understanding of the dot dynamics within nanowire waveguides.

This work was supported by the Natural Sciences and Engineering Research Council of Canada and the Canadian Space Agency. J.M., A.A., M.C., P.L., E.Y., and P.H. acknowledge funding by NSERC Discovery, QSC2 SPG, QC2DM SPG, and UOttawa URC grants. M.C. acknowledges funding from the Humboldt Foundation and UOttawa.

DATA AVAILABILITY

The data that support the findings of this study are available from the corresponding author upon reasonable request.

REFERENCES

[1]M. Bayer, O. Stern, P. Hawrylak, S. Fafard, and A. Forchel, "Hidden symmetries in the energy levels of excitonic 'artificial' atoms," Nature **405**, 923–926 (2000).
[2]O. Benson, C. Santori, M. Pelton, and Y. Yamamoto, "Regulated and entangled photons from a single quantum dot," Phys. Rev. Lett. **84**, 2513–2516 (2000).
[3]D. Fattal, K. Inoue, J. Vučković, C. Santori, G. S. Solomon, and Y. Yamamoto, "Entanglement formation and violation of Bell's inequality with a semiconductor single photon source," Phys. Rev. Lett. **92**, 037903 (2004).
[4]N. Akopian, N. H. Lindner, E. Poem, Y. Berlatzky, J. Avron, and D. Gershoni, "Entangled photon pairs from semiconductor quantum dots," Phys. Rev. Lett. **96**, 130501 (2006).
[5]I. Schwartz, D. Cogan, E. R. Schmidgall, Y. Don, L. Gantz, O. Kenneth, N. H. Lindner, and D. Gershoni, "Deterministic generation of a cluster state of entangled photons," Science **354**, 434 (2016).
[6]M. Bayer, G. Ortner, O. Stern, A. Kuther, A. A. Gorbunov, A. Forchel, P. Hawrylak, S. Fafard, K. Hinzer, T. L. Reinecke, S. N. Walck, J. P. Reithmaier, F. Klopf, and F. Schäfer, "Fine structure of neutral and charged excitons in self-assembled In(Ga)As/(Al)GaAs quantum dots," Phys. Rev. B **65**, 195315 (2002).
[7]M. Zieliński, "Fine structure of light-hole excitons in nanowire quantum dots," Phys. Rev. B **88**, 115424 (2013).
[8]M. Korkusinski and P. Hawrylak, Phys. Rev. B **87**, 115310 (2013).

[9]E. Kadantsev and P. Hawrylak, "Theory of exciton fine structure in semiconductor quantum dots: Quantum dot anisotropy and lateral electric field," Phys. Rev. B **81**, 045311 (2010).
[10]A. H. Trojnar, E. S. Kadantsev, M. Korkusiński, and P. Hawrylak, "Theory of fine structure of correlated exciton states in self-assembled semiconductor quantum dots in a magnetic field," Phys. Rev. B **84**, 245314 (2011).
[11]M. Cygorek, M. Korkusinski, and P. Hawrylak, "Atomistic theory of electronic and optical properties of InAsP/InP nanowire quantum dots," Phys. Rev. B **101**, 075307 (2020).
[12]R. Singh and G. Bester, "Nanowire quantum dots as an ideal source of entangled photon pairs," Phys. Rev. Lett. **103**, 063601 (2009).
[13]T. Kuroda, T. Mano, N. Ha, H. Nakajima, H. Kumano, B. Urbaszek, M. Jo, M. Abbarchi, Y. Sakuma, K. Sakoda, I. Suemune, X. Marie, and T. Amand, "Symmetric quantum dots as efficient sources of highly entangled photons: Violation of Bell's inequality without spectral and temporal filtering," Phys. Rev. B **88**, 041306(R) (2013).
[14]T. Seidelmann, F. Ungar, M. Cygorek, A. Vagov, A. M. Barth, T. Kuhn, and V. M. Axt, "From strong to weak temperature dependence of the two-photon entanglement resulting from the biexciton cascade inside a cavity," Phys. Rev. B **99**, 245301 (2019).
[15]M. Korkusinski, M. E. Reimer, R. L. Williams, and P. Hawrylak, "Engineering photon cascades from multiexciton complexes in a self-assembled quantum dot by a lateral electric field," Phys. Rev. B **79**, 035309 (2009).
[16]M. E. Reimer, M. P. van Kouwen, A. W. Hidma, M. H. M. van Weert, E. P. A. M. Bakkers, L. P. Kouwenhoven, and V. Zwiller, "Electric field induced removal of the biexciton binding energy in a single quantum dot," Nano Lett. **11**, 645–650 (2011).
[17]M. Zeeshan, N. Sherlekar, A. Ahmadi, R. L. Williams, and M. E. Reimer, "Proposed scheme to generate bright entangled photon pairs by application of a quadrupole field to a single quantum dot," Phys. Rev. Lett. **122**, 227401 (2019).
[18]T. Heindel, A. Thoma, M. von Helversen, M. Schmidt, A. Schlehahn, M. Gschrey, P. Schnauber, J.-H. Schulze, A. Strittmatter, J. Beyer, S. Rodt, A. Carmele, A. Knorr, and S. Reitzenstein, "A bright triggered twin-photon source in the solid state," Nat. Commun. **8**, 14870 (2017).
[19]D. Dalacu, D. B. Northeast, P. J. Poole, G. C. Aers, R. L. Williams, K. A. Owen, and D. Oblak, "Pump power control of photon statistics in a nanowire quantum dot," Phys. Rev. B **102**, 115401 (2020).
[20]J. Claudon, J. Bleuse, N. S. Malik, M. Bazin, P. Jaffrennou, N. Gregersen, C. Sauvan, P. Lalanne, and J.-M. Gérard, "A highly efficient single-photon source based on a quantum dot in a photonic nanowire," Nat. Photonics **4**, 174 (2010).
[21]M. E. Reimer, G. Bulgarini, N. Akopian, M. Hocevar, M. B. Bavinck, M. A. Verheijen, E. P. A. M. Bakkers, L. P. Kouwenhoven, and V. Zwiller, "Bright single-photon sources in bottom-up tailored nanowires," Nat. Commun. **3**, 737 (2012).
[22]D. Dalacu, K. Mnaymneh, J. Lapointe, X. Wu, P. J. Poole, G. Bulgarini, V. Zwiller, and M. E. Reimer, "Ultraclean emission from InAsP quantum dots in defect-free wurtzite InP nanowires," Nano Lett. **12**, 5919–5923 (2012).
[23]M. A. M. Versteegh, M. E. Reimer, K. D. Jöns, D. Dalacu, P. Poole, A. Gulinatti, A. Giudice, and V. Zwiller, "Observation of strongly entangled photon pairs from a nanowire quantum dot," Nat. Commun. **5**, 6298 (2014).
[24]D. Dalacu, K. Mnaymneh, X. Wu, J. Lapointe, G. C. Aers, P. J. Poole, and R. L. Williams, "Selective-area vapor-liquid-sold growth of tunable inasp quantum dots in nanowires," Appl. Phys. Lett. **98**, 251101 (2011).
[25]D. Dalacu, P. J. Poole, and R. L. Williams, "Nanowire-based sources of non-classical light," Nanotechnology **30**, 232001 (2019).
[26]K. A. Dick, J. Bolinsson, M. E. Messing, S. Lehmann, J. Johansson, and P. Caroff, "Parameter space mapping of InAs nanowire cyrstal structure," J. Vac. Sci. Technol. B **29**, 04D103 (2011).
[27]L. E. Fröberg, B. A. Wacaser, J. B. Wagner, S. Jeppesen, B. J. Ohlsson, K. Deppert, and L. Samuelson, "Transients in the formation of nanowire heterostructures," Nano Lett. **8**, 3815–3818 (2008).
[28]S. Haffouz, P. J. Poole, J. Jin, X. Wu, L. Giner, K. Mnaymneh, D. Dalacu, and R. L. Williams, "Single quantum dot-in-a-rod embedded in a photonic nanowire waveguide for telecom band emission," Appl. Phys. Lett. **117**, 113102 (2020).
[29]M. E. Reimer, G. Bulgarini, A. Fognini, R. W. Heeres, B. J. Witek, M. A. M. Versteegh, A. Rubino, T. Braun, M. Kamp, S. Höfling, D. Dalacu, J. Lapointe, P. J. Poole, and V. Zwiller, "Overcoming power broadening of the quantum dot emission in a pure wurtzite nanowire," Phys. Rev. B **93**, 195316 (2016).
[30]A. Fognini, A. Ahmadi, M. Zeeshan, J. T. Fokkens, S. J. Gibson, N. Sherlekar, S. J. Daley, D. Dalacu, P. J. Poole, K. D. Jöns, V. Zwiller, and M. E. Reimer, "Dephasing free photon entanglement with a quantum dot," ACS Photonics **6**, 1656 (2019).
[31]A. Kiraz, S. Fälth, C. Becher, B. Gayral, W. V. Schoenfeld, P. M. Petroff, L. Zhang, E. Hu, and A. Imamoglŭ, "Photon correlation spectroscopy of a single quantum dot," Phys. Rev. B **65**, 161303(R) (2002).
[32]C. Santori, D. Fattal, J. Vuckovic, G. S. Solomon, E. Waks, and Y. Yamamoto, "Submicrosecond correlations in photoluminescence from InAs quantum dots," Phys. Rev. B **69**, 205324 (2004).
[33]G. Sallen, A. Tribu, T. Aichele, R. André, L. Besombes, C. Bougerol, S. Tatarenko, K. Kheng, and J. P. Poizat, "Exciton dynamics of a single quantum dot embedded in a nanowire," Phys. Rev. B **80**, 085310 (2009).
[34]B. Piętka, J. Suffczyński, M. Goryca, T. Kazimierczuk, A. Golnik, P. Kossacki, A. Wysmolek, J. A. Gaj, R. Stępniewski, and M. Potemski, Phys. Rev. B **87**, 035310 (2013).
[35]E. Moreau, I. Robert, L. Manin, V. Thierry-Mieg, J. M. Gérard, and I. Abram, "Quantum cascade of photons in semiconductor quantum dots," Phys. Rev. Lett. **87**, 183601 (2001).
[36]D. V. Regelman, U. Mizrahi, D. Gershoni, E. Ehrenfreund, W. V. Schoenfeld, and P. M. Petroff, "Semiconductor quantum dot: A quantum light source of multicolor photons with tunable statistics," Phys. Rev. Lett. **87**, 257401 (2001).
[37]W. Sheng and P. Hawrylak, "Atomistic theory of electronic and optical properties of InAs/InP self-assembled quantum dots on patterned substrates," Phys. Rev. B **72**, 035326 (2005).
[38]M. Zieliński, M. Korkusinski, and P. Hawrylak, "Atomistic tight-binding theory of multiexciton complexes in a self-assembled InAs quantum dot," Phys. Rev. B **81**, 085301 (2010).

Chapter 6

Article 2: Unity yield of deterministically positioned quantum dot single-photon sources

This chapter contains the following article:

P. Laferrière, E. Yeung, I. Miron, D. B. Northeast, Sofiane Haffouz, Jean Lapointe, M. Korkusinski, P. J. Poole, R. L. Williams, & D. Dalacu, "Unity Yield of deterministically positioned quantum dot single photon sources", Scientific Reports **12**, 6376 (2022).

DOI: https://doi.org/10.1038/s41598-022-10451-1

scientific reports

Check for updates

OPEN

Unity yield of deterministically positioned quantum dot single photon sources

Patrick Laferrière[1,2], Edith Yeung[1,2], Isabelle Miron[1,2], David B. Northeast[1], Sofiane Haffouz[1], Jean Lapointe[1], Marek Korkusinski[1], Philip J. Poole[1], Robin L. Williams[1] & Dan Dalacu[1,2]✉

We report on a platform for the production of single photon devices with a fabrication yield of 100%. The sources are based on InAsP quantum dots embedded within position-controlled bottom-up InP nanowires. Using optimized growth conditions, we produce large arrays of structures having highly uniform geometries. Collection efficiencies are as high as 83% and multiphoton emission probabilities as low as 0.6% with the distribution away from optimal values associated with the excitation of other charge complexes and re-excitation processes, respectively, inherent to the above-band excitation employed. Importantly, emission peak lineshapes have Lorentzian profiles indicating that linewidths are not limited by inhomogeneous broadening but rather pure dephasing, likely elastic carrier-phonon scattering due to a high phonon occupation. This work establishes nanowire-based devices as a viable route for the scalable fabrication of efficient single photon sources and provides a valuable resource for hybrid on-chip platforms currently being developed.

It has long been recognized that the radiative decay of excitonic complexes in epitaxial quantum dots can produce non-classical photon states e.g. single photons[1–3] and entangled photon pairs[4–6]. By incorporating the quantum dots within appropriate photonic structures, very bright and very efficient sources can be produced[7–12]. The cited sources employed randomly nucleated dots formed by strain-driven processes (i.e. self-assembly) and it has been a long term goal to develop techniques to control where such dots nucleate[13–19]. Site-control techniques facilitate the coupling of the emitters to photonic structures[20–22] and make device manufacture compatible with standard semiconductor processing techniques. They will also be essential in many quantum technologies that rely on the availability of a large number of such sources e.g. linear optical quantum computing[23], quantum simulation[24,25] and Boson sampling[26–28].

An approach employing site-control of self-assembled quantum dots that produces with high yield devices emitting high optical quality single photons has not yet been realised. In contrast, quantum dots incorporated within nanowires grown using vapour–liquid–solid epitaxy[29] offer a straight forward approach to site-control[30,31]. High efficiency devices are possible using appropriate nanowire geometries designed for single-mode waveguiding operation[7]. The bottom-up approach is well suited to providing high efficiency devices as the incorporated dot is naturally aligned on-axis for optimal coupling to the fundamental waveguide mode. Importantly, the processing required for the site-controlled growth does not degrade the optical quality of the emitted photons. Sources based on position-controlled bottom-up nanowires have demonstrated single photon collection efficiencies of $>$ 40% with near-transform limited linewidths of 880 MHz[32] and single photon purities greater than 99%[33].

In the present work, we extend the bottom-up site-controlled approach to realize unity yield of bright sources of high optical quality single photons. We analyse a large 10×10 array of nanowires and find each and every device displays bright, single emission lines associated with recombination of excitonic complexes from the single quantum dot embedded within. From a detailed characterization of a representative subset of the nanowires in the array, we observe devices that operate with efficiencies that approach theoretical limits given by the calculated dot-mode coupling $\beta \sim 95\%$[34]. A statistical analysis of the performance of the devices afforded by the high yield provides insight into possible mechanisms responsible for preventing universal optimal performance.

Key properties relevant in quantum technology applications were also measured, in particular single photon and spectral purity. Using above-band excitation we achieve close to optimal performance which, for self-assembled quantum dots, is typically reserved for devices employing charge tunable cavity structures operated under resonant excitation[8,11,35,36]. This surprising result is attributed to having one and only one emitter per device

[1]National Research Council Canada, Ottawa, ON K1A 0R6, Canada. [2]University of Ottawa, Ottawa, ON K1N 6N5, Canada. ✉email: Dan.Dalacu@nrc.ca

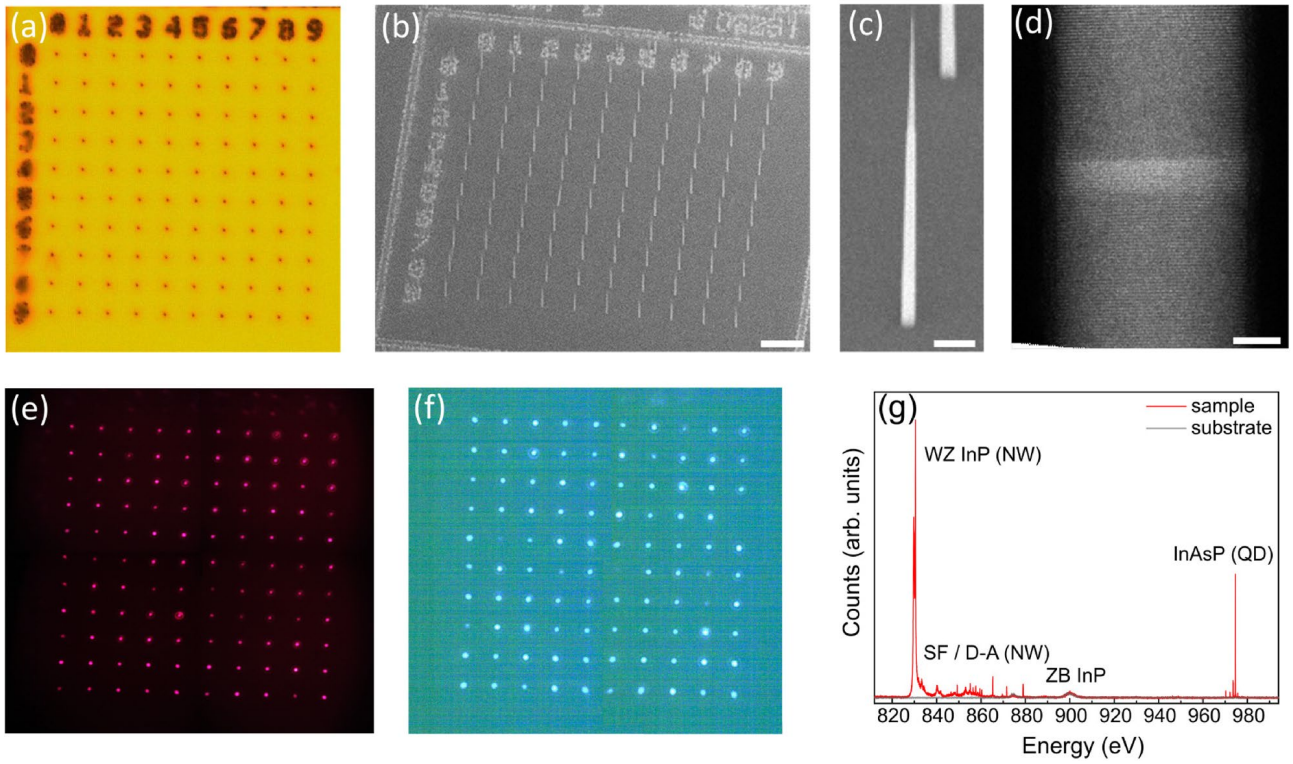

Figure 1. (**a**) Optical image of a 10 × 10 array of InP photonic nanowires. (**b**) Scanning electron microscopy (SEM) image viewed at 40° of the same array with (**c**) showing a higher magnification image of a single nanowire. Scale bars are 10 and 1 μm, respectively. (**d**) Transmission electron microscopy image of the InAsP quantum dot embedded within a nanowire. Scale bar is 5 nm. Spatially-resolved photoluminescence (PL) from the array in (**a**) showing emission from (**e**) the InP photonic nanowire waveguide and (**f**) the embedded quantum dot. (**g**) Spectrally-resolved emission from a single device (red curve) showing InP nanowire (NW) and InAsP quantum dot (QD) emission. The NW shows band-to-band emission from wurtzite (WZ) InP as well as emission from stacking faults (SFs) and donor–acceptor (D–A) levels. Emission from the substrate (grey curve) shows two broad features at 875 nm and 900 nm associated with band-to-band and D-A recombination, respectively, in zincblende (ZB) InP.

and to the absence of the 2D wetting layer (WL) that is present in self-assembled dots. The former eliminates the detrimental effects of nearby dots (i.e. spectral pollution) which is a persistent issue when employing randomly nucleated dots. The latter eliminates the detrimental effects associated with hybridization of dot and WL states[37] (i.e. enhanced exciton-phonon scattering[38]).

Results

Yield. The quantum dots studied here are InAsP segments incorporated within site-controlled, bottom-up wurtzite InP nanowires grown using selective-area vapour-liquid-solid epitaxy using gold catalysts[31]. To efficiently collect the emission, the quantum dots are incorporated in photonic nanowire waveguides, see "Methods". Optical and scanning electron microscopy (SEM) images of a 10 × 10 array of nanowires pitched at 7.5 μm are shown in Fig. 1a,b, respectively. Each gold catalyst nucleates a well-formed photonic nanowire (Fig. 1c) with a uniform geometry consisting of a 250 nm diameter base tapered to a 20 nm tip (size of catalyst) over a length of 10 μm. Within each nanowire is a single InAsP quantum dot having a well-defined geometry, shown in the transmission electron image of Fig. 1d.

Photoluminescence (PL) measurements were performed with the sample held at 4 K in a closed-cycle He cryostat. Images of spatially-resolved emission from the array are shown in Figs. 1e,f. The array is illuminated by a white light source and the PL is imaged onto a CMOS camera. In (e), a $\lambda = 800$ nm long-wave-pass (LWP) filter is used to filter the white light, and the observed image corresponds to emission predominantly from the InP nanowire (see spectrum in Fig. 1g, discussed below). All the nanowires in the array show bright emission with approximately the same intensity. In (f), a LWP filter with a bandedge at $\lambda = 950$ nm is used to filter out both the white light and the InP emission. The image thus corresponds to quantum dot emission. The majority of devices are sufficiently bright to be observed on a simple CMOS camera.

Figure 1g shows the spectrally-resolved PL from one of the nanowires in the array. In this case, excitation is from a $\lambda = 780$ nm laser focused onto a single nanowire and the PL is dispersed using a grating spectrometer and detected with a CCD (see "Methods"). The PL is recorded over a wavelength range that includes both the InP nanowire-related emission and InAsP quantum dot emission. The InP emission includes band-to-band recombination at $\lambda \sim 832$ nm as well as longer wavelength emission associated with stacking faults[39,40] (i.e. zincblende

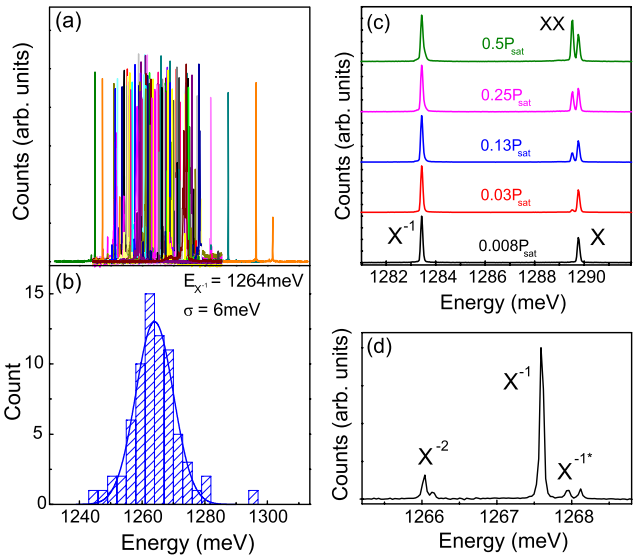

Figure 2. (**a**) Photoluminescence spectra of the 100 nanowires in the array under weak pumping conditions. (**b**) Histogram of the X^- emission energies extracted from the spectra in (**a**). (**c**) Power-dependence of the emission from a typical dot in a nanowire. (**d**) Example of a dot which shows emission from additional charge complexes.

sections in the predominantly wurtzite crystal structure) and donor-acceptor levels[33]. The InAsP dot emission is observed at $\lambda \sim 975$ nm, spectrally isolated from the InP emission by ~ 100 nm, allowing for the facile spectral selection employed in Fig. 1e,f.

The PL spectra from all 100 nanowires in the array are plotted in Fig. 2a. Excitation was above-band with a $\lambda = 780$ nm continuous wave (CW) laser using an excitation power, P, equal to $\sim 1\%$ of that required to saturate the ground state dot levels, P_{sat}. The spectrum of each of the 100 dots consists of a few narrow lines and of these 72% show just two dominant peaks, as in the bottom spectrum of Fig. 2c. We identify these two peaks using excitation power-dependence, cross-correlation spectroscopy[41] and polarization-resolved PL[32]. The high energy peak is associated with emission from the neutral exciton, X, whilst the low energy peak with the negative trion (singly charged exciton with both electrons in the s-shell), X^{-1}. The relative probability of emitting a neutral or charged exciton photon, given by the relative peak intensities, is dot-specific and can vary from strongly dominant charged exciton emission to strongly dominant neutral exciton emission, see Ref.[42]. As the excitation power is increased, a third peak typically appears spectrally located between X^{-1} and X which we associate with emission from the biexciton, XX. For these 72 nanowires we find most dots have an average charge state corresponding to X^{-1} (i.e. X^{-1} peak is typically brighter than the X peak). Focusing on X^{-1}, we show in Fig. 2b the distribution of peak energies extracted from the PL spectra, obtaining a mean energy $E_{X^{-1}} = 1264$ meV with a standard deviation $\sigma = 6$ meV. In addition to the 2 dominant lines, approximately 50% of the 72 devices also show weaker peaks around X^{-1}, see Fig. 2d. We associate these peaks with recombination from complexes which feature an electron in the p-shell. The peak redshifted with respect X^{-1} is associated with a doubly charged negative trion, X^{-2}, whilst the 2 blueshifted peaks correspond to the 2 (doubly generate) bright triplet states of the excited trion[43], X^{-1*}. The remaining 28 devices show additional bright peaks suggesting the presence of additional charge states.

Count rates. From the 72 devices that showed simple two peak spectra, we selected 14 for further measurements. For these devices, the emission from single excitonic complexes were selected using a tunable 0.1 nm bandwidth filter and detected with an avalanche photodiode (APD) (see "Methods"). We chose nanowires for which (1) the dominant charge state corresponded to the charged exciton, as in Fig. 2c, and (2) the emission energy of the X^- photon was within the range of our tunable filter (950 ± 30 nm). The power-dependent count rates obtained from all 14 devices using CW excitation at $\lambda = 780$ nm are shown in Fig. 3a. We observe a significant variation in count rates at saturation from device to device, ranging from 0.4 to 1.2 Mcps.

For an idealized 2-level system, CW excitation generates the highest count rates achievable, limited by the lifetime of the excited state, here the radiative lifetime of the X^- complex, τ_{X^-}. To assess the role of lifetime in determining the CW count rate, we measured the PL decay curves of the 14 devices, shown in Fig. 3b. All the dots display a two-component decay process which we fit with a bi-exponential of the form $\sim a\exp(-t/\tau_{X^-}) + b\exp(-t/\tau_{X^{-*}})$ to extract the fast component τ_{X^-} (the slow component $\tau_{X^{-*}}$ is discussed later in the article). The distribution of extracted radiative lifetimes is shown in the inset of the figure from which we determine an average $\tau_{X^-} \sim 1.5 \pm 0.5$ ns. Comparison of the lifetime-limited emission rates $\Gamma \sim 1/\tau_{X^-}$ and the CW count rates at P_{sat} did not reveal any clear correlation, suggesting that other factors besides the radiative lifetime play a role in determining the ultimate count rate. They are addressed below.

To exclude any count rate variation with radiative lifetime τ_{X^-}, we measure the count rates at saturation using pulsed excitation with a pulse period of 12.5 ns, significantly greater than τ_{X^-}. Detected count rates at saturation

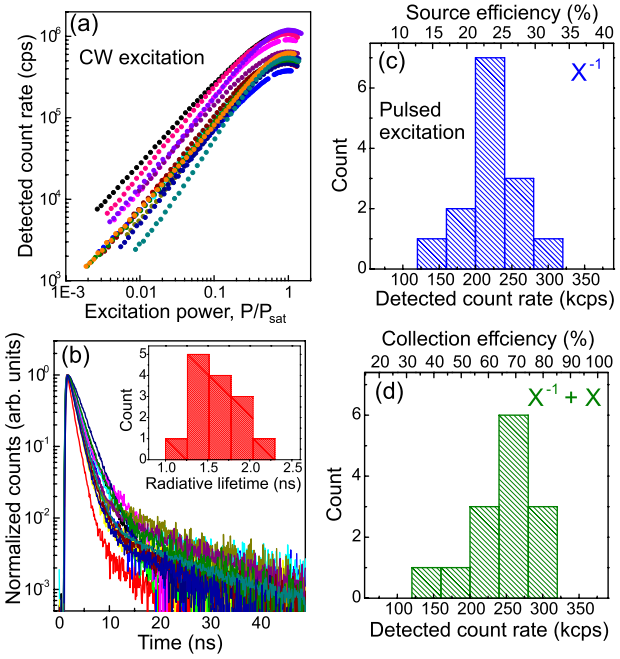

Figure 3. (**a**) Detected count rate of X^- photons as a function of CW excitation power for 14 nanowire devices. (**b**) Radiative decay rates of the charged exciton complexes in (**a**). (**c**) Histogram of detected count rates at P_{sat} of X^{-1} photons using pulsed excitation at 80 MHz. Top axis shows source efficiency (i.e. counts at first lens) (**d**) As above but counting both X^{-1} and X photons. Top axis shows collection efficiency (i.e. counts from unfiltered photons directed up the nanowire).

from the 14 devices are plotted in Fig. 3c and show a narrow distribution around 220 kcps with $\sigma = 39$ kcps. From these measurements we determine the source efficiency η_s (fraction of excitation pulses that produce an X^- photon at the first lens). Using the measured transmission of the optical system ($\eta_t = 7.8\%$) and the detector efficiency ($\eta_d = 15\%$) at $\lambda = 980$ nm, we obtain a mean source efficiency of 23% with a peak value of 30%. The distribution of calculated source efficiencies are displayed along the top axis of Fig. 3c.

Using these measurements, we also determine the collection efficiency of the devices (fraction of photons emitted from the top of the nanowire that are collected). We assume only 50% of the emitted photons are directed towards the tip of the nanowire. Of these, only 80% reach the detector, assuming 20% of the photons are emitted from phonon sidebands[44] and are filtered out by the 0.1 nm bandpass filter. To obtain an accurate measure of the collection efficiency, all mutually exclusive excitonic complexes that produce photons should be included. Here, we include counts from the two dominant peaks, X and X^-, seen in Fig. 3d. Compared to Fig. 3c, the distribution is shifted to higher rates and the mean count rate increases to 247 kcps. Using $\eta_t = 7.8\%$ and $\eta_d = 15\%$ as above, we obtain a mean collection efficiency of 66% and a peak value of 83% (see the top axis of Fig. 3d).

The peak collection value is lower than expected based on the device design, for which a coupling of the dot emission to the waveguide mode $\beta = 95\%$ is predicted[34]. As we do not observe any obvious structural difference between the nanowires from inspection of SEM images and the growth process inherently has the quantum dot positioned on-axis for optimal coupling, we would expect a uniformly high collection efficiency that approaches $\beta = 95\%$. One possible explanation for the observed discrepancy is the omission of counts from other excitonic complexes, for example, photons associated with X^{-2} and X^{-1*} recombination seen in Fig. 2d.

We also note that collection efficiencies are likely underestimated due to the incoherent excitation employed which can excite dark spin configurations within the dot. For example, the neutral exciton created using above band excitation would be in a dark configuration (i.e. parallel electron and hole spins) 50% of the time. Similarly, one of the 4 doubly degenerate excited trions states is also dark. These configurations require a spin-flip process to unblock the emission[45,46]. Spin-flip rates that are slower than the excitation rate would impact the measured count rate. For the case of the spin-polarized excited trion, a spin-flip and subsequent decay of the p-shell electron produces X^{-1}. As such, the spin-flip rate is given by the slow component, $\tau_{x^{-1*}}$, observed in the decay of X^{-1} (see Fig. 3b). Median $\tau_{x^{-1*}}$ values extracted from fits to the decay curves were $\sim$ 30 ns, i.e. longer than the pulse rate of 12.5 ns, and varied significantly, from 8 to 120 ns. These values are comparable to spin-flip rates measured on the neutral exciton in InAs/GaAs self-assembled quantum dots where values of 68 to 215 ns were reported[45].

Although devices operating with efficiencies approaching the theoretical maximum can be obtained using above-band excitation, it is clear that the yield of these devices will be limited by the excitation of more than one possible charge and spin configuration. The average charge state can be manipulated to a certain extent using quasi-resonant excitation[3] or with additional weak laser excitation at specific above-band energies[43]. Alternatively, some degree of control may be possible by manipulating the band-bending at the nanowire surface due to Fermi-level pinning[47] e.g. by tailoring the surface passivation. Improved charge-state control (e.g. via application

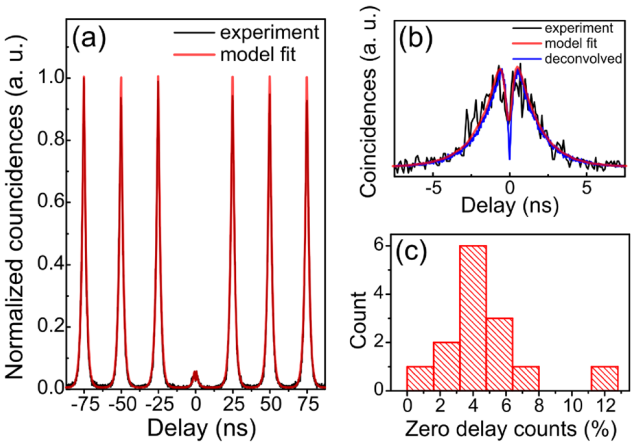

Figure 4. (**a**) Autocorrelation coincidence counts for a device showing re-excitation effects when pumped at saturation. (**b**) Expanded view of (**a**) showing the zero delay peak and $\tau = 0$ dip. (**c**) Histogram of the coincidence counts in the zero-delay peak normalized to the counts in the side peaks for the devices pumped at $P = P_{sat}$.

of an electric field[48]) would necessitate modifications to the device design that would allow for the addition of metallic gates.

It appears, however, that consistent (dot-independent) efficiencies may also require coherent pumping of a specific complex using strictly resonant excitation[49]. Whether resonant excitation in a charge tunable device will ultimately produce the highest efficiency sources is still unclear and depends on the development of techniques[50–53] that address the 50% loss incurred when using conventional polarization-based rejection of the resonant pump laser[54].

Single photon purity. We look next at the single photon purity of the emitted photons from the 14 devices when operated at $P = P_{sat}$. The second-order autocorrelation, $g^{(2)}(\tau)$, is measured in a standard Hanbury Brown and Twiss experiment with above-band, pulsed excitation at 40 MHz, see "Methods". A spectrum of the measured coincidences for a device which shows re-excitation (discussed below) is shown in Fig. 4a. At $\tau = 0$ all the devices show $g^{(2)}(\tau = 0) \sim 0$ after deconvolution of the spectrum with the 200 ps jitter in the detector response (see Fig. 4b). The absence of coincidence counts at zero delay for all sources, which is observed at $P = P_{sat}$, is expected from the single emitter nature of the devices i.e. the deterministic growth eliminates the possibility of spectral pollution from nearby quantum dots.

For increasing absolute delay times, coincidence counts are observed to increase rapidly before decaying back to zero with a time constant τ_{x-}. This is seen clearly in Fig. 4b which is an expanded view of Fig. 4a around $\tau = 0$. Such coincidence spectra are typical when pumping above-band and are a signature of re-excitation processes in which carriers from the excitation pulse repopulate the quantum dot after emission of the first photon[55,56]. Subsequent recombination of the carriers produces a second photon that has a corresponding probability of producing a detector click. We simulate the statistics of detection events using a stochastic model which includes a carrier re-capture probability, see Ref.[57] for details. The model quantitatively reproduces the measured correlations (red curves in Fig. 4a,b) and we extract a time constant associated with re-excitation (i.e. time constant associated with the dip at $\tau = 0$) of $\sim$ 50 ps.

The coincidence counts associated with re-excitation (i.e counts in the zero-delay peak) normalized with respect to the counts in the side peaks are summarized in the histogram shown in Fig. 4c for the 14 devices. We obtain a distribution of single photon purities centred around 96% with extreme values as high as 99.4% and as low as 88.2%. As expected from a pump power-dependent re-excitation process, the relative coincidence count rates in the zero delay peak decrease (i.e. purities approach 100%) as the excitation power is decreased from $P = P_{sat}$ (not shown, see Ref.[57]).

Spectral purity. Finally, we measure the spectral purity of the emitted photons from the nanowire devices. The linewidths of the X^{-1} emission peaks were measured using a scanning Fabry-Perot etalon (BW = 1.3 GHz), see "Methods". 13 of the measured lines revealed a Lorentzian profile (black curve in Fig. 5a) having linewidths ranging from 1.68 to 3.28 GHz. Only one device displayed an inhomogeneously broadened line profile i.e. the emission line was better described by a Voigt profile with a Gaussian component contributing 50% to the linewidth.

The absence of inhomogeneous broadening, suggested by the prevalence of Lorentzian lineshapes, demonstrates the high quality of the epitaxial material of the devices. The density of traps in close proximity to the dot, which are typically associated with a fluctuating charge environment responsible for spectral wandering of the emission line[3], appears to be insignificant. We attribute the absence of spectral fluctuation-mediated inhomogeneous broadening to an increase in the growth temperature used during deposition of the InP shell compared to previous experiments[32].

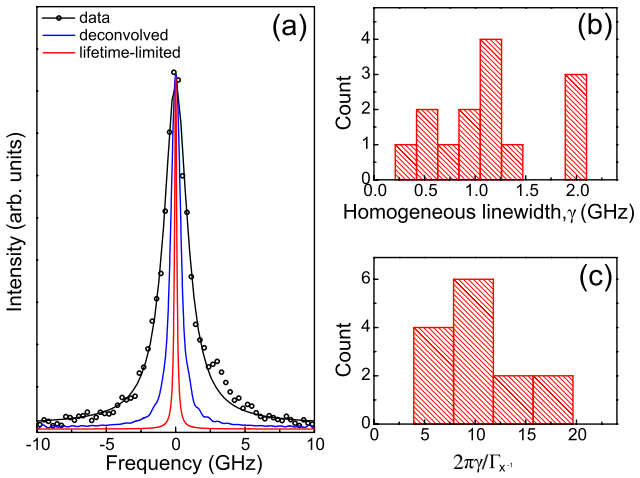

Figure 5. (**a**) Measured linewidth of X^- (symbols) and a Lorentzian fit (black curve). Deconvolved linewidth is $\gamma = 0.77$ GHz (blue curve) which is 8× life-time limit of 0.094 GHz calculated from measured lifetime (1.7 ns). (**b**) Deconvolved linewidths and (**c**) excess broadening beyond the transform limit extracted from the 14 devices.

The observation of Lorentzian lineshapes allows for direct access to homogeneous linewidths, γ, from which coherence times $T_2 = 1/\pi\gamma$ can be calculated. To extract the homogeneous linewidths, the measured spectra were deconvolved from the etalon response (blue curve in Fig. 5a) and are plotted in Fig. 5b. The majority of the devices show γ-values uniformly distributed from 0.4 to 1.5 GHz with a few lines showing a broader γ around 2 GHz. In the ideal case, where the coherence is governed by population relaxation dynamics and assumed to be purely radiative, one obtains a maximum coherence time $T_2 = 2T_1$ (here $T_1 = \tau_{X^-}$). Generally, T_2 times are limited by pure dephasing mechanisms (e.g. elastic exciton-exciton and exciton-phonon scattering[58]) which results in linewidths broadened in comparison to lifetime transform-limited values $1/2\pi\,\tau_{X^-} = \Gamma_{X^-}/2\pi$ (red curve in Fig. 5a).

To evaluate the broadening in excess of the transform limit, we plot in Fig. 5c the linewidths of the 14 devices in units of $2\pi\gamma/\Gamma_{X^-}$ using the measured lifetimes τ_{X^-} from Fig. 3b. The devices show a wide range of values, from 4× to 20× greater than the transform limit. Although it is not clear why we observe such a large variation, the fact that they are not transform-limited is not surprising. It has been established[35] that the attainment of transform-limited single photons from quantum dots not only requires high quality material, but also the use of resonant excitation. With above-band excitation, as is the case here, thermalization of generated carriers to the InP bandedge followed by subsequent capture to the quantum dot levels is expected to generate a high density of phonons. Broadening due to pure dephasing via elastic carrier-phonon interactions is therefore inevitable.

Discussion

In summary, we have reported on the performance of nanowire-based single photon sources fabricated using a platform that provides unity device yield. The broadband single emitter device allows for the facile characterization of source performance metrics using above-band excitation. From a sampling of 14 devices, we obtained a peak source efficiency of 30%, a peak collection efficiency of 83%, a minimum multiphoton emission probability of 0.6% measured at saturation and a minimum linewidth of 400 MHz (maximum coherence time of 2.5 ns) corresponding to 4× the transform limit.

From the reliable statistical analysis afforded by the unity yield we quantify the distribution away from optimum efficiencies. The role of emission from more than one possible charge complex is identified as a limiting factor preventing universal peak efficiencies. Achieving uniformly high efficiencies thus entails charge state control using approaches compatible with the nanowire geometry, either on the growth substrate or integrated on-chip[59], see, for example, Refs.[60,61], respectively.

Non-zero multiphoton emission probabilities were associated with a re-excitation process whereas non-transform limited linewidths with phonon-mediated pure dephasing. Both can be traced to the above-band excitation employed. Routes to mitigating these effects are already established and requires coherent pumping of a target charge state. Additionally, the observation of homogeneous linewidths broadened due to phonon-mediated pure dephasing from the high energy excitation suggests that below-gap pumping should provide significant improvements in the coherence of the emitted photons. In conclusion, we have established nanowire quantum dots as a viable route towards efficiently generating high quality single photons using a process that achieves unity yield. Such devices are a valuable resource for quantum technologies requiring multiple sources. They are particularly relevant in hybrid on-chip platforms utilizing pick and place techniques.

Methods

Fabrication and growth. The quantum dots were incorporated in site-controlled, bottom-up nanowires grown by selective-area vapour–liquid–solid epitaxy[31] in the wurtzite InAs/InP material system. The growth was carried out using chemical beam epitaxy on patterned InP substrates with single gold catalysts centered in circular openings in an SiO_2 mask (see Ref.[62] for details). The first of a two-step growth process produces a nanowire core into which was incorporated a single $InAs_x P_{1-x}$ dot (Fig. 1d) with a thickness of $\sim$ 5 nm, a diameter of $\sim$ 20 nm and a composition of x $\sim$ 25%. In the second growth step, the nanowire core was clad with a $\sim$ 125 nm InP shell[33] which defines the photonic nanowire waveguide[7] into which the dot emits. For the shell growth, the temperature was increased by 20°C to 450°C and the III/V ratio was adjusted to produce the tapered geometry[63] observed in Fig. 1c in order to obtain a an emission profile suitable for efficient collection[64,65].

Optical characterization. Photoluminescence (PL) measurements were made in a closed-cycle helium cryostat at 4 K. The nanowire quantum dots were excited through a 100× objective (numerical aperture = 0.81) using either CW ($\lambda = 780$ nm) or pulsed ($\lambda = 670$ nm, pulse width = 100 ps) excitation. Emission was collected through the same microscope objective and, for low-resolution (60 μeV) spectrally-resolved measurements, was directed to a 0.5 m grating spectrometer equipped with a liquid nitrogen-cooled CCD array detector. For source efficiency, high-resolution and time-resolved measurements, the emission was fibre-coupled and single photon avalanche photodiodes (APDs, timing jitter $\sim$ 200 ps) were used for detection. A fibre-based tunable filter (bandwidth 0.1 nm) was used to isolate specific quantum dot emission lines. For second-order correlation measurements, the filtered line was directed to two APDs via a 50:50 splitter in a typical Hanbury Brown and Twiss (HBT) experiment. The high-resolution measurements were performed by scanning a tunable fibre-based Fabry–Perot etalon (bandwidth 1.3 GHz) through the selected line.

Data availability

The data that support the findings of this study are available from the corresponding author upon request.

Received: 8 November 2021; Accepted: 23 March 2022
Published online: 16 April 2022

References

1. Gérard, J-M. & Gayral, B. Strong purcell effect for INAS quantum boxes in three-dimensional solid-state microcavities. *J. Lightwave Technol.* **17**, 2089 (1999).
2. Michler, P. *et al.* A quantum dot single-photon turnstile device. *Science* **290**, 2282–2285 (2000).
3. Santori, C., Fattal, D., Vučković, J., Solomon, G. & Yamamoto, Y. Indistinguishable photons from a single-photon device. *Nature* **419**, 594–597 (2002).
4. Benson, O., Santori, C., Pelton, M. & Yamamoto, Y. Regulated and entangled photons from a single quantum dot. *Phys. Rev. Lett.* **84**, 2513–2516 (2000).
5. Stevenson, R. M. *et al.* A semiconductor source of triggered entangled photon pairs. *Nature* **439**, 197–182 (2006).
6. Jayakumar, H. *et al.* Time-bin entangled photons from a quantum dot. *Nat. Commun.* **5**, 4251 (2014).
7. Claudon, J. *et al.* A highly efficient single-photon source based on a quantum dot in a photonic nanowire. *Nat. Photon.* **4**, 174 (2010).
8. Somaschi, N. *et al.* Near-optimal single-photon sources in the solid state. *Nat. Photon.* **10**, 340–345 (2016).
9. Unsleber, S. *et al.* Highly indistinguishable on-demand resonance fluorescence photons from a deterministic quantum dot micropillar device with 74% extraction efficiency. *Opt. Exp.* **24**, 8539–8546 (2016).
10. Loredo, J. C. *et al.* Scalable performance in solid-state single-photon sources. *Optica* **3**, 443 (2016).
11. Wang, H. *et al.* Near-transform-limited single photons from an efficient solid-state quantum emitter. *Phys. Rev. Lett.* **116**, 213601 (2016).
12. Ding, Xing *et al.* On-demand single photons with high extraction efficiency and near-unity indistinguishability from a resonantly driven quantum dot in a micropillar. *Phys. Rev. Lett.* **116**, 020401 (2016).
13. Chithrani, D., Williams, R. L., Lefebvre, J., Poole, P. J. & Aers, G. C. Optical spectroscopy of single, site-selected, INAS/INP self-assembled quantum dots. *Appl. Phys. Lett.* **84**, 978 (2004).
14. Baier, M. H. *et al.* Single photon emission from site-controlled pyramidal quantum dots. *Appl. Phys. Lett.* **84**, 648–650 (2004).
15. Schneider, C. *et al.* Lithographic alignment to site-controlled quantum dots for device integration. *Appl. Phys. Lett.* **92**, 183101 (2008).
16. Strittmatter, A. *et al.* Site-controlled quantum dot growth on buried oxide stressor layers. *Phys. Status Solidi.* **209**, 2411–2420 (2012).
17. Jöns, K. D. *et al.* Triggered indistinguishable single photons with narrow line widths from site-controlled quantum dots. *Nano Lett.* **13**, 126–130 (2012).
18. Unsleber, S. *et al.* Observation of resonance fluorescence and the mollow triplet from a coherently driven site-controlled quantum dot. *Optica* **2**, 1072–1077 (2015).
19. Strauß, M. *et al.* Resonance fluorescence of a site-controlled quantum dot realized by the buried-stressor growth technique. *Appl. Phys. Lett.* **110**, 111101 (2017).
20. Gallo, P. *et al.* Integration of site-controlled pyramidal quantum dots and photonic crystal membrane cavities. *Appl. Phys. Lett.* **92**, 263101 263101 (2008).
21. Schneider, C. *et al.* Single photon emission from a site-controlled quantum dot-micropillar cavity system. *Appl. Phys. Lett.* **94**, 111111 (2009).
22. Dalacu, D. *et al.* Deterministic emitter-cavity coupling using a single-site controlled quantum dot. *Phys. Rev. B* **82**, 033381 (2010).
23. Knill, E., Laflamme, R. & Milburn, G. A scheme for efficient linear optics quantum computation. *Nature* **409**, 46–52 (2001).
24. Aspuru-Guzik, A. & Walther, P. Photonic quantum simulators. *Nat. Phys.* **8**, 285 (2012).
25. Sparrow, Chris *et al.* Simulating the vibrational quantum dynamics of molecules using photonics. *Nature* **557**, 660 (2018).
26. Loredo, J. C. *et al.* Boson sampling with single-photon fock states from a bright solid-state source. *Phys. Rev. Lett.* **118**, 130503 (2017).
27. Hui Wang, Yu. *et al.* High-efficiency multiphoton boson sampling. *Nat. Photon.* **11**, 361–365 (2017).
28. Wang, Hui *et al.* Boson sampling with 20 input photons and a 60-mode interferometer in a 10^{14}-dimensional hilbert space. *Phys. Rev. Lett.* **123**, 250503 (2019a).

29. Borgström, M., Zwiller, V., Müller, E. & Imamoglu, A. Optically bright quantum dots in single nanowires. *Nano Lett.* **5**, 1439–1443 (2005).
30. Björk, M. T. *et al.* One-dimensional steeplechase for electrons realized. *Nano Lett.* **2**, 87–89 (2002).
31. Dalacu, D. *et al.* Selective-area vapor–liquid–solid growth of tunable INASP quantum dots in nanowires. *Appl. Phys. Lett.* **98**, 251101 (2011).
32. Reimer, M. E. *et al.* Overcoming power broadening of the quantum dot emission in a pure wurtzite nanowire. *Phys. Rev. B* **93**, 195316 (2016).
33. Dalacu, D. *et al.* Ultraclean emission from INASP quantum dots in defect-free wurtzite INP nanowires. *Nano Lett.* **12**, 5919–5923 (2012).
34. Dalacu, Dan, Poole, Philip J. & Williams, Robin L. Nanowire-based sources of non-classical light. *Nanotechnology* **30**, 232001 (2019).
35. Kuhlmann, Andreas V. *et al.* Transform-limited single photons from a single quantum dot. *Nat. Commun.* **6**, 8204 (2015).
36. Zhai, Liang *et al.* Low-noise gaas quantum dots for quantum photonics. *Nat. Commun.* **11**, 4745 (2020).
37. Löbl, Matthias C. *et al.* Excitons in ingaas quantum dots without electron wetting layer states. *Commun. Phys.* **2**, 93 (2018).
38. Urbaszek, B. *et al.* Temperature-dependent linewidth of charged excitons in semiconductor quantum dots: Strongly broadened ground state transitions due to acoustic phonon scattering. *Phys. Rev. B* **69**, 035304 (2004).
39. Akopian, N., Patriarche, G., Liu, L., Harmand, J.-C. & Zwiller, V. Crystal phase quantum transients dots. *Nano Lett.* **10**, 1198–1201 (2010).
40. Bavinck, M. B. *et al.* Controlling a nanowire quantum dot band gap using a straining dielectric envelope. *Nano Lett.* **12**, 6206–6211 (2012).
41. Laferriére, P. *et al.* Systematic study of the emission spectra of nanowire quantum dots. *Appl. Phys. Lett.* **118**, 161107 (2021).
42. Dalacu, Dan *et al.* Pump power control of photon statistics in a nanowire quantum dot. *Phys. Rev. B* **102**, 115401 (2020).
43. Benny, Y. *et al.* Excitation spectroscopy of single quantum dots at tunable positive, neutral, and negative charge states. *Phys. Rev. B* **86**, 085306 (2012).
44. Lodahl, P., Mahmoodian, S. & Stobbe, S. Interfacing single photons and single quantum dots with photonic nanostructures. *Rev. Mod. Phys.* **87**, 347 (2015).
45. Johansen, Jeppe, Julsgaard, Brian, Stobbe, Søren., Hvam, Jørn. M. & Lodahl, Peter. Probing long-lived dark excitons in self-assembled quantum dots. *Phys. Rev. B* **81**, 081304(R) (2010).
46. Benny, Y. *et al.* Electron-hole spin flip-flop in semiconductor quantum dots. *Phys. Rev. B* **89**, 035316 (2014).
47. van Weert, M. H. M. *et al.* Large redshift in photoluminescence of p-doped INP nanowires induced by fermi-level pinning. *Appl. Phys. Lett.* **88**, 043109 (2009).
48. Baier, M., Findeis, F., Zrenner, A., Bichler, M. & Abstreiter, G. Optical spectroscopy of charged excitons in single quantum dot photodiodes. *Phys. Rev. B* **64**, 195326–1 (2001).
49. Yu-Ming He, Yu. *et al.* On-demand semiconductor single-photon source with near-unity indistinguishability. *Nat. Nano.* **8**, 213–217 (2013).
50. Ates, S. *et al.* Post-selected indistinguishable photons from the resonance fluorescence of a single quantum dot in a microcavity. *Phys. Rev. Lett.* **103**, 167402 (2009).
51. Muller, A. *et al.* Resonance fluorescence from a coherently driven semiconductor quantum dot in a cavity. *Phys. Rev. Lett.* **99**, 187402 (2007).
52. Wang, H. *et al.* Towards optimal single-photon sources from polarized microcavities. *Nat. Photon.* **13**, 770 (2019).
53. Tomm, Natasha *et al.* A bright and fast source of coherent single photons. *Nat. Nanotechnol.* **16**, 399–403 (2021).
54. Kuhlmann, A. V. *et al.* A dark-field microscope for background-free detection of resonance fluorescence from single semiconductor quantum dots operating in a set-and-forget mode. *Rev. Sci. Inst.* **84**, 073905 (2013).
55. Aichele, T., Zwiller, V. & Benson, O. Visible single-photon generation from semiconductor quantum dots. *New J. Phys.* **6**, 90 (2004).
56. Santori, C., Fattal, D., Vuckovic, J., Solomon, G. S. & Yamamoto, Y. Single-photon generation with InAs quantum dots. *New J. Phys.* **6**, 89 (2004).
57. Laferriere, Patrick *et al.* Multiplexed single-photon source based on multiple quantum dots embedded within a single nanowire. *Nano Lett.* **20**, 3688–3693 (2020).
58. Scully, M. O. & Zubairy, M. S. *Quantum Optics* (Cambridge University Press, 1997).
59. Mnaymneh, K *et al.* On-chip integration of single photon sources via evanescent coupling of tapered nanowires to SiN waveguide. *Adv. Quantum Technol.* **3**, 1900021 (2020).
60. Zeeshan, M., Sherlekar, N., Ahmadi, A., Williams, R. L. & Reime, M. E. Proposed scheme to generate bright entangled photon pairs by application of a quadrupole field to a single quantum dot. *Phys. Rev. Lett.* **122**, 227401 (2019).
61. Reimer, Michael E. *et al.* Electric field induced removal of the biexciton binding energy in a single quantum dot. *Nano Lett.* **11**, 645–650 (2011).
62. Dalacu, D. *et al.* Selective-area vapour–liquid–solid growth of InP nanowires. *Nanotechnology.* **20**, 395602 (2009).
63. Dalacu, D., Poole, P. J. & Williams, R. L. Tailoring the geometry of bottom-up nanowires: Application to high efficiency single photon sources. *Nano Mater.* **11**, 1201 (2021).
64. Gregersen, N., Nielsen, T. R., Claudon, J., Gérard, J.-M. & Mørk, J. Controlling the emission profile of a nanowire with a conical taper. *Opt. Lett.* **33**, 1693–1695 (2008).
65. Bulgarini, G. *et al.* Nanowire waveguides launching single photons in a gaussian mode for ideal fiber coupling. *Nano Lett.* **7**, 4102–4106 (2014).

Acknowledgements

This work was supported by the Canadian Space Agency through a collaborative project on Development of Quantum Dot Based QKD-relevant Light Sources and by the Natural Sciences and Engineering Research Council of Canada (Grant no. RGPIN-2018-05438) through a Strategic Partnership Grant Quantum-secured Communications for Canada.

Author contributions

All authors contributed equally to the article.

Competing interests

The authors declare no competing interests.

Additional information

Correspondence and requests for materials should be addressed to D.D.

Chapter 7

Article 3: Correlation spectroscopy of nanowire quantum dots

This chapter contains the following article:

P. Laferrière, E. Yeung, M. Korkusinski, P. J. Poole, R. L. Williams, & D. Dalacu, "Correlation spectroscopy of nanowire quantum dots", in preperation (2022).

Targeted journal: Physical Review B

This article presents a preliminary interpretation of the extensive correlation measurements performed.

Correlation spectroscopy of nanowire quantum dots

Patrick Laferrière,[1,2,a)] Edith Yeung,[1,2] Marek Korkusinski,[1,2] Philip J. Poole,[2] Robin L. Williams,[2] and Dan Dalacu[1,2]

[1)] *Department of physics, University of Ottawa, Ottawa, Ontario, Canada, K1N 6N5.*

[2)] *National Research Council Canada, Ottawa, Ontario, Canada, K1A 0R6.*

Correlation spectroscopy of quantum dots under continuous wave excitation has been instrumental in establishing the single photon nature of the emission in these systems. It can also provide insight into the carrier dynamics for cases where there exists multiple possible excitonic configurations. We perform extensive correlation measurements on two quantum dots in a nanowire device which emit from different excitonic complexes. We find drastically different responses in both auto- and cross-correlations depending on the presence or absence of an additional complex. The observed behaviour is described in terms of carrier-dependent capture rates and single carrier versus pair capture probabilities using simulations from a multi-level stochastic model.

I. INTRODUCTION

Semiconductor quantum dots have become a promising candidate as an ideal source for quantum information applications[1]. Different excitonic complexes in these sources have been shown to emit on-demand (i.e. non-probabilistic) single photons with negligible multi-photon probability[2,3] and high spectral purity in devices with high extraction efficiencies[4,5]. They have also been shown to emit on-demand entangled photon pairs through multi-exciton cascades[6–9]. The solid-state environment in which the quantum dots are embedded require the fabrication of photonic structures (e.g. microlenses[10], micropillars[11], circular Bragg gratings[12], and nanowires[13,14]) to improve collection efficiencies. These structures are typically fabricated using dry-etching techniques which lead to high surface defect densities. Time-dependent occupation of these surface traps results in a fluctuating charge environment[15] and leads to undesired effects such as spectral diffusion and memory effects i.e. blinking[16].

The identification of the multiexciton complexes in quantum dots is an important step in order to control and manipulate their states. Different methods are available to achieve this e.g. power-dependent photoluminescence measurements or measurements of anisotropic exchange splittings of the exciton state[17,18]. Other methods include autocorrelation and cross-correlation measurements[19,20] where more information about the excitonic complexes can be extracted. In general, second-order correlation measurements have become the standard tool to measure the single-photon purity of a source with the second-order correlation function, $g^{(2)}(\tau)$, being one of the most important characteristic functions for a light source, allowing one to distinguish between classical and non-classical (i.e. single-photon) emitters.

In this work, we investigate second-order correlations between complexes in InAsP quantum dots embedded within InP nanowire photonic waveguides. We use excitation power-dependent second-order correlation spectroscopy to identify different excitonic complexes of the quantum dot. To understand the observed correlations, we develop a multi-level stochastic model which includes the dynamics of carrier capture in the dot. We find that these dynamics, which play an important role in determining the time-dependent correlations, are strongly dot-dependent. Understanding the general behaviour may pave the way to engineering devices with unwanted mem-

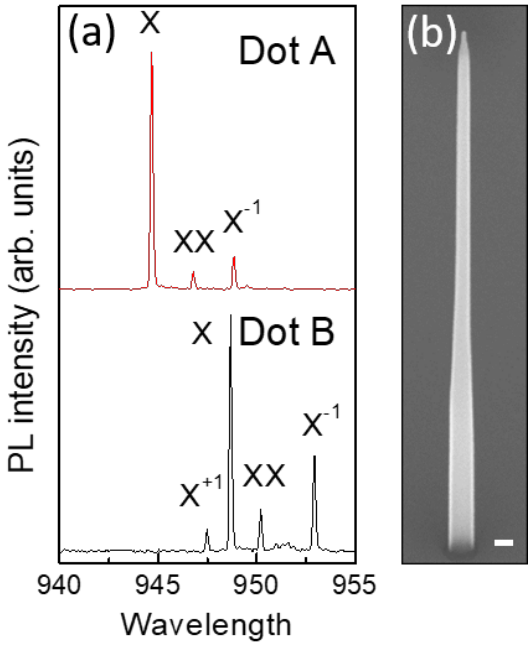

FIG. 1. (a) Spectra of the two quantum dots studied in this work at low excitation power. Dot A exhibits three main emission lines associate with the neutral exciton (X) and biexciton (XX) and the negatively charged exciton (X^{-1}). Dot B shows an additional line associated with a positively charged exciton (X^{+1}). (b) A scanning electron microscopy (SEM) image of a typical quantum dot nanowire device. Scale bar is 200 nm.

[a)] Electronic mail: plaferr3@uottawa.ca

ory effects.

II. SAMPLES

The nanowire quantum dots studied in this work were grown by chemical beam epitaxy with pre-cracked trimethylindium, PH_3 and AsH_3 precursors and using a combination of vapour-liquid-solid (VLS) and selective-area (SA) growth modes (see Ref. 21 for details). InP substrates were patterned with single gold catalysts centered in circular openings of an SiO_2 mask. InP nanowire cores were grown in these openings using the VLS growth mode and InAsP quantum dots were embedded within the cores a distance of $\sim 1\,\mu$m from the base. The gold catalyst diameter $D \sim 20$ nm sets the diameter of the quantum dot whilst the dot thickness $t \sim 5$ nm is set by the growth time. This geometry together with the composition $InAs_{0.25}P_{0.75}$, set using the AsH_3 flow rate, produces dots with emission wavelengths around $\lambda \sim 950$ nm[22].

After completion of the core, growth conditions were adjusted to deposit a shell around the core which increases the base diameter to ~ 250 nm[14] that tapers down to 20 nm over a length of $10\,\mu$m (see Fig. 1(b)). This geometry provides collection efficiencies of $\sim 40\%$[23] for quantum dots emitting at 950 nm[24]. Such devices have demonstrated highly efficient single photon operation and wavelength multiplexing capabilities[23,25,26]. The high device collection efficiency provides high detected count rates required for excitation power-dependent measurements.

This study will focus on two quantum dots, Dot A and Dot B, the photoluminescence (PL) spectra of which are shown in Fig. 1 (a). Dot A emits from three distinct complexes, the neutral exciton (X), the negatively charged exciton (X^{-1}), and the neutral biexciton (XX), whilst Dot B also shows emission from the positively charged exciton (X^{+1}).

III. EXPERIMENT

All optical measurements were made with the samples placed in a closed-cycle helium cryostat at a temperature of 4 K. Above-band continuous wave (cw) excitation was provided by either a HeNe laser operating at 632 nm or a diode laser operating at 780 nm. For time-resolved photoluminescence measurements, a pulsed diode laser was used (wavelength: 670 nm, pulse width: 100 ps, repetition rate: 10 MHz). Individual nanowires were excited from the top by focusing the laser through a 100X objective (numerical aperture of 0.81). The dot emission was collected through the same objective and directed to a grating spectrometer (resolution $\sim 25\mu$eV) equipped with a liquid nitrogen cooled silicon charged coupled device for spectroscopic measurements.

For autocorrelation measurements, the emission was directed to a typical Hanbury-Brown and Twiss (HBT) set-up where individual emission lines were first filtered using a fiber-based tunable filter (bandwidth ~ 0.075 nm) then split using a 50:50 fibre beamsplitter and detected using two fiber-coupled single photon detectors. Two types of single photon detectors were employed for 'start'/'stop' click detection: silicon avalanche photodiodes (APDs) with a timing jitter of ~ 200 ps and superconducting nanowire single photon detectors (SNSPDs) with a jitter time of ~ 60 ps. For cross-correlation measurements, the full spectrum was directed first to the 50:50 beamsplitter and two filters were used, one on each output arm of the splitter, to select individual emission lines. The selected lines were then sent to either the 'start' or 'stop' detector.

IV. RESULTS

A. Autocorrelation

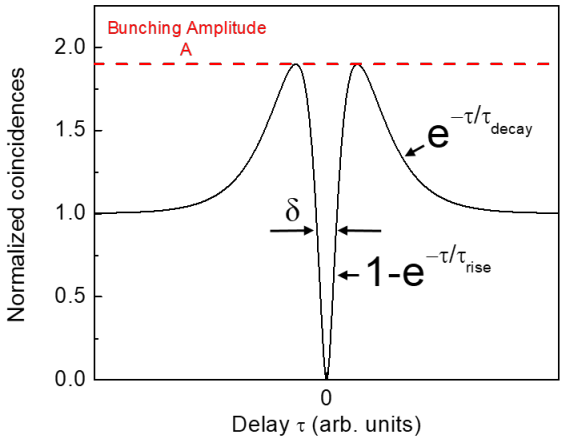

FIG. 2. Simulated correlation spectrum $g^{(2)}(\tau)$ of an arbitrary complex highlighting the relevant temporal characteristics: antibunching dip width δ and rise time τ_{rise}, short delay bunching amplitude A and decay time τ_{decay}.

Second-order autocorrelation measurements will exhibit different behaviour depending on which excitonic complex is being investigated[19]. Fig. 2 shows the simulated autocorrelation of an arbitrary excitonic complex highlighting the relevant temporal features used to quantify the correlation spectra. The zero-delay dip, a consequence of single photon emission, is characterised by a rise time, τ_{rise}, and associated width, δ, which quantify the time required to emit a 'stop' photon after detection of a 'start' photon. For the simple case of only a single observable complex that has as a ground state an empty dot (i.e. the neutral exciton X), this time scale is deter-

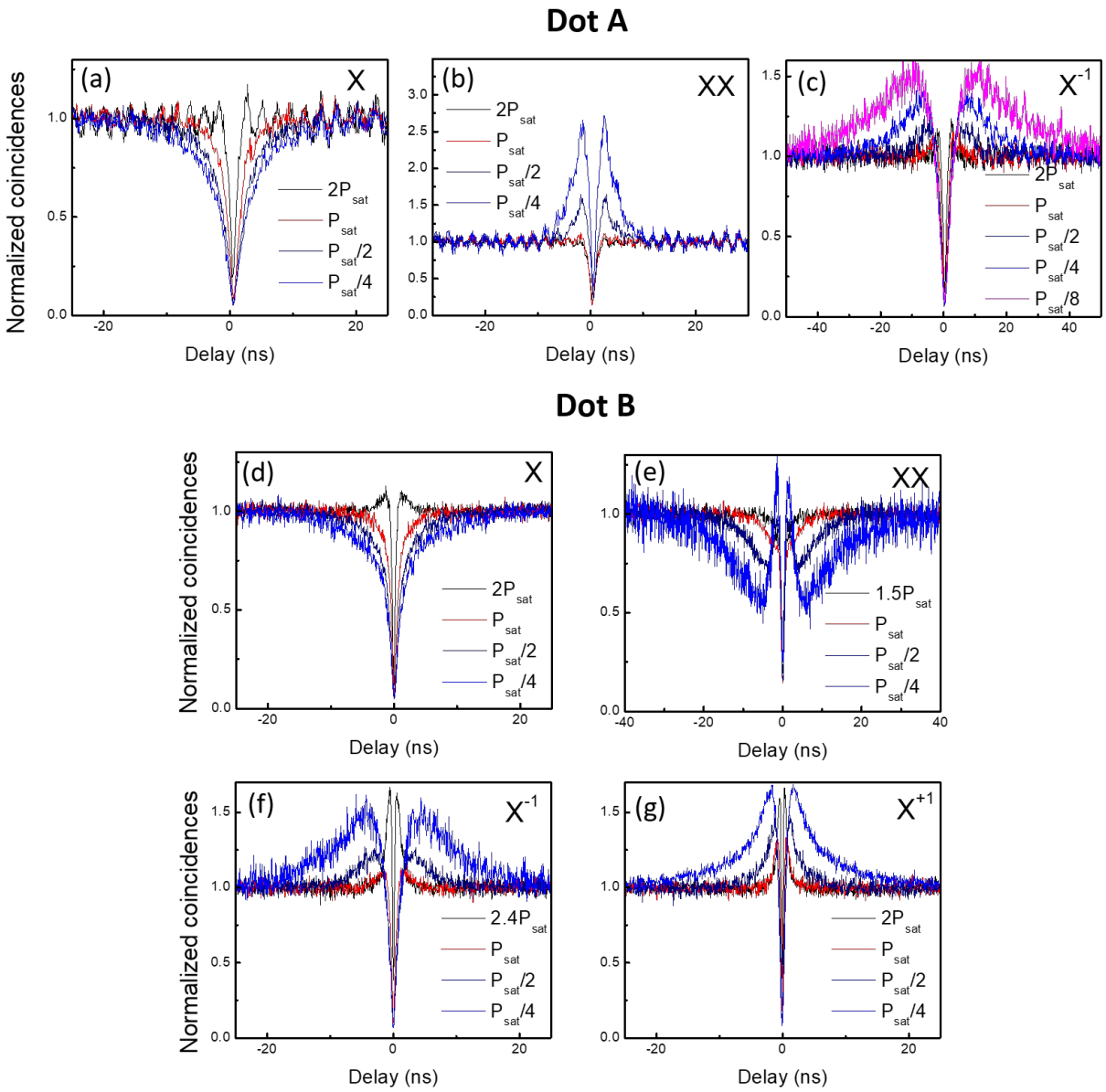

FIG. 3. Autocorrelation spectra of the different exciton complexes at different excitation powers. Dot A: (a) X, (b) XX, (c) X^{-1}. Dot B: (d) X, (e) XX, (f) X^{-1}, (g) X^{+1}.

mined by excitation rate, R_x, and the complex's radiative recombination rate, $\Gamma_x = 1/\tau_x$, where τ_x is the radiative lifetime e.g. $g^{(2)}(\tau) = 1 - e^{-(R_x+\Gamma_x)|\tau|}$.

For cases where the final state of the dot after emission of the 'stop' photon is not empty, i.e. complexes other than X, bunching at short delays will be observed in the limit of low excitation rates. In this limit, the average number of carriers in the dot will tend to zero (i.e. the dot will be typically empty) whereas right after detection of the 'start' photon, the dot will be occupied by one or more carriers depending on the complex being measured. Hence the probability of creating a 'stop' photon (capture of an electron-hole pair and subsequent radiative decay) is higher compared to long delays where the dot is empty. The short delay bunching can be quantified by an amplitude A and associated decay time τ_{decay} which reflects the timescale required to empty the dot. Depending on the complex involved, this bunching can also be interpreted as 'blinking'[16,27,28]. In this case, the charge configuration varies on a time scale τ_{decay} such that the dot switches between different excitonic complexes emitting at different wavelengths (i.e. not counted during the measurement).

We note that in the case of autocorrelations, the spectra are always symmetric about $\tau = 0$. In the following we present autocorrelations measured on the exciton complexes observed in Dot A and B at different excitation powers. The parameters listed above are extracted

from the measured correlations.

We look first at the autocorrelations of the excitonic complexes present in Dot A, a dot which has an emission spectrum representative of that typically observed in our nanowire quantum dots (see, for example, Ref. 19). Fig. 3(a) shows the autocorrelations of the X emission line, $g^{(2)}_{\mathrm{x,x}}(\tau)$, at different excitation powers. The excitation power is expressed as a fraction of the power required to saturate the transition, $\mathrm{P_{sat}}$, and for simplicity we use $\mathrm{P_{sat}}$ corresponding to the X transition throughout the article i.e. even when describing other transitions. The figure shows the behaviour expected of a two-level system described above.

In Fig. 3(b), we plot the XX autocorrelation, $g^{(2)}_{\mathrm{xx,xx}}(\tau)$ measured at different pump powers. Right after the detection of a biexciton photon, the dot is populated with one electron-hole pair which may then decay to the ground state or capture a second pair to form a new biexciton. As the excitation power is decreased it becomes comparatively more likely to form a new biexciton at short delays when the dot already contains one electron-hole pair relative to long delays when the dot will typically be empty and requires the capture of two electron-hole pairs. Hence a power-dependent bunching amplitude A is observed, increasing as the pump power is decreased, which is the typical behaviour expected for biexcitons[29]. Here the rise time τ_{rise} is associated with the time it takes to capture an electron-hole pair after the emission of an XX photon, whilst the decay of the bunching, τ_{decay}, represents the X lifetime.

The last investigated complex in Dot A is $\mathrm{X^{-1}}$ for which the power-dependent autocorrelations, $g^{(2)}_{\mathrm{x^{-1},x^{-1}}}(\tau)$, are shown in Fig. 3(c). The observed bunching at short delays is similar to that observed for XX but here the bunching amplitude at low pump power ($P < P_{\mathrm{sat}}$) is significantly smaller and the bunching decay time, τ_{decay}, is pump power-dependent, increasing with decreasing power. We observe decay times as long as $\tau_{decay} \sim 50\,\mathrm{ns}$ at a power of $P = P_{\mathrm{sat}}/32$ (not shown) which is longer then that expected from a radiative recombination process. This behaviour is associated with blinking, described above. We note that here the width of the anti-bunching dip δ shows a reduced dependence on the excitation power with δ nearly constant for powers $P < P_{\mathrm{sat}}/2$, in contrast to e.g. measurements of X photons, compare Fig. 3(a).

In Fig. 3(d)-(g) we plot the equivalent autocorrelation spectra measured on Dot B. Below we highlight several notable differences compared to dot A. The X autocorrelation displays a similar behavior except here we observe bunching at high excitation rates ($P > P_{\mathrm{sat}}$), up to $A = 2.1$ at $4P_{\mathrm{sat}}$ (not shown). Similarly, the $\mathrm{X^{-1}}$ autocorrelation displays a similar behaviour to that observed in Dot A except here we observe more significant short-delay bunching, reaching values of $A = 1.64$ at $2.4P_{\mathrm{sat}}$. The autocorrelation of the additional complex, $\mathrm{X^{+1}}$, is very similar to that of $\mathrm{X^{-1}}$ with some slight differences in bunching amplitudes and decay constants. The biexciton, on the other hand, shows a significantly different behaviour compared to XX in Dot A: although bunching at low excitation powers is observed, here the bunching decays to values below the uncorrelated coincidence count rates before rising back up at long delays. The dot-specific behaviour will be discussed later in the article where we introduce a stochastic multilevel model to interpret the various temporal features observed in the correlations.

B. Cross-correlation

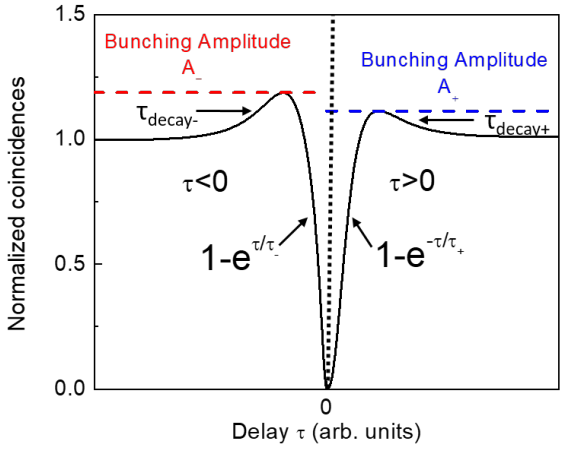

FIG. 4. Simulated correlation spectrum $g^{(2)}(\tau)$ between two different complexes highlighting the relevant temporal characteristics: antibunching dip width $\delta = \delta_- + \delta_+$ and rise times τ_- and τ_+, short delay bunching amplitudes A_- and A_+ and decay times τ_{decay-} and τ_{decay+}.

Fig. 4 shows the simulated cross-correlation between two arbitrary excitonic complexes X_a and X_b with detection of X_a signalling a 'start' and detection of X_b signalling a 'stop'. In this configuration, at $\tau = 0$ the system has emitted an X_a photon. For $\tau > 0$, the measurement waits for detection of the X_b photon i.e. the system has to wait for the capture of carriers (electrons and/or holes) needed to create the X_b complex. This capture process is characterized by the capture rate $1/\tau_+$. For negative delays ($\tau < 0$), the system is reversed: after detection of an X_b photon, the system has to wait to capture carriers that will create the X_a complex with associated capture rate $1/\tau_-$. As in autocorrelations, cross-correlations involving complexes with more than two carriers will exhibit short-delay bunching at low excitation rates quantified by amplitudes A_- and A_+ for $\tau < 0$ and $\tau > 0$, respectively. As the complexes in cross-correlation measurements are distinct, both the capture times $\tau_\pm$ and the bunching amplitudes $A_\pm$ will, in general, be different, producing correlations that are asymmetric about $\tau = 0$. Below we

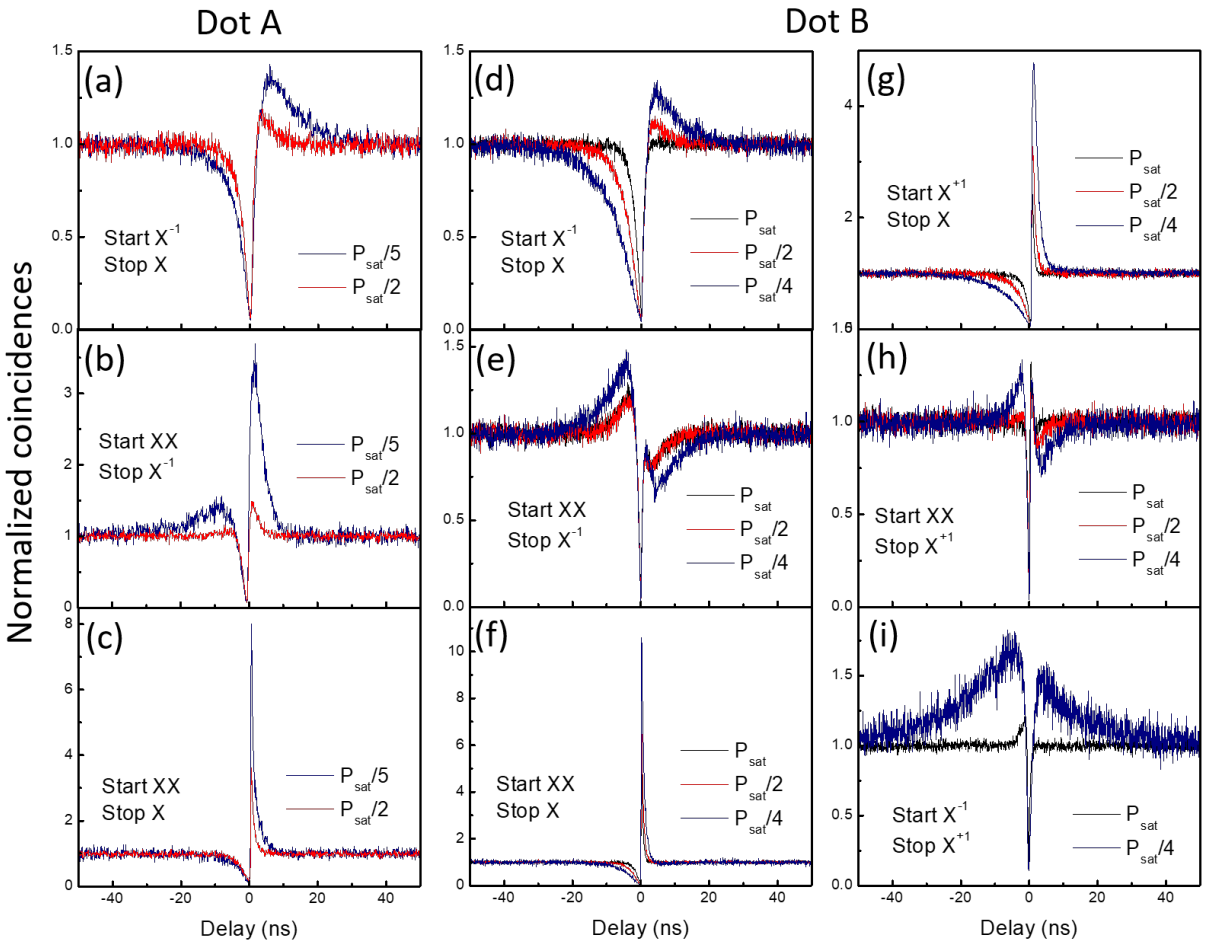

FIG. 5. Excitation-dependent cross-correlations in Dot A and B: (a), (d) X^{-1}-X, (b), (e) XX-X^{-1}, (c), (f) XX-X. Additional cross-correlations for Dot B: (g) X-X^{+1}, (h) XX-X^{+1}, (i) X^{-1}-X^{+1}.

discuss the cross-correlation measurements of Dot A and B in terms of these parameters.

1. Dot A

We first look at the cross-correlations between the three complexes in Dot A: X-XX, X-X^{-1}, and X^{-1}-XX. These have been previously reported in Ref. 19 and are reproduced here. Fig. 5(a) shows power-dependent correlations between X^{-1} and X, $g^{(2)}_{X^{-1},X}(\tau)$. We use the convention that the first subscript X^{-1} triggers a 'start' click and the second subscript X triggers a 'stop' click. For $\tau < 0$, having just detected an X photon, the dot is empty. No bunching is observed ($A_- = 1$) and the correlation represents the typical antibunching dip expected from a single photon emitter. For $\tau > 0$, having just detected an X^{-1} photon, the dot is occupied with a single electron and requires a single hole to create the neutral X. In the limit of low excitation, where the average number of carriers in the dot tends to zero, the presence of this electron at $\tau = 0$ makes it more likely to create an exciton at short delays compared to long delays where an electron and a hole needs to be captured. Hence bunching is observed which increases in amplitude as the excitation power is reduced. We also note the asymmetry in the rise times ($\tau_- > \tau_+$) indicating that the creation of the X complex after the emission of an X^{-1} photon is faster ($\tau_+ = 1.6$ ns at $P = P_{\rm sat}/5$) compared to the creation of an X^{-1} complex after emission of an X photon ($\tau_- = 4.45$ ns), the latter requiring two more carriers to be captured compared to the former.

Fig. 5(b) shows the cross-correlations $g^{(2)}_{XX,X^{-1}}(\tau)$. Bunching is observed for both $\pm\tau$ with $A_+ > A_-$ and both of these increase with decreasing excitation power. The asymmetry in bunching amplitudes arises from relative difference in likelyhoods of populating the dot with the required complex to produce a click at short delays compared to long delays. For $\tau > 0$, having just detected an XX photon, the dot is necessarily occupied with one electron and one hole. To put the dot in the X^{-1} state requires the capture of just a single electron. The proba-

bility of capturing a single carrier is more likely than capturing three carriers (two electrons and a hole), which is required at longer delays when the dot is typically empty (for low excitation rates). This produces the observed excitation rate-dependent bunching at short positive delays. For $\tau < 0$, having just detected an X^{-1} photon, the dot is left occupied with a single electron. To put the dot in the XX state requires the capture of one electron and two holes, which is more likely compared to the four carriers required (two electrons and two holes) when the dot is empty. This produces the observed excitation rate-dependent bunching at short negative delays. The rise times $\tau_{\pm}$ differ significantly ($\tau_-/\tau_+ = 2.52/0.59$ at $P_{\rm sat}/5$) since the probability of capturing a single electron is higher compared to the probability of capturing an electron and two holes.

The $g^{(2)}_{\rm xx,x}(\tau)$ cross-correlations in Fig. 5(c) show the conventional asymmetric profile[29,30] indicative of the cascaded biexciton-exciton emission process. For $\tau > 0$, right after the detection of a biexciton photon the dot is populated with one electron-hole pair which may then decay to the ground state or capture a second pair to form a new biexciton. As the excitation power is decreased, reducing the capture rate of electron-hole pairs, it becomes comparatively more likely to form a new biexciton at short delays when the dot already contains one electron-hole pair relative to long delays when the dot likely empty. Hence, the decay of the bunching, τ_{decay} corresponds to the X lifetime. For $\tau < 0$, an X photon has just been detected and the dot is empty: the correlation represents the typical antibunching dip expected from a single photon emitter.

2. Dot B

The six possible cross-correlations between the four complexes in Dot B, each measured at different excitation powers, are shown in Fig. 5(d)-(i). The correlations $g^{(2)}_{\rm x^{-1},x}(\tau)$ shown in Fig. 5(d) are very similar to that observed in Dot A, compare Fig. 5(d). For $g^{(2)}_{\rm x^{+1},x}(\tau)$, Fig. 5(g), the asymmetry is similar but for $\tau > 0$ the bunching amplitudes are significantly higher and the rise and decay times are significantly shorter. The rise time here, $\tau_+ = 0.29\,$ns at $P_{\rm sat}/4$, is associated with the capture of a single electron, a faster process compared to the capture of a single hole ($\tau_+ = 1.44\,$ns at $P_{\rm sat}/4$ from Fig. 5(d)). The large bunching amplitude A_+ and short decay rate τ_{decay+} suggests it is unlikely for the dot to be in a configuration where it is populated with a single hole.

Fig 5(e) shows the correlations $g^{(2)}_{\rm xx,x^{-1}}(\tau)$. For $\tau < 0$, the behaviour is similar to Dot A but with faster rise times, $\tau_- = 2.52\,$ns compared to $\tau_- = 1.14\,$ns. For $\tau > 0$, the behaviour is markedly different. Instead of simple bunching, we observe local bunching that decays to values below the uncorrelated coincidence count rates before rising back up its normalized value for long delays, similar to that observed in the XX autocorrelation, see Fig. 3(e). The correlations $g^{(2)}_{\rm xx,x^{+1}}(\tau)$, Fig. 5(h), show a similar behaviour but with slightly different time constants, expected since here the ratio of carriers to be captured is reversed.

TABLE I. Capture rates and bunching amplitudes extracted from cross-correlation measurements on Dot A and Dot B.

Dot	start	stop	τ_- (ns)	A_-	τ_{decay-} (ns)	τ_+ (ns)	A_+	τ_{decay+} (ns)
A	X^{-1}	X	4.45	1	NA	1.6	1.34	8.36
A	XX	X^{-1}	2.52	1.40	12.41	0.59	3.4	2.55
A	XX	X	3.95	1	NA	0	7.98	1.45
B	X^{-1}	X	8.09	1	NA	1.44	1.26	7.36
B	X^{+1}	X	7.99	1	NA	0.29	4.75	1.27
B	XX	X^{-1}	1.14	1.39	6.92	0.49	0.92	1.32
B	XX	X^{+1}	0.88	1.25	3.6	0.36	1.21	0.92
B	XX	X	4.24	1	NA	0	10.6	0.77
B	X^{-1}	X^{+1}	0.89	1.65	15.68	1.95	1.48	13.92

NA - not applicable: no time-scale is given for cases where bunching is not observed i.e. $A = 1$.

The cross-correlations corresponding the the biexciton-exciton cascade, $g^{(2)}_{\rm xx,x}(\tau)$ are shown in Fig. 5(f). The behaviour is very similar to XX-X correlations observed in Dot A, compare Fig. 5(c).

Finally, we discuss $g^{(2)}_{\rm x^{-1},x^{+1}}(\tau)$, shown in Fig. 5(i). For $\tau > 0$, after the emission of an X^{-1} photon we observe a rise time, $\tau_+ = 1.95\,$ns, linked to the capture time of two holes required to create an X^{+1} photon. For $\tau < 0$, after the emission of an X^{+1} photon, the system has to wait for the capture of two electrons to create an X^{-1} complex, a faster process with $\tau_- = 0.89\,$ns. The asymmetry is also observed in the bunching with $A_+/A_- = 1.48/1.65$. The asymmetric behaviour here is a clear indication that electrons are captured at higher rates than holes, as previously suggested by the autocorrelations of X^{-1} and X^{+1}, compare Fig. 3(f) and (g).

The capture rates, $\tau_{\pm}$, and bunching amplitudes, $A_{\pm}$, extracted from exponential fits to the correlations are summarized in Table I. The values listed correspond to measurements at $P_{\rm sat}/5$ for Dot A and $P_{\rm sat}/4$ for Dot B. For completion, we also include the decay rates of the bunching amplitudes, $\tau_{decay\pm}$.

V. STOCHASTIC MODELING OF AUTOCORRELATIONS

The correlation measurements of the previous section highlight the rich variety of temporal features observable in the nanowire quantum dot system where multiple charge configurations exist. These correlations vary from dot to dot since the relative probabilities of specific charge configurations are dot-dependent. One aspect common to all correlations involving charged complexes suggested by experiment is that electrons and

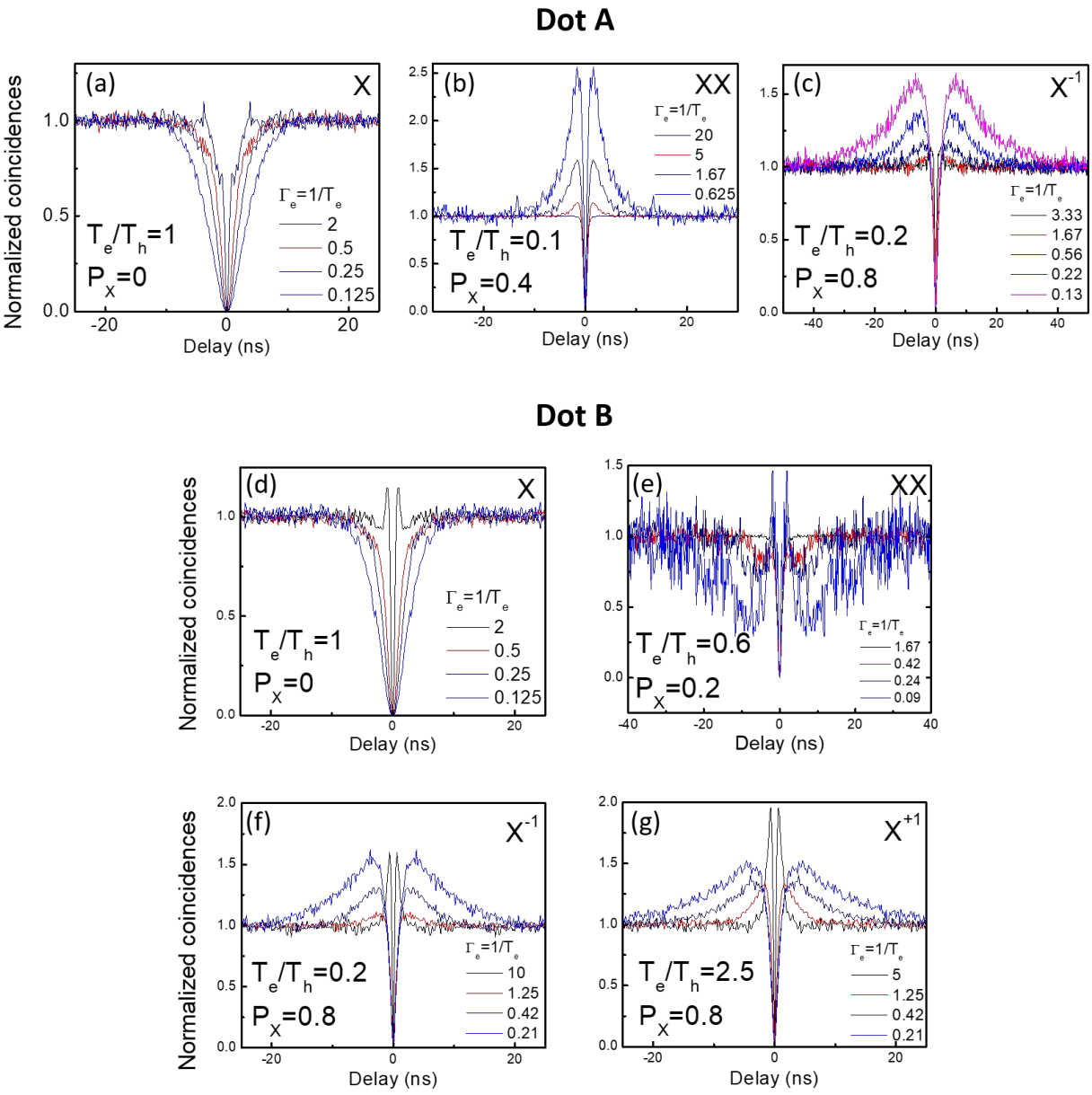

FIG. 6. Simulated autocorrelations of the excitonic complexes in Dot A (a)-(c) and Dot B (d)-(g).

holes are being admitted within the quantum dots at different rates. To gain insight into the role of disparate carrier capture rates in determining the complex-specific temporal correlations, we have developed a sixteen-level stochastic model with adjustable parameters accessible to the experiment.

The model includes the four neutral excitons (two bright and two dark spin configurations), the four spin configurations of the singly charged excitons, X^{-1} and X^{+1}, and the biexciton. Also included are the 4 single carrier states (spin-up and spin-down electron and hole), the two electron state, the two hole state, and the vacuum state. We assume the capture times of the carriers are spin-independent and take into account the Pauli exclusion principle, i.e., if a dot level is already occupied, only an opposite spin carrier can be admitted.

TABLE II. Measured parameters used in simulations.

Dot	τ_{x} (ns)	τ_{xx} (ns)	$\tau_{\mathrm{x}^{-1}}$ (ns)	$\tau_{\mathrm{x}^{+1}}$ (ns)	$\tau_{\mathrm{x_d}}$ (ns)
A	1.84	0.61	2.26	2.26*	10.5
B	1.23	1.04	1.29	1.24	22.3

*Lifetime of $\tau_{\mathrm{x}^{+1}}$ in Dot A set to same value as $\tau_{\mathrm{x}^{-1}}$.

The simulation is organized as follows. The central loop advances the global time by a preselected timestep.

The timestep as well as the total simulation time are chosen to obtain a sufficient set of radiative transitions to support a meaningful statistical analysis. At each time step, the state of the quantum dot is examined and a decision is made as to whether the confined complex should recombine by emitting a photon. The decision is made by generating a random number and comparing it to the cumulative probability distribution corresponding to the exponential radiative decay profile characterized by the lifetime (different for different excitonic complexes). If the complex is set to recombine, the state of the dot is altered to remove one electron-hole pair, and one photon is added to the appropriate photon stream with the information about the global time corresponding to the event. Further, a similar decision is made as to whether to admit an electron, a hole, or a pair of carriers. These processes are similarly governed by exponential probability distributions with characteristic times for each process. Lastly, we also implemented a process whereby a dark exciton can convert to a bright exciton, governed by the probability distribution scaled by the dark exciton lifetime. Once the simulation is completed, we are left with four photon streams, one for each X, XX, X^{+1}, and X^{-1}. We extract the second-order correlation functions by analyzing the timing of each photon in each stream in a manner closely resembling the experimental technique.

To make contact between the simulation and the experiment, we allow for independent control of the electron (hole) capture time, T_e (T_h) for admitting one electron (hole) of either spin and adjust the ratio T_e/T_h. The excitation rate is controlled using T_e. We also allow for the possibility of single carrier or pair capture through P_X, the pair admission probability. Input parameters listed in Table II are taken from measurements and include the lifetimes τ_{x}, τ_{xx}, $\tau_{\mathrm{x}^{-1}}$ and $\tau_{\mathrm{x}^{+1}}$ of X, XX, X^{-1} and X^{+1}, respectively. For Dot A, we keep a contribution of the X^{+1} complex in the simulation although it is not observed in the PL and set its lifetime to be the same as X^{-1} (i.e. $\tau_{\mathrm{x}^{-1}}=\tau_{\mathrm{x}^{+1}}$), an assumption that should hold for typical quantum dot systems. The dark exciton lifetime, τ_d, represents the time associated with a spin-flip process[31].

1. Dot A

The simulated correlations $g^{(2)}_{\mathrm{x,x}}(\tau)$ are shown in Fig. 6(a). The behaviour observed in experiment, Fig. 3(a), is reproduced using equal electron and hole capture rates $T_e/T_h = 1$ and single carrier capture $P_X = 0$. For the X complex, other values of T_e/T_h or P_X produce bunching at low excitation rates which is not observed experimentally.

To reproduce the correlations $g^{(2)}_{\mathrm{xx,xx}}(\tau)$ shown in Fig. 3(b) requires a reduced T_e/T_h value (the electron capture rate here is faster than the hole capture rate) and a higher P_X value (there is an non-negligible probability of pair capture). The simulated correlations using $T_e/T_h = 0.1$ and $P_X = 0.4$ are plotted in Fig. 6(b). We note that different parameters produce similar results and in Fig. 7 we plot the power dependent bunching amplitude under different simulations conditions. In (a) P_X is kept fixed and T_e/T_h is varied from 0.05 to 0.15. From the figure, quantitative agreement with experiment is obtained for all T_e/T_h values shown notwithstanding an offset in excitation rate. In (b), T_e/T_h is kept fixed at 0.1 and P_X is varied from 0 to 0.4. We observe similar excitation-dependent bunching amplitudes for moderate values of P_X. For $P_X > 0.5$ (not shown), the autocorrelations exhibit long decay times associated with blinking, which is not observed experimentally.

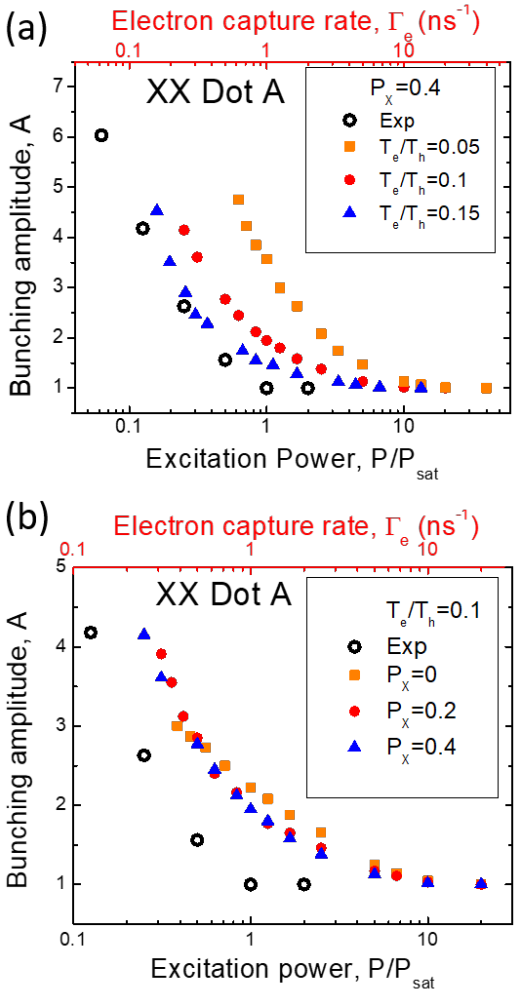

FIG. 7. Experimental (open symbols) and simulated (closed symbols) excitation rate dependence of the bunching amplitude, A, from $g^{(2)}_{\mathrm{xx,xx}}(\tau)$ of Dot A. (a) Simulations performed for different T_e/T_h values with P_X fixed. (b) Simulations performed for different P_X values with T_e/T_h fixed.

The simulated autocorrelations $g^{(2)}_{\mathrm{x^{-1},x^{-1}}}(\tau)$ are shown in Fig. 6(c) where we have used $T_e/T_h = 0.2$ and $P_X = 0.8$ to reproduce the experiment. Here, P_X controls the broadening of the antibunching dip δ. In Fig. 8 we com-

pare the simulated and experimental decay rates τ_{decay} and bunching amplitudes A. The model reproduces the power-dependence of both τ_{decay} and A with some slight discrepancy at both high and low excitation rates. Since we have assumed an excitation rate-independent T_e/T_h ratio, such deviations are expected at low and high pump rates, where different values of T_e/T_h may be more appropriate. We note that for larger values of T_e/T_h, the simulations predict a transition from a decreasing to increasing bunching amplitude as the excitation rate is increased. Although there are hints of this transition in Dot A, it is prominent in Dot B and is discussed below.

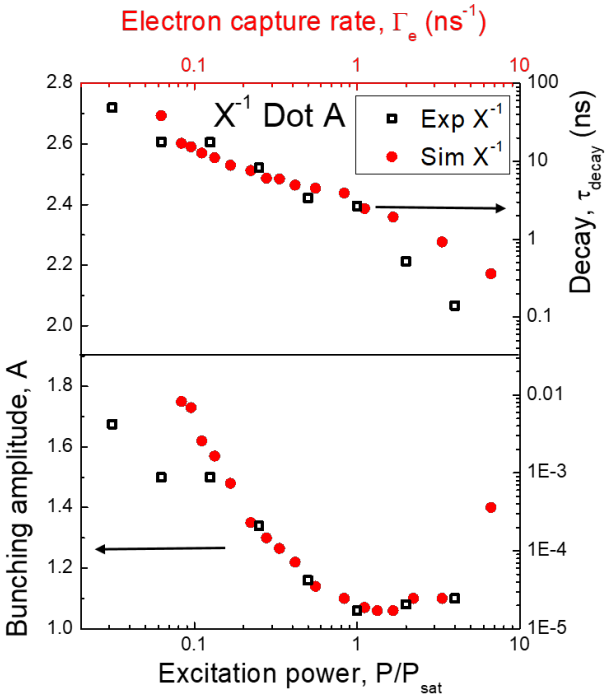

FIG. 8. Experimental (open symbols) and simulated (closed symbols) excitation rate dependence of the bunching amplitude, A, and the decay time, τ_{decay}, from $g^{(2)}_{\mathrm{x}^{-1},\mathrm{x}^{-1}}(\tau)$ of Dot A.

2. Dot B

The most notable difference in $g^{(2)}_{\mathrm{x,x}}(\tau)$ between Dot A and B is the bunching observed in the latter for $P/P_{\mathrm{sat}} > 1$, compare Figs. 3(a) and (d). To reproduce a similar bunching behaviour in the model we the use a power dependent dark exciton contribution. For $T_e < 2$, we set $\tau_d = 0.01\,\mathrm{ns}$ whilst for $T_e \geq 2$ we set $\tau_d = 22.3\,\mathrm{ns}$, as per Table II. The simulated correlations are shown in Fig. 6(d) using $T_e/T_h = 1$ and $P_X = 0$.

The simulated correlations $g^{(2)}_{\mathrm{xx,xx}}(\tau)$ are shown in Fig. 6(e) calculated using $T_e/T_h = 0.6$ and $P_X = 0.2$. These parameters reproduce the behaviour seen in experiment, compare Fig. 3(e), but with slight offsets in the local bunching amplitude, A, and the local antibunching dip at $\tau \neq 0$, see Fig. 9.

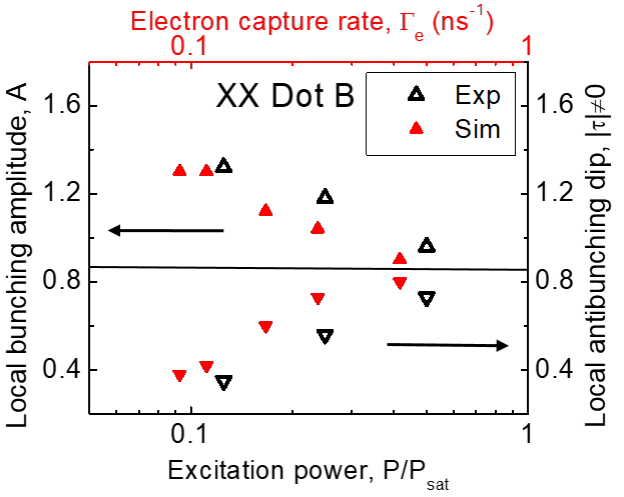

FIG. 9. Experimental (open symbols) and simulated (closed symbols) excitation rate dependence of the local bunching amplitude, A, and local antibunching dip at $|\tau| \neq 0$ from $g^{(2)}_{\mathrm{xx,xx}}(\tau)$ of Dot B.

Simulated correlations of $g^{(2)}_{\mathrm{x}^{-1},\mathrm{x}^{-1}}(\tau)$ and $g^{(2)}_{\mathrm{x}^{+1},\mathrm{x}^{+1}}(\tau)$ are plotted in Figs. 6(f) and (g), respectively. To reproduce the experimental correlations shown in Fig. 3, we have set $P_X = 0.8$ and have used $T_e/T_h = 0.2$ ($T_e/T_h = 2.5$) for $g^{(2)}_{\mathrm{x}^{-1},\mathrm{x}^{-1}}(\tau)$ ($g^{(2)}_{\mathrm{x}^{+1},\mathrm{x}^{+1}}(\tau)$), In Fig. 10 we compare simulated excitation rate dependence of the decay time and bunching amplitude with experiment for both X^{-1} and X^{+1}. Good agreement is obtained for excitation rates spanning two orders of magnitude, although the model underestimates the bunching at the highest pump powers, likely due to the assumption of a power independent T_e/T_h ratio, as above.

VI. DISCUSSION

Differences in the time-integrated PL spectra between quantum dots having nominally identical geometry and composition implies that the electrostatic environment varies from dot to dot. Different environments will result in variations of the relative intensities between two complexes or the observation of different complexes. What is responsible for producing a different environment is unclear: it may be a variation in the Fermi level pinning from one dot to another or a variation in the density and distribution of traps in close proximity to the dot. Whatever the reason, any difference in the electrostatic environment will affect a change in the carrier capture processes responsible for populating the dot with different excitonic complexes. This variation in the carrier cap-

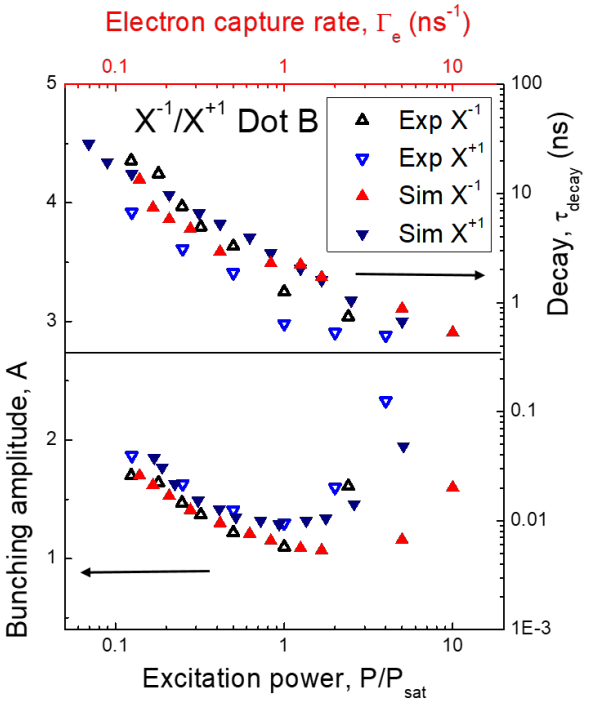

FIG. 10. Experimental (open symbols) and simulated (closed symbols) excitation rate dependence of the bunching amplitude, A, and the decay time, τ_{decay}, from $g^{(2)}_{\mathrm{x}^{-1},\mathrm{x}^{-1}}(\tau)$ and $g^{(2)}_{\mathrm{x}^{+1},\mathrm{x}^{+1}}(\tau)$ of Dot B.

ture dynamics is responsible for the vastly different temporal correlations observed for nominally identical dots. Below we attempt to interpret the variation in the correlations in terms of the carrier capture dynamics, focusing on the autocorrelations for which we have performed the simulations.

The behaviour of the neutral exciton X for both dots studied is trivial and can be described simply using equal electron and hole capture rate, $T_e/T_h = 1$ and single carrier injection, $P_X = 0$. For the neutral biexciton XX, Dot A exhibits a typical response expected from this complex whilst Dot B exhibits 'local bunching' i.e. a transition from positive to negative correlations. The simulations suggest that the difference in response is due to a higher T_e/T_h value in the latter dot. For this complex, it is not clear why the presence of the additional X^+ complex and the associated pathways to generating it would lead to a higher capture rate for electrons relative to holes, or if it is even related.

Autocorrelations of the charged complexes differ from the neutrals in that they exhibit blinking. Blinking is inherent in the multi-level model as it includes more than one possible excitonic configuration. From the simulations, the temporal features associate with blinking (bunching amplitude and decay) depend on the ratio of capture rates and whether they are captured singly or in pairs. We note that the blinking can be quenched in the simulations by using significantly different capture rates ($T_e/T_h \leq 0.2$) and single carrier injection. The small T_e/T_h ratio ensures that the dot is populated with one carrier at a time. Using these input parameters removes the possible pathways to other complexes, always building the same complex. In other words, these conditions simulate charge state control, allowing only one possible charge state and thus removing the possibility of blinking between charge states.

Although the autocorrelation spectra of the three charged complexes appear to differ significantly, they all exhibit the same behaviour: as the excitation rate is increased, decay times decrease and bunching amplitudes initially decrease but at some pump power start to increase. What is different between the complexes is the power at which the bunching amplitude transitions from decreasing to increasing. This behaviour can be simulated simply by adjusting the T_e/T_h ratio.

We note that even dots which emit from the same complexes may exhibit vastly different blinking behaviour. Fig. 11 shows measured and simulated autocorrelations $g^{(2)}_{\mathrm{x}^{-1},\mathrm{x}^{-1}}(\tau)$ from another dot, Dot C, that has a time-integrated spectrum (not shown) similar to Dot A. This dot does not show any sign of bunching for the excitation rates used. To reproduce the non-blinking behaviour, both T_e/T_h and P_X are reduced.

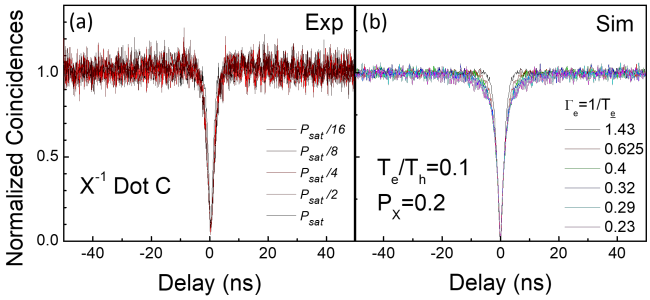

FIG. 11. (a) Measured and (b) simulated autocorrelations $g^{(2)}_{\mathrm{x}^{-1},\mathrm{x}^{-1}}(\tau)$ of Dot C for which no blinking was observed.

Finally, we note certain limitations present in the current model which may account some of the discrepancies observed between the simulations and the experiment. First, we only consider s-shell states whilst a more realistic approach would include levels in the p-shell. Second, we have assumed that the ratio of electron to hole capture rates is independent of excitation power. One would, however, expect this ratio to change at the extremes of low and high pumping rates. Lastly, we have only simulated autocorrelations, employing complex-dependent capture rates. In order to simulate cross-correlations, a more sophisticated model is required that would allow for individual capture rates to be assigned to electrons and holes that are specific to the complex being investigated.

VII. CONCLUSION

We have performed extensive temporal correlation measurements on two nominally identical quantum dots whose time-integrated PL differs only by the presence of an additional excitonic complex. Increasing the number of possible complexes that can radiatively decay has a dramatic effect on the time-correlated response. Using a multi-level stochastic model, we account for the observed behaviour in terms of carrier capture rates and single carrier versus pair capture probabilities. These results demonstrate that correlation spectroscopy is a useful method for gaining insight into the carrier dynamics of multi-exciton systems and may help in engineering quantum dots structures with specific proprieties.

ACKNOWLEDGMENTS

This work was supported by the Natural Sciences and Engineering Research Council and the Canadian Space Agency.

REFERENCES

[1] J. L. O'Brien, A. Furusawa, and J. Vučković, "Photonic quantum technologies," Nat. Photon. **3**, 687 (2009).
[2] J.-M. Gérard and B. Gayral, "Strong purcell effect for InAs quantum boxes in three-dimensional solid-state microcavities," J. Lightwave Tech. **17**, 2089 (1999).
[3] P. Michler, A. Kiraz, C. Becher, W. V. Schoenfeld, P. Petroff, L. Zhang, E. Hu, and A. Imamoglŭ, "A quantum dot single-photon turnstile device," Science **290**, 2282–2285 (2000).
[4] H. Wang, Z.-C. Duan, Y.-H. Li, S. Chen, J.-P. Li, Y.-M. He, M.-C. Chen, Y. He, X. Ding, C.-Z. Peng, C. Schneider, M. Kamp, S. Höfling, C.-Y. Lu, and J.-W. Pan, "Near-transform-limited single photons from an efficient solid-state quantum emitter," Phys. Rev. Lett. **116**, 213601 (2016).
[5] X. Ding, Y. He, Z.-C. Duan, N. Gregersen, M.-C. Chen, S. Unsleber, S. Maier, C. Schneider, M. Kamp, S. Höfling, C.-Y. Lu, and J.-W. Pan, "On-demand single photons with high extraction efficiency and near-unity indistinguishability from a resonantly driven quantum dot in a micropillar," Phys. Rev. Lett. **116**, 020401 (2016).
[6] O. Benson, C. Santori, M. Pelton, and Y. Yamamoto, "Regulated and entangled photons from a single quantum dot," Phys. Rev. Lett. **84**, 2513–2516 (2000).
[7] D. Fattal, K. Inoue, J. Vučković, C. Santori, G. S. Solomon, and Y. Yamamoto, "Entanglement formation and violation of bell's inequality with a semiconductor single photon source," Phys. Rev. Lett. **92**, 037903 (2004).
[8] N. Akopian, N. H. Lindner, E. Poem, Y. Berlatzky, J. Avron, and D. Gershoni, "Entangled photon pairs from semiconductor quantum dots," Phys. Rev. Lett. **96**, 130501 (2006).
[9] I. Schwartz, D. Cogan, E. R. Schmidgall, Y. Don, L. Gantz, O. Kenneth, N. H. Lindner, and D. Gershoni, "Deterministic generation of a cluster state of entangled photons," Science **354**, 6311 (2016).
[10] A. N. Vamivakas, Y. Zhao, C. Y. Lu, and M. Atatüre, "Spin-resolved quantum-dot resonance fluorescence," Nat. Photon. **5**, 198–202 (2009).
[11] M. Pelton, C. Santori, J. Vučković, B. Zhang, G. S. Solomon, J. Plant, and Y. Yamamoto, "Efficient source of single photons: A single quantum dot in a micropost microcavity," Phys. Rev. Lett. **89**, 233602 (2002).
[12] O. Iff, Q. Buchinger, M. Moczała-Dusanowska, M. Kamp, S. Betzold, M. Davanco, K. Srinivasan, S. Tongay, C. Antón-Solanas, S. Höfling, and C. Schneider, "Purcell-enhanced single photon source based on a deterministically placed wse$_2$ monolayer quantum dot in a circular bragg grating cavity," Nano Lett. **21**, 4715–4720 (2021).
[13] J. Claudon, J. Bleuse, N. S. Malik, M. Bazin, P. Jaffrennou, N. Gregersen, C. Sauvan, P. Lalanne, and J.-M. Gérard, "A highly efficient single-photon source based on a quantum dot in a photonic nanowire," Nat. Photon. **4**, 174 (2010).
[14] D. Dalacu, K. Mnaymneh, J. Lapointe, X. Wu, P. J. Poole, G. Bulgarini, V. Zwiller, and M. E. Reimer, "Ultraclean emission from inasp quantum dots in defect-free wurtzite inp nanowires," Nano Lett. **12**, 5919–5923 (2012).
[15] H. D. Robinson and B. B. Goldberg, "Light-induced spectral diffusion in single self-assembled quantum dots," Phys. Rev. B **61**, R5086 (2000).
[16] C. Santori, D. Fattal, J. Vučković, G. S. Solomon, E. Waks, and Y. Yamamoto, "Submicrosecond correlations in photoluminescence from inas quantum dots," Phys. Rev. B **69**, 205324 (2004).
[17] M. Abbarchi, C. A. Mastrandrea, T. Kuroda, T. Mano, K. Sakoda, N. Koguchi, S. Sanguinetti, A. Vinattieri, and M. Gurioli, "Exciton fine structure in strain-free GaAs/Al$_{0.3}$Ga$_{0.7}$As quantum dots: Extrinsic effects," Phys. Rev. B **78**, 125321 (2008).
[18] M. Bayer, G. Ortner, O. Stern, A. Kuther, A. A. Gorbunov, A. Forchel, P. Hawrylak, S. Fafard, K. Hinzer, T. L. Reinecke, S. N. Walck, J. P. Reithmaier, F. Klopf, and F. Schäfer, "Fine structure of neutral and charged excitons in self-assembled In(Ga)As/(Al)GaAs quantum dots," Phys. Rev. B **65**, 195315 (2002).
[19] P. Laferrière, E. Yeung, M. Korkusinski, P. J. Poole, R. L. Williams, D. Dalacu, J. Manalo, M. Cygorek, A. Altintas, and P. Hawrylak, "Systematic study of the emission spectra of nanowire quantum dots," Appl. Phys. Lett. **118** (2021).
[20] M. Abbarchi, C. Mastrandrea, T. Kuroda, T. Mano, A. Vinattieri, K. Sakoda, and M. Gurioli, "Poissonian statistics of excitonic complexes in quantum dots," J. Appl. Phys. **106**, 053504 (2009).
[21] D. Dalacu, A. Kam, D. G. Austing, X. Wu, J. Lapointe, G. C. Aers, and P. J. Poole, "Selective-area vapour-liquid-solid growth of InP nanowires," Nanotech. **20**, 395602 (2009).
[22] D. Dalacu, K. Mnaymneh, X. Wu, J. Lapointe, G. C. Aers, P. J. Poole, and R. L. Williams, "Selective-area vapor-liquid-sold growth of tunable inasp quantum dots in nanowires," Appl. Phys. Lett. **98**, 251101 (2011).
[23] M. E. Reimer, G. Bulgarini, A. Fognini, R. W. Heeres, B. J. Witek, M. A. M. Versteegh, A. Rubino, T. Braun, M. Kamp, S. Höfling, D. Dalacu, J. Lapointe, P. J. Poole, and V. Zwiller, "Overcoming power broadening of the quantum dot emission in a pure wurtzite nanowire," Phys. Rev. B **93**, 195316 (2016).
[24] D. Dalacu, P. J. Poole, and R. L. Williams, "Nanowire-based sources of non-classical light," Nanotechnology **30**, 232001 (2019).
[25] P. Laferrière, E. Yeung, L. Giner, S. Haffouz, J. Lapointe, G. C. Aers, P. J. Poole, R. L. Williams, and D. Dalacu, "Multiplexed single-photon source based on multiple quantum dots embedded within a single nanowire," Nano Lett. **20**, 3688–3693 (2020).
[26] P. Laferrière, E. Yeung, I. Miron, D. B. Northeast, S. Haffouz, J. Lapointe, M. Korkusinski, P. J. Poole, R. L. Williams, and D. Dalacu, "Unity yield of deterministically positioned quantum dot single photon sources," Sci. Rep. **12**, 1–9 (2022).
[27] G. Sallen, A. Tribu, T. Aichele, R. André, L. Besombes, C. Bougerol, S. Tatarenko, K. Kheng, and J. P. Poizat, "Exciton dynamics of a single quantum dot embedded in a nanowire," Phys. Rev. B **80**, 085310 (2009).
[28] B. Piętka, J. Suffczyński, M. Goryca, T. Kazimierczuk, A. Golnik, P. Kossacki, A. Wysmolek, J. A. Gaj, R. Stępniewski, and

M. Potemski, "Photon correlation studies of charge variation in a single GaAlAs quantum dot," Phys. Rev. B **87**, 035310 (2013).
[29]A. Kiraz, S. Fälth, C. Becher, B. Gayral, W. V. Schoenfeld, P. M. Petroff, L. Zhang, E. Hu, and A. Imamoglŭ, "Photon correlation spectroscopy of a single quantum dot," Phys. Rev. B **65**, 161303(R) (2002).
[30]E. Moreau, I. Robert, L. Manin, V. Thierry-Mieg, J. M. Gérard, and I. Abram, "Quantum cascade of photons in semiconductor quantum dots," Phys. Rev. Lett. **87**, 183601 (2001).
[31]J. Johansen, B. Julsgaard, S. Stobbe, J. M. Hvam, and P. Lodahl, "Probing long-lived dark excitons in self-assembled quantum dots," Phys. Rev. B **81**, 081304(R) (2010).

Chapter 8

Article 4: Approaching transform-limited photons from nanowire quantum dots excited above-band

This chapter contains the following article:

P. Laferrière, A. Yin, E. Yeung, L. Kusmic, M. Korkusinski, P. Rasekh, D. B. Northeast, S. Haouz, J. Lapointe, P. J. Poole, R. L. Williams, & D. Dalacu, "Approaching transform-limited photons using nanowire quantum dots", arXiv:2208.00066 (2022)

Submitted to Physical Review Letters, August 2022.

DOI: https://doi.org/10.48550/arXiv.2208.00066

Approaching transform-limited photons from nanowire quantum dots excited above-band

Patrick Laferrière,[1,2,*] Aria Yin,[1,2] Edith Yeung,[1,2] Leila Kusmic,[1,2] Marek Korkusinski,[1] Payman Rasekh,[1] David B. Northeast,[1] Sofiane Haffouz,[1] Jean Lapointe,[1] Philip J. Poole,[1] Robin L. Williams,[1] and Dan Dalacu[1,2]

[1] *National Research Council Canada, Ottawa, Ontario, Canada, K1A 0R6.*
[2] *University of Ottawa, Ottawa, Ontario, Canada, K1N 6N5.*

We demonstrate that, even when employing above-band excitation, photons emitted from semiconductor quantum dots can have linewidths that approach their transform-limited values. This is accomplished by using quantum dots embedded in bottom-up photonic nanowires, an approach which mitigates several potential mechanisms that can result in linewidth broadening: (i) only a single quantum dot is present in each device, (ii) dot nucleation proceeds without the formation of a wetting layer, and (iii) the sidewalls of the photonic nanowire are comprised not of etched facets, but of epitaxially grown crystal planes. Using these structures we achieve linewidths of 2x the transform limit, unprecedented for above-band excitation. We also demonstrate a highly nonlinear dependence of the linewidth on both excitation power and temperature which can be described by an independent Boson model that considers both deformation and piezoelectric exciton-phonon coupling. We find that for sufficiently low excitation powers and temperatures, the observed excess broadening is not dominated by phonon dephasing, a surprising result considering the high phonon occupation that occurs with above-band excitation.

Quantum interference between two or more indistinguishable photons lies at the heart of most photonic quantum technologies[1] and high visibilities require highly coherent photons. Solid-state two-level emitters[2], e.g. epitaxial semiconductor quantum dots[3], can provide single photons with high efficiency provided they are incorporated within appropriate photonic structures supporting a single optical mode into which all photons are emitted. Within this solid-state environment, however, fluctuations in charge and spin or interactions with phonons can lead to broadening of the emitted photon linewidth compared to the Fourier transform limit and, consequently, a reduction of the two-photon interference visibility, ν_{TPI}[4].

Excess broadening can be limited through the use of optical cavities[5,6] and resonant excitation[7], resulting in the observation of $\nu_{\mathrm{TPI}} > 90\%$ between sequential photons emitted from the same source over times scales $> 1\mu$sec[8,9]. Linewidths, typically measured over longer time scales, remain, however, broadened compared to the transform limit[8,10], a broadening typically attributed to a slowly varying charge environment. One can therefore expect a reduction of ν_{TPI} for times scales longer than a few microseconds and, in the case of remote emitters[11–17] for which noise correlations are absent, the reduction may be particularly severe.

It is therefore essential to address this persistent broadening which arises from a time-dependent occupation of traps close to the dot, producing a wandering of the exciton energy via the Stark effect[18]. These traps can be defects or impurities located in either the bulk semiconductor material[19], at surfaces (e.g. the growth surface[20] or the etched sidewall surface[21]) or epitaxial interfaces[22]. Additionally, quantum dots themselves are, by design, carrier traps and the impact on linewidth, at least of crystal phase dots[23] (i.e. stacking faults), is well established[24].

In this work we investigate a quantum dot system[25] distinct from the more conventional GaAs-based self-assembled dots[26] in several aspects that impact excess broadening. The dots are segments of InAsP within [0001] wurtzite-phase InP nanowires and are fabricated using a bottom-up technique. Here the only surfaces in close proximity to the dot are the crystal lattice growth facets that make up the sidewalls of the nanowire, surfaces which have a lower defect density compared to the dry-etched sidewalls present in top-down structures[27]. Using the InP material system, we can also expect an order of magnitude reduction in the surface recombination velocity compared to GaAs[28]. The quantum dots are nucleated via a vapour-liquid-solid (VLS) growth process[29] in which no 2D wetting layer forms, a layer associated with several broadening mechanisms[30]. The VLS growth mode is also unique in that the number of dots in each device is controlled[31] and by using devices that contain only a single emitter, potential charge fluctuations associated with carriers trapped in nearby quantum dots are eliminated.

We observe a significant reduction of excess broadening compared to conventional quantum dot emitters operated under the same conditions, with measured linewidths as low as 2x the transform limit. Remarkably, these narrow lines are observed using above-band excitation i.e. conditions expected to promote fluctuations in the charge environment. We also find that, at sufficiently low temperatures, broadening due to phonon dephasing is insignificant with an onset for strong broadening observed for $T > 8\,\mathrm{K}$. This is similar to that observed using resonant excitation[30] and four-wave mixing techniques[32] and consistent with a significant reduction in ν_{TPI} observed in Ref. 33. This behaviour can be fully described by an independent boson model[34] that considers phonons propagating along the nanowire growth direction and which takes into account both deformation and piezoelectric

exciton-phonon coupling. Importantly, we do not need to invoke virtual transitions between ground and excited states[33,35], for which the energy scales are inconsistent with our dot level structure. Instead, the nonlinearity is traced to the interplay of deformation and piezoelectric coupling mechanisms and their distinct dependence on phonon energy.

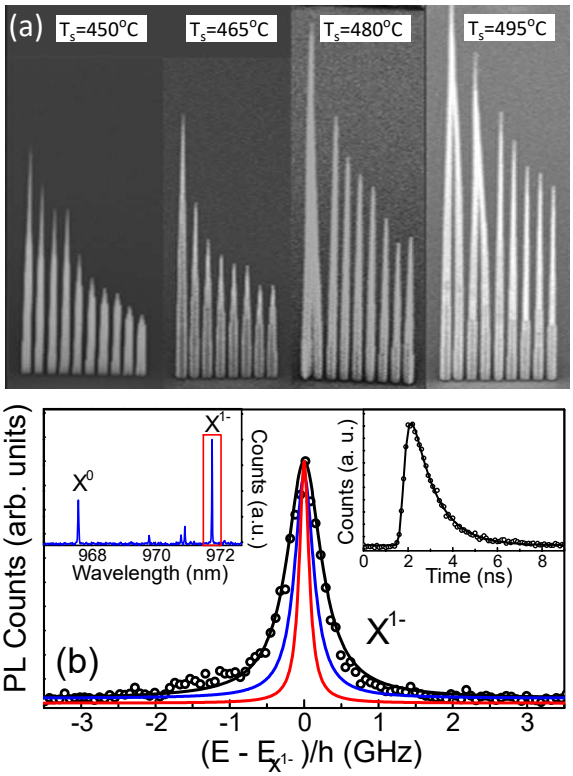

FIG. 1. (a) Scanning electron microscope images of linear arrays of nanowires pitched at 400 nm, each nanowire in an array having a different core diameter and each array grown at a different T_s, see Ref. 36 for details. (b) High resolution PL spectrum measured at 4 K and $P = 0.1P_{\rm sat}$ (black open circles) of the X^{1-} line emission highlighted in the left inset. Also plotted are a Lorentzian fit to the data (black curve), the spectrum after deconvolution with the etalon response (blue curve) and the predicted transform-limited spectrum (solid red curve) calculated using the transition lifetime T_1 extracted from the PL decay curve shown in the right inset.

The nanowire-based devices were grown using a two-step growth process[36]. First, a 20 nm diameter InP nanowire core is grown using growth conditions that promote axial growth (e.g. low Group V flux) and in this core we incorporate a $\sim$ 5 nm thick $InAs_{0.25}P_{0.75}$ quantum dot. Second, the core is clad with a shell using growth conditions that promote radial growth (high Group V flux). The resulting photonic nanowire has a base diameter of 250 nm that tapers to $\sim$ 100 nm over a length of $\sim 15\,\mu$m, Figure 1(a). Previously, we have used growth temperatures of 420°C for both the core and shell growths which produced quantum dots emitting exciton photons with linewidths of 880 MHz of which the inhomogeneous contribution was 730 MHz[37] and was associated with a higher defect density in the InP causing charge fluctuations discussed above. In order to improve the material quality, in this study we increased the nanowire core growth temperature to 435°C, thought to be an upper limit above which reasonable axial growth rates could not be maintained[38]. For the shell growth we can access higher temperatures and here we study samples where the shell is grown at temperatures up to $T_s = 495$°C.

Photoluminescence (PL) measurements were performed in a closed-cycle helium cryostat. The nanowire quantum dots were excited through a 100x objective (numerical aperture of 0.81) and the emission was collected through the same objective and directed to a grating spectrometer equipped with a liquid nitrogen cooled charged-coupled device (CCD). For time-integrated PL measurements, the excitation was a continuous wave laser operating at 780 nm whilst for time-resolved measurements, a pulsed laser operating at 670 nm was used. To measure linewidths, the dot emission was coupled to a single mode fiber and a single peak was selected using a fiber-based tunable filter with a 0.1 nm bandwidth. The spectral width of the filtered peak was resolved using a fiber-based piezo-driven scanning Fabry-Pérot etalon (bandwidth of 250 MHz, free-spectral range of 40 GHz) and detected with an avalanche photodiode.

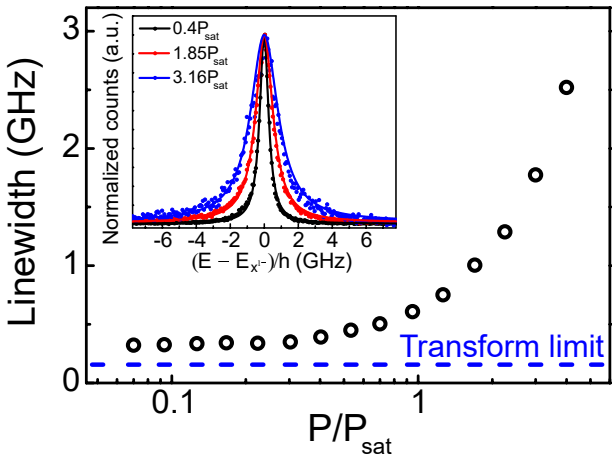

FIG. 2. Excitation power-dependence of the homogeneous linewidth extracted from the PL spectra after deconvolution with the etalon response function. Inset shows the high resolution PL spectra of the X^{1-} emission measured at $T = 4$ K for selected excitation powers. Solid lines correspond to Lorentzian fits to the data.

We first look at the linewidth of an excitonic photon at low temperature (4 K) and low excitation power ($P = 0.1P_{\rm sat}$) in a device where the shell is deposited at $T_s = 450$°C. Figure 1 shows the high-resolution PL spectrum of an X^{1-} photon emitting at $E_{X^{1-}} = 1.276$ eV. The emission peak was fit with a Lorentzian function to extract the homogeneous linewidth which, after deconvolution with the etalon response, is $\delta_\omega = 322$ MHz. We note that fitting with a Voigt profile produced a negligible

Gaussian contribution (i.e. we did not observe any significant inhomogeneous broadening). Using the radiative recombination lifetime of $T_1 = 1.02\,\text{ns}$ from the PL decay curve (see inset in Figure 1), we calculate the width of the transform-limited spectrum from $\delta_\omega = 1/2\pi T_1$. From these two widths we obtain the ratio $2T_1/T_2 = 2$, i.e. 2x the transform limit. This value is significantly improved compared to previous measurements of quantum dots using above-band excitation[39–44], including our own nanowire devices grown at lower temperature[37]. It is also an improvement compared to measurements made using p-shell excitation[40,44]. Instead, the values here are typically observed only when the emitter is excited resonantly[22,43,45,46] and are not significantly greater than those observed in state of the art devices[8,44,47].

We note that further increases in T_s did not result in any additional reduction of the linewidths suggesting that the excess broadening is not related to defects in the shell material[48]. To rule out broadening associated with phonon dephasing, we performed both power- and temperature-dependent measurements. In Figure 2 we show the linewidth dependence on excitation power for powers up to $P = 4P_{\text{sat}}$. All power-dependent spectra show Lorentzian lineshapes (see inset) from which the homogeneous linewidths plotted in the figure are extracted. The dependence is highly nonlinear with the linewidth independent of excitation power for $P < 0.4P_{\text{sat}}$ above which strong broadening is observed.

In Figure 3 we show temperature-dependent measurements under weak pumping conditions ($P < 0.2P_{\text{sat}}$). With increasing temperature the emission peak red-shifts due to lattice dilation[49] and broadens. For temperatures up to $T = 14\,K$ the lineshape remains Lorentzian whilst for $T > 14\,K$ a slight asymmetry develops. We focus on the spectra measured for $T \leq 14\,K$ from which we can extract the homogeneous linewidths plotted in the figure. Significant broadening is observed for $T > 8\,K$ whilst for $T < 8\,K$, linewidths show only a small temperature dependence. We conclude that for sufficiently low temperatures ($T < 8\,K$) and excitation powers ($P < 0.4P_{\text{sat}}$) phonon dephasing, notwithstanding above-band excitation, is not the source of the remaining excess broadening. Instead, it likely arises from some residual inhomogeneous broadening, that either does not sufficiently alter Lorentzian lineshapes such that it can be revealed by a simple lineshape fitting procedure or that manifests as a homogeneous broadening[42].

We next consider the nonlinear behaviour observed with temperature which is in stark contrast to the linear dependence seen in earlier studies[50] that also employed non-resonant excitation[39–41,51–53]. To date, the existence of the linear broadening is accounted for in InAs/GaAs zincblende dots by considering the independent boson model[34], in which the exciton causes a renormalization of phonon modes without itself being excited by the lattice vibrations. The origin of the quadratic term, on the other hand, is traced to the virtual transitions between the ground and excited exciton states caused by

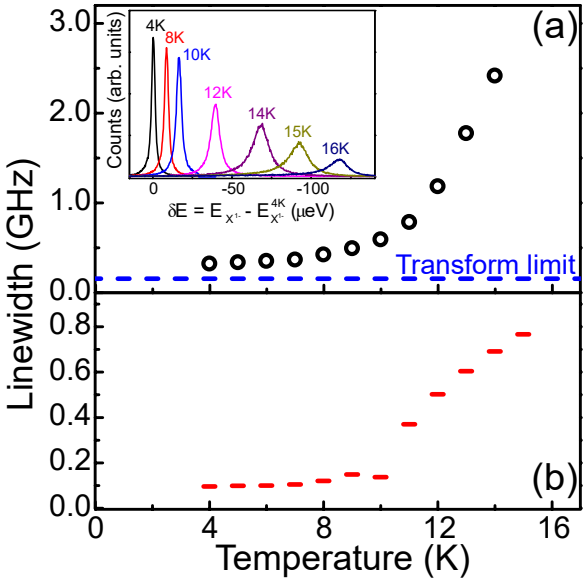

FIG. 3. (a) Deconvolved linewidth as a function of temperature in the low excitation power regime. Inset shows PL spectra, normalized to the integrated intensity, as a function of relative emission energy for selected temperatures. (b) Predicted broadening based on model described in text.

the absorption and re-emission of the phonons[33,35]. In each of these approximations, only longitudinal phonon modes are accounted for, and the main exciton-phonon coupling mechanism is taken to be the deformation potential. In addition, the virtual transitions appear to be thermally activated only above a threshold temperature (of order of 10 K), below which only the linear broadening is expected[35]. Within this general approach, it is straightforward to understand the similarity between the linewidth broadening as a function of excitation power (Figure 2) and as a function of temperature (Figure 3). Indeed, above-bandgap excitation creates electron-hole pairs in the InP continuum with energy higher than the bare bandgap. As the carriers have to thermalize before their capture by the quantum dot, increasing the excitation power is equivalent to increasing the temperature, as it leads to the increase in phonon mode population.

While we do not discount the possibility of a similar mechanism being present here, we do find that both the wurtzite lattice type of our system as well as its one-dimensional geometry suggest an alternative origin of the nonlinear linewidth broadening. Indeed, the coupling between the carriers and the phonons is expressed as $M_a^{ij}(\vec{k}) = A_a(\vec{k}) \int d^3r \psi_{ia}^*(\vec{r})\psi_{j,a}(\vec{r})e^{i\vec{k}\cdot\vec{r}}$, where the parameter $A_a(\vec{k})$ depends on the type of coupling (deformation or piezoelectric), material parameters, and phonon energy, $\vec{k}$ is the phonon wavevector, and $\psi_{i,a}(\vec{r})$ is the wave function of the carrier a (electron or hole) corresponding to the single-particle state i (Ref. 33–35). Owing to the nanowire geometry, the only phonon modes with sufficiently low energy are those propagating along

the wire, i.e., with $\vec{k} = [0, 0, k]$, while the lattice vibrations in the transverse direction are quantized with energies equivalent to hundreds of Kelvin. As a result, the longitudinal phonon modes are unlikely to cause electronic transitions (even virtual ones) since they would need to straddle the intersubband energy gaps of hundreds of meV brought about by the small height of the quantum dot. This allows us to approximate, in the low phonon energy limit, $M_a^{ij}(\vec{k}) = A_a(\vec{k})\delta_{i,j}$.

To date, the theoretical modeling of the linewidth broadening included the deformation potential as the only relevant mechanism of exciton-phonon coupling in zincblende materials[33–35]. In that mechanism, the coupling parameter for the one-dimensional phonon modes is $A_{def}(k) = \sqrt{\frac{\hbar\omega_k}{2\rho_M u_s^2 V}} D$, where the phonon energy $\hbar\omega_k = \hbar u_s k$, u_s is the speed of sound, ρ_M is the mass density, V is the phonon normalization volume, and $D = D_e - D_h$ is the deformation potential constant, expressed as the difference between the electron-phonon and hole-phonon coupling owing to the opposite signs of these charges. The piezoelectric coupling mechanism was found to be negligibly small, as it requires the shear strain tensor components, which are vanishingly small for longitudinal phonon modes. This is in contrast to the wurtzite crystal lattice, in which the piezoelectric effects enter through diagonal strain tensor element via the piezoelectric constant c_{33}. The relevant coupling parameter, adapted for the zincblende material from Ref. 34, has the form $A_{piezo}(k) = -16\pi e e_{33}\sqrt{\frac{\hbar^2}{2\rho_M \omega_k V}}$, where e is the electron charge. We note that the contributions from the electron-phonon and hole-phonon interactions add (rather than subtract as in the deformation coupling). Moreover, crucially, the piezoelectric coupling has (i) the opposite sign to that of the deformation mechanism, and (ii) a different dependence on the phonon energy, $A_{piezo}(k) \propto (\omega_k)^{-1/2}$ compared to $A_{def}(k) \propto (\omega_k)^{1/2}$. As a result, the total coupling $A(k) = A_{def}(k) + A_{piezo}(k)$ is expected to depend strongly and nonlinearly on the phonon energy.

The Hamiltonian of the exciton-phonon system accounting for the approximations discussed above is:

$$\hat{H}_{X-ph} = E_X|X\rangle\langle X| + \sum_{\vec{k}} \hbar\omega_{\vec{k}} a_{\vec{k}}^+ a_{\vec{k}} + \sum_{\vec{k}} A(|\vec{k}|)(a_{\vec{k}} + a_{\vec{k}}^+) \tag{1}$$

arising because the coupling $A(|\vec{k}|)$ depends only on the magnitude of the phonon wave vector $\vec{k} = [0, 0, k]$. Here, the operator $a_{\vec{k}}$ ($a_{\vec{k}}^+$) annihilates (creates) a phonon in mode $\vec{k}$. This independent boson model is exactly solvable in terms of displaced phonon operators $b_{\vec{k}} = a_{\vec{k}} + \Lambda_{\vec{k}}$ and $b_{\vec{k}}^+ = a_{\vec{k}}^+ + \Lambda_{\vec{k}}$, where the displacement $\Lambda_{\vec{k}} = A(k)/\hbar\omega_{\vec{k}}$. Upon this transformation, our Hamiltonian is diagonal both in the excitonic and phononic degrees of freedom and reads

$$\hat{H}_{X-ph} = E_X|X\rangle\langle X| + \sum_{\vec{k}} \hbar\omega_{\vec{k}} b_{\vec{k}}^+ b_{\vec{k}} - \sum_{\vec{k}} \hbar\omega_{\vec{k}} (\Lambda_{\vec{k}})^2. \tag{2}$$

The eigenvectors of our Hamiltonian can be written as the tensor products $|X\rangle \prod_{\vec{k}} |N_{\vec{k}}\rangle$, where the phonon Fock states $|N_{\vec{k}}\rangle = \frac{1}{\sqrt{N_{\vec{k}}!}} (b_{\vec{k}}^+)^N |0\rangle$, and the state $|0\rangle$ is the zero-phonon state for the mode $\vec{k}$.

Upon exciton recombination, we deal with the system of non-displaced phonons described simply by the Hamiltonian $\hat{H}_{ph} = \sum_{\vec{k}} \hbar\omega_{\vec{k}} a_{\vec{k}}^+ a_{\vec{k}}$ with eigenstates in the form of non-displaced phonon Fock states $|n_{\vec{k}}\rangle = \frac{1}{\sqrt{n_{\vec{k}}!}} (a_{\vec{k}}^+)^n |0\rangle$. Working with the Fock phonon configurations, both in the initial and final states of the system, and considering only one phonon mode with energy $\hbar\omega_{\vec{k}}$, we can now derive the emission spectrum in the form of a series of maxima found at energies

$$E(N_{\vec{k}}, n_{\vec{k}}, \Lambda_{\vec{k}}) = E_X - \hbar\omega_{\vec{k}} (\Lambda_{\vec{k}})^2 + \hbar\omega_{\vec{k}} (N_{\vec{k}} - n_{\vec{k}}). \tag{3}$$

The radiative transitions can be accompanied by phonon emission ($N_{\vec{k}} < n_{\vec{k}}$) or phonon absorption ($N_{\vec{k}} > n_{\vec{k}}$), placing the relevant maxima on the lower or higher side of the zero phonon line, respectively. However, owing to the very small energy scale of the relevant phonon modes, the emission spectrum will be seen as a single, broadened peak, whose intensity will be modulated by an envelope expressed in terms of the well-known Franck-Condon formula

$$W(N_{\vec{k}}, n_{\vec{k}}, \Lambda_{\vec{k}}) = e^{-\Lambda_{\vec{k}}^2} \Lambda_{\vec{k}}^{2(n_{\vec{k}} - N_{\vec{k}})} \frac{N_{\vec{k}}!}{n_{\vec{k}}!} \left[L_{N_{\vec{k}}}^{n_{\vec{k}} - N_{\vec{k}}} (\Lambda_{\vec{k}}^2) \right]^2, \tag{4}$$

where $n_{\vec{k}} \geq N_{\vec{k}}$ and $L_n^m(x)$ is the associated Laguerre polynomial (for $n_{\vec{k}} < N_{\vec{k}}$ the indices are interchanged).

The emission spectrum as a function of temperature T and accounting for statistical occupation of the phonon modes is computed as a weighted superposition of the single-mode spectra. Upon normalization by the zero-phonon line intensity, we have:

$$I(\hbar\omega, T) \propto \sum_{\vec{k}} \frac{1}{I_0(\vec{k})} \sum_{N_{\vec{k}}} \sum_{n_{\vec{k}}} p(N_{\vec{k}}, T) W(N_{\vec{k}}, n_{\vec{k}}, \Lambda_{\vec{k}}) \times \delta(\hbar\omega - E(N_{\vec{k}}, n_{\vec{k}}, \Lambda_{\vec{k}})), \tag{5}$$

with $\hbar\omega$ being the measured photon energy. Here, we consider all possible initial and final occupations of each phonon mode $\vec{k}$, weighted by the probabilities $p(N_{\vec{k}}, T) = \exp\left(-\frac{N_{\vec{k}}\hbar\omega_{\vec{k}}}{k_B T}\right) / Z(\vec{k})$, where the statistical sum $Z(\vec{k}) = \sum_{n=0}^{\infty} \exp\left(-\frac{n\hbar\omega_{\vec{k}}}{k_B T}\right)$, and k_B is the Boltzmann constant. The modal zero-phonon line intensity is $I_0(\vec{k}) = \sum_{N_{\vec{k}}} p(N_{\vec{k}}, T) |\langle n_{\vec{k}} = N_{\vec{k}} | N_{\vec{k}} \rangle|^2$. Our approach takes into account the fact that, calculated individually, the low occupations of any given phonon mode $\vec{k}$ are exponentially more probable than the high occupations, and therefore give more contribution to the overall emission spectrum.

We propose that the experimentally observed nonlinearity of the emission peak broadening is captured by our model – even without the virtual excitation scheme

– in two aspects. The first, crucial aspect is the dependence of the displacement parameter $\Lambda_{\vec{k}}$ on the phonon mode energy $\hbar\omega_{\vec{k}}$. We have $\Lambda_{\vec{k}} = \Lambda_{\vec{k}}^{(def)} - \Lambda_{\vec{k}}^{(piezo)} = \Lambda_0^{(def)}(\hbar\omega_{\vec{k}})^{-1/2} - \Lambda_0^{(piezo)}(\hbar\omega_{\vec{k}})^{-3/2}$, where $\Lambda_0^{(def)}$ and $\Lambda_0^{(piezo)}$ are energy-independent material constants describing the two coupling mechanisms, respectively. Even if the piezoelectric coupling constant is smaller than the deformation one, at sufficiently small phonon energies these two terms will cancel each other out, giving the overall displacement parameter of zero. As the material parameters for wurtzite InAs and InP are not yet known, our experimental data suggest that this cancellation occurs most likely for phonon energies of order of 0.1 μeV, resulting in the very small emission peak broadening for low temperatures. On the other hand, at higher phonon energies the piezoelectric contribution to the parameter $\Lambda_{\vec{k}}$ decays faster than the deformation one, resulting in an effective, nonlinear increase of that parameter. As a result, the higher-energy modes, which become more populated at higher temperatures, cause the peak broadening visible at higher temperatures.

The crossover between the two regimes is systematically accounted for by the second aspect of our model, i.e., the mode occupation probabilities $p(N_{\vec{k}}, T)$. As already mentioned, at low temperatures these probabilities strongly favour low-energy modes occupied with few phonons, for which the effective exciton-phonon coupling is negligibly small due to the cancellation discussed above. However, as the temperature increases, the probabilities are redistributed towards increasing occupations of more energetic phonon modes, which are more strongly coupled to the exciton. As a result, these higher modes contribute more to the emission spectrum, resulting in the nonlinear increase of the peak broadening.

We illustrate the above theoretical model with a calculation accounting for four phonon modes, with energies $\hbar\omega_{\vec{k}} = 0.25$ μeV, 0.5 μeV, 1 μeV, and 2 μeV. We chose the following dependence of the displacement parameter on the mode energy: $\Lambda(\varepsilon) = A_0\left(\varepsilon^{-1/2} - \varepsilon^{-3/2}\right)$, where $\varepsilon = \hbar\omega_{\vec{k}}/\varepsilon_0$, $\varepsilon_0 = 0.1$ μeV, and A_0 was taken as a model value of 0.2. This functional form follows directly from the subtraction of the deformation and piezoelectric contributions, and was adjusted to vanish for $\hbar\omega_{\vec{k}} = 0.1$ μeV. We generated the emission spectra at a grid of photon energies with step of 2 μeV on both sides of the zero-phonon line, but we excluded the zero phonon line itself, as its emission peak contains contributions from all phonon modes present in the system and therefore would be poorly reproduced by our model. The FWHM obtained by fitting the resulting emission peak by a Lorentzian is presented in Figure 3. Unsurprisingly, the theoretical approach, accounting only for four modes, underestimates the line broadening, but reproduces the experimental temperature trend qualitatively.

In summary, we have shown that it is possible to generate near-transform-limited photons from quantum dots, even when excited above-band, by using structures that eliminate many potential broadening mechanisms. The drastic reduction in excess broadening revealed a non-linear temperature dependence that can be fully described within an independent Boson model that considers both deformation and piezoelectric coupling mechanisms, the latter expected to be more important in these wurtzite structures compared to the more typical zincblende quantum dots.

This work was supported by Natural Sciences and Engineering Research Council of Canada

* plaferr3@uottawa.ca

[1] J. L. O'Brien, A. Furusawa, and J. Vučković, "Photonic quantum technologies," Nat. Photon. **3**, 687 (2009).

[2] I. Aharonovich, D. Englund, and M. Toth, "Solid-state single-photon emitters," Nat. Photonics **10**, 631–641 (2016).

[3] P. Senellart, G. Solomon, and A. White, "High-performance semiconductor quantum-dot single-photon sources," Nat. Nanotech. **12**, 1026 (2017).

[4] H. Vural, S. L. Portalupi, and P. Michler, "Perspective of self-assembled InGaAs quantum-dots for multi-source quantum implementations," Appl. Phys. Lett. **117**, 030501 (2020).

[5] J.-M. Gérard and B. Gayral, "Strong purcell effect for InAs quantum boxes in three-dimensional solid-state microcavities," J. Lightwave Tech. **17**, 2089 (1999).

[6] X. Ding, Y. He, Z.-C. Duan, N. Gregersen, M.-C. Chen, S. Unsleber, S. Maier, C. Schneider, M. Kamp, S. Höfling, C.-Y. Lu, and J.-W. Pan, "On-demand single photons with high extraction efficiency and near-unity indistinguishability from a resonantly driven quantum dot in a micropillar," Phys. Rev. Lett. **116**, 020401 (2016).

[7] A. Muller, E. B. Flagg, P. Bianucci, X.Y. Wang, D. G. Deppe, W. Ma, J. Zhang, G. J. Salamo, M. Xiao, and C. K. Shih, "Resonance fluorescence from a coherently driven semiconductor quantum dot in a cavity," Phys. Rev. Lett. **99**, 187402 (2007).

[8] H. Wang, Z.-C. Duan, Y.-H. Li, Si Chen, J.-P. Li, Y.-M. He, M.-C. Chen, Y. He, X. Ding, C.-Z. Peng, C. Schneider, M. Kamp, S. Höfling, C.-Y. Lu, and J.-W. Pan, "Near-transform-limited single photons from an efficient solid-state quantum emitter," Phys. Rev. Lett. **116**, 213601 (2016).

[9] N. Tomm, A. Javadi, N. O. Antoniadis, D. Najer, M. C. Löbl, Al. R. Korsch, R. Schott, S. R. Valentin, A. D. Wieck, A. Ludwig, and R. J. Warburton, "A bright and fast source of coherent single photons," Nature Nano. **16**, 399 (2021).

[10] We note that since pulsed excitation, required for on-demand operation, is spectrally broader compared to CW excitation, it is less effective in mitigating linewidth broadening, .

[11] R. B. Patel, A. J. Bennett, I. Farrer, C. A. Nicoll, D. A. Ritchie, and A. J. Shields, "Two-photon interference of the emission from electrically tunable remote quantum dots,"

Nat. Photonics **4**, 632 (2010).
[12] E. B. Flagg, A. Muller, S. V. Polyakov, A. Ling, A. Migdall, and Glenn S. Solomon, "Interference of single photons from two separate semiconductor quantum dots," Phys. Rev. Lett. **104**, 137401 (2010).
[13] W.B. Gao, P. Fallahi, E. Togan, A. Delteil, Y.S. Chin, J. Miguel-Sanchez, and A. Imamoğlu, "Quantum teleportation from a propagating photon to a solid-state spin qubit," Nature Commun. **4**, 2744 (2016).
[14] P. Gold, A. Thoma, S. Maier, S. Reitzenstein, C. Schneider, S. Höfling, and M. Kamp, "Two-photon interference from remote quantum dots with inhomogeneously broadened linewidths," Phys. Rev. B **89**, 035313 (2014).
[15] V. Giesz, S. L. Portalupi, T. Grange, C. Antón, L. De Santis, J. Demory, N. Somaschi, I. Sagnes, A. Lemaître, L. Lanco, A. Auffeves, and P. Senellart, "Cavity-enhanced two-photon interference using remote quantum dot sources," Phys. Rev. B **92**, 161302 (2015).
[16] M. Reindl, K. D. Jöns, D. Huber, C. Schimpf, Y. Huo, V. Zwiller, A. Rastelli, and R. Trotta, "Phonon-assisted two-photon interference from remote quantum emitters," Nano Lett. **17**, 4090–4095 (2017).
[17] J. H. Weber, J. Kettler, H. Vural, M. Müller, J. Maisch, M. Jetter, S. L. Portalupi, and P. Michler, "Overcoming correlation fluctuations in two-photon interference experiments with differently bright and independently blinking remote quantum emitters," Phys. Rev. B **97**, 195494 (2018).
[18] H. D. Robinson and B. B. Goldberg, "Light-induced spectral diffusion in single self-assembled quantum dots," Phys. Rev. B **61**, R5086 (2000).
[19] B. D. Gerardot, R. J. Barbour, D. Brunner, A. Badolato P. A. Dalgarno and, N. Stoltz, P. M. Petroff, J. Houel, and R. J. Warburton, "Laser spectroscopy of individual quantum dots charged with a single hole," Appl. Phys. Lett. **99**, 243112 (2011).
[20] C. F. Wang, A. Badolato, P. M. Petroff I. Wilson-Rae and, and E. Hu, "Optical properties of single InAs quantum dots in close proximity to surfaces," Appl. Phys. Lett. **85**, 3423 (2004).
[21] J. Liu, K. Konthasinghe, M. Davanço, J. Lawall, V. Anant, V. Verma, R. Mirin, S. W. Nam, J. D. Song, B. Ma, Z. S. Chen, H. Q. Ni, Z. C. Niu, and K. Srinivasan, "Single self-assembled InAs/GaAs quantum dots in photonic nanostructures: The role of nanofabrication," Phys. Rev. Appl. **9**, 064019 (2018).
[22] J. Houel, A. V. Kuhlmann, L. Greuter, F. Xue, M. Poggio, B. D. Gerardot, P. A. Dalgarno, A. Badolato, P. M. Petroff, A. Ludwig, D. Reuter, A. D. Wieck, and R. J. Warburton, "Probing single-charge fluctuations at a GaAs/AlAs interface using laser spectroscopy on a nearby ingaas quantum dot," Phys. Rev. Lett. **108**, 107401 (2012).
[23] M. B. Bavinck, K. D. Jöns, M. Zieliński, G. P., J.-C. Harmand, N. Akopian, and V. Zwiller, "Photon cascade from a single crystal phase nanowire quantum dot," Nano Lett. **16**, 1081–1085 (2016).
[24] D. Dalacu, P. J. Poole, and R. L. Williams, "Nanowire-based sources of non-classical light," Nanotechnology **30**, 232001 (2019).
[25] P. Laferrière, E. Yeung, I. Miron, D. B. Northeast, S. Haffouz, J. Lapointe, M. Korkusinski, P. J. Poole, R. L. Williams, and D. Dalacu, "Unity yield of deterministically positioned quantum dot single photon sources," Sci. Rep. **12**, 6376 (2022).
[26] C. P. Dietrich, A. Fiore, M. G. Thompson, M. Kamp, and S. Höfling, "Gaas integrated quantum photonics: Towards compact and multi-functional quantum photonic integrated circuits," Laser and Photon. Rev. **10**, 870 (2016).
[27] J. Claudon, J. Bleuse, N. S. Malik, M. Bazin, P. Jaffrennou, N. Gregersen, C. Sauvan, P. Lalanne, and J.-M. Gérard, "A highly efficient single-photon source based on a quantum dot in a photonic nanowire," Nat. Photon. **4**, 174 (2010).
[28] C. A. Hoffman, H. J. Gerritsen, and A. V. Nurmikko, "Study of surface recombination in GaAs and InP by picosecond optical techniques," J. Appl. Phys. **51**, 1603 (1980).
[29] M. Borgström, V. Zwiller, E. Müller, and A. Imamoglu, "Optically bright quantum dots in single nanowires," Nano Lett. **5**, 1439–1443 (2005).
[30] M. C. Löbl, S. Scholz, I. Söllner, J. Ritzmann, T. Denneulin, A. Kovács, B. E. Kardynał, A. D. Wieck, A. Ludwig, and R. J. Warburton, "Excitons in InGaAs quantum dots without electron wetting layer states," Commun. Phys. **2**, 93 (2018).
[31] P. Laferrière, E. Yeung, L. Giner, S. Haffouz, J. Lapointe, G. C. Aers, P. J. Poole, R. L. Williams, and D. Dalacu, "Multiplexed single-photon source based on multiple quantum dots embedded within a single nanowire," Nano Lett. **20**, 3688–3693 (2020).
[32] P. Borri, W. Langbein, U. Woggon, V. Stavarache, D. Reuter, and A. D. Wieck, "Exciton dephasing via phonon interactions in InAs quantum dots: Dependence on quantum confinement," Phys. Rev. B **71**, 115328 (2005).
[33] A. Reigue, J. Iles-Smith, F. Lux, L. Monniello, M. Bernard, F. Margaillan, A. Lemaitre, A. Martinez, D. P. S. McCutcheon, J. Mørk, R. Hostein, and V. Voliotis, "Probing electron-phonon interaction through two-photon interference in resonantly driven semiconductor quantum dots," Phys. Rev. Lett. **118**, 233602 (2017).
[34] T. Takagahara, "Theory of exciton dephasing in semiconductor quantum dots," Phys. Rev. B **60**, 2638 (1999).
[35] E. A. Muljarov and R. Zimmermann, Phys. Rev. Lett. **93**, 237401 (2004).
[36] D. Dalacu, K. Mnaymneh, X. Wu, J. Lapointe, G. C. Aers, P. J. Poole, and R. L. Williams, "Selective-area vapor-liquid-sold growth of tunable InAsP quantum dots in nanowires," Appl. Phys. Lett. **98**, 251101 (2011).
[37] M. E. Reimer, G. Bulgarini, A. Fognini, R. W. Heeres, B. J. Witek, M. A. M. Versteegh, A. Rubino, T. Braun, M. Kamp, S. Höfling, D. Dalacu, J. Lapointe, P. J. Poole, and V. Zwiller, "Overcoming power broadening of the quantum dot emission in a pure wurtzite nanowire," Phys. Rev. B **93**, 195316 (2016).
[38] D. Dalacu, A. Kam, D. G. Austing, X. Wu, J. Lapointe, G. C. Aers, and P. J. Poole, "Selective-area vapour-liquid-solid growth of InP nanowires," Nanotech. **20**, 395602 (2009).
[39] D. Birkedal, K. Leosson, and J. M. Hvam, "Long lived coherence in self-assembled quantum dots," Phys. Rev. Lett. **87**, 227401 (2001).
[40] M. Bayer and A. Forchel, "Temperature dependence of the exciton homogeneous linewidth in $In_{0.60}Ga_{0.40}As/GaAs$ self-assembled quantum dots," Phys. Rev. B **65**, 041308(R) (2002).
[41] B. Urbaszek, E. J. McGhee, M. Krüger, R. J. Warburton, K. Karrai, T. Amand, B. D. Gerardot, P. M. Petroff, and J. M. Garcia, "Temperature-dependent linewidth of

charged excitons in semiconductor quantum dots: Strongly broadened ground state transitions due to acoustic phonon scattering," Phys. Rev. B **69**, 035304 (2004).

[42] A. Berthelot, I. Favero, G. Cassabois, C. Voisin, C. Delalande, Ph. Roussignol, R. Ferreira, and J. M. Gérard, "Unconventional motional narrowing in the optical spectrum of a semiconductor quantum dot," Nature Physics **2**, 759 (2006).

[43] A. V. Kuhlmann, J. Houel, A. Ludwig, L. Greuter, D. Reuter, A. D. Wieck, M. Poggio, and R. J. Warburton, "Charge noise and spin noise in a semiconductor quantum device," Nature Photonics **9**, 570 (2013).

[44] Y.-M. He, Y. He, Y.-J. Wei, D. Wu, M. Atatüre, C. Schneider, S. Höfling, M. Kamp, C.-Y. Lu, and J.-W. Pan, "On-demand semiconductor single-photon source with near-unity indistinguishability," Nat. Nano. **8**, 213–217 (2013).

[45] A. Högele, S. Seidl, M. Kroner, K. Karrai, R. J. Warburton, B. D. Gerardot, and P. M. Petroff, "Voltage-controlled optics of a quantum dot," Phys. Rev. Lett. **93**, 217401 (2004).

[46] M. Atatüre, J. Dreiser, A. Badolato, A. Högele, K. Karrai, and A. Imamoglu, "Quantum-dot spin-state preparation with near-unity fidelity," Science **312**, 551 (2006).

[47] A. V. Kuhlmann, J. H. Prechtel, J. Houel, A. Ludwig, D. Reuter, A. D. Wieck, and R. J. Warburton, "Transform-limited single photons from a single quantum dot," Nat. Commun. **6**, 8204 (2015).

[48] We note that we observe an increase in the axial growth rate with increasing temperature (see Figure 1(a)) in contrast to previous experiments[38] where the axial growth was quenched at $\sim 450^{\circ}$C. This is likely due to a higher Group V flux used for the shell growth in these experiments and raises the possibility of improving the material quality of the nanowire core by growing it at higher temperatures., .

[49] Y.P. Varshni, "Temperature dependence of the energy gap in semiconductors," Physica **34**, 149 (1967).

[50] We note that in these studies the excess broadening was significantly greater than that presented here and has been described in terms of phonon scattering from sidewalls and interfaces[54]., .

[51] L. Besombes, K. Kheng, L. Marsal, and H. Mariette, "Acoustic phonon broadening mechanism in single quantum dot emission," Phys. Rev. B **63**, 155307 (2001).

[52] G. Ortner, D. R. Yakovlev, M. Bayer, S. Rudin, T. L. Reinecke, S. Fafard, Z. Wasilewski, and A. Forchel, "Temperature dependence of the zero-phonon linewidth in In(Ga)As/(Al)GaAs quantum dots," Phys. Rev. B **70**, 201301 (2004).

[53] I. Favero, A. Berthelot, G. Cassabois, C. Voisin, C. Delalande, Ph. Roussignol, R. Ferreira, and J.-M. Gérard, "Temperature dependence of the zero-phonon linewidth in quantum dots: An effect of the fluctuating environment," Phys. Rev. B **75**, 073308 (2007).

[54] S. Rudin, T. L. Reinecke, and M. Bayer, "Temperature dependence of optical linewidth in single InAs quantum dots," Phys. Rev. B **74**, 161305(R) (2006).

Chapter 9

Article 5: Multiplexed Single-Photon Source Based on Multiple Quantum Dots Embedded within a Single Nanowire

This chapter contains the following article:

P. Laferrière, E. Yeung, L. Giner, S. Haouz, J. Lapointe, G. C. Aers, P. J. Poole, R. L. Williams, & D. Dalacu, "Multiplexed Single-Photon Source Based on Multiple Quantum Dots Embedded within a Single Nanowire", Nano Letters **20**, 3688-3693 (2020).

DOI: https://doi.org/10.1021/acs.nanolett.0c00607

pubs.acs.org/NanoLett Letter

Multiplexed Single-Photon Source Based on Multiple Quantum Dots Embedded within a Single Nanowire

Patrick Laferrière,* Edith Yeung, Lambert Giner, Sofiane Haffouz, Jean Lapointe, Geof C. Aers, Philip J. Poole, Robin L. Williams, and Dan Dalacu

Cite This: *Nano Lett.* 2020, 20, 3688–3693 Read Online

ACCESS | Metrics & More | Article Recommendations

ABSTRACT: Photonics-based quantum information technologies require efficient, high emission rate sources of single photons. Position-controlled quantum dots embedded within a broadband nanowire waveguide provide a fully scalable route to fabricating highly efficient single-photon sources. However, emission rates for single-photon devices are limited by radiative recombination lifetimes. Here, we demonstrate a multiplexed single-photon source based on a multidot nanowire. Using epitaxially grown nanowires, we incorporate multiple energy-tuned dots, each optimally positioned within the nanowire waveguide, providing single photons with high efficiency. This linear scaling of the single-photon emission rate with number of emitters is demonstrated using a five-dot nanowire with an average multiphoton emission probability of <4% when excited at saturation. This represents the first ever demonstration of multiple single-photon emitters deterministically incorporated in a single photonic device and is a major step toward achieving GHz single-photon emission rates from a scalable multi-quantum-dot system.

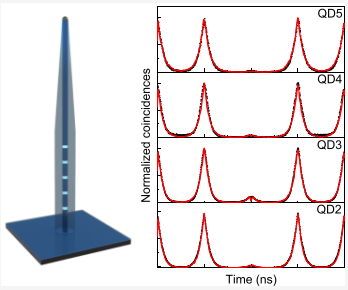

KEYWORDS: *quantum dot, nanowire, single-photon source, multiplexing*

Sources of quantum light are an important resource in many quantum information processing applications, including quantum key distribution (QKD)[1] and linear optical quantum computing (LOQC).[2] Single-photon sources based on semiconductor quantum dots offer close to ideal performance in terms of efficiency and suppression of multiphoton emission probabilities.[3−6] Emission rates, however, are limited by the radiative lifetimes of the excitonic complexes from which the quantum light is generated. Higher rates can be obtained via Purcell enhancement of the radiative decay using 3D microcavities[7] but will be limited by the onset of strong coupling effects,[8] undesired in certain applications.

An alternative approach, based on active multiplexing, has been proposed to overcome the fundamental limitations inherent to probabilistic sources based on parametric down-conversion.[9] For example, frequency multiplexing has been demonstrated using heralded sources from broadband spontaneous parametric down-conversion in a periodically poled lithium niobate crystal.[10] Using Bragg scattering four-wave mixing for frequency translation, the authors multiplexed three frequency modes generated by the crystal. Frequency multiplexed single-photon sources based on single emitters (i.e., suitable for on-demand operation) have also been demonstrated.[11] The sources were based on single quantum dots deterministically incorporated in bottom-up photonic nanowires,[12,13] with the emission from two dots in two separate nanowires coupled to the same ridge waveguide using a pick and place approach.[14] Frequency multiplexed sources that offer higher single-photon count rates are desirable in applications which do not require the photons to be indistinguishable, for example, QKD based on the BB84 protocol.[1] Furthermore, combining a frequency multiplexed source with the recently demonstrated technique for frequency converting a single-photon source[15] allows one to envision applications that also require the photons to be indistinguishable, such as measurement-device-independent QKD[16] or LOQC.[2]

A unique feature of bottom-up grown nanowires is the ability to incorporate multiple quantum dot emitters in the same nanowire, each optimally positioned for maximum coupling to the same optical mode supported by the photonic nanowire waveguide.[17,18] In this work, we use this ability to deterministically incorporate multiple frequency-tuned InAsP quantum dot emitters within the same InP photonic nanowire. We show that each dot emits single photons, and owing to the broadband operation of nanowire sources[19] combined with the optimal positioning of each emitter, the photon emission rate scales linearly with the number of emitters, an important step

Received: February 13, 2020
Revised: March 18, 2020
Published: April 9, 2020

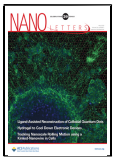

https://dx.doi.org/10.1021/acs.nanolett.0c00607
Nano Lett. 2020, 20, 3688−3693

toward the development of high repetition rate single-photon sources.

Scanning electron microscope (SEM) images of the nanowire sources used in this work are shown in Figure 1.

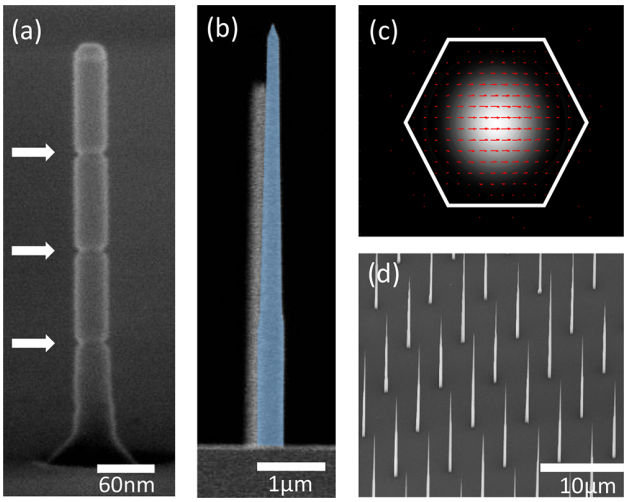

Figure 1. (a) SEM image of an InP nanowire core with three embedded InAsP quantum dots indicated by arrows. The dots were delineated using a H_2SO_4 dip, which selectively etches arsenic-containing sections. (b) SEM image of the photonic nanowire (i.e., a nanowire core after shell growth). (c) Calculated electric field intensity of one of the two degenerated HE_{11} modes supported by the photonic nanowire. (d) SEM showing an array of site-controlled photonic nanowires.

The sources are fabricated by first growing an InP nanowire core into which are embedded InAsP quantum dots (Figure 1a). The quantum dots are separated by InP spacers with thicknesses of >50 nm to avoid dot−dot electronic coupling.[17,18] The nanowire core is then clad[13] to produce the photonic nanowire waveguide (Figure 1b), with a diameter tailored to optimally couple the dot emission to the two degenerate orthogonally polarized HE_{11} waveguide modes. The electric field intensity of one of these modes is shown in Figure 1c, with the red arrows indicating the direction of the electric field. The top section of the cladding is tapered to increase the coupling to the external optics, producing devices with collection efficiencies in excess of 40%.[20] Ground-state emission occurs at $\lambda \sim 950$ nm with near-transform-limited line widths of 4 μeV[20] and mean fine structure splittings of ∼3 μeV.[21] Further details of the nanowire growth are given below.

In order to use the embedded quantum dots for wavelength multiplexing, the emission energy of each dot needs to be controlled and distinguished from its neighbors. This is achieved by adjusting the composition of each dot using AsH_3 flow rates.[22] We first calibrate the emission wavelength dependence on AsH_3 flow using a three-dot nanowire where the flow is increased from 20 to 25% (measured as a percent of a 5 sccm flow meter) for each subsequently incorporated dot. The ground-state emission wavelengths for each flow were determined from low-temperature photoluminescence (PL) measurements using above-band continuous-wave (cw) excitation (see below). The emission wavelengths from measurements on 19 three-dot nanowires (57 quantum dots) are summarized in the histograms of Figure 2a. The observed distribution of ground-state emission wavelengths for nominally identical quantum dots is typical of the nanowire system.[22,23] We attribute the variation to a dependence of the ground-state emission wavelength on the distribution of arsenic atoms in the dilute quantum dot system[24] as well as the distribution in gold catalyst size.[25] Using the resulting calibration curve (Figure 2b), a five-dot sample was grown targeting a spectral separation of 15 nm (chosen to clearly identify which line corresponds to which dot in the nanowire assuming an inhomogeneous broadening of ∼10 nm observed in the histograms of Figure 2a).

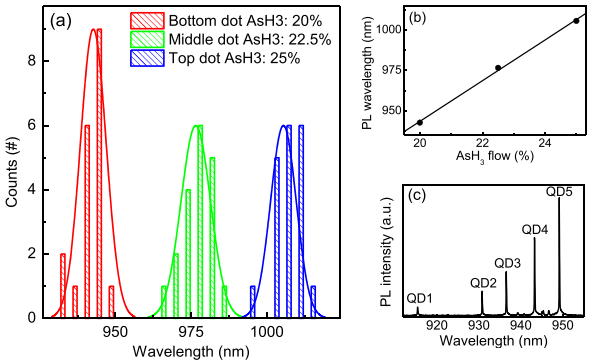

Figure 2. (a) Histograms of the emission wavelengths of 57 quantum dots from photoluminescence measurements of 19 three-dot nanowires. (b) Calibration of the emission wavelength dependence on AsH_3 flow obtained from the data in (a). (c) Photoluminescence spectrum using cw excitation of a single nanowire (NW A) with five quantum dots. The dot number indicates the position of the dot in the nanowire, with QD1 being at the bottom and QD5 at the top.

A PL spectrum of a five-dot nanowire (NW A) pumped using cw excitation is shown in Figure 2c. Five peaks are visible, and the dot associated with each peak has been labeled according to its position within the nanowire, with QD1 at the bottom and QD5 at the top. Although the total wavelength range covered is consistent with that expected from the calibration measurements, QD2−QD5 are clustered toward longer wavelengths and are separated by ∼7 nm, that is, a factor of 2 smaller than expected. This may be due to initial arsenic loading in the catalyst upon the first exposure to AsH_3. Nonetheless, Figure 2c demonstrates the required frequency control to achieve frequency multiplexed operation.

We look next at the photon statistics of the emission from a multidot nanowire. In this case, we choose a nanowire from the same growth with quantum dot emission lines at λ = 915, 929, 931, 941, and 951 nm (NW B, Figure 3a). We first determine the excitation power required to saturate the individual transitions from power-dependent PL measurements using above-band pulsed excitation at a repetition rate of 80 MHz (see below). All transitions were observed to saturate at approximately the same excitation power ($P_{sat} \sim 1$ μW), and the detected count rate at saturation of each dot, N_{sat}, was approximately equal (see Figure 3b). This suggests that both excitation and collection efficiency are not strongly dependent on the dot position or wavelength.

The pulsed second-order correlation function of each dot, $g^{(2)}(\tau)$, was measured using a fiber-coupled Hanbury−Brown and Twiss (HBT) configuration.[26] The nanowire emission was coupled to a single-mode fiber and directed to a tunable, fiber-coupled filter to select the transition to be measured. The isolated transition line was sent to two fiber-coupled silicon

https://dx.doi.org/10.1021/acs.nanolett.0c00607
Nano Lett. 2020, 20, 3688−3693

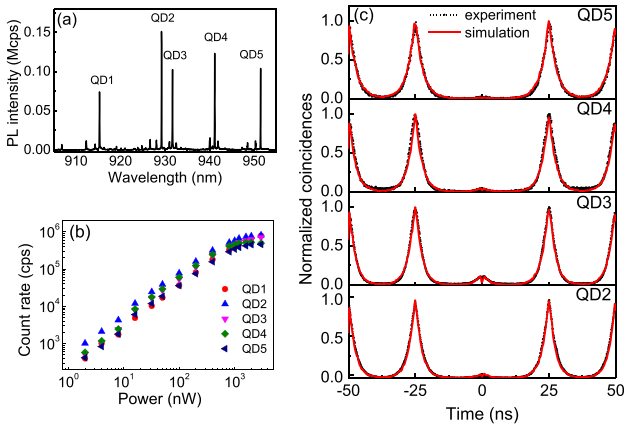

Figure 3. (a) PL spectrum of NW B measured at an excitation power P_{sat} = 1 μW using pulsed excitation at 80 MHz. (b) Power-dependent detected count rate for each dot line in (a). (c) Second-order correlation function using pulsed excitation at 40 MHz of quantum dots QD2, QD3, QD4, and QD5 in NW B measured at P_{sat} = 1 μW. Solid red curves are model fits.

single-photon avalanche photodiodes (APDs) using a 50:50 fiber-coupled beamsplitter (see below). Of the five quantum dot lines seen in the emission from the nanowire, only the four at longer wavelengths were addressable by the tuning range of the filter. The second-order correlation function from these four lines are shown in Figure 3c, measured at an excitation power of P_{sat} = 1 μW (i.e., where the count rates are highest).

Each quantum dot shows strong antibunching, with $g^{(2)}(0) < 0.5$ indicating that they are all operating as single-photon emitters. The background-corrected coincidences in the zero-delay peak normalized to the side peaks for the four addressable dots are shown in Table 1. No systematic

Table 1. Background-Corrected $g^{(2)}(\tau)$ in the Zero-Delay Peak for the Four Dots in NW B at Different Excitation Powers

power	QD2	QD3	QD4	QD5
$0.5P_{sat}$	0.016	0.051	0.026	0.010
P_{sat}	0.029	0.094	0.023	0.012
$2P_{sat}$	0.056	0.165	0.060	0.021

dependence of the coincidence counts in the zero-delay peak on the position of the dot in the nanowire is evident. The middle quantum dot (QD3) does show a markedly higher value than the others, suggesting that absorption of photons emitted from higher-energy dots may be contributing to the counts at zero-delay for this particular dot (discussed below).

In Figure 4, we plot the total count rate detected at saturation, $N_T = \sum_1^n N_{sat}$, as a function of the number of emitters, n, incorporated in the nanowire, where N_{sat} is taken from Figure 3b. The total detected count rate for this source (i.e., with five emitters) is N_T > 2.2 Mcps. Moreover, the linear scaling versus emitter number demonstrates equal collection efficiency from each dot. Based on the average single-photon purity of the emitters given in Table 1, we estimate a single-photon count rate from the multiplexed source of $0.961nN_{sat}$ (i.e., limited only by the number of incorporated emitters).

We discuss next the dot-dependent probability of detecting multiple photons per excitation pulse, which varies from 1 to 9% when pumping at saturation. All four dots in Figure 3c

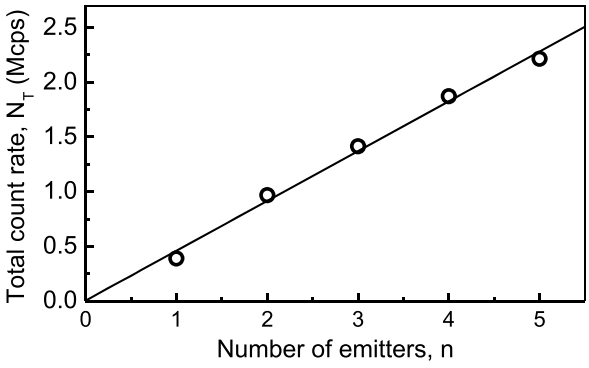

Figure 4. Total detected count rate, N_T, from Figure 3b as a function of the number of quantum dot emitters incorporated in the nanowire, n.

show coincidence counts that approach zero at τ = 0, limited by the timing resolution of the detectors. This demonstrates a very low background emission from other sources in the nanowire system. Moving in time away from τ = 0, the coincidence counts increase and then decay. This is associated with re-emission of photons from the quantum dot and varies from dot to dot. The re-emission is seen more clearly in Figure 5, where we plot the power-dependent $g^{(2)}(\tau)$ for QD3.

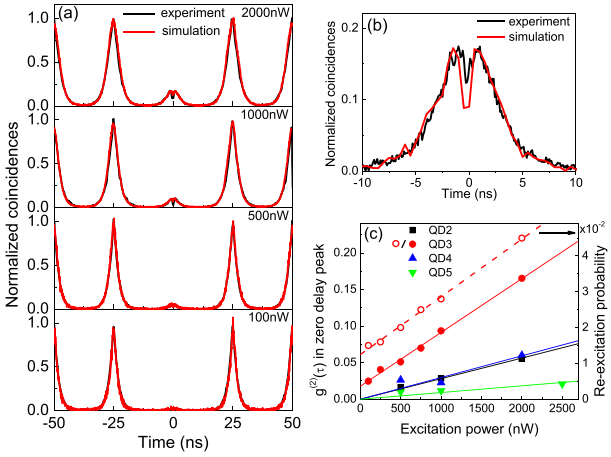

Figure 5. (a) Excitation power-dependent second-order correlation function for QD3 in NW B. Solid red curves are model fits. (b) $g^{(2)}(\tau)$ measured at $P = 2P_{sat}$, showing the short-delay bunching. (c) Power-dependent $g^{(2)}(\tau)$ in the zero-delay peak for the four quantum dots (solid symbols) and re-excitation probability extracted from the model for quantum QD3 (open red circles).

This type of re-emission has been associated with re-excitation of the quantum dot after the initial radiative decay by carriers generated during the same excitation pulse.[27,28] Re-excitation processes are typically observed when using above-band pumping, which produces an excess carrier density within the dot matrix (i.e., in the InP) that is available to repopulate the dot. This process will be excitation-power-dependent with a higher degree of re-excitation occurring at higher pump power.

For the dots studied here, the re-excitation probabilities are seen to vary from dot to dot, whereas re-excitation directly from pump-generated carriers should result in equal probabilities for each dot for uniform excitation. Here, we argue

https://dx.doi.org/10.1021/acs.nanolett.0c00607
Nano Lett. 2020, 20, 3688−3693

against a nonuniform absorption of the pump (for example, carriers predominantly generated at the top of the nanowire) as that would produce a systematic variation in re-excitation probabilities based on the dot position, which is not observed. For re-excitation directly from pump-generated carriers, the probability of re-excitation will necessarily go to zero in the absence of excitation, which is the case for QDs 2, 4, and 5 but not QD3 (see Figure 5c). We believe a more likely source of re-excitation when pumping weakly is the absorption of a ground-state photon from a higher-energy dot that is resonant with an excited state of QD3.

To get a better insight into the processes responsible for the zero-delay counts, we simulate the re-excitation process using a stochastic model to describe the exciton emission and detection processes with re-excitation included as a competition between the barrier material band to band decay rate, the carrier capture rate into the dot, and the radiative decay rate of the dot (for details, see below and also ref 29). The model applies to re-excitation from both carriers directly generated by the pump as well as reabsorption of photons emitted by other dots, with the capture rate in the latter interpreted as an absorption probability. The simulated correlations, convoluted with the detector response, are plotted in Figure 3c (solid red curves) and are in good agreement with the measured spectra, reproducing both the $\tau = 0$ dip and the re-excitation peaks at short delay.

We apply the model to the power-dependent correlations for QD3, which demonstrated the highest $g^{(2)}(\tau)$ in the zero-delay peak of the four dots. The fits are shown in Figure 5a for pump powers of 0.1 to $2P_{sat}$ and a close-up of the counts near zero-delay for $2P_{sat}$ in Figure 5b. The power-dependent re-excitation probability extracted from the model is shown in Figure 5c (open red symbols) together with the measured power-dependent $g^{(2)}(\tau)$ in the zero-delay peak corrected for background counts (solid red symbols). From a linear fit to the data, we extract a finite probability of re-excitation at a zero pump power of 0.012 for QD3. This nonzero re-excitation probability in the limit where the pump power is extremely low is consistent with a re-excitation process based on the absorption of photons emitted by the other dots.

Although photon-mediated interactions between quantum dots is of interest in other photonic-based quantum technologies,[30] here, it is undesirable and should be minimized. This can be achieved, for example, by engineering the quantum dots to have large ground- to excited-state splittings,[24,25] such that there is no overlap between the ground states of the higher energy dots with any excited states of lower-energy dots.

In conclusion, we have demonstrated controlled emission wavelength tuning of individual quantum dots in a single nanowire with each dot emitting single photons. As each dot is optimally coupled to the fundamental waveguide mode of the nanowire, they behave as independent single-photon sources with approximately equal efficiencies, evidenced by the similar count rates at saturation. As a result, the total emission rate was found to scale with the number of emitters, paving the way for producing wavelength multiplexed single-photon sources where the emission rate is limited by the number of incorporated emitters. This number is limited by the spatial constraints of the system and the tuning range and line widths of the emitters. Single-photon emission in the InAs/InP nanowire system has been demonstrated for wavelengths of λ = 900 to 1300 nm,[13,22] whereas measured line widths of the excitonic transitions are 4 μeV.[20] One can therefore envision a source consisting of 30 emitters in a 2 μm length nanowire core energetically spaced by 5 meV. Given that nanowire sources have demonstrated count rates at first lens in excess of 30 Mcps using 76 MHz pulsed excitation,[20] such a source would produce single photons with an aggregate emission rate in the GHz range.

Although we have only discussed multidot single nanowires suitable for frequency multiplexing (i.e., nondegenerate dots), the ability to control the position and energy of individual emitters in a single nanowire waveguide is relevant in the study of other quantum-optical phenomena. For example, similar devices grown using dots with degenerate ground states can be used to produce super-radiant emission from the coherent interaction of resonant emitters.[31,32] Alternatively, reducing the spacing between degenerate emitters is of interest in the study of electronically coupled quantum dot systems.[17,18]

Samples. The nanowires were grown using chemical beam epitaxy on patterned InP substrates consisting of single gold catalysts centered in circular openings in a SiO_2 mask (see ref 12 for details). First, an InP core with embedded InAsP quantum dots was grown using a vapor−liquid−solid growth mode. The diameter of the core and embedded quantum dots was determined by the catalyst size (~ 20 nm), whereas the thickness of the dots (~ 5 nm) was controlled by the growth time. The composition (i.e., emission wavelength) of the dots was determined via control of the AsH_3 flow rate during dot incorporation.[22] After completion of the core, growth conditions were adjusted to grow a shell around the core, increasing the diameter to ~250 nm[13] while simultaneously introducing a tapered tip in order to obtain devices with collection efficiencies of ~40%.[20]

Experimental Setup. PL measurements were made in a closed-cycle helium cryostat operating at 4 K. The nanowire quantum dots were pumped along the axis of the photonic nanowire waveguide through a 100× objective. Continuous-wave excitation was provided by a HeNe laser (λ = 633 nm). For pulsed excitation, a diode laser at λ = 670 nm with a pulse width of 100 ps and a repetition rate of 40 MHz (80 MHz) was used for correlation (photoluminescence) measurements. The dot emission was collected through the same microscope objective and for spectral measurements was dispersed using a grating spectrometer and detected with a liquid-nitrogen-cooled CCD. The second-order correlation measurements were made using a fiber-based HBT arrangement. The emission from the nanowire was fiber-coupled and sent to a fiber-based tunable filter (bandwidth ~0.1 nm, tuning range λ = 950 ± 30 nm) for spectral filtering of individual quantum dot emission lines. The filtered emission was sent to two fiber-coupled APDs (timing jitters ~200 ps) via a 50:50 fiber beamsplitter.

Modeling. Photon statistics are simulated using a stochastic model to describe exciton emission and detection processes.[29] Excitons are created by a continuous train of pump pulses with a given period, followed by exciton emission at a time determined by a random number selected from a distribution weighted with the appropriate exciton lifetime. The model assumes two possible states for the system: vacuum (no excitons created) and a single exciton. The excitation rate is controlled by adjusting the probability of elevating the system from the vacuum to the exciton state. The resulting exciton to vacuum decay leads to photon emission and detection at times, which are stored, and the process is repeated through the pulse train until a sufficiently accurate time distribution can be

https://dx.doi.org/10.1021/acs.nanolett.0c00607
Nano Lett. 2020, 20, 3688−3693

obtained. The completed detection time stream is allocated by random selection into start and stop detector streams. Exciton re-excitation after a particular pulse due to the decaying band-edge carrier population is included via a competition between carrier recombination time and exciton decay time.

AUTHOR INFORMATION

Corresponding Author

Patrick Laferrière − *National Research Council of Canada, Ottawa, Ontario, Canada K1A 0R6; University of Ottawa, Ottawa, Ontario, Canada K1N 6N5;* orcid.org/0000-0002-1569-387X; Email: plaferr3@uottawa.ca

Authors

Edith Yeung − *National Research Council of Canada, Ottawa, Ontario, Canada K1A 0R6; University of Ottawa, Ottawa, Ontario, Canada K1N 6N5*

Lambert Giner − *National Research Council of Canada, Ottawa, Ontario, Canada K1A 0R6; University of Ottawa, Ottawa, Ontario, Canada K1N 6N5*

Sofiane Haffouz − *National Research Council of Canada, Ottawa, Ontario, Canada K1A 0R6*

Jean Lapointe − *National Research Council of Canada, Ottawa, Ontario, Canada K1A 0R6*

Geof C. Aers − *National Research Council of Canada, Ottawa, Ontario, Canada K1A 0R6*

Philip J. Poole − *National Research Council of Canada, Ottawa, Ontario, Canada K1A 0R6*

Robin L. Williams − *National Research Council of Canada, Ottawa, Ontario, Canada K1A 0R6; University of Ottawa, Ottawa, Ontario, Canada K1N 6N5*

Dan Dalacu − *National Research Council of Canada, Ottawa, Ontario, Canada K1A 0R6; University of Ottawa, Ottawa, Ontario, Canada K1N 6N5*

Complete contact information is available at: https://pubs.acs.org/10.1021/acs.nanolett.0c00607

Notes

The authors declare no competing financial interest.

ACKNOWLEDGMENTS

This work was supported by the Natural Sciences and Engineering Research Council of Canada and the Canadian Space Agency.

REFERENCES

(1) Bennett, C.; Brassard, G. Quantum cryptography: Public key distribution and coin tossing. *Proceedings of IEEE International Conference on Computers, Systems and Signal Processing*; IEEE, 1984; Vol. *175*, p 8.

(2) Knill, E.; Laflamme, R.; Milburn, G. A Scheme for efficient linear optics quantum computation. *Nature* **2001**, *409*, 46−52.

(3) Claudon, J.; Bleuse, J.; Malik, N. S.; Bazin, M.; Jaffrennou, P.; Gregersen, N.; Sauvan, C.; Lalanne, P.; Gérard, J.-M. A highly efficient single-photon source based on a quantum dot in a photonic nanowire. *Nat. Photonics* **2010**, *4*, 174.

(4) Gazzano, O.; Michaelis de Vasconcellos, S.; Arnold, C.; Nowak, A.; Galopin, E.; Sagnes, I.; Lanco, L.; Lemaitre, A.; Senellart, P. Bright solid-state sources of indistinguishable single photons. *Nat. Commun.* **2013**, *4*, 1425.

(5) Somaschi, N.; et al. Near-optimal single-photon sources in the solid state. *Nat. Photonics* **2016**, *10*, 340−345.

(6) Unsleber, S.; He, Y.-M.; Gerhardt, S.; Maier, S.; Lu, C.-Y.; Pan, J.-W.; Gregersen, N.; Kamp, M.; Schneider, C.; Höfling, S. Highly indistinguishable on-demand resonance fluorescence photons from a deterministic quantum dot micropillar device with 74% extraction efficiency. *Opt. Express* **2016**, *24*, 8539−8546.

(7) Gérard, J. M.; Sermage, B.; Gayral, B.; Legrand, B.; Costard, E.; Thierry-Mieg, V. Enhanced Spontaneous Emission by Quantum Boxes in a Monolithic Optical Microcavity. *Phys. Rev. Lett.* **1998**, *81*, 1110.

(8) Reithmaier, J. P.; Sek, G.; Loffler, A.; Hofmann, C.; Kuhn, S.; Reitzenstein, S.; Keldysh, L. V.; Kulakovskii, V. D.; Reinecke, T. L.; Forchel, A. Strong coupling in a single quantum dot-semiconductor microcavity system. *Nature* **2004**, *432*, 197.

(9) Christ, A.; Silberhorn, C. Limits on the deterministic creation of pure single-photon states using parametric down-conversion. *Phys. Rev. A: At., Mol., Opt. Phys.* **2012**, *85*, No. 023829.

(10) Joshi, C.; Farsi, A.; Clemmen, S.; Ramelow, S.; Gaeta, A. L. Frequency multiplexing for quasi-deterministic heralded single-photon sources. *Nat. Commun.* **2018**, *9*, 847.

(11) Elshaari, A. W.; Zadeh, I. E.; Fognini, A.; Reimer, M. E.; Dalacu, D.; Poole, P. J.; Zwiller, V.; Jöns, K. D. On-chip single photon filtering and multiplexing in hybrid quantum photonic circuits. *Nat. Commun.* **2017**, *8*, 379.

(12) Dalacu, D.; Kam, A.; Guy Austing, D; Wu, X.; Lapointe, J.; Aers, G. C; Poole, P. J Selective-area vapour-liquid-solid growth of InP nanowires. *Nanotechnology* **2009**, *20*, 395602.

(13) Dalacu, D.; Mnaymneh, K.; Lapointe, J.; Wu, X.; Poole, P. J.; Bulgarini, G.; Zwiller, V.; Reimer, M. E. Ultraclean Emission from InAsP Quantum Dots in Defect-Free Wurtzite InP Nanowires. *Nano Lett.* **2012**, *12*, 5919−5923.

(14) Zadeh, I. E.; Elshaari, A. W.; Jöns, K. D.; Fognini, A.; Dalacu, D.; Poole, P. J.; Reimer, M. E.; Zwiller, V. Deterministic Integration of Single Photon Sources in Silicon Based Photonic Circuits. *Nano Lett.* **2016**, *16*, 2289.

(15) Singh, A.; Li, Q.; Liu, S.; Yu, Y.; Lu, X.; Schneider, C.; Hofling, S.; Lawall, J.; Verma, V.; Mirin, R.; Nam, S. W.; Liu, J.; Srinivasan, K. Quantum frequency conversion of a quantum dot single-photon source on a nanophotonic chip. *Optica* **2019**, *6*, 563.

(16) Lo, H.-K.; Curty, M.; Qi, B. Measurement-Device-Independent Quantum Key Distribution. *Phys. Rev. Lett.* **2012**, *108*, 130503.

(17) Khoshnegar, M.; Huber, T.; Predojević, A.; Dalacu, D.; Prilmüller, M.; Lapointe, J.; Wu, X.; Tamarat, P.; Lounis, B.; Poole, P.; Weihs, G.; Majedi, H. A solid state source of photon triplets based on quantum dot molecules. *Nat. Commun.* **2017**, *8*, 15716.

(18) Carlson, C.; Dalacu, D.; Gustin, C.; Haffouz, S.; Wu, X.; Lapointe, J.; Williams, R. L.; Poole, P. J.; Hughes, S. Theory and experiments of coherent photon coupling in semiconductor nanowire waveguides with quantum dot molecules. *Phys. Rev. B: Condens. Matter Mater. Phys.* **2019**, *99*, 085311.

(19) Friedler, I.; Sauvan, C.; Hugonin, J. P.; Lalanne, P.; Claudon, J.; Gérard, J. M. Solid-state single photon sources: the nanowire antenna. *Opt. Express* **2009**, *17*, 2095.

(20) Reimer, M. E.; Bulgarini, G.; Fognini, A.; Heeres, R. W.; Witek, B. J.; Versteegh, M. A. M.; Rubino, A.; Braun, T.; Kamp, M.; Hofling, S.; Dalacu, D.; Lapointe, J.; Poole, P. J.; Zwiller, V. Overcoming power broadening of the quantum dot emission in a pure wurtzite nanowire. *Phys. Rev. B: Condens. Matter Mater. Phys.* **2016**, *93*, 195316.

(21) Versteegh, M. A. M.; Reimer, M. E.; Jöns, K. D.; Dalacu, D.; Poole, P.; Gulinatti, A.; Giudice, A.; Zwiller, V. Observation of strongly entangled photon pairs from a nanowire quantum dot. *Nat. Commun.* **2014**, *5*, 6298.

(22) Haffouz, S.; Zeuner, K. D.; Dalacu, D.; Poole, P. J.; Lapointe, J.; Poitras, D.; Mnaymneh, K.; Wu, X.; Couillard, M.; Korkusinski, M.; Schöll, E.; Jöns, K. D.; Zwiller, V.; Williams, R. L. Bright Single InAsP Quantum Dots at Telecom Wavelengths in Position-Controlled InP Nanowires: The Role of the Photonic Waveguide. *Nano Lett.* **2018**, *18*, 3047.

(23) Chen, Y.; Zadeh, I. E.; Jöns, K. D.; Fognini, A.; Reimer, M. E.; Zhang, J.; Dalacu, D.; Poole, P. J.; Ding, F.; Zwiller, V.; Schmidt, O.

G. Controlling the exciton energy of a nanowire quantum dot by strain fields. *Appl. Phys. Lett.* **2016**, *108*, 182103.
(24) Cygorek, M.; Korkusinski, M.; Hawrylak, P. Atomistic theory of electronic and optical properties of InAsP/InP nanowire quantum. *Phys. Rev. B: Condens. Matter Mater. Phys.* **2020**, *101*, No. 075307.
(25) Dalacu, D.; Mnaymneh, K.; Wu, X.; Lapointe, J.; Aers, G. C.; Poole, P. J.; Williams, R. L. Selective-area vapor-liquid-sold growth of tunable InAsP quantum dots in nanowires. *Appl. Phys. Lett.* **2011**, *98*, 251101.
(26) Brown, H. R.; Twiss, R. Q. Correlation between photons in two coherent beams of light. *Nature* **1956**, *177*, 27−29.
(27) Aichele, T.; Zwiller, V.; Benson, O. Visible single-photon generation from semiconductor quantum dots. *New J. Phys.* **2004**, *6*, 90.
(28) Santori, C.; Fattal, D.; Vuckovic, J.; Solomon, G. S.; Yamamoto, Y. Single-photon generation with InAs quantum dots. *New J. Phys.* **2004**, *6*, 89.
(29) Mnaymneh, K.; Dalacu, D.; McKee, J.; Lapointe, J.; Haffouz, S.; Weber, J. F.; Northeast, D. B.; Poole, P. J.; Aers, G. C.; Williams, R. L. On-Chip Integration of Single Photon Sources via Evanescent Coupling of Tapered Nanowires to SiN Waveguide. *Adv. Quantum Technol.* **2020**, *3*, 1900021.
(30) Minkov, M.; Savona, V. Radiative coupling of quantum dots in photonic crystal structures. *Phys. Rev. B: Condens. Matter Mater. Phys.* **2013**, *87*, 125306.
(31) Kim, J.-H.; Aghaeimeibodi, S.; Richardson, C. J. K.; Leavitt, R. P.; Waks, E. Super-Radiant Emission from Quantum Dots in a Nanophotonic Waveguide. *Nano Lett.* **2018**, *18*, 4734−4740.
(32) Grim, J. Q.; Bracker, A. S.; Zalalutdinov, M.; Carter, S. G.; Kozen, A. C.; Kim, M.; Kim, C. S.; Mlack, J. T.; Yakes, M.; Lee, B.; Gammon, D. Scalable in operando strain tuning in nanophotonic waveguides enabling three quantum-dot superradiance. *Nat. Mater.* **2019**, *18*, 963.

https://dx.doi.org/10.1021/acs.nanolett.0c00607
Nano Lett. 2020, 20, 3688−3693

Chapter 10

Article 6: Position-controlled Telecom Single Photon Emitters Operating at Elevated Temperatures

This chapter contains the following article:

P. Laferrière, S. Haffouz, D. B, Northeast, P. J. Poole, R. L. Williams, & D. Dalacu, "Position-controlled Telecom Single Photon Emitters Operating at Elevated Temperatures", Nano Letters **23**, 3, 962-968 (2023)

DOI: https://doi.org/10.1021/acs.nanolett.2c04375

NANO LETTERS

100

pubs.acs.org/NanoLett

Letter

Position-Controlled Telecom Single Photon Emitters Operating at Elevated Temperatures

Patrick Laferrière, Sofiane Haffouz, David B. Northeast, Philip J. Poole, Robin L. Williams, and Dan Dalacu*

Cite This: *Nano Lett.* 2023, 23, 962−968

Read Online

ACCESS | Metrics & More | Article Recommendations

ABSTRACT: A key resource in quantum-secured communication protocols are single photon emitters. For long-haul optical networks, it is imperative to use photons at wavelengths compatible with telecom single mode fibers. We demonstrate high purity single photon emission at 1.31 μm using deterministically positioned InP photonic waveguide nanowires containing single InAsP quantum dot-in-a-rod structures. At excitation rates that saturate the emission, we obtain a single photon collection efficiency at first lens of 27.6% and a probability of multiphoton emission of $g^{(2)}(0) = 0.021$. We have also evaluated the performance of the source as a function of temperature. Multiphoton emission probability increases with temperature with values of 0.11, 0.34, and 0.57 at 77, 220 and 300 K, respectively, which is attributed to an overlap of temperature-broadened excitonic emission lines. These results are a promising step toward scalably fabricating telecom single photon emitters that operate under relaxed cooling requirements.

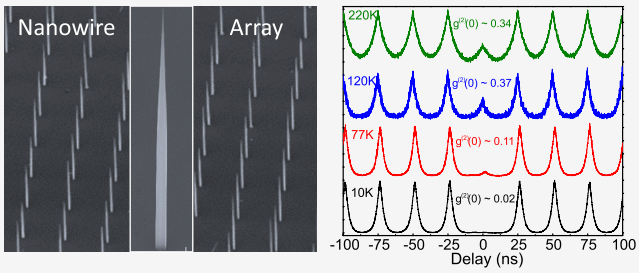

KEYWORDS: *nanowire quantum dot, photonic waveguide, selective-area vapor−liquid−solid epitaxy, telecom single photon source*

The prospect of a future fiber-based quantum network[1] relies on the on-demand availability of high quality single photons at telecom wavelengths. Sources based on semiconductor quantum dots, which can be tuned over a wide wavelength range through the choice of material system,[2] are a promising candidate for delivering such photons. Telecom single photon emission was first demonstrated in both the InAs/GaAs[3] and the InAs/InP[4] material systems in 2005. Since these early studies, device performance has dramatically improved for both GaAs-based[5−15] and InP-based[16−31] quantum dots with current state-of-the-art devices possessing a first-lens brightness of 36% in the InP system using photonic crystal cavities[21] and 23% in the GaAs system using circular Bragg gratings.[15]

Here we report state-of-the-art O-band quantum dot single photon emitters manufactured using a position-control technique that can operate at elevated temperatures. The emitters are based on bottom-up InAsP/InP nanowire quantum dots embedded within photonic nanowire waveguides grown using selective-area vapor−liquid−solid (S-A VLS) epitaxy.[32] In an earlier study[24] we tuned the quantum dot emission to telecom wavelengths by increasing the dot thickness, since memory effects of the Group V concentration in the gold catalyst limited the amount of arsenic that could be incorporated. Device collection efficiencies were low, which we attribute to a ground state consisting of both heavy- and light-hole levels,[33,34] the latter of which results in photons that do not couple to the fundamental mode of the nanowire waveguide.[35] We adopt a dot-in-a-rod structure[36] such that the thickness of the dot is nominally the same as in devices which have demonstrated high collection efficiencies,[37] and further optimized the nanowire geometry for O-band emission.

At 4 K, the devices generated 1.86 Mcps at the detector when excited at a rate of 80 MHz. End-to-end efficiency was 2.82%, and a first lens single photon collection efficiency was 27.6%, measured at saturation where the probability of multiphoton emission was $g^{(2)}(0) = 0.021$. The devices also demonstrated single photon emission up to 220 K, albeit at significantly reduced single photon purities of ∼34%, which permits operation with a simple multistage thermoelectric cooler.

The nanowires were grown by chemical beam epitaxy using the S-A VLS growth technique that allows positioning of individual emitters at specified locations on the growth substrate, see refs.[32] and[36] for details. A single $InAs_xP_{1-x}$ quantum dot with composition $x \sim 0.68$ and thickness $t_d \sim 3$ nm was embedded within an $InAs_yP_{1-y}$ nanowire rod with composition $y \sim 0.5$ and thickness $t_r \sim 20$ nm, itself embedded within an InP nanowire core. The diameters for the dot and rod

Received: November 7, 2022
Revised: January 25, 2023
Published: January 27, 2023

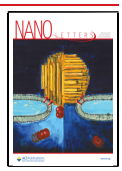

https://doi.org/10.1021/acs.nanolett.2c04375
Nano Lett. 2023, 23, 962−968

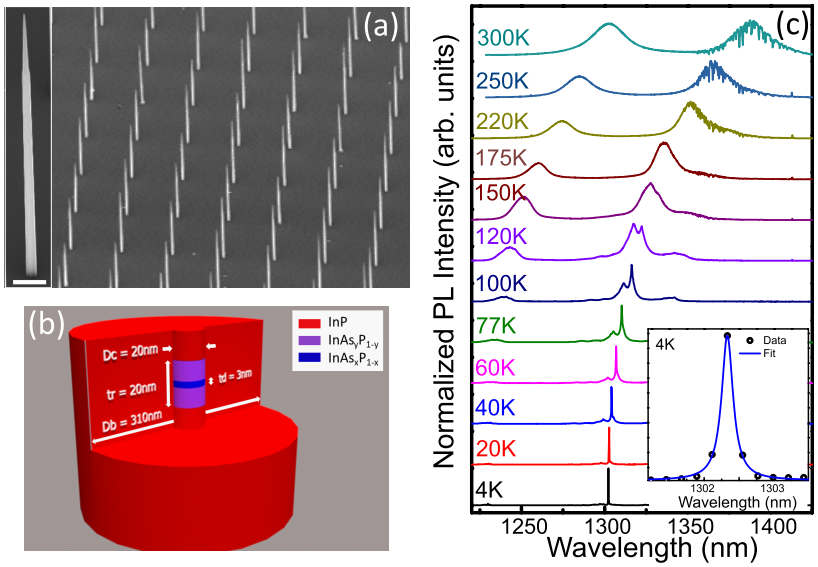

Figure 1. (a) Scanning electron microscopy image at 45° of an array of nanowires pitched at 7.5 μm. Inset: close-up of a single nanowire. Scale bar is 1 μm. (b) Schematic of a cutaway cross-section of the dot-in-a-rod structure. (c) PL spectra from 4 to 300 K of a single nanowire excited at P_{sat} with a CW laser. Inset: zoom-in of the PL spectrum at 4 K.

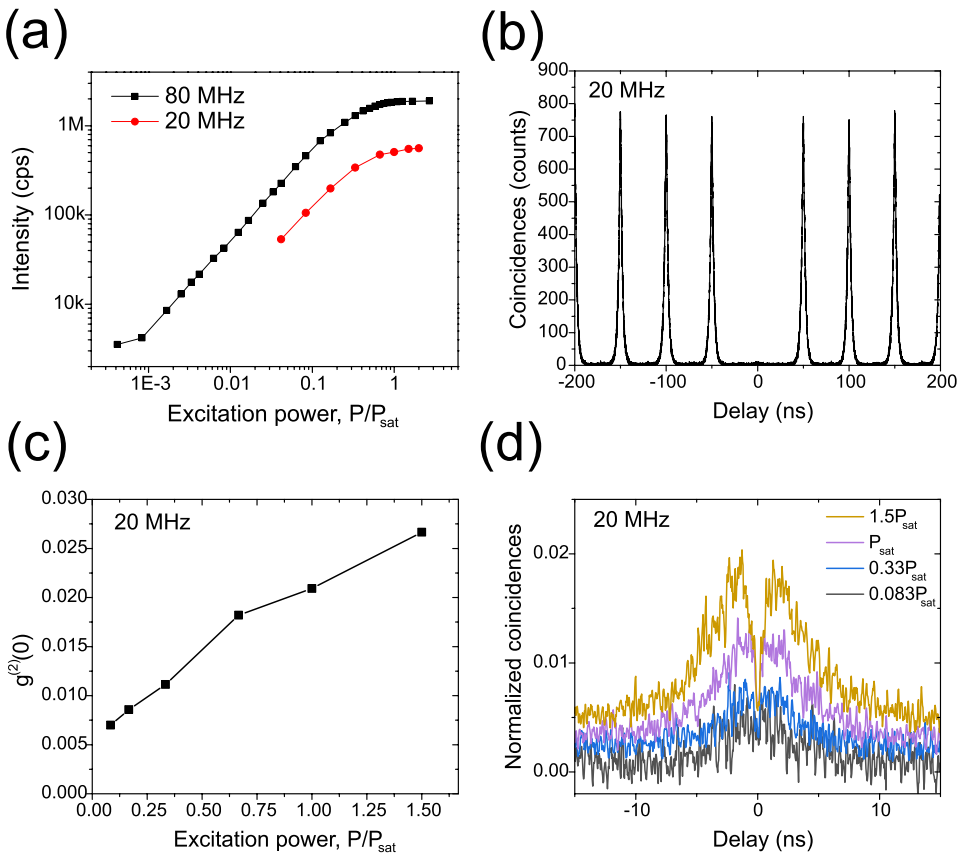

Figure 2. Low temperature (4 K) measurements: (a) Detected counts as a function of excitation power using 80 MHz (black) and 20 MHz (red) pulse rates showing a saturation count level of 1.86 Mcps and 0.507 Mcps, respectively. (b) Coincidence counts measured at 0.1 P_{sat} pumped at 20 MHz for which $g^{(2)}(0) = 0.007$. (c) Integrated counts in the $g^{(2)}(\tau)$ zero-delay peak relative to side peaks as a function of excitation power at 20 MHz. (d) Zoom in of the correlation peak around $\tau = 0$ ns as a function of excitation power showing evidence of re-excitation.

are dictated by the core diameter $D_c \sim 20$ nm. The core was clad with an InP shell to produce a photonic waveguide targeting a base diameter of $D_b = 310$ nm tapered to 20 nm over the 12 μm length of the waveguide. A schematic of the dot-in-a-rod structure is shown in Figure 1b and scanning electron microscopy images of the clad nanowire devices are shown in Figure 1a.

https://doi.org/10.1021/acs.nanolett.2c04375
Nano Lett. 2023, 23, 962−968

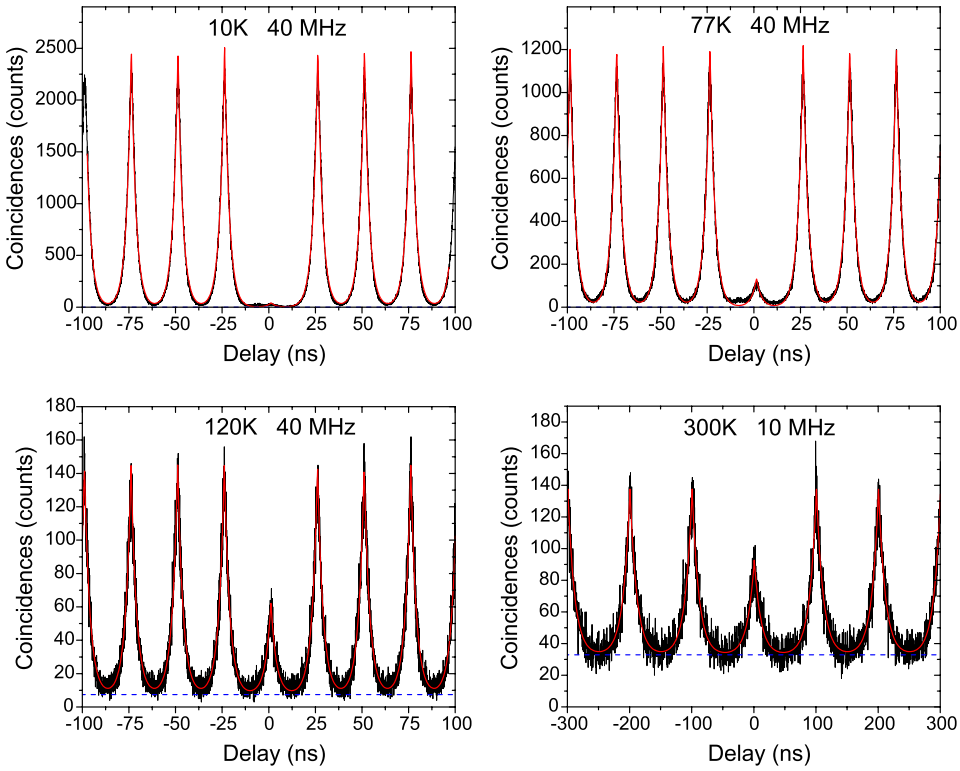

Figure 3. Second-order correlation measurements of the source at different temperatures. The excitation power was 0.5 P_{sat} at temperatures up to 120 K and reduced to ~0.25 P_{sat} at 220 K and above. The red line is a curve fit to the data and the blue dashed line is the fitted background count level. A separate measurement of the lifetime was made to allow the background level to be determined.

Temperature-dependent optical measurements were made with the device in a closed-cycle helium cryostat. The nanowire was excited through a 100x cryogenic objective (numerical aperture NA = 0.81) located in the cryostat. Spectrally resolved photoluminescence (PL) measurements were performed using a continuous-wave (CW) laser while for time-resolved photoluminescence (TRPL) measurements, a pulsed laser operating at 10 to 80 MHz was used. In both case, excitation was above-band at λ = 670 nm. The PL was collected through the same objective and directed to a spectrometer with a liquid nitrogen-cooled InGaAs detector for the spectrally resolved measurements. For TRPL measurements, the emission was coupled to a fiber and sent to two superconducting nanowire single photon detectors (SNSPDs) via a 50/50 beamsplitter. For the latter, the emission line to be measured was isolated using a filter with a bandwidth appropriate for the measurement, discussed below.

Typical PL spectra as a function of temperature from a device emitting around 1300 nm are shown in Figure 1b at an excitation power $P = P_{sat}$ which corresponds to the power required to saturate the excitonic transition. At 4 K the PL spectrum is characteristically dominated by a narrow single peak with a full width half-maximum value of 44 μeV, limited by the resolution of the spectrometer. The peak is attributed to an excitonic transition within the quantum dot and, with increasing temperature, shifts continuously to longer wavelength, starting at 1301.28 nm at 4 K and reaching 1397.8 nm at 300 K. As the temperature is increased the predominant peak broadens and starts to overlap with the adjacent higher energy transition line that rises up, becoming one single broad peak above 150 K. Above 100 K a broad short wavelength peak associated with p-shell transitions can also be seen. It should be noted that emission from a single quantum dot can be readily observed at room temperature.

Exciting at 80 MHz we measured, at saturation, 1.86 Mcps on the SNSPDs (3.8 Mcps under CW excitation) after filtering with a 0.1 nm filter. To facilitate the discrimination between coincidence and background counts in the correlation measurements discussed later, we have also made measurements at lower repetition rates. For example, using 20 MHz we measure count rates at saturation of 0.507 Mcps, approximately equal to the expected 4-fold reduction compared to 80 MHz. Integrated count rates versus excitation rate for both laser repetition rates are are shown in Figure 2a. The end-to-end source efficiency, which is defined by dividing the maximum collected count rates at the SNSPDs by the repetition rate of the pumping laser (20 MHz was used) is thus 2.54% at saturation. If we account for the detector efficiency of 90%, the end-to-end efficiency is 2.82% and by taking into account a throughput of 10% for the experimental setup a collection efficiency at the first-lens of 28.2% is obtained. This value is reduced to 27.6% after correcting for the multiphoton emission probability measured at the above count rate (see below). The efficiency increases to 34.5% if we include photons emitted into the phonon sidebands, estimated to be 20% of the total emission at 4 K,[38] which we have filtered out using the narrow passband filter. In principle the efficiency can be nearly doubled using a mirror (Au layer) at the bottom of the nanowire to allow collection of the photons that are emitted toward the InP substrate. A theoretical model reflectivity of about 0.91 can be achieved using a gold layer under the nanowire base.[39]

To assess the single-photon purity, second-order correlation measurements, $g^{(2)}(\tau)$, were performed in a standard Hanbury–Brown and Twiss experiment. As mentioned above, a pulse

https://doi.org/10.1021/acs.nanolett.2c04375
Nano Lett. 2023, 23, 962−968

repetition rate of 20 MHz was used to avoid significant overlap between consecutive pulses and a 0.1 nm bandpass filter was used to isolate the emission from a single transition. A typical correlation measurement is shown in Figure 2b when the source is excited at ~0.1 P_{sat}. We fit the $g^{(2)}(\tau)$ curves using the expression BG + $A[g^{(2)}(0)\exp(-|\tau_d|/\tau_l) + \Sigma_{n\neq 0}\exp(-|\tau_d + nT|/\tau_l)]$, where BG is the background counts, A is the normalization constant, τ_d is the time delay, τ_l is the measured lifetime, and T is the pulse period. The integrated counts in the zero-delay peak relative to the side peaks gives a probability of multiphoton emission of $g^{(2)}(0) = 0.007$. As the pump power is increased the multiphoton probability increases, as shown in Figure 2c, with a value $g^{(2)}(0) = 0.021$ at saturation. The reason for this increase is the presence of re-excitation of the dot due to the use of above band excitation, with a characteristic dip in the center of the peak observed around zero delay;[40,41] see Figure 2d. This behavior is a consequence of an excess of carriers in the barrier material at high pump powers that can be captured by the dot after the first photon emission event has occurred, leading to the re-excitation of the dot. The rise time from 0 ns is associated with the carrier capture and subsequent relaxation within the dot, while the decay time is associated with the lifetime of the exciton.

Next we assess the temperature dependence of the single-photon purity through coincidence measurements from 4 to 300 K. In Figure 3 we show correlations at four selected temperatures that span the measured range. We have adjusted the pulse excitation rate between 10 and 40 MHz depending on temperature in order to minimize the overlap between adjacent correlation peaks while maintaining sufficient count rates to limit excessive integration times. The increased peak-to-peak overlap and decreased count rates with increasing temperature is discussed below.

We first note that as the temperature was increased the emission lines broadened and started to overlap, as shown in Figure 1b. Importantly, the line width broadening with increasing temperature will have two effects on the second-order correlation measurements: First the use of a narrow pass band filter will reduce the count rates arriving at the SNSPDs. To maintain reasonable count rates for the measurements, the bandpass of the filter employed was widened as the temperature was raised, from 0.1 to 12 nm at 175 K and to 25 nm at 300 K. Second, the overlap between the adjacent optical emission lines will make the selection of a single transition difficult. Both of the above can potentially result in photons from different transitions reaching the detectors and affecting the $g^{(2)}(0)$ value. If two transitions are not the result of a sequential decay in a cascade process, for example, a neutral and charged exciton, then $g^{(2)}(0)$ can remain zero. On the other hand if the two transitions correspond to a cascade process, such as for the biexciton and exciton, then the value of $g^{(2)}(0)$ will rise.

To obtain accurate values of the coincidence counts in the zero delay peak, the curve fitting procedure described above (which included an uncorrelated background signal) was applied to the measured $g^{(2)}(\tau)$ curves. To enable accurate fitting, a TRPL measurement was made before each correlation measurement to determine the lifetime to be used for each fit. Without this extra piece of information a wide range of background levels and lifetimes could be used to fit the same data, in particular at high temperature. The fits are plotted in Figure 3 (red curves) and the extracted $g^{(2)}(0)$ values are plotted in Figure 5 (red stars).

Before discussing the observed $g^{(2)}(0)$ dependence on temperature, we first look at the lifetime dependence extracted from the TRPL measurements, plotted in Figure 4a. We observed a dramatic increase in lifetime with increasing temperature, from 2.1 ns at 4 K to 10.8 ns at 300 K. We attribute this increase in part to a dependence of the spontaneous emission rate into the detected waveguide mode, HE_{11}, on the emission wavelength.[24] In Figure 4b, we plot the lifetime as a function of emission wavelength which redshifts with increasing temperature as shown in Figure 1c. In the inset, we show the calculated wavelength-dependent spontaneous emission rate normalized to that for bulk, plotted as a lifetime (i.e., the reciprocal of the rate) to compare with experiment for three different nanowire diameters. For the nanowire diameters used here the shift in emission wavelength from 1300 to 1400 nm, as seen when going from 4 to 300 K, results in a drop in emission rate or equivalently an increase in lifetime (shaded region in inset).

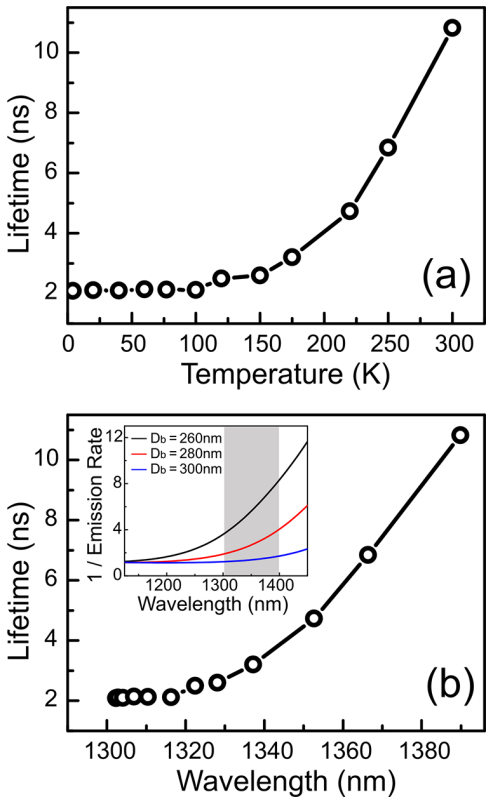

Figure 4. Measured lifetime as a function of (a) temperature and (b) emission wavelength The inset in (b) shows the reciprocal of the calculated spontaneous emission rate, normalized to that for bulk, as a function of wavelength for three different nanowire diameters.

This alone is insufficient to account for the observed increase and we consider a second mechanism proposed in ref 42. to describe the increase in lifetime with temperature observed in InAs/GaAs quantum dots for temperatures up to 250 K. The authors attributed the increase to Boltzmann spreading over dark states, i.e. thermal excitation of electrons and holes out of the ground state into higher lying states that do not have allowed optical transitions. Based on the s-p level spacing of 60 meV in our dot, this mechanism alone underestimates the increase in lifetime observed. If, however, we include both of the above mechanisms we can reach qualitative agreement with the observed lifetimes.

https://doi.org/10.1021/acs.nanolett.2c04375
Nano Lett. 2023, 23, 962−968

We consider now the temperature dependence of $g^{(2)}(0)$ plotted in Figure 5 that shows a steady rise as the temperature is

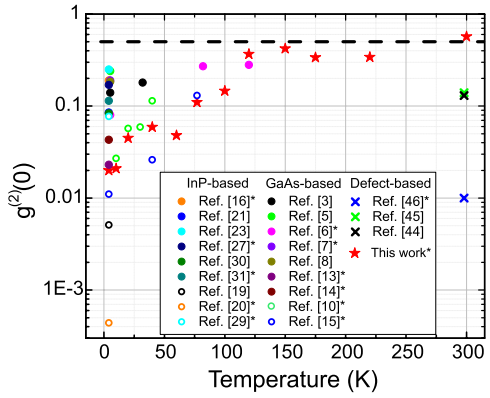

Figure 5. Temperature dependence of $g^{(2)}(0)$ for quantum dot-based telecom single photon emitters. Dashed line corresponds to $g^{(2)}(0) = 0.5$. Filled symbols: above-band excitation. Open symbols: p-shell excitation. Crosses: Defect-based sources. Values measured at close to maximum count rates indicated by an asterisk in the legend.

increased from 10 to 120 K. Above 120 K it saturates at just under 0.5 until 300 K where it is just over 0.5. A measured nonzero $g^{(2)}(0)$ for a quantum dot can arise from a number of mechanisms; detector dark counts, scattered excitation laser, multiple independent emitters, re-excitation of the dot from the same excitation pulse, and multiple emission lines from a single dot. The increase in $g^{(2)}(0)$ with increasing temperature is clearly not a consequence of dark counts (which would be a uniform background), or scattered laser emission (which would be a narrower peak with a width limited by the detector timing jitter of 60 ps). Multiple independent emitters are also very unlikely since the nanowire can contain one and only one dot by design and has a very low $g^{(2)}(0)$ at low temperature. This leaves re-excitation and multiple emission events from the dot as the likely causes. Re-excitation of the dot typically results in a dip in the $g^{(2)}(\tau)$ value around zero delay, which is not observed here, although the time scale for re-excitation at higher temperatures may be too short to resolve.

Multiple emission events from the dot, such as biexciton followed by exciton emission are also quite likely. At low temperature these transitions can be separated spectrally. With increasing temperature these transitions broaden and eventually overlap so they can no longer be isolated, increasing $g^{(2)}(0)$. By dropping the excitation power at high temperatures the $g^{(2)}(0)$ should improve due to the decreased probability of creating a biexciton, and indeed this is observed, but at the expense of overall count rates. Considering the apparent saturation $g^{(2)}(0)$ at a value of ~0.5 (i.e., two photons per excitation pulse) observed in Figure 5, it is likely that this last mechanism, involving only a single additional transition, dominates the observed temperature dependence.

For comparison, we also plot literature values of $g^{(2)}(0)$ from other quantum dot-based single photon sources emitting at telecom wavelengths. Only results obtained from nonpost-selected measurements (i.e., using pulsed excitation) are included. Measurements where the excitation power was specified to be at or close to P_{sat}, as is the case here, are indicated by an asterisk in the legend. This applies strictly to the low temperature measurements since at higher temperatures it is difficult to observe saturation of a single transition when it overlaps with another.

We first consider experiments performed using above-band excitation, as is the case here, indicated in the figure by filled symbols. The sources in this study, under these operating conditions, outperform, to our knowledge, all other existing approaches based on quantum dots. Next we consider experiments performed using quasi-resonant excitation (i.e., exciation via a p-shell level in the dot), indicated in the figure by open symbols. Here we observe several sources[15,19,20] that display reduced multiphoton emission probabilities compared to the devices in this study. In approaches utilizing randomly nucleated quantum dots such that multiple emitters may be simultaneous probed, quasi-resonant excitation will mitigate both spectral pollution from other emitters as well as re-excitation from the same emitter. For the sources studied here, which are fabricated using a site-selection technique that assures each device contains only one emitter, quasi-resonant excitation is also expected to improve the single photon purity by mitigating re-excitation process responsible for the nonzero $g^{(2)}(0)$ values, specifically at lower temperatures (see Figure 2d).

For completion, we also include other solid-state 2-level systems that have demonstrated telecom single photon emission, specifically at room temperature, indicated in the figure by crosses. These include sources based on defects in SiC,[43] GaN,[44] and carbon nanotubes.[45] Although the nanowire-based sources described here technically generate nonclassical light up to temperatures of 220 K, devices with such high multiphoton emission probabilities are of limited practical application.[46] To achieve high temperature operation with reduced multiphoton emission probability to levels comparable to these defect-based systems will require engineering of the quantum dot electronic levels[47] such that they are sufficiently separated when severely broadened to eliminate any overlap between them.

In conclusion, we have demonstrated high purity telecom single photon emission from devices operating with high efficiency and grown using a position-control technique. We have also evaluated the temperature-dependent performance of the sources, quantifying the degradation of single photon purity with temperature. Finally, we note that the structures described can be incorporated in a hybrid on-chip platform[48] to provide a stable and robust plug and play[49] field-ready source that will be required to scalably build a future telecom quantum network.

AUTHOR INFORMATION

Corresponding Author

Dan Dalacu − *National Research Council of Canada, Ottawa, Ontario, Canada K1A 0R6; University of Ottawa, Ottawa, Ontario, Canada K1N 6N5;* orcid.org/0000-0001-6204-3952; Email: dan.dalacu@nrc.ca

Authors

Patrick Laferrière − *National Research Council of Canada, Ottawa, Ontario, Canada K1A 0R6; University of Ottawa, Ottawa, Ontario, Canada K1N 6N5*

Sofiane Haffouz − *National Research Council of Canada, Ottawa, Ontario, Canada K1A 0R6;* orcid.org/0000-0003-1220-2622

David B. Northeast − *National Research Council of Canada, Ottawa, Ontario, Canada K1A 0R6*

Philip J. Poole − *National Research Council of Canada, Ottawa, Ontario, Canada K1A 0R6*

https://doi.org/10.1021/acs.nanolett.2c04375
Nano Lett. 2023, 23, 962−968

Robin L. Williams − *National Research Council of Canada, Ottawa, Ontario, Canada K1A 0R6*

Complete contact information is available at: https://pubs.acs.org/10.1021/acs.nanolett.2c04375

Notes

The authors declare no competing financial interest.

■ ACKNOWLEDGMENTS

This work was supported by the Natural Sciences and Engineering Research Council of Canada through the Discovery Grant SNQLS, by the National Research Council of Canada through the Small Teams Ideation Program QPIC and by the Canadian Space Agency through a collaborative project entitled "Field Deployable Single Photon Emitters for Quantum Secured Communications".

■ REFERENCES

(1) Kimble, H. J. The Quantum Internet. *Nature* **2008**, *453*, 1023−1030.
(2) Arakawa, Y.; Holmes, M. J. Progress in quantum-dot single photon sources for quantum information technologies: A broad spectrum overview. *Appl. Phys. Rev.* **2020**, *7*, 021309.
(3) Ward, M. B.; Karimov, O. Z.; Unitt, D. C.; Yuan, Z. L.; See, P.; Gevaux, D. G.; Shields, A. J.; Atkinson, P.; Ritchie, D. A. On-demand single-photon source for 1.3 μm telecom fiber. *Appl. Phys. Lett.* **2005**, *86*, 201111.
(4) Miyazawa, T.; Takemoto, K.; Sakuma, Y.; Hirose, S.; Usuki, T.; Yokoyama, N.; Takatsu, M.; Arakawa, Y. Single-Photon Generation in the 1.55μm Optical-Fiber Band from an InAs/InP Quantum Dot. *J. J. Appl. Phys.* **2005**, *44*, L620.
(5) Zinoni, C.; Alloing, B.; Monat, C.; Zwiller, V.; Li, L. H.; Fiore, A.; Lunghi, L.; Gerardino, A.; de Riedmatten, H.; Zbinden, H.; Gisin, N. Time-resolved and antibunching experiments on single quantum dots at 1300nm. *Appl. Phys. Lett.* **2006**, *88*, 131102.
(6) Xue, Y.; Chen, Z.; Ni, H.; Niu, Z.; Jiang, D.; Dou, X.; Sun, B. 1.3μm single-photon emission from strain-coupled bilayer of InAs/GaAS quantum dots at the temperature up to 120K. *Appl. Phys. Lett.* **2017**, *111*, 182102.
(7) Chen, Z.-S.; Ma, B.; Shang, X.-J.; Ni, H.-Q.; Wang, J.-L.; Niu, Z.-C. Bright Single-Photon Source at 1.3*mu*m Based on InAs Bilayer Quantum Dot in Micropillar. *Nanoscale Res. Lett.* **2017**, *12*, 378.
(8) Paul, M.; Olbrich, F.; Hoschele, J.; Schreier, S.; Kettler, J.; Portalupi, S. L.; Jetter, M.; Michler, P. Single-photon emission at 1.55μm from MOVPE-grown InAs qauntum dots on InGaAs/GaAs metamorphic buffers. *Appl. Phys. Lett.* **2017**, *111*, 033102−1.
(9) Carmesin, C.; et al. Structural and optical properties of InAs/(In)GaAs/GaAs quantum dots with single-photon emission in the telecom C-band up to 77K. *Phys. Rev. B* **2018**, *98*, 125407.
(10) Srocka, N.; Mrowinski, P.; Große, J.; von Helversen, M.; Heindel, T.; Rodt, S.; Reitzenstein, S. Determinastically fabricated quantum dot single-photon source emitting indistinguishable photons in the telecom O-band. *Appl. Phys. Lett.* **2020**, *116*, 231104.
(11) Holewa, P.; Burakowski, M.; Musiał, A.; Srocka, N.; Quandt, D.; Strittmatter, A.; Rodt, S.; Reitzenstein, S.; Sęk, G. Thermal stability of emission from single InGaAs/GaAs quantum dots at the telecom O-band. *Sci. Rep.* **2020**, *10*, 21816.
(12) Bauer, S.; Wang, D.; Hoppe, N.; Nawrath, C.; Fischer, J.; Witz, N.; Kaschel, M.; Schweikert, C.; Jetter, M.; Portalupi, S. L.; Berroth, M.; Michler, P. Achieving stable fiber coupling of quantum dot telecom C-band single-photons to an SOI photonic device. *Appl. Phys. Lett.* **2021**, *119*, 211101.
(13) Nawrath, C.; Vural, H.; Fischer, J.; Schaber, R.; Portalupi, S. L.; Jetter, M.; Michler, P. Resonance fluorescence of single In(Ga)As quantum dots emitting in the telecom C-band. *Appl. Phys. Lett.* **2021**, *118*, 244002.
(14) Zeuner, K. D.; Jons, K. D.; Schweickert, L.; Reuterskiold Hedlund, C.; Nunez Lobato, C.; Lettner, T.; Wang, K.; Gyger, S.; Scholl, E.; Steinhauer, S.; Hammar, M.; Zwiller, V. On-Demand Generation of Entangled Photon Pairs in the Telecom C-Band with InAs Quantum Dots. *ACS Photon.* **2021**, *8*, 2337−2344.
(15) Kolatschek, S.; Nawrath, C.; Bauer, S.; Huang, J.; Fischer, J.; Sittig, R.; Jetter, M.; Portalupi, S. L.; Michler, P. Bright Purcell Enhanced Single-Photon Source in the Telecom O-Band Based on a Quantum Dot in a Circular Bragg Grating. *Nano Lett.* **2021**, *21*, 7740.
(16) Takemoto, K.; Takatsu, M.; Hirose, S.; Yokoyama, N.; Sakuma, Y.; Usuki, T.; Miyazawa, T.; Arakawa, Y. An optical horn structure for single-photon source using quantum dots at telecommunication wavelength. *J. Appl. Phys.* **2007**, *101*, 081720.
(17) Birowosuto, M.; Sumikura, H.; Matsuo, S.; Taniyama, H.; van Veldhoven, P.; Nötzel, R.; Notomi, M. Fast Purcell-enhanced single photon source in 1,550-nm telecom band from a resonant quantum dot-cavity coupling. *Sci. Rep.* **2012**, *2*, 321.
(18) Benyoucef, M.; Yacob, M.; Reithmaier, J. P.; Kettler, J.; Michler, P. Telecom-wavelength (1.5*mu*m) single photon emission from InP-based quantum dots. *Appl. Phys. Lett.* **2013**, *103*, 162101.
(19) Takemoto, K.; Nambu, Y.; Miyazawa, T.; Sakuma, Y.; Yamamoto, T.; Yorozu, S.; Arakawa, Y. Quantum key distribution over 120 km using ultrahigh purity single-photon source and superconducting single-photon detectors. *Sci. Rep.* **2015**, *5*, 14383.
(20) Miyazawa, T.; Takemoto, K.; Nambu, Y.; Miki, S.; Yamashita, T.; Terai, H.; Fujiwara, M.; Sasaki, M.; Sakuma, Y.; Takatsu, M.; Yamamoto, T.; Arakawa, Y. Single-photon emission at 1.5μm from an InAs/InP quantum dot with highly suppressed multi-photon emission probabilities. *Appl. Phys. Lett.* **2016**, *109*, 132106.
(21) Kim, J.; Cai, T.; Richardson, C. J. K.; Leavitt, R.; Waks, E. Two-photon interference from a bright single-photon source at telecom wavelengths. *Optica* **2016**, *3*, 577−584.
(22) Dusanowski, Ł; Syperek, M.; Misiewicz, J.; Somers, A.; Höfling, S.; Kamp, M.; Reithmaier, J. P.; Sęk, G. Single-photon emission of InAs/InP quantum dashes at 1.55mum and temperatures up to 80K. *Appl. Phys. Lett.* **2016**, *108*, 163108.
(23) Kim, J.-H.; Aghaeimeibodi, S.; Richardson, C. J. K.; Leavitt, R. P.; Englund, D.; Waks, E. Hybrid Integration of Solid-State Quantum Emitters on a Silicon Photonic Chip. *Nano Lett.* **2017**, *17*, 7394−7400.
(24) Haffouz, S.; Zeuner, K. D.; Dalacu, D.; Poole, P. J.; Lapointe, J.; Poitras, D.; Mnaymneh, K.; Wu, X.; Couillard, M.; Korkusinski, M.; Schöll, E.; Jöns, K. D.; Zwiller, V.; Williams, R. L. Bright Single InAsP Quantum Dots at Telecom Wavelengths in Position-Controlled InP Nanowires: The Role of the Photonic Waveguide. *Nano Lett.* **2018**, *18*, 3047.
(25) Müller, T.; Skiba-Szymanska, J.; Krysa, A.; Huwer, J.; Felle, M.; Anderson, M.; Stevenson, R.; Heffernan, J.; Ritchie, D.; Shields, A. A quantum light-emitting diode for the standard telecom window around 1,550 nm. *Nat. Commun.* **2018**, *9*, 862.
(26) Jaffal, A.; Redjem, W.; Regreny, P.; Nguyen, H. S.; Cueff, S.; Letartre, X.; Patriarche, G.; Rousseau, E.; Cassabois, G.; Gendry, M.; Chauvin, N. InAs quantum dot in needlelike tapered InP nanowire: a telecom band single photon source monolithically grown on silicon. *Nanoscale* **2019**, *11*, 21847.
(27) Lee, C.-M.; Buyukkaya, M. A.; Aghaeimeibodi, S.; Karasahin, A.; Richardson, C.; Waks, E. A fiber-integrated nanobeam single photon source emitting at telecom wavelengths. *Appl. Phys. Lett.* **2019**, *114*, 171101.
(28) Anderson, M.; Müller, T.; Huwer, J.; Skiba-Szymanska, J.; Krysa, A. B.; Stevenson, R. M.; Heffernan, J.; Ritchie, D. A.; Shields, A. J. Quantum teleportation using highly coherent emission from telecom C-band quantum dots. *NPJ. Quant. Inform.* **2020**, *6*, 14.
(29) Lee, C.-M.; Buyukkaya, M. A.; Harper, S.; Aghaeimeibodi, S.; Richardson, C. J. K.; Waks, E. Bright Telecom-Wavelength Single Photons Based on a Tapered Nanobeam. *Nano Lett.* **2021**, *21*, 323.
(30) Musiał, A.; Mikulicz, M.; Mrowinski, P.; Zielinska, A.; Sitarek, P.; Wyborski, P.; Kuniej, M.; Reithmaier, J. P.; Sek, G.; Benyoucef, M. InP-based single-photon sources operating at telecom C-band with increased extraction efficiency. *Appl. Phys. Lett.* **2021**, *118*, 221101.

(31) Holewa, P.Ł; Sakanas, A.; Gur, U. M.; Mrowinski, P.Ł; Huck, A.; Wang, B.-Y.; Musiał, A.; Yvind, K.; Gregersen, N.; Syperek, M.; Semenova, E. Bright Quantum Dot Single-Photon Emitters at Telecom Bands Heterogeneously Integrated on Si. *ACS Photon.* **2022**, *9*, 2273−2279.
(32) Dalacu, D.; Mnaymneh, K.; Wu, X.; Lapointe, J.; Aers, G. C.; Poole, P. J.; Williams, R. L. Selective-area vapor-liquid-sold growth of tunable InAsP quantum dots in nanowires. *Appl. Phys. Lett.* **2011**, *98*, 251101.
(33) Zieliński, M. Fine structure of light-hole excitons in nanowire quantum dots. *Phys. Rev. B* **2013**, *88*, 115424.
(34) Jeannin, M.; Artioli, A.; Rueda-Fonseca, P.; Bellet-Amalric, E.; Kheng, K.; André, R.; Tatarenko, S.; Cibert, J.; Ferrand, D.; Nogues, G. Light-hole exciton in a nanowire quantum dot. *Phys. Rev. B* **2017**, *95*, 035305.
(35) Jeannin, M.; Cremel, T.; Häyrynen, T.; Gregersen, N.; Bellet-Amalric, E.; Nogues, G.; Kheng, K. Enhanced Photon Extraction from a Nanowire Quantum Dot Using a Bottom-Up Photonic Shell. *Phys. Rev. Appl.* **2017**, *8*, 054022.
(36) Haffouz, S.; Poole, P. J.; Jin, J.; Wu, X.; Ginet, L.; Mnaymneh, K.; Dalacu, D.; Williams, R. L. Single quantum dot-in-a-rod embedded in a photonic nanowire waveguide for telecom band emission. *Appl. Phys. Lett.* **2020**, *117*, 113102.
(37) Laferrière, P.; Yeung, E.; Miron, I.; Northeast, D. B.; Haffouz, S.; Lapointe, J.; Korkusinski, M.; Poole, P. J.; Williams, R. L.; Dalacu, D. Unity yield of deterministically positioned quantum dot single photon sources. *Sci. Rep.* **2022**, *12*, 6376.
(38) Lodahl, P.; Mahmoodian, S.; Stobbe, S. Interfacing single photons and single quantum dots with photonic nanostructures. *Rev. Mod. Phys.* **2015**, *87*, 347.
(39) Claudon, J.; Bleuse, J.; Malik, N. S.; Bazin, M.; Jaffrennou, P.; Gregersen, N.; Sauvan, C.; Lalanne, P.; Gérard, J.-M. A highly efficient single-photon source based on a quantum dot in a photonic nanowire. *Nat. Photonics* **2010**, *4*, 174.
(40) Laferrière, P.; Yeung, E.; Giner, L.; Haffouz, S.; Lapointe, J.; Aers, G. C.; Poole, P. J.; Williams, R. L.; Dalacu, D. Multiplexed Single-Photon Source Based on Multiple Quantum Dots Embedded within a Single Nanowire. *Nano Lett.* **2020**, *20*, 3688−3693.
(41) Aichele, T.; Zwiller, V.; Benson, O. Visible single-photon generation from semiconductor quantum dots. *New J. Phys.* **2004**, *6*, 90.
(42) Harbord, E.; Spencer, P.; Clarke, E.; Murray, R. Radiative lifetimes in undoped and p-doped InAs/GaAs quantum dots. *Phys. Rev. B* **2009**, *80*, 195312.
(43) Wang, J.; Zhou, Y.; Wang, Z.; Rasmita, A.; Yang, J.; Li, X.; von Bardeleben, H. J.; Gao, W. Bright room temperature single photon source at telecom range in cubic silicon carbide. *Nat. Commun.* **2018**, *9*, 4106.
(44) Zhou, Y.; Wang, Z.; Rasmita, A.; Kim, S.; Berhane, A.; Bodrog, Z.; Adamo, G.; Gali, A.; Aharonovich, I.; Gao, W.-B. Room-temperature solid-state quantum emitters in the telecom range. *Sci. Adv.* **2018**, *4*, 3580.
(45) He, X.; Hartmann, N.; Ma, X.; Kim, Y.; Ihly, R.; Blackburn, J.; Gao, W.; Kono, J.; Yomogida, Y.; Hirano, A.; Tanaka, T.; Kataura, H.; Htoon, H.; Doorn, S. Tunable room-temperature single-photon emission at telecom wavelengths from sp3 defects in carbon nanotubes. *Nat. Photonics* **2017**, *11*, 577.
(46) Aharonovich, I.; Englund, D.; Toth, M. Solid-state single-photon emitters. *Nat. Photonics* **2016**, *10*, 631−641.
(47) Cygorek, M.; Korkusinski, M.; Hawrylak, P. Atomistic theory of electronic and optical properties of InAsP/InP nanowire quantum dots. *Phys. Rev. B* **2020**, *101*, 075307.
(48) Mnaymneh, K.; Dalacu, D.; McKee, J.; Lapointe, J.; Haffouz, S.; Weber, J. F.; Northeast, D. B.; Poole, P. J.; Aers, G. C.; Williams, R. L. On-Chip Integration of Single Photon Sources via Evanescent Coupling of Tapered Nanowires to SiN Waveguides. *Adv. Quant. Technol.* **2020**, *3*, 1900021.
(49) Northeast, D. B.; Dalacu, D.; Weber, J. F.; Phoenix, J.; Lapointe, J.; Aers, G. C.; Poole, P. J.; Williams, R. L. Optical fibre-based single photon source using InAsP quantum dot nanowires and gradient-index lens collection. *Sci. Rep.* **2021**, *11*, 22878.

https://doi.org/10.1021/acs.nanolett.2c04375
Nano Lett. 2023, 23, 962−968

Chapter 11

Conclusion

In this work, we conducted six independent studies on the quantum optical properties of InAsP/InP nanowire quantum dots grown using a position-control technique (SA-VLS epitaxy).

In Chapter 5 (Article 1), we characterized 42 nominally identical nanowire quantum dots. We provided a study on the characterization of excitonic emission by their power-dependent photoluminescence and correlation measurements which included both auto- and cross-correlations. We show that different excitonic complexes exhibit different correlation spectra and that the cross-correlations between excitonic complexes provided a more accurate way to discern between them. We show that the mean biexciton-exciton, $XX - X$, separation is $\sim 2\,\text{meV}$ and the mean charged exciton-exciton, $X^- - X$, separation is $\sim 6\,\text{meV}$. A simulation was also provided to calculate the emission spectra, which highlight the importance of the distribution of arsenic (As) atoms within the quantum dot. We show that a decreased $XX - X$ binding energy can be obtained by assuming an inhomogeneous distribution of As atoms.

In Chapter 6 (Article 2), we looked at a 10×10 array of nanowire quantum dots which showed $100\,\%$ growth yield. We characterized the nanowires in terms of their source efficiency, single-photon purity, and spectral purity. From sampling 14 devices, we found that the devices yielded a mean source efficiency of $\eta = 23\%$ with a peak value of $30\,\%$, a mean single-photon purity of $96\,\%$ with a peak value of $99.4\,\%$, and linewidths ranged from $4\times$ to $20\times$ greater than their transform-limited values. We established that nanowire quantum dots provide a viable route towards efficiently generating single-photons.

In Chapter 7 (Article 3), we performed power-dependent correlation spectroscopy of two distinct nanowire quantum dots. We provided a comparison of the auto- and cross-correlation

measurements between nominally identical nanowire quantum dots emitting from three complexes, the neutral exciton, X, the charged exciton, X^-, and the neutral biexciton, XX, and a second emitting a fourth complex, the positively charged exciton, X^+. We describe the rich temporal features observed in the correlation measurements in terms of capture rates of carriers, bunching amplitudes, and decay rates. The results suggest that electrons and holes are captured within quantum dots at different rates. We developed a 16-level stochastic model to simulate the auto-correlation measurements which allows for the individual control of the capture times of electrons and holes. The model provided reasonable fits to the measured data and highlighted the rich carrier dynamics within nanowire quantum dot systems. We describe memory effect in terms of carrier capture rates and unwanted memory effects can be obtained using simulations that provide a much larger capture rate of electrons compared to holes.

In Chapter 8 (Article 4), we investigated the linewidth of an optimized nanowire quantum dot which showed a Lorantzian linewidth corresponding to $2\times$ its lifetime limited value at low excitation power and temperature. We investigated the effect of increasing the growth temperature of the shell of the nanowire on the optimal linewidth and found that defects within the shell did not significantly affect the measured linewidth. We further studied the linewidth as a function of excitation power and temperature where we observed significant broadening of the linewidth for temperatures above 8 K. We concluded that, for low excitation powers, $P < 0.4P_{\text{sat}}$, and temperatures, $T < 8\,\text{K}$, phonon dephasing was not the source of the excess broadening. We speculated that, instead, it likely arises from residual inhomogeneous broadening, which is not revealed using a simple lineshape fitting procedure. We also provide a calculation for the temperature dependent linewidth broadening using an independent Boson model that considers both deformation and piezoelectric exciton-phonon coupling.

In Chapter 9 (Article 5), we studied a nanowire system consisting of five quantum dots, which were selectively positioned within a single nanowire core. Individual quantum dot emission wavelengths were tuned by changing the As concentration within the dots which provided a spacing of $\sim 7\,\text{nm}$. We characterize each quantum dots by their single-photon purity and detected count rates. We found that the total count rates scaled linearly with the number of emitters and provided an average multiphoton emission probability of $< 4\,\%$ when excited at saturation. We further studied the single-photon purity of each dot as a function of excitation power. Using a stochastic model, which included band-to-band decay rates, carrier capture rates, and the radiative decay rates of the dot, the re-excitation probability as a function of excitation power was extracted. We showed that re-excitation scaled linearly with excitation power and, in most cases, tended to zero. Due to the emission rate of the quantum dots being

limited by their emission lifetimes, this multiplexing method provides a way to increase the emission rate which would only be limited by the number of emitters.

Finally, in Chapter 10 (Article 6), we studied a nanowire quantum dot-in-a-rod structure which provided excitonic emission at 1310 nm (O-band). The emission is characterized by its single-photon purity, and efficiency at 4 K. We measure detector count rates up to 1.9 Mcps under above-band pulsed excitation at 80 MHz corresponding to a source efficiency of $\sim 28\,\%$ with a single-photon purity of $\sim 98\,\%$ measured at saturation. Such a source operating at 4 K is on par with state-of-the-art devices. We further investigated the single-photon purity as a function of temperature where we measured a steady rise in multi-photon emission probability as the temperature was increase from 10 K to 120 K. The single-photon purity is shown to saturate at $\sim 40\,\%$ for $T > 120$ K and increased to $\sim 57\,\%$ at 300 K. To my knowledge these results demonstrate superior performance compared to all other quantum dot based approaches operating at telecom wavelengths.

Chapters 1 and 2 describes the fundamental characteristics required for ideal single-photon sources in terms of efficiency, single-photon purity, coherence, and indistinguishability. The above-band excitation scheme utilized throughout this work showed promise in efficiently generating single-photons with high single-photon purity, at a repetition rate limited by the lifetime of the emitter. Such source can be utilized in some implementation of QKD protocols such as BB84 where the single-photon purity is only required to be $> 90\,\%$ without the requirement of indistinguishability.

However, most proposed applications for quantum photonic information technologies require the generation of indistinguishable photons. The timing jitter and charge noise introduced by the above-band excitation scheme provides a source of distinguishability in the emission times of sequential photons, limiting its two-photon interference visibility at a beamsplitter. Although instrumental in developing the sources, above-band excitation is not the envisioned mode of operation in the long term. For sources exhibiting highly indistinguishable photons over long time scales, coherent excitation schemes will be required, including strictly resonant, two photons excitation, notch-filtered adiabatic rapid passage (NARP)[160], and swing-up[161].

To summarize, we have shown that InAsP/InP quantum dot nanowires grown using the SA-VLS position control technique provides a viable route towards the efficient generation of high quality single-photons. Such devices also show promise for its integration with hybrid on-chip platforms. Using a "pick and place" technique, Mnaymneh et al.[162] showed the integration of these nanowires on SiN waveguides. The transfer process was shown to be

a promising method of creating hybrid integrated devices. Using this approach with more complicated structures such as ring resonators, one can utilize the Purcell enhancement within the ring cavities which would allow faster emission rates by decreasing the lifetime of the emitters[163]. One can envision many wavelength multiplexed nanowire quantum dot sources integrated on chip where total emission rates would benefit from the multi-dot usage and the Purcell enhancement. Such devices would provide a route towards several GHz emission rates.

Bibliography

[1] P. Michler, editor. *Quantum Dots for Quantum Information Technologies*. Nano-Optics and Nanophotonics. Springer, Switzerland, 2017.

[2] P. Laferrière, E. Yeung, I. Miron, D. B. Northeast, S. Haffouz, J. Lapointe, M. Korkusinski, P. J. Poole, R. L. Williams, and D. Dalacu. Unity yield of deterministically positioned quantum dot single photon sources. *Sci. Rep.*, 12(1):1–9, 2022.

[3] D. Dalacu, P. J. Poole, and R. L. Williams. Nanowire-based sources of non-classical light. *Nanotech.*, 30:232001, 2019.

[4] C.H. Bennett and G. Brassard. Quantum cryptography: Public key distribution and coin tossing. *Proc. of IEEE Int. Conf. on Comput. Sys. and Sign. Proces.*, 175:8, 1984.

[5] A. K. Ekert. Quantum cryptography based on Bell's theorem. *Phys. Rev. Lett.*, 67:661–663, 1991.

[6] N. Gisin, G. Ribordy, W. Tittel, and H. Zbinden. Quantum cryptography. *Rev. Mod. Phys.*, 74:145–195, 2002.

[7] E. Knill, R. Laflamme, and G. Milburn. A scheme for efficient linear optics quantum computation. *Nature*, 409:46–52, 2001.

[8] P. Kok, W. J. Munro, K. Nemoto, T. C. Ralph, J. P. Dowling, and G. J. Milburn. Linear optical quantum computing with photonic qubits. *Rev. Mod. Phys.*, 79:135–174, 2007.

[9] T. Nagata, R. Okamoto, J. L. O'Brien, K. Sasaki, and S. Takeuchi. Beating the standard quantum limit with four-entangled photons. *Science*, 316(5825):726–729, 2007.

[10] T. Ono, R. Okamoto, and S. Takeuchi. An entanglement-enhanced microscope. *Nat. Commun*, 4:1–7, 2013.

[11] M. Müller, H. Vural, C. Schneider, A. Rastelli, O. G. Schmidt, S. Höfling, and P. Michler. Quantum-dot single-photon sources for entanglement enhanced interferometry. *Phys. Rev. Lett.*, 118(257402), 2017.

[12] V. Giovannetti, S. Lloyd, and L. Maccone. Quantum metrology. *Phys. Rev. Lett.*, 96(1):010 401, 2006.

[13] A. Müller, H. Zbinden, and N. Gisin. Quantum cryptography over 23 km in installed under-lake telecom fibre. *EPL*, 33:335, 1996.

[14] J. Yin, Y. Li, S. Liao, M. Yang, Y. Cao, L. Zhang, J. Ren, W. Cai, W. Liu, S. Li, R. Shu, Y. Huang, L. Deng, L. Li, Q. Zhang, N. Liu, Y. Chen, C. Lu, X. Wang, F. Xu, J. Wang, C. Peng, A. K. Ekert, and J. Pan. Entanglement-based secure quantum cryptography over 1,120 kilometres. *Nature*, 582:501–505, 2020.

[15] G. Ribordy, J. Brendel, J-D. Gautier, N. Gisin, and H. Zbinden. Long-distance entanglement-based quantum key distribution. *Phys. Rev. A*, 63(012309), 2000.

[16] W. Tittel, J. Brendel, H. Zbinden, and N. Gisin. Quantum cryptography using entangled photons in energy-time Bell states. *Phys. Rev. Lett.*, 84(4737), 2000.

[17] A. Mair, A. Vaziri, G. Weihs, and A. Zeilinger. Entanglement of the orbital angular momentum states of photons. *Nature*, 412:313–316, 2001.

[18] C. Joshi, A. Farsi, S. Clemmen, S. Ramelow, and A. L. Gaeta. Frequency multiplexing for quasi-deterministic heralded single-photon sources. *Nat. Commun.*, 8:847, 2018.

[19] I. Aharonovich, D. Englund, and M. Toth. Solid-state single-photon emitters. *Nat. Photonics*, 10:631–641, 2016.

[20] G. Grynberg, A. Aspect, and C. Fabre. *Introduction to Quantum Optics: From the Semi-classical Approach to Quantized Light.* Cambridge University Press, 2010.

[21] A. Migdall, S. V. Polyakov, J. Fan, and J. C. Bienfang. *Single-Photon Generation and Detection, Volume 45.* Elsevier, 2013.

[22] R. J. Glauberl. The quantum theory of optical coherence. *Phys. Rev.*, 130:2529, 1963.

[23] R. Hanbury Brown and R. Q. Twiss. A test of a new type of stellar interferometer on sirius. *Nature*, 178:1046–1048, 1956.

[24] C. Gerry and P. Knight. *Introductory Quantum Optics.* Cambridge University Press, 2010.

[25] R. Loudon. *The quantum theory of light.* Oxford Science Publications, 2000.

[26] P. Grangier, G. Roger, and A. Aspect. Experimental evidence for a photon anticorrelation effect on a beam splitter: A new light on single-photon interferences. *EPL*, 1(173), 1986.

[27] M. Fox. *Quantum Optics.* Oxford, 2006.

[28] D. Bouwmeester, J-W. Pan, K. Mattle, M. Eibl, H. Weinfurter, and A. Zeilinger. Experimental quantum teleportation. *Nature*, 390(6660), 1998.

[29] H. Lee, P. Kok, and J. P. Dowling. A quantum rosetta stone for interferometry. *J. Mod. Opt.*, 49(14-15):2325–2338, 2002.

[30] K. J. Resch, K. L. Pregnell, R. Prevedel, A. Gilchrist, G. J. Pryde, J. L. O'Brien, and A. G. White. Time-reversal and super-resolving phase measurements. *Phys. Rev. Lett.*, 98(223601), 2007.

[31] H. J. Kimble. The quantum internet. *Nature*, 453:1023–1030, 2008.

[32] C. K. Hong, Z. Y. Ou, and L. Mandel. Measurement of picosecond time intervals between two photons by interference. *Phys. Rev. Lett.*, 59:2044–2046, 1987.

[33] N. Somaschi, V. Giesz, J.C. Loredo, M. P. Almeida, G. Hornecker, S.L. Portalupi, T. Grange, C. Antón, J. Demory, C. Gómez, I. Sagnes, N. D. Lanzillotti-Kimura, A. Lemaître, A. Auffèves, A. G. White, L. Lanco, and P. Senellart. Near-optimal single-photon sources in the solid state. *Nat. Photon.*, 10:340–345, 2016.

[34] P. Senellart, G. Solomon, and A. White. High-performance semiconductor quantum-dot single-photon sources. *Nat. Nanotech.*, 12:1026, 2017.

[35] X. Guo, C. L. Zou, C. Schuck, H. Jung, R. Cheng, and H. X. Tang. Parametric down-conversion photon-pair source on a nanophotonic chip. *Light: Sci. Appl.*, 6:e16249, 2017.

[36] M. J. Collins, C. Xiong, I. H. Rey, T. D. Vo, J. He, S. Shahnia, C. Reardon, T. F. Krauss, M. J. Steel, A. S. Clark, and B. J. Eggleton. Integrated spatial multiplexing of heralded single-photon sources. *Nat. Commum.*, 4(2582), 2013.

[37] H. J. Kimble, M. Dagenais, and L. Mandel. Photon antibunching in resonance floures-cence. *Phys. Rev. Lett.*, 39:691–695, 1977.

[38] F. Diedrich and H. Walther. Nonclassical radiation of a single stored ion. *Phys. Rev. Lett.*, 58:203–206, 1987.

[39] A. Kuhn, M. Hennrich, T. Bondo, and G. Rempe. Controlled generation of single photons from a strongly coupled atom-cavity system. *Appl. Phys. B.*, 69:373–377, 1999.

[40] M. Hennrich, T. Legero, A. Kuhn, and G. Rempe. Vacuum-stimulated raman scattering based on adiabatic passage in a high-finesse optical cavity. *Phys. Rev. Lett.*, 85(4872), 2000.

[41] A. Kuhn, M. Hennrich, and G. Rempe. Deterministic single-photon source for distributed quantum networking. *Phys. Rev. Lett.*, 89:067901, 2002.

[42] T. Basché, W. E. Moerner, M. Orrit, and H. Talon. Photon antibunching in the fluorescence of a single dye molecule trapped in a solid. *Phys. Rev. Lett.*, 69(1516), 1992.

[43] L. Fleury, J. Segura, G. Zumofen, B Hecht, and U. P. Wild. Nonclassical photon statistics in single-molecule fluorescence at room temperature. *Phys. Rev. Lett.*, 84(1148), 2000.

[44] F. De Martini, G. Di Giuseppe, and M. Marrocco. Single-mode generation of quantum photon states by excited single molecules in a microcavity trap. *Phys. Rev. Lett.*, 76(900), 1996.

[45] Christian Brunel, Brahim Lounis, Philippe Tamarat, and Michel Orrit. Triggered source of single photons based on controlled single molecule fluorescence. *Phys. Rev. Lett.*, 83(2722), 1999.

[46] B. Lounis and W. E. Moerner. Single photons on demand from a single molecule at room temperature. *Nature*, 407:491–493, 2000.

[47] J. McKeever, A. Boca, A. D. Boozer, R. Miller, J. R. Buck, A. Kuzmich, and H. J. Kimble. Deterministic generation of single photons from one atom trapped in a cavity. *Science*, 303:1992–1994, 2004.

[48] C. Kurtsiefer, S. Mayer, P. Zarda, and H. Weinfurter. Stable solid-state source of single photons. *Phys. Rev. Lett.*, 85:290–293, 2000.

[49] R. Brouri, A. Beveratos, J. P. Poizat, and P. Grangier. Photon antibunching in the fluorescence of individual color centers in diamond. *Opt. Lett.*, 25(17):1294–1296, 2000.

[50] A. Beveratos, R. Brouri, T. Gacoin, A. Villing, J.-P. Poizat, and P. Grangier. Single photon quantum crytography. *Phys. Rev. Lett.*, 13:187901, 2002.

[51] F. Sledz, S. Piccolomo, A. M. Flatae, S. Lagomarsino, R. Rechenberg, M. F. Becker, S. Sciortino, N. Gelli, I. A. Khramtsov, D. Yu. Fedyanin, G. Speranza, L. Giuntini, and M. Agio. Photoluminescence of nitrogen-vacancy and silicon-vacancy color centers in phosphorus-doped diamond at room and higher temperatures. *arXiv preprint arXiv:2101.05904*, 2021.

[52] E. Wu, J. R. Rabeau, F. Treussart, H. Zeng, P. Grangier, S. Prawer, and J. F. Roch. Nonclassical photon statistics in a single nickel-nitrogen diamond color center photoluminescence at room temperature. *Journal of Modern Optics*, 55(17), 2008.

[53] P. Michler, A. Kiraz, C. Becher, W. V. Schoenfeld, P.M. Petroff, L. Zhang, E. Hu, and A. Imamoglŭ. A quantum dot single-photon turnstile device. *Science*, 290:2282–2285, 2000.

[54] C. Santori, M. Pelton, G. Solomon, Y. Dale, and Y. Yamamoto. Triggered single photons from a quantum dot. *Phys. Rev. Lett.*, 86(8):1502–1505, 2001.

[55] V. Zwiller, H. Blom, P. Jonsson, N. Panev, S. Jeppesen, T. Tsegaye, E. Goobar, M.-E. Pistol, L. Samuelson, and G. Björk. Single quantum dots emit single photons at a time: Antibunching experiments. *Appl. Phys. Lett.*, 78(17):2476–2478, 2001.

[56] E. Moreau, J. M. Gérard, I. Abram, L. Manin, and V. Thierry-Mieg. Single-mode solid-state single photon source based on isolated quatum dots in pillar microcavities. *Appl. Phys. Lett.*, 79(18):2865–2867, 2001.

[57] R. M. Thompson, R. M. Stevenson, A. J. Shields, I. Farrer, C. J. Lobo, D. A. Ritchie, M. L. Leadbeater, and M. Pepper. Single-photon emission from exciton complexes in individual quantum dots. *Phys. Rev. B*, 64(201302(R)), 2001.

[58] M. Pelton, C. Santori, J. Vucković, B. Zhang, G. S. Solomon, J. Plant, and Y. Yamamoto. Efficient source of single photons: A single quantum dot in a micropost microcavity. *Phys. Rev. Lett.*, 89(23):233602, 2002.

[59] C. Santori, D. Fattal, J. Vučković, G. Solomon, and Y. Yamamoto. Indistinguishable photons from a single-photon device. *Nature*, 419:594–597, 2002.

[60] Z Yuan, B. E. Kardynal, R. M. Stevenson, A. J. Shields, C. J. Lobo, K. Cooper, N. S. Beattie, D. A. Ritchie, and M. Pepper. Electrically driven single-photon source. *Science*, 295(5552):102–105, 2001.

[61] N. Akopian, N. H. Lindner, E. Poem, Y. Berlatzky, J. Avron, and D. Gershoni. Entangled photon pairs from semiconductor quantum dots. *Phys. Rev. Lett.*, 96:130501, 2006.

[62] R. M. Stevenson, R. J. Young, P. Atkinson, K. Cooper, D. A. Ritchie, and A. J. Shields. A semiconductor source of triggered entangled photon pairs. *Nature*, 439:197–182, 2006.

[63] R. Hafenbrak, S. M. Ulrich, P Michler, L. Wang, A Rastelli, and O. G. Schmidt. Triggered polarization-entangled photon pairs from a single quantum dot up to 30 K. *New J. Phys.*, 9(315), 2007.

[64] H. Wang, Z.-C. Duan, Y.-H. Li, Si Chen, J.-P. Li, Y.-M. He, M.-C. Chen, Y. He, X. Ding, C.-Z. Peng, C. Schneider, M. Kamp, S. Höfling, C.-Y. Lu, and J.-W. Pan. Near-transform-limited single photons from an efficient solid-state quantum emitter. *Phys. Rev. Lett.*, 116:213601, 2016.

[65] N. Tomm, A. Javadi, N. O. Antoniadis, D. Najer, M. C. Löbl, Al. R. Korsch, R. Schott, S. R. Valentin, A. D. Wieck, A. Ludwig, and R. J. Warburton. A bright and fast source of coherent single photons. *Nature Nano.*, 16:399, 2021.

[66] L. Schweickert, K. D. Jöns, K. D. Zeuner, S. F. Covre da Silva, H. Huang, T. Lettner, M. Reindl, J. Zichi, R. Trotta, A. Rastelli, and V. Zwiller. On-demand generation of background-free single photons from a solid-state source. *Appl. Phys. Lett.*, 112(093106), 2018.

[67] C. Schimpf, M. Reindl, D. Huber, B. Lehner, S. F. Covre Da Silva, S. Manna, M. Vyvlecka, P. Walther, and A. Rastelli. Quantum cryptography with highly entangled photons from semiconductor quantum dots. *Sci. Adv.*, 7(16):eabe8905, 2021.

[68] J. H. Kim, S. Aghaeimeibodi, J. Carolan, D. Englund, and E. Waks. Hybrid integration methods for on-chip quantum photonics. *Optica*, 7(4):291–308, 2020.

[69] P. Guyot-Sionnest. Quantum dots: An emerging class of soluble optical nanomaterials. *Material Matters*, 2(1), 2007.

[70] S. J. Angus, A. J. Ferguson, A. S. Dzurak, and R. G. Clark. Gate-defined quantum dots in intrinsic silicon. *Nano. Lett.*, 7:2051–2055, 2007.

[71] M. Bayer. Bridging two worlds: Colloidal versus epitaxial quantum dots. *Annalen der Physik*, 531(6), 2019.

[72] P. J. Poole, J. McCaffrey, R. L. Williams, J. Lefebvre, and D. Chitrani. Chemical beam epitaxy of self-assembled InAs/InP quantum dots. *J. Vac. Sci. Technol. B*, 19(4):1467–1470, 2001.

[73] D. Bimberg, M. Grundmann, and NN Ledentsov. *Quantum dot Heterostructures*. John Wiler & Sons, 1999.

[74] M. Fox. *Optical properties of solids*. Oxford University Press, 2010.

[75] I. Vurgaftman, J. R. Meyer, and L. R. Ram-Mohanl. Band parameters for iii-v compound semiconductors and their alloys. *J. Appl. Phys.*, 89(11):5815–5875, 2001.

[76] Y. H. Huo, B. J. Witek, S. Kumar, J. R. Cardenas, J. X. Zhang, N. Akopian, R. Singh, E. Zallo, R. Grifone, D. Kriegner, R. Trotta, F. Ding, J. Stangl, V. Zwiller, G. Bester, A. Rastelli, and O. G. Schmidt. Electronic structure of self-assembled InAs/InP quantum dots: Comparison with self-assembled InAs/GaAs quantum dots. *Phys. Rev. B*, 77:045326, 2008.

[77] E. G. Gadret, G. O. Dias, L. C. O. Dacal, Jr. M. M. de Lima, C. V. R. S. Ruffo, F. Iikawa, M. J. S. P. Brasil, T. Chiaramonte, M. A. Cotta, L. H. G. Tizei, D. Ugarte, and A. Cantarero. Valence-band splitting energies in wurtzite InP nanowires: Photoluminescence spectroscopy and *ab initio* calculations. *Phys. Rev. B*, 182:125327, 2010.

[78] Y. H. Huo, B. J. Witek, S. Kumar, J. R. Cardenas, J. X. Zhang, N. Akopian, R. Singh, E. Zallo, R. Grifone, D. Kriegner, R. Trotta, F. Ding, J. Stangl, V. Zwiller, G. Bester, A. Rastelli, and O. G. Schmidt. A light-hole exciton in a quantum dot. *Nat. Phys.*, 10:46–51, 2014.

[79] P. Hawrylak. Excitonic artificial atoms: Engineering optical properties of quantum dots. *Phys. Rev. B*, 8(60):5597, 1999.

[80] B. J. Witek, R. W. Heeres, U. Perinetti, E. P. A. M. Bakkers, L. P. Kouwenhoven, and V. Zwiller. Measurement of the g-factor tensor in a quantum dot and disentanglement of exciton spins. *Phys. Rev. B*, 84:195305, 2011.

[81] Y. Benny, R. Presman, Y. Kodriano, E. Poem, D. Gershoni, T. A. Truong, and P. M. Petroff. Electron-hole spin flip-flop in semiconductor quantum dots. *Phys. Rev. B*, 89:035316, 2014.

[82] J. M. Smith, P. A. Dalgarno, R. J. Warburton, A. O. Govorov, K. Karrai, B. D. Gerardot, and P. M. Petroff. Voltage control of the spin dynamics of an exciton in a semiconductor quantum dot. *Phys. Rev. Lett.*, 94(197402), 2005.

[83] O. Labeau, P. Tamarat, and B. Lounis. Temperature dependence of the luminescence lifetime of single CdSe/ZnS quantum dots. *Phys. Rev. Lett.*, 90(25), 2003.

[84] S. Strauf, N. G. Stoltz, M. T. Rakher, L. A. Coldren, P. M. Petroff, and D. Bouwmeester. High-frequency single-photon source with polarization control. *Nat. Photonics*, 1:704–708, 2007.

[85] T. Lund-Hansen, S. Stobbe, B. Julsgaard, H. Thyrrestrup, T. SÃŒnner, M. Kamp, A. Forchel, and P. Lodahl. Experimental realization of highly efficient broadband coupling of single quantum dots to a photonic crystal waveguide. *Phys. Rev. Lett.*, 101(113903), 2008.

[86] M. Cygorek, M. Korkusinski, and P. Hawrylak. Atomistic theory of electronic and optical properties of InAsP/InP nanowire quantum dots. *Phys. Rev. B*, 101:075307, 2020.

[87] D. Dalacu, K. Mnaymneh, J. Lapointe, X. Wu, P. J. Poole, G. Bulgarini, V. Zwiller, and M. E. Reimer. Ultraclean emission from InAsP quantum dots in defect-free wurtzite InP nanowires. *Nano Lett.*, 12:5919–5923, 2012.

[88] C. Santori, D. Fattal, J. Vuckovic, G. S. Solomon, and Y. Yamamoto. Single-photon generation with InAs quantum dots. *New. J. Phys.*, 6:89, 2004.

[89] C. Santori, D. Fattal, J. Vučković, G. S. Solomon, Edo Waks, and Y. Yamamoto. Submicrosecond correlations in photoluminescence from InAs quantum dots. *Phys. Rev. B*, 69:205324, 2004.

[90] O. Gazzano, T. Huber, V. Loo, S. Polyakov, E. B. Flagg, and G. S. Solomon. Effects of resonant-laser excitation on the emission properties in a single quantum dot. *Optica*, 5(4):354–359, 2018.

[91] G. Bulgarini, M. E. Reimer, and V. Zwiller. Optical polarization properties of a nanowire quantum dot probed along perpendicular orientations. *Appl. Phys. Lett.*, 101(111112), 2012.

[92] A. V. Kuhlmann, J. Houel, D. Brunner, A. Ludwig, D. Reuter, A. D. Wieck, and R. J. Warburton1. A dark-field microscope for background-free detection of resonance fluorescence from single semiconductor quantum dots operating in a set-and-forget mode. *Rev. Sci. Inst.*, 84:073905, 2013.

[93] S. Unsleber, Y.-M. He, S. Gerhardt, S. Maier, C.-Y. Lu, J.-W. Pan, N. Gregersen, M. Kamp, C. Schneider, and S. Höfling. Highly indistinguishable on-demand resonance fluorescence photons from a deterministic quantum dot micropillar device with 74% extraction efficiency. *Opt. Exp.*, 24:8539–8546, 2016.

[94] L. Leandro, J. Hastrup, R. Reznik, G. Cirlin, and N. Akopian. Resonant excitation of nanowire quantum dots. *npj Quantum Inf.*, 6(93), 2020.

[95] M. Müller, S. Bounouar, K. D. Jöns, M. Glässl, and P. Michler. On-demand generation of indistinguishable polarization-entangled photon pairs. *Nat. Photon.*, 8:224, 2014.

[96] D. Huber, M. Reindl, Y. Huo, H. Huang, J. S. Wildmann, O. G. Schmidt, A. Rastelli, and R. Trotta. Highly indistinguishable and strongly entangled photons from symmetric GaAs quantum dots. *Nat. Commun.*, 8:15506, 2017.

[97] U. Bockelmann, W. Heller, A. Filoramo, and Ph. Roussignol. Microphotoluminescence studies of single quantum dots. I.Time-resolved experiments. *Phys. Rev. B*, 55(7), 1997.

[98] Ph. Roussignol, W. Heller, A. Filoramo, and U. Bockelmann. Time-resolved spectroscopy of single quantum dots. *Physica E*, 2(588), 1998.

[99] V. Zwiller, M.-E. Pistol, D. Hessman, R. Cederstrom, W. Seifert, and L. Samuelson. Time-resolved studies of single semiconductor quantum dots. *Phys. Rev. B*, 59(7), 1999.

[100] E. Dekel, D.V. Regelman, D. Gershonia, E. Ehrenfreund, W. V. Schoenfeld, and P. M. Petroff. Radiative lifetimes of single excitons in semiconductor quantum dots - manifestation of the spatial coherence effect. *Solid State Communications*, 117(7):395–400, 2001.

[101] C. Santori, G. S. Solomon, M. Pelton, and Y. Yamamoto. Time-resolved spectroscopy of multiexcitonic decay in an InAs quantum dot. *Phys. Rev. B*, 65(073310), 2002.

[102] G. Bacher, R. Weigand, J. Seufert, V. D. Kulakovskii, N. A. Gippius, A. Forchel, K. Leonardi, and D. Hommel. Biexciton versus exciton lifetime in a single semiconductor quantum dot. *Phys. Rev. Lett.*, 83:4417–4420, 1999.

[103] R. Seguin, A. Schliwa, S. Rodt, K. Pötschke, U. W. Pohl, and D. Bimberg. Size-dependent fine-structure splitting in self-organized InAs/GaAs quantum dots. *Phys. Rev. Lett.*, 95:257402, 2005.

[104] M. Bayer, G. Ortner, O. Stern, A. Kuther, A. A. Gorbunov, A. Forchel, P. Hawrylak, S. Fafard, K. Hinzer, T. L. Reinecke, S. N. Walck, J. P. Reithmaier, F. Klopf, and F. Schäfer. Fine structure of neutral and charged excitons in self-assembled In(Ga)As/(Al)GaAs quantum dots. *Phys. Rev. B*, 65:195315, 2002.

[105] H. Y. Ramirez, C. H. Lin, C. C. Chao, Y. Hsu, W. T. You, S. Y. Huang, Y. T. Chen, H. C. Tseng, W. H. Chang, S. D. Lin, and S. J. Cheng. Electrically driven single-photon source. *Science*, 295(5552):102–105, 2001.

[106] A. J. Bennett, M. A. Pooley, R. M. Stevenson, M. B. Ward, R. B. Patel, A. Boyer de la Giroday, N. Sköld, I. Farrer, C. A. Nicoll, D. A. Ritchie, and A. J. Shields. Electric-field-induced coherent coupling of the exciton states in a single quantum dot. *Nat. Phys.*, 6:947–950, 2010.

[107] R. Singh. Tuning fine structure splitting and exciton emission energy in semiconductor quantum dots. *J. Lumin.*, 202:118–131, 2018.

[108] A. J. Hudson, R. M. Stevenson, A. J. Bennett, R. J. Young, C. A. Nicoll, P. Atkinson, K. Cooper, D. A. Ritchie, and A. J. Shields. Coherence of an entangled exciton-photon state. *Phys. Rev. Lett.*, 99:266802, 2007.

[109] R. Mark Stevenson, Andrew J. Hudson, Anthony J. Bennett, Robert J. Young, Christine A. Nicoll, David A. Ritchie, and Andrew J. Shields. Evolution of entanglement between distinguishable light states. *Phys. Rev. Lett.*, 101(170501), 2008.

[110] R. Winik, D. Cogan, Y. Don, I. Schwartz, L. Gantz, E. R. Schmidgall, N. Livneh, R. Rapaport, E. Buks, and D. Gershoni. On-demand source of maximally entangled photon pairs using the biexciton-exciton radiative cascade. *Phys. Rev. B*, 95(235435), 2017.

[111] A. Fognini, A. Ahmadi, M. Zeeshan, J. T. Fokkens, S. J. Gibson, N. Sherlekar, S. J. Daley, D. Dalacu, P. J. Poole, K. D. Jöns, V. Zwiller, , and M. E. Reimer. Dephasing free photon entanglement with a quantum dot. *ACS Photonics*, 6:1656, 2019.

[112] D. Dalacu, D. B. Northeast, P. J. Poole, G. C. Aers, R. L. Williams, K. A. Owen, and D. Oblak. Pump power control of photon statistics in a nanowire quantum dot. *Phys. Rev. B*, 102:115401, Sep 2020.

[113] A. Kiraz, S. Fälth, C. Becher, B. Gayral, W. V. Schoenfeld, P. M. Petroff, Lidong Zhang, E. Hu, and A. Imamoglŭ. Photon correlation spectroscopy of a single quantum dot. *Phys. Rev. B*, 65:161303(R), 2002.

[114] T. Aichele, V. Zwiller, and O. Benson. Visible single-photon generation from semiconductor quantum dots. *New J. Phys.*, 6:90, 2004.

[115] Y. He, O. Iff, N. Lundt, V. Baumann, M. Davanco, K. Srinivasan, S. Höfling, and C. Schneider. Cascaded emission of single photons from the biexciton in monolayered WSe_2. *Nat. Commun.*, 7(13409), 2016.

[116] T. Heindel, A. Thoma, I. Schwartz, E. R. Schmidgall, L. Gantz, D. Cogan, M. Straub, P. Schnauber, M. Gschrey, J.-H. Schulze, A. Strittmatter, S. Rodt, D. Gershoni, and S. Reitzenstein. Accessing the dark exciton spin in deterministic quantum-dot microlenses. *APL Photonics*, 2(121303), 2017.

[117] J. Kettler, M. Paul, F. Olbrich, K. Zeuner, M. Jetter, P. Michler, M. Florian, C. Carmesin, and F. Jahnke. Neutral and charged biexciton-exciton cascade in near-telecom-wavelength quantum dots. *Phys. Rev. B*, 94(045303), 2016.

[118] K. D. Jöns, L. Schweickert, M. A. M. Versteegh, D. Dalacu, P. J. Poole, A. Gulinatti, A. Giudice, V. Zwiller, and M. E. Reimer. Bright nanoscale source of deterministic entangled photon pairs violating Bell's inequality. *Sci. Rep.*, 7:1700, 2017.

[119] E. Moreau, I. Robert, L. Manin, V. Thierry-Mieg, J. M. Gérard, and I. Abram. Quantum cascade of photons in semiconductor quantum dots. *Phys. Rev. Lett.*, 87:183601, 2001.

[120] G. Sallen, A. Tribu, T. Aichele, R. André, L. Besombes, C. Bougerol, S. Tatarenko, K. Kheng, , and J. Ph. Poizat. Exciton dynamics of a single quantum dot embedded in a nanowire. *Phys. Rev. B*, 80:085310, 2009.

[121] B. Piętka, J. Suffczyński, M. Goryca, T. Kazimierczuk, A. Golnik, P. Kossacki, A. Wysmolek, J. A. Gaj, R. Stępniewski, and M. Potemski. Photon correlation studies of charge variation in a single GaAlAs quantum dot. *Phys. Rev. B*, 87:035310, 2013.

[122] P. Laferrière, E. Yeung, M. Korkusinski, P. J. Poole, R. L. Williams, D. Dalacu, J. Manalo, M. Cygorek, A. Altintas, and P. Hawrylak. Systematic study of the emission spectra of nanowire quantum dots. *Appl. Phys. Lett.*, 2021.

[123] A. V. Kuhlmann, J. H. Prechtel, J. Houel, A. Ludwig, D. Reuter, A. D. Wieck, and R. J. Warburton. Transform-limited single photons from a single quantum dot. *Nat. Commun.*, 6:8204, 2015.

[124] J. Houel, A. V. Kuhlmann, L. Greuter, F. Xue, M. Poggio, B. D. Gerardot, P. A. Dalgarno, A. Badolato, P. M. Petroff, A. Ludwig, D. Reuter, A. D. Wieck, and R. J. Warburton. Probing single-charge fluctuations at a GaAs/AlAs interface using laser spectroscopy on a nearby InGaAs quantum dot. *Phys. Rev. Lett.*, 108:107401, 2012.

[125] M. E. Reimer, G. Bulgarini, A. Fognini, R. W. Heeres, B. J. Witek, M. A. M. Versteegh, A. Rubino, T. Braun, M. Kamp, S. Höfling, D. Dalacu, J. Lapointe, P. J. Poole, and V. Zwiller. Overcoming power broadening of the quantum dot emission in a pure wurtzite nanowire. *Phys. Rev. B*, 93:195316, 2016.

[126] A. V. Kuhlmann, J. Houel, A. Ludwig, L. Greuter, D. Reuter, A. D. Wieck, M. Poggio, and R. J. Warburton. Charge noise and spin noise in a semiconductor quantum device. *Nat. Photonics*, 9:570, 2013.

[127] Y.-M. He, Y. He, Y.-J. Wei, D. Wu, M. Atatüre, C. Schneider, S. Höfling, M. Kamp, C.-Y. Lu, and J.-W. Pan. On-demand semiconductor single-photon source with near-unity indistinguishability. *Nat. Nano.*, 8:213–217, 2013.

[128] A. Högele, S. Seidl, M. Kroner, K. Karrai, R. J. Warburton, B. D. Gerardot, and P. M. Petroff. Voltage-controlled optics of a quantum dot. *Phys. Rev. Lett.*, 93:217401, 2004.

[129] M. Atatüre, J. Dreiser, A. Badolato, A. Högele, K. Karrai, and A. Imamoglu. Quantum-dot spin-state preparation with near-unity fidelity. *Science*, 312:551, 2006.

[130] J.-M. Gérard and B. Gayral. Strong purcell effect for InAs quantum boxes in three-dimensional solid-state microcavities. *J. Lightwave Tech.*, 17:2089, 1999.

[131] X. Ding, Y. He, Z.-C. Duan, N. Gregersen, M.-C. Chen, S. Unsleber, S. Maier, C. Schneider, M. Kamp, S. Höfling, C.-Y. Lu, and J.-W. Pan. On-demand single photons with high extraction efficiency and near-unity indistinguishability from a resonantly driven quantum dot in a micropillar. *Phys. Rev. Lett.*, 116:020401, 2016.

[132] A. Muller, E. B. Flagg, P. Bianucci, X.Y. Wang, D. G. Deppe, W. Ma, J. Zhang, G. J. Salamo, M. Xiao, and C. K. Shih. Resonance fluorescence from a coherently driven semiconductor quantum dot in a cavity. *Phys. Rev. Lett.*, 99:187402, 2007.

[133] F. J. Torcal-Milla, J.Lobera, A. M. Lopez, V. Palero, N. Andres, and M. P. Arroyo. Mach-zehnder-based measurement of light emitting diodes temporal coherence. *Optik*, 267(169722), 2022.

[134] P. K. Shukla, K. K. Sarangpani, S. Talwar, G. S. Purbia, S. V. Nakhe, and H. S. Vora. A modified Mach-Zehnder inferometer for the study of coherence of laser. In François Flory, editor, *Ninth International Topical Meeting on Education and Training in Optics and Photonics*, volume 9664, page 96642G. International Society for Optics and Photonics, SPIE, 2005.

[135] P. Gold, A. Thoma, S. Maier, S. Reitzenstein, C. Schneider, S. Höfling, and M. Kamp. Two-photon interference from remote quantum dots with inhomogeneously broadened linewidths. *Phys. Rev. B*, 89:035313, 2014.

[136] I. Favero, A. Berthelot, G. Cassabois, C. Voisin, C. Delalande, Ph. Roussignol, R. Ferreira, and J.-M. Gérard. Temperature dependence of the zero-phonon linewidth in quantum dots: An effect of the fluctuating environment. *Phys. Rev. B*, 75:073308, 2007.

[137] H.-K. Lo, M. Curty, and B. Qi. Measurement-device-independent quantum key distribution. *Phys. Rev. Lett.*, 108:130503, 2012.

[138] H.-K. Lo and H.-F. Chau. Unconditional security of quantum key distribution over arbitrarily long distances. *Science*, 283:2050–2056, 1999.

[139] H. Vural, S. L. Portalupi, and P. Michler. Perspective of self-assembled InGaAs quantum-dots for multi-source quantum implementations. *Appl. Phys. Lett.*, 117:030501, 2020.

[140] A. Kiraz, M. Atatüre, , and A. Imamoglu. Quantum-dot single-photon sources: Prospects for applications in linear optics quantum-information processing. *Phys. Rev. A*, 69:032305, 2004.

[141] Gabija Kiršanskė, Henri Thyrrestrup, Raphaël S. Daveau, Chris L. Dreeßen, Tommaso Pregnolato, Leonardo Midolo, Petru Tighineanu, Alisa Javadi, Søren Stobbe, Rüdiger Schott, Arne Ludwig, Andreas D. Wieck, Suk In Park, Jin D. Song, Andreas V. Kuhlmann, Immo Söllner, Matthias C. Löbl, Richard J. Warburton, and Peter Lodahl. Indistinguishable and efficient single photons from a quantum dot in a planar nanobeam waveguide. *Phys. Rev. B*, 96:165306, 2017.

[142] Ł. Dusanowski, S.-H. Kwon, C. Schneider, and S. Höfling. Near-unity indistinguishability single photon source for large-scale integrated quantum optics. *Phys. Rev. Lett.*, 122:173602, 2019.

[143] R. Uppu, H. T. Eriksen, H. Thyrrestrup, A. D. Uğurlu, Y. Wang, S. Scholz, A. D. Wieck, A. Ludwig, M. C. Löbl, . J. Warburton, P. Lodahl, and L. Midolo. On-chip deterministic operation of quantum dots in dual-mode waveguides for a plug-and-play single-photon source. *Nat. Commun.*, 11:3782, 2020.

[144] Ł. Dusanowski, D. Köck, E. Shin, S.-H. Kwon, C. Schneider, and S. Höfling. Purcell-enhanced and indistinguishable single-photon generation from quantum dots coupled to on-chip integrated ring resonators. *Nano Lett.*, 20:6357, 2020.

[145] I. N. Stranski and Von L. Krastanow. *Akad. Wiss. Lit. Mainz Abh. Math. Naturwiss. Kl. II b*, 146:797, 1939.

[146] A. N. Vamivakas, Y. Zhao, C. Y. Lu, and M. Atatüre. Spin-resolved quantum-dot resonance fluorescence. *Nat. Photon.*, 5:198–202, 2009.

[147] O. Iff, Q. Buchinger, M. Moczała-Dusanowska, M. Kamp, S. Betzold, M. Davanco, K. Srinivasan, S. Tongay, C. Antón-Solanas, Sven Höfling, and Christian Schneider. Purcell-enhanced single photon source based on a deterministically placed WSe_2 monolayer quantum dot in a circular bragg grating cavity. *Nano Lett.*, 21:4715–4720, 2021.

[148] J. Claudon, J. Bleuse, N. S. Malik, M. Bazin, P. Jaffrennou, N. Gregersen, C. Sauvan, P. Lalanne, and J.-M. Gérard. A highly efficient single-photon source based on a quantum dot in a photonic nanowire. *Nat. Photon.*, 4:174, 2010.

[149] D. Dalacu, A. Kam, D. G. Austing, X. Wu, J. Lapointe, G. C. Aers, and P. J. Poole. Selective-area vapour-liquid-solid growth of InP nanowires. *Nanotech.*, 20:395602, 2009.

[150] M. E. Reimer, G. Bulgarini, N. Akopian, M. Hocevar, M. Bouwes Bavinck, M. A. Verheijen, E. P. A. M. Bakkers, L. P. Kouwenhoven, and V. Zwiller. Bright single-photon sources in bottom-up tailored nanowires. *Nat. Commun.*, 3:737, 2012.

[151] I. Friedler, P. Lalanne, J. P. Hugonin, J. Claudon, J. M. Gérard, A. Beveratos, and I. Robert-Philip. Efficient photonic mirrors for semiconductor nanowires. *Opt. Lett.*, 33:2635–2637, 2008.

[152] O. Gazzano, S. Michaelis de Vasconcellos, C. Arnold, A. Nowak, E. Galopin, I. Sagnes, L. Lanco, A. Lemaître, and P. Senellart. Bright solid-state sources of indistinguishable single photons. *Nat. Commun.*, 4:1425, 2013.

[153] J. Brendel, N. Gisin, W. Tittel, and H. Zbinden. Pulsed energy-time entangled twin-photon source for quantum communication. *Phys. Rev. Lett.*, 82(12):2594–2597, 1999.

[154] P. G. Kwiat, K. Mattle, H. Weinfurter, A. Zeilinger, A. V. Sergienko, and Y. Shih. New high-intensity source of polarization-entangled photon pairs. *Phys. Rev. Lett.*, 75(24):4337–4341, 1995.

[155] F. Kaneda and P. G. Kwiat. High-efficiency single-photon generation via large-scale active time multiplexing. *Sci. Adv.*, 5(10):1–7, 2019.

[156] S. Haffouz, K. D. Zeuner, D. Dalacu, P. J. Poole, J. Lapointe, D. Poitras, K. Mnaymneh, X. Wu, M. Couillard, M. Korkusinski, E. Schöll, K. D. Jöns, V. Zwiller, and R. L. Williams. Bright single InAsP quantum dots at telecom wavelengths in position-controlled InP nanowires: The role of the photonic waveguide. *Nano Lett.*, 18(5):3047–3052, 2018.

[157] S. Haffouz, K. D. Zeuner, D. Dalacu, P. J. Poole, J. Lapointe, D. Poitras, K. Mnaymneh, X. Wu, M. Couillard, M. Korkusinski, E. Schöll, K. D. Jöns, V. Zwiller, and R. L. Williams. Bright single InAsP quantum dots at telecom wavelengths in position-controlled InP nanowires: The role of the photonic waveguide. *Nano Lett.*, 18:3047, 2018.

[158] D. Dalacu, K. Mnaymneh, X. Wu, J. Lapointe, G. C. Aers, P. J. Poole, and R. L. Williams. Selective-area vapor-liquid-sold growth of tunable InAsP quantum dots in nanowires. *Appl. Phys. Lett.*, 98:251101, 2011.

[159] S. Haffouz, P. J. Poole, J. Jin, X. Wu, L. Ginet, K. Mnaymneh, D. Dalacu, and R. L. Williams. Single quantum dot-in-a-rod embedded in a photonic nanowire waveguide for telecom band emission. *Appl. Phys. Lett.*, 117(113102), 2020.

[160] G. R. Wilbur, A. Binai-Motlagh, A. Clarke, A. Ramachandran, N. Milson, J. P. Healey, S. O'Neal, D. G. Deppe, and K. C. Hall. Notch-filtered adiabatic rapid passage for optically driven quantum light sources. *APL Photon.*, 7:111302, 2022.

[161] T. K. Bracht, M. Cosacchi, T. Seidelmann, Moritz Cygorek, Alexei Vagov, V. M. Axt T. Heindel, and D. E. Reiter. Swing-up of quantum emitter population using detuned pulses. *PRX Quantum*, 2:040354, 2021.

[162] K. Mnaymneh, D. Dalacu, J. McKee, J. Lapointe, S. Haffouz, J. F. Weber, D. B. Northeast, P. J. Poole, G. C. Aers, and R. L. Williams. On-chip integration of single photon sources via evanescent coupling of tapered nanowires to sin waveguide. *Adv. Quantum Tech.*, 3:1900021, 2020.

[163] Marcelo Davanco, Jin Liu, Luca Sapienza, Chen-Zhao Zhang, José Vinícius De Miranda Cardoso, Varun Verma, Richard Mirin, Sae Woo Nam, Liu Liu, and Kartik Srinivasan. Heterogeneous integration for on-chip quantum photonic circuits with single quantum dot devices. *Nat. Commun.*, 8:889, 2017.